

**AUTOMATED REFLECTION PHOTOELASTICITY:
DIGITAL DATA ACQUISITION AND USE**

SU JUAN ZHANG

**THESIS SUBMITTED FOR THE DEGREE OF
DOCTOR OF PHILOSOPHY**

**DEPARTMENT OF MECHANICAL ENGINEERING
UNIVERSITY OF SHEFFIELD**

JUNE 2000

Automated Reflection Photoelasticity: Digital Data acquisition and Use

Su Juan Zhang

Summary

Automation of reflection photoelasticity has simplified the stress and strain analysis of real engineering components and reduced analysis time. However, images obtained from automated reflection photoelasticity contain noise and accuracy of the analysis will be affected by the degraded intensity images. In the present study, major sources of noise in automated reflection photoelasticity have been found to be the photoelastic coating and the electronic instrumentation. An automated reflection polariscope PSIOS developed by Patterson and Wang (1998) for the simultaneous observation and capture of four phase-stepped photoelastic images was used as an example. The majority of the noise is in the high spatial frequency domain. The zero-phase, low pass Butterworth filter was found to be the most effective and flexible smoothing method for reducing the effect of noise in the intensity images.

Results from experiments performed for assessing the ability of the PSIOS indicated that it is capable of yielding accurate results for the stress analysis of real components in both static and dynamic conditions and that it is fast and easy to use.

Full-field experimental methods are often used to validate the stress distribution generated from numerical analysis. A common practice is to plot data along a line across the maps and to include both experimental and numerical results on the same axes. This approach is used widely and usually a reasonable, quantitative conclusion can be made. However, it cannot obtain more information about the relationship between the stress maps. Another method is to compare hot spots on experimental maps to the numerical maps. If the hot spots on the two maps match well, the numerical method is considered valid. However, when designs are being optimised for weight or crack paths are being investigated, comparison of the positions of the hot spots alone will not be enough and the correlation elsewhere in the data field should be taken into account. It has been shown that fit between the stress map from an experimental method and the stress map from the numerical analysis can be represented by a statistical parameter, the scaled standard deviation. An evaluation of the method was performed using stress maps from transmission photoelasticity, thermoelasticity and the finite element method as examples. The results from experiments using a curved tie-bar, a circular ring and a real engineering component in this case, a race car hub carrier indicated that the scaled standard deviation represents the fitness between the two stress maps. If the scaled standard deviation is smaller than 0.1, then the experimental map and the numerical map can be considered to be in good agreement.

Acknowledgements

Firstly, I would like to express my sincere gratitude to my supervisor Professor Eann. A. Patterson for his superb guidance, encouragement and support over the past three years.

I am very grateful to Mr. Michel Taroni, SNECM, Paris, for allowing me to access the vibration data, Dr Sandro Barone, the University of Pisa, for providing the FE data of the car hub carrier, and Mr. Huseyin Caglayan, University of Southampton, for his help on computer programming. Special thanks are given to Mr. Richard Greene, for providing the thermoelastic data of the car hub carrier and the proof reading of this thesis.

I would like to thank: Dr Mark Pacey, Dr Elizabeth Olden, Dr Zhifan Wang, Dr James Hobbs, Dr Alaster Yoxall, Dr Richard Burgete, Dr Rachel Tomlinson, Dr Steve Haake, Dr Wenyan Ji, Dr U. Galietti, Dr G. Burriesci, Mrs. Mei Cen, Mr. J. R. Estrada, Mr. M. H. Ortiz, Mr. G. Pitarresi and Mr. G. Tripoli and other colleagues in the experimental stress analysis group for their various help and advice during my research. Technical supports from Mr. Richard Kay and Mr. Terry Senior during the experimental work are also acknowledged.

In addition, I would like to thank the University of Sheffield for awarding me a Postgraduate Research Scholarship.

Finally, I am greatly indebted to my parents for their love, encouragement and continuing support. I am very grateful to my husband Yaohou for his patience and understanding, and to my lovely children Ang and Jade.

Contents

SUMMARY	i
ACKNOWLEDGEMENTS	ii
CONTENTS	iii
LIST OF FIGURES	ix
LIST OF TABLES	xvi
NOMENCLATURE	xvii

CHAPTER 1

INTRODUCTION	1
1.1 Objectives of the Study.....	2
1.2 Structure of the Thesis.....	4

CHAPTER 2

LITERATURE REVIEW	5
2.1 Photoelasticity.....	6
2.1.1 Fundamental Principles of Photoelasticity.....	6
2.1.2 Reflection Photoelasticity.....	10
2.1.3 Automated Photoelasticity.....	12
2.1.3.1 Point-by-point Approach.....	13
2.1.3.1.1 Acquisition of Automated Data Using Manual Polariscopes	13
2.1.3.1.2 Spectral Analysis.....	14
2.1.3.2 Full-field Approach.....	16
2.1.3.2.1 Full-field Method Using Image Processing.....	16
2.1.3.2.2 Phase-stepping Method.....	19
2.1.3.2.3. RGB Photoelasticity.....	24
2.1.3.2.4. The Fast Fourier Transform Method.....	24

2.2 Phase-stepping Systems (Patterson and Wang)	27
2.2.1. Automated Transmission Photoelasticity	27
2.2.1.1 Theory.....	27
2.2.1.2 System Configuration.....	29
2.2.2. Automated Reflection Photoelasticity (PSIOS)	33
2.2.2.1 Theory.....	33
2.2.2.2 System Configuration.....	36
2.3 Smoothing Methods in Automated Full-Field Photoelasticity.....	39
2.4 Comparison of Maps from Full Field Experimental, Theoretical and Numerical Method.....	42
2.5 Discussion.....	44
2.5.1 Photoelasticity.....	44
2.5.2 Phase-stepping Systems.....	45
2.5.3 Smoothing Methods in Automated Full-Field Photoelasticity.....	45
2.5.4 Comparison of Maps from Full-Field Experimental, Theoretical and Numerical Methods.....	47
2.6 Conclusions.....	49
Tables	50
Figures.....	51

CHAPTER 3

INITIAL ASSESSMENT OF THE AUTOMATED REFLECTION

POLARISCOPE, PSIOS.....	65
3.1 Introduction.....	66
3.2 Formulae of Stress Intensity Factor K_I for Strain Gauge and Photoelastic Methods.....	67
3.2.1 Strain Gauge Method.....	68
3.2.2 Conventional Photoelastic Method.....	71
3.2.3 Photographic and Automated Photoelastic Method.....	72
3.3 Experiments.....	75
3.3.1 Specimens.....	75

3.3.2 Strain Gauge Method.....	75
3.3.3 Conventional Reflection Photoelastic Method.....	76
3.3.4 Photographic Method (Nurse & Patterson, 1991).....	77
3.3.5 Automated Reflection Photoelasticity Method (PSIOS)	77
3.3.6 Newman's Numerical Solution.....	78
3.4 Discussion.....	79
3.5 Conclusion.....	81
Figures.....	82

CHAPTER 4

SOURCES OF NOISE AND EVALUATION OF SOME SMOOTHING

METHODS.....	87
4.1 Introduction.....	88
4.2 Sources of Noise.....	89
4.2.1 Experiments.....	89
4.2.2 Discussion.....	90
4.3 Evaluation of some Smoothing Methods.....	93
4.3.1 Evaluation of Smoothing Methods Using an Image Generated by a Computer Program.....	93
4.3.2 The Nine-point Smoothing Method.....	93
4.3.3 The Low-pass Butterworth Filter.....	94
4.4 Evaluation of Smoothing Methods Using an Image from the PSIOS.....	100
4.5 Discussion	101
4.6 Conclusion.....	102
Figures.....	103

CHAPTER 5

IMPLEMENTATION OF THE BUTTERWORTH FILTER AND

EVALUATION OF THE PROGRAM <u>SIUP</u>.....	119
---	------------

5.1 Introduction.....	120
-----------------------	-----

5.2 Selection of Ratio of the Cut-off to Nyquist Frequency in the Butterworth Filter.....	122
5.2.1 Method One (Counting the Number of Turning point)	122
5.2.2 Method Two (Empirical Method)	124
5.3 Description of the program <i>SIUP</i>	127
5.4 Validation of the Subroutine Butterworth Filter in the program <i>SIUP</i>	128
5.5 Evaluation of the Butterworth Filter in the Program <i>SIUP</i>	129
5.5.1 Plate with a Right Angle Fillet.....	129
5.5.1.1 Specimen.....	129
5.5.1.2 Experimental Procedure.....	129
5.5.1.3 Results and Discussion.....	129
5.5.2 The Compressor Blade.....	130
5.5.2.1 Apparatus.....	130
5.5.2.2 Experimental Procedures.....	132
5.5.2.2.1 Data Acquisition.....	132
5.5.2.2.2 Data Processing.....	132
5.5.2.3 Results and Discussion.....	133
5.6. Discussion.....	134
5.7 Conclusion.....	136
Tables.....	137
Figures.....	139

CHAPTER 6

COMPARATIVE METHOD FOR STRESS MAPS FROM EXPERIMENTAL METHOD AND NUMERICAL ANALYSIS.....

6.1 Introduction.....	186
6.2 Description of the Problem.....	188
6.3 Sampling Procedure.....	189
6.4 Correlation Method.....	190
6.4.1 Coefficient of Determination, R^2	190
6.4.2 Comparison of Stress Maps Using Correlation Coefficient r	192

6.4.3 Residual Analysis.....	194
6.5 Implementation of the Correlation Method.....	195
6.6 Experiments.....	196
6.6.1 Comparison of the Stress Maps from the Automatic Photoelasticity and Finite Element Analysis.....	196
6.6.2 Comparison of the Stress Maps from Thermoelasticity and Finite Element Analysis.....	197
6.6.2.1 Theory.....	197
6.6.2.2 Experiment.....	198
6.7 Discussion.....	201
6.8 Conclusion.....	203
Tables.....	204
Figures.....	205
CHAPTER 7	
DISCUSSION AND SUGGESTION FOR THE FUTURE WORK.....	217
7.1 Discussion.....	218
7.2 Suggestion for the Future Work.....	220
CHAPTER 8	
CONCLUSIONS.....	221
REFERENCES.....	223
APPENDIX A:	
Calculation of the Coefficients of the Butterworth Filter.....	231
A.1 Prewarp the Cut-off Frequency.....	232
A.2 Frequency Scale the Chosen $H(s)$	232
A.3 Use of Bilinear Transformation to Convert the Analog Filter into a Digital Filter.....	232

APPENDIX B:

Program <i>SIUP</i> : Software Description	233
B.1 Introduction.....	234
B.2 Running the program.....	234
B.3 Image Processing.....	234
B.4 Dialogue Boxes.....	235
B.5 Source code of the program <i>SIUP</i>	236
Figures.....	245

APPENDIX C:

Instruction for the Program <i>COCIMS</i>	246
---	-----

APPENDIX D:

Source Code of the Program <i>COCIMS</i>	247
D.1 Source Code for the Filename: co_fem.h.....	248
D.2 Source Code for the Filename: co_epe.h.....	248
D.3 Source Code for the Filename: COCIMS.cpp.....	250
D.4 Source Code for the Filename: co_fem.cpp.....	252

List of Figures

Chapter 2 Literature Review

2.1	Absolute retardation by a refracting plate in an immersion medium	51
2.2	Passage of light through a plane polariscope	51
2.3	Schematic illustration of a circular polariscope	52
2.4	Reflection Polariscope	52
2.5	Diagrams of light paths through photo-stress meter LF/2 as a crossed (a) plane polariscope; (b) a circular polariscope.	53
2.6	Schematic drawing of a system of spectral photoelasticity	54
2.7	The phase-stepping method in automated transmission photoelasticity	54
2.8	System configuration of the automated transmission photoelasticity based on the principles of phase-stepping	55
2.9	Maps of six phase-stepped light intensity data recorded using the automated transmission polariscope.	56- 57
2.10	The isochromatic and isoclinic parameters of the disc using the program <i>VIZION</i> .	57
2.11	The phase-stepping method in automated photoelasticity with beamsplitter inserted	58
2.12	Schematic diagram of the PSIOS system	59
2.13	Maps of light intensity data recorded using the automated reflection polariscope, PSIOS. The quadrant of a disk subject to a vertical compressive load	60
2.14	The isochromatic and isoclinic parameters of the disc using the program <i>PECAN</i>	60
2.15	Schematic diagram of the Seguchi <i>et al</i> formula	61
2.16	Kernel of the median filter 3x3 pixels	61
2.17	Kernel of the median filter 5x5 pixels	62
2.18	Schematic diagram of the Liebmann's formula	62
2.19	Schematic diagram of the Sixth difference method	63

2.20	Distribution of principal stress direction using FFT photoelastic method	63
2.21	Maximum shear stress contours	64
2.22	Comparison of fringe orders for a circular disc under diametrical compression	64

Chapter 3 Initial Assessment of the Automated Reflection Polariscopes, PSIOS

3.1	Field adjacent to the crack tip is divided into three regions. The region <i>I</i> is the very near field, region <i>II</i> is the near field and region <i>III</i> is the far field.	82
3.2	Orientation of single element strain gauge on specimen B (not to scale), with loading applied in the Y-direction	82
3.3	Specimen A, an aluminium plate with cracks emanating from the central hole	83
3.4	Experimental set up of the conventional reflection photoelasticity	83
3.5	Experimental set up of the PSIOS system	84
3.6	Stress intensity factors founded by five methods for various loads on specimen A	85
3.7	Stress intensity factors founded by five methods for various loads on specimen B	86

Chapter 4 Source of Noise and Evaluation of some Smoothing Methods

4.1	First image of the four images of a plate with cracks from a central hole under tensile load obtained using the PSIOS instrument	103
4.2	The intensity data of the image in Fig. 4.1	103
4.3	System configuration of a transmission polariscopes with automated data acquisition (Experiment No.1)	104
4.4	System configuration of a reflection polariscopes with automated data acquisition (Experiment No.2).	104
4.5	System configuration of an automated transmission polariscopes using the PSIOS optical head (Experiment No. 3).	105
4.6	System configuration of an automated reflection polariscopes, PSIOS	

	(Experiment No. 4).	105
4.7	The intensity data from the four experiments (a) Experiment No. 1 (b) Experiment No. 2 (c) Experiment No. 3 (d) Experiment No. 4.	106
4.8	Quantization for rounding	107
4.9	An image generated using a computer program	107
4.10	An image with added speckle noise	107
4.11	The smoothed image of Fig.4.10 using Median filter 3x3	108
4.12	The smoothed image of Fig.4.10 using Median filter 3x3 double used	108
4.13	The smoothed image of Fig.4.10 using Median filter 5x5	108
4.14	The smoothed image of Fig.4.10 using Median filter 5x5 double used	108
4.15	The smoothed image of Fig.4.10 using Liebmann method	109
4.16	The smoothed image of Fig.4.10 using Liebmann method double use	109
4.17	The smoothed image of Fig.4.10 using Sixth difference method	109
4.18	The smoothed image of Fig.4.10 using Sixth difference method double use	109
4.19	Comparison of the original, speckle noised and smoothed data in a line, row 80, median 3x3	110
4.20	Comparison of the original, speckle noised and smoothed data in a line, row 80, median 5x5	110
4.21	Comparison of the original, speckle noised and smoothed data in a line, row 80, Liebmann method	111
4.22	Comparison of the original, speckle noised and smoothed data in a line, row 80, sixth difference method	111
4.23	Schematic diagram of the Nine-point smoothing method	112
4.24	The smoothed image of Fig.4.10 using Nine-point method	112
4.25	The smoothed image of Fig.4.10 using Nine-point method double use	112
4.26	Comparison of the original, speckle noised and smoothed data in a line, row 80, Nine-point method	113
4.27	Frequency response of the Butterworth filter	113
4.28	The smoothed image of Fig.4.10 using the Butterworth filter with normalised cut off ratio 0.15	114
4.29	Comparison of the original, speckle noised and smoothed data in a	

	line, row 80, the Butterworth filter with normalised cut off ratio 0.15	114
4.30	The intensity data of the image inside the rectangular area in Fig. 4.1	115
4.31	The smoothed intensity data using the Sixth difference method	115
4.32	The smoothed intensity data using the Median method 3x3	116
4.33	The smoothed intensity data using the Median method 5x5	116
4.34	The smoothed intensity data using Liebmann smoothing method	117
4.35	The smoothed intensity data using the Nine-point method	117
4.36	The smoothed intensity data using the low pass, zero- phase, 3rd order Butterworth filter with ratio of cut-off to Nyquist frequency 0.2	118

Chapter 5 Implementation of the Butterworth Filter and Evaluation of the Program SIUP

5.1	Flow chart of the algorithm of the program <u>CTP</u>	139
5.2	Image of HCAU1	140
5.3	Image of DISKM4	140
5.4	Image of ANL31	140
5.5	Image of ANH11	140
5.6	Image of ENL21	141
5.7	Relationship of number of turning point and the cut-off ratios used in the Butterworth filter.	141
5.8-	Original data and filtered data, for image ANL31 and HCAU1	142-
5.11		143
5.12-	Power spectrum for different specimens	144-
5.21		145
5.22-	Comparison of raw and smoothed intensity data	146-
5.27		163
5.28	Feature of the program <u>SIUP</u>	164
5.29	Flow chart of the Butterworth filter in the program <u>SIUP</u>	165
5.30	Image of a plate with right angle fillet	166
5.31	Image of a plate with cracks from central hole	166
5.32-	The raw and smoothed intensity data in Fig. 5.30 and Fig. 5.31 along	167-
5.35	lines AB and CD	168

5.36	Geometry and dimensions of the plate with right-angle fillet	169
5.37	First raw and smoothed images of the four images of the plate with right-angle fillet	170
5.38	The retardation maps from the raw and smoothed image of the plate	171
5.39	The isochromatic maps from the raw and smoothed image of the plate	172
5.40	The isoclinic maps from the raw and smoothed image of the plate	173
5.41	The comparison of the fringe orders from the raw and smoothed image of the plate	174
5.42	The comparison of the isoclinic angles from the raw and smoothed image of the plate	174
5.43	The compressor blade	175
5.44	Experimental set-up	175
5.45	Set-up of the compressor blade	176
5.46	Schematic diagram of the compressor blade in tension and compression	176
5.47	(a) Raw and (b) smoothed intensity data of first of the four images using the Butterworth filter. Cut-off ratio in column direction is 0.3 and in row direction is 0.2. The compressor blade is in tension at first mode of vibration, frequency 257 Hz, energy level 1 g	177
5.48	(a) Raw and (b) smoothed intensity data of first of the four images using the Butterworth filter. Cut-off ratio is 0.2. The compressor blade (lower part) is in tension at first mode of vibration, frequency 257 Hz, energy level 1 g	178
5.49	The comparison of retardation maps, from (a) raw (b) smoothed intensity data. (Upper part of the compressor blade in tension at second mode of vibration, frequency 617 Hz and energy level 5.01 g)	179
5.50	The comparison of the fringe order maps, from (a) raw (b) smoothed intensity data. (Upper part of the compressor blade in tension at second mode of vibration, frequency 617 Hz and energy level 5.01 g)	180
5.51	The comparison of isoclinic maps, from (a) raw (b) smoothed intensity data. (Upper part of the compressor blade in tension at	

	second mode of vibration, frequency 617 Hz and energy level 5.01 g)	181
5.52	The comparison of retardation maps, from (a) raw (b) smoothed intensity data. (Upper part of the compressor blade in tension at first mode of vibration, frequency 257 Hz and energy level 1 g)	182
5.53	The comparison of fringe order maps, from (a) raw (b) smoothed intensity data. (Upper part of the compressor blade in tension at first mode of vibration, frequency 257 Hz and energy level 1 g)	183
5.54	The comparison of isoclinic maps, from (a) raw (b) smoothed intensity data. (Upper part of the compressor blade in tension at first mode of vibration, frequency 257 Hz and energy level 1 g)	184

Chapter 6 Comparative Method for Stress Maps from Experimental Method and Numerical Analysis

6.1	Components of variation in Y	205
6.2	Tight fit versus loose fit of a regression line	205
6.3	Regression line of (a) 5 points and (b) repeated points	206
6.4	Flow chart of the program <i>COCIMS</i>	207
6.5	Profile of the program <i>COCIMS</i>	208
6.6	Dimensions of the curved tie-bar	209
6.7	Dimensions of the circular ring	209
6.8	Correlation coefficient r for different number of points in samples (curved tie-bar)	210
6.9	Correlation coefficient r for different number of points in samples (circular ring)	210
6.10	The isochromatic maps of the curved tie-bar (a) from photoelasticity (b) from FEM	211
6.11	The isochromatic maps of the circular ring (a) from photoelasticity (b) from FEM	212
6.12	Relationship between FEM and the photoelastic method for selected points (curved bar)	213
6.13	Relationship between FEM and the photoelastic method for selected points (circular ring)	213

6.14	Dimensions of the car hub carrier	214
6.15	Maps of the sum of the principal stresses from (a) SPATE, (b) Delta Therm and (c) FEM	215
6.16	Relationship between FEM and the SPATE for selected 82 data points (hub carrier)	216
6.17	The relationship between FEM and the Delta Therm for selected 87 data points (hub carrier)	216

Appendix B

B.4.1	Warning message for use of image that is not a RGB image	245
B.4.2	Dialog box for input of cut-off ratio in the Butterworth Filter	245

List of Tables

Chapter 2 Literature Review

- | | | |
|-----|--|----|
| 2.1 | Orientations of quarter-wave plate ϕ and analyser β in the automated transmission polariscope | 50 |
| 2.2 | Orientations of quarter-wave plate ϕ and analyser β in the automated reflection polariscope | 50 |

Chapter 4 Source of Noise and Evaluation of some Smoothing Methods

- | | | |
|-----|--|----|
| 4.1 | Specimens and instruments used in the four experiments | 89 |
|-----|--|----|

Chapter 5 Implementation of the Butterworth Filter and Evaluation of the Program SIUP

- | | | |
|-----|---|-----|
| 5.1 | Number of turning points of different images for different number data points | 137 |
| 5.2 | Filenames for specimen under different mode and energy levels | 138 |
| 5.3 | Switch position of the CCD colour camera in the PSIOS system | 138 |

Chapter 6 Comparative Method for Stress Maps from Experimental Method and Numerical Analysis

- | | | |
|-----|---|-----|
| 6.1 | Correlation coefficient of maps using curved tie-bar | 204 |
| 6.2 | Correlation coefficient of maps using curved tie-bar (100 & 200 points) | 204 |
| 6.3 | Correlation coefficient of maps using circular ring | 204 |

Nomenclature

- a : amplitude of light, crack length
- a_i, b_i : coefficient of the Butterworth filter
- A : calibration constant in thermoelasticity
- A_m, B_m : coefficients of stress function
- C_1, C_2 : absolute photoelastic coefficients
- C_p : specific heat at constant pressure
- C_ϵ : strain-optic coefficient
- C_σ : stress-optic coefficient
- d : plate of thickness
- d_s : scaled standard deviation
- E : electromagnetic radiation, elastic modulus
- $e(n)$: error between digital signal and analogue signal
- \hat{e}_i : i th residual
- f : gauge factor, stress optical constant
- f_c : cut-off frequency
- h : distance between the two adjacent points
- $h(i, j)$: separable transfer function
- i_v : intensity emerging when all the axes of the polariscope and specimen are parallel
- k : shift index
- k_x, k_y : transmission coefficients
- K_I : stress intensity factor under tensile opening mode loading conditions
- K_{AP} : apparent stress intensity factor
- l : gauge length
- n_0 : index of medium
- n_j : refractive index
- n_{j0} : relative refractive index
- N : fringe order
- $P_x(w)$: power spectral density
- P_β : Mueller matrix of an ideal linear polariser
- r : distance from the gauge to the crack tip, correlation coefficient
- $r_{xx}(k)$: autocorrelation function

- R : relative retardation
 R_I : absolute retardation of the light by the refracting plate
 $R_\alpha(\delta)$: Mueller matrix
 R^2 : coefficient of determination
 R_a^2 : adjusted coefficient of determination
 S : thermoelastic signal
 S, S' : stokes vector
 s^2 : mean square error
 t : time of the propagation, thickness of photoelastic coating
 T : absolute temperature of the material
 v : velocity of propagation
 v_1, v_2 : velocity of propagation
 w : sampling frequency
 x_{ij} : intensity at point i, j
 $x(n)$: analogue signal, discrete-time sequence
 $x_q(n)$: digital signal
 $x(n_1, n_2)$: digitized 2-D data is the input signal
 $y(n_1, n_2)$: output signal
 Y : geometric factor
 z : position along the axis of propagation
 z_{1i}, z_{2i} : values of data points on the maps from experiment and numerical analysis
 $Z(z)$: complex stress function
 Z_A, Z_B : function of coordinates x and y on maps A and B

Greek Symbols

- λ : wavelength of light
 ϕ : angle between a reference axis output quarter wave plate
 β : angle between a reference axis and the slow axis of the analyser
 α : isochromatic angle, angle for strain gauge orientation, linear coefficient of thermal expansion of the material
 θ : isoclinic angle, angle for strain gauge orientation
 δ : retardation
 ν : Poisson's ratio
 ρ : crack tip radius, density of the material

- Φ_{ij} : intensity at point i, j
 τ_{\max} : maximum shear stress
 M_{xx} : strain gauge output
 N_{ij} : stress change tensor
 $\sigma_{\alpha\alpha}$: second order non-singular term
 σ_1, σ_2 : principle stresses

Chapter One

Introduction

1.1 Objectives of the Study

1.2 Structure of the Thesis

1.1 Objectives of the Study

Full-field automated photoelasticity has been developed in last two decades and stress analysis using the technique has become easier, more precise and faster. The system based on the principles of phase stepping developed by Patterson and Wang (1991) for transmission photoelasticity can be used to acquire six stepped images to produce isochromatic and isoclinic maps, thus full-field stress and strain distributions for a model can be generated. In addition, stress intensity factors can be calculated from the above information. The automated reflection polariscope, PSIOS (Phase Stepped Images Obtained Simultaneously) (Patterson and Wang, 1998) requires only four stepped images to obtain these parameters. The PSIOS is designed to solve static and dynamic problems since the four stepped images can be obtained simultaneously. It is more sensitive than conventional polariscopes which means thin coatings can be applied to the component. The real component can be tested under service loads and there is no need to scale the stress and strain distribution of the component. However, a drawback of the PSIOS instrument is that the noise in the intensity images is more severe than in automated transmission photoelasticity. The degraded images affect the quality of the isochromatic and isoclinic maps and, subsequently, the stress and strain maps calculated from these parameters. Therefore, it is necessary to discern the sources of noise in the intensity images in order to remove the effect of the noise. Moreover, since the PSIOS instrument is newly developed, an assessment of the capabilities of the instrument is needed.

Stress maps from full-field photoelasticity can be used to validate stress maps from numerical analysis. Methods for comparing full-field stress maps obtained from experimental, theoretical and numerical methods can be classified into two main types. In the first type, maps are obtained using different methods when a specimen is loaded under the same conditions. A map of the difference of the two stress maps is used to present the error between the two methods. The second type of comparison uses data along a single line through the stress field and data from several sources are plotted on a single graph. These methods are used widely and usually a reasonable, quantitative conclusion can be made. Comparison between two digital images can be done using pixel-by-pixel comparison for corresponding points.

However, for stress maps from a numerical analysis and an experimental method, the pixel-by-pixel comparison is not as simple as for two digital images, because the data between the nodal points in the numerical analysis are obtained by interpolation which may not be used for problems of non-linear elastic fracture mechanics. It is necessary to find a comparative method for assessing quantitatively the correlation between the stress maps from full-field experimental methods and numerical analysis.

Therefore, objectives of the present study are:

- to find suitable methods to reduce the effect of noise in the intensity images obtained from the automated reflection polariscope, PSIOS;
- to find a correlation method for the comparison of stress maps obtained from full-field experimental methods and from numerical analysis;
- to assess capabilities of the automated reflection polariscope, PSIOS.

1.2 Structure of the Thesis

Chapter 2 is a literature review of the fundamentals of photoelasticity, the development of automated photoelasticity, smoothing methods employed to full-field images, and methods of comparison for two full-field stress maps.

Chapter 3 is an initial assessment of the automated reflection polariscope, PSIOS.

Chapter 4 is divided into two parts. The first part describes experiments conducted to find the sources of noise in the intensity images obtained from PSIOS instrument. The second part is a report of an evaluation of several smoothing methods using images obtained from the PSIOS instrument.

Chapter 5 describes the implementation and evaluation of the zero phase, third order, low pass Butterworth filter.

Chapter 6 concentrates on the development of a method for comparing stress maps from experimental method and numerical analysis.

Chapter 7 contains the discussion of results from the study and suggestion for future work.

Chapter 8 is the conclusions of the study.

Chapter Two

Literature Review

2.1 Photoelasticity

2.2 Phase-stepping Systems

2.3 Smoothing Methods in Full-field Automated Photoelasticity

2.4 Methods for Comparison of Maps from Full-field Experimental,
Theoretical and Numerical Methods

2.5 Discussion

2.6 Conclusions

2.1 Photoelasticity

Photoelasticity is an optical technique for measuring deformation that utilises the temporary birefringence exhibited by most transparent media when they are subjected to strain. It is the oldest and most useful form of measurement for engineering purposes. The fundamental principle of photoelasticity was established by Sir David Brewster in 1816. Since then, photoelasticity has been developed along with developments in material science and computer technology. Nowadays, automation of photoelasticity has made the application of the technique easier, more precise and quicker. The following sections are reviews of the fundamental principles of photoelasticity, reflection photoelasticity and automated photoelasticity.

2.1.1 Fundamental Principles of Photoelasticity

The simplest form of electromagnetic radiation can be described by the equation

$$E = A \cos \frac{2\pi}{\lambda} (z - vt) \quad (2.1)$$

where A and λ are maximum amplitude and wavelength of the light, z is position along the axis of propagation, and t , and v are the time and velocity of the propagation respectively.

Consider a ray of light passing through a plane parallel plate of thickness d and refractive index n_1 that is immersed in a medium of index n_0 , the ray that travels a distance d through the plate lags behind an undisturbed ray by an amount

$$R_1 = (n_{10} - 1)d \quad (2.2)$$

where R_1 is called the absolute retardation of the light by the refracting plate and n_{10} is relative refractive index. Figure 2.1 shows a schematic illustration of the process.

Birefringent media possess two refractive indices such that when a beam of plane polarised light enters the medium it becomes circularly polarised. It is thought that the ray of light is divided into two beams with orthogonal vectors. Absolute retardation of the two beams emerging from a birefringent plate can be represented by Equation (2.2) and

$$R_2 = (n_{20} - 1)d \quad (2.3)$$

The relative retardation or phase difference between the two beams is given by

$$R = R_1 - R_2 = (n_{10} - n_{20})d \quad (2.4)$$

There are relationships between stress, strain and birefringence for various materials. Experiments have shown that the principal axes of refraction correspond to the principal stress axes and each principal index of refraction is a linear function of the two stress components (Cloud, 1995, p. 65). The relative retardation can be expressed in terms of the stress through the use of the absolute photoelastic coefficients C_1 and C_2 , as

$$R = (C_1 - C_2)(\sigma_1 - \sigma_2)d \quad (2.5)$$

where σ_1 and σ_2 are principal stresses acting in directions normal to the propagation of light.

Equation (2.5) can be written in form

$$R = C_\sigma(\sigma_1 - \sigma_2)d \quad (2.6)$$

where $C_\sigma = C_1 - C_2$ is called the stress-optic coefficient.

Alternatively, it can be formulated in terms of strain

$$R = C_\epsilon(\epsilon_1 - \epsilon_2)d \quad (2.7)$$

where C_ϵ is the strain-optic coefficient.

The relative retardation is conveniently expressed as a fraction called the fringe order, N ,

$$N = \frac{R}{\lambda} = \frac{C_\sigma d}{\lambda}(\sigma_1 - \sigma_2) \quad (2.8)$$

In the application of photoelasticity, a simple set-up called a plane polariscope can be used in which a specimen is positioned between a polariser and an analyser. The passage of light through a plane polariscope is illustrated in Figure 2.2. The mathematical explanation of photoelastic stress analysis based on the determination of birefringence in a body through the use of polarised light is given as follows.

Consider a ray of light of wavelength λ , travelling in the z direction with velocity v and polarised in the yz plane. The ray impinges normally on a birefringent plate of thickness d whose principal refractive axes are inclined at angles θ and $\theta+90^\circ$ to the x -axis. The wave is split into two components that propagate through the plate at

different velocities v_1 and v_2 . As the two components leave the birefringent plate they have been retarded by different amounts. The light emerging from the analyser can be obtained by trigonometric calculation (Cloud, 1995, p.69)

$$E_e = A \sin \left[\frac{\pi}{\lambda} (n_{10} - n_{20}) d \right] \left(\sin \beta \sin 2\theta - \cos \beta \cos 2\theta \right) \sin \left[\frac{2\pi}{\lambda} \left(z - vt - \left(\frac{n_{10} + n_{20} - 2}{2} \right) d \right) \right] \\ + A \cos \left[\frac{\pi}{\lambda} (n_{10} - n_{20}) d \right] \cos \beta \cos \left[\frac{2\pi}{\lambda} \left(z - vt - \left(\frac{n_{10} + n_{20} - 2}{2} \right) d \right) \right] \quad (2.9)$$

Dark-field set up

When the polariser and analyser are crossed, $\beta = 90^\circ$, equation (2.9) reduces to

$$E_e = A \sin \left[\frac{\pi}{\lambda} (n_{10} - n_{20}) d \right] \sin 2\theta \sin \left[\frac{2\pi}{\lambda} \left(z - vt - \left(\frac{n_{10} + n_{20} - 2}{2} \right) d \right) \right] \quad (2.10)$$

This arrangement of the components is called a *dark-field* linear set-up. Extinction of intensity will occur when

$$(a) \theta = m\pi, \text{ where } m = 0, 1, 2, \dots$$

i.e. the polariser and analyser are aligned with the principal axes of refractive index or stress, this condition gives *isoclinic* fringes, or

$$(a) \frac{(n_{10} - n_{20})d}{\lambda} = 0, 1, 2, \dots$$

i.e. the relative retardation is an integer multiple of the wavelength, this condition gives *isochromatic* fringes.

Light-field set up

When the polariser and analyser are parallel, $\beta = 0^\circ$, equation (2.9) becomes

$$E_e = -A \sin \left[\frac{\pi}{\lambda} (n_{10} - n_{20}) d \right] \cos 2\theta \sin \left[\frac{2\pi}{\lambda} \left(z - vt - \left(\frac{n_{10} + n_{20} - 2}{2} \right) d \right) \right] \\ + A \cos \left[\frac{\pi}{\lambda} (n_{10} - n_{20}) d \right] \cos \left[\frac{2\pi}{\lambda} \left(z - vt - \left(\frac{n_{10} + n_{20} - 2}{2} \right) d \right) \right] \quad (2.11)$$

This arrangement of the components is called a *light-field* linear set-up. Extinction of intensity will occur when

$$(a) \theta = \pi/4,$$

i.e. the polariser and analyser are at 45° to the principal axes, or

$$(b) \frac{(n_{10} - n_{20})d}{\lambda} = (2m+1)/2$$

where m is an integer.

Isoclinic fringes are lines along which the principal stresses are at a constant angle to a set of arbitrary reference axes.

Isochromatic fringes are lines in the stress field along which there is constant principal stress difference or constant maximum shear stress value as shown by

$$\sigma_1 - \sigma_2 = 2\tau_{\max} = \frac{N\lambda}{C_\sigma d} \quad (2.12)$$

Isochromatic and isoclinic fringes are superimposed in a plane polariscope. To eliminate the isoclinic fringes from the whole field map, two quarter-wave ($\lambda/4$) plates are inserted into the polariscope. The axes of the $\lambda/4$ plates should be crossed and at 45° to the axes of polariser and analyser. This set-up is called a circular polariscope and is shown schematically in Figure 2.3. Both the plane and circular polariscopes reviewed above are configured as transmission polariscopes.

Photoelasticity embraces three broad categories: (1) photoelastic reflection coatings; (2) two-dimensional model analysis; and (3) three-dimensional model analysis. For two-dimensional model analysis, design geometry and cross sections are made from flat sheets of photoelastic material and analysed in a transmission polariscope. Three-dimensional model testing uses a stress-freezing process. The stress-freezing method of locking deformations into a model is based on the diphasic behaviour of many polymeric materials when they are heated. Polymeric materials are composed of long-chain hydrocarbon molecules. Some of the molecular chains are well bonded into a three-dimensional network of primary bonds, but a large number of molecules are loosely bonded together into shorter secondary chains. When the polymer is at room temperature, both sets of molecular bonds, the primary and the secondary, act to resist deformation due to applied load. However, as the temperature of the polymer is increased, the secondary bonds break down and the primary bonds carry the entire applied load. Since the secondary bonds constitute a very large portion of the polymer, the deflections in which the primary bonds

undergo are quite large and elastic in character. If the temperature of the polymer is lowered to room temperature while the load is maintained, the secondary bonds will re-form between the highly elongated primary bonds and serve to lock them into their extended positions. When the load is removed, the primary bonds relax slightly, but a significant portion of their deformation is not recovered. The elastic deformation of the primary bonds is permanently locked into the body by re-formed secondary bonds. Moreover, these deformations are locked in on a molecular scale; thus the deformation and accompanying birefringence are maintained in any small section cut from the original body (Dally and Riley, 1991, p.479). The procedure for three-dimensional model testing is that, first, a scaled three-dimensional model is made from a specially formulated epoxy resin, then the model is placed in an oven with loading applied and subjected to a carefully prescribed heating and cooling cycle to 'freeze' the deformations resulting from the loads. After the stress-freezing, the model is sectioned to permit removal of slices from various planes of interest. Finally a transmission polariscope is used to measure the complete stress distribution in the plane of the slice.

The photoelastic coating is observed in reflection and this method will be reviewed in next section.

2.1.2 Reflection Photoelasticity

The method of application of birefringent coatings represents an extension of the procedures of photoelasticity to the determination of surface strains in opaque two- and three- dimensional bodies. The thin coating is bonded to the surface of the prototype. When the prototype is loaded, surface displacements are transmitted to the coating to produce a strain field through the thickness of the coating. The distribution of the strain differences is determined by employing a reflection polariscope to record the fringe orders as a whole-field response of the coating. Since the coatings can be bonded directly to the prototype, the prototype can be used under service loading conditions. With appropriately selected coating materials, the method is applicable over a wide range of elastic and plastic strains. The photoelastic coating method is also very useful in converting the analysis of

complex non-linear stress situations in a prototype to the analysis of relatively simple linear elastic problems in the coating. Similarly, the anisotropic characteristics of composite materials can be examined in terms of an isotropic response in the coating (Zandman *et al*, 1977, p. xii).

The concept of birefringent coatings was first introduced by Mesnager (1930). He pointed out that, if an artificial coating is silvered on the rear face and glued to the component, the transparent coating will carry identical deformations that can be measured by double refraction. At that time he was unable to obtain practical results due to the lack of suitable sensitive photoelastic materials. Later in 1934, Mindlin implemented Mesnager's idea in a reflection polariscope. The set-up of the reflection polariscope is diagrammatically shown in Figure 2.4. Monochromatic light from a source S is collected by a lens L_1 and is converged to the centre of a polarising prism $P-A$ after being reflected from the surface of a partial mirror G . The diverging cone passes through a crystal retardation plate C and a lens L_2 to the model M . The reflected light passes through L_2 , the retardation plate the prism and partial mirror G , and finally onto the screen or photographic plate F . The method was tested using a Bakelite model of a U-frame with forces at the free ends of the vertical members, a circular disk under diametrical forces, and a glass model under three-point bending. The advantages of the method are that: (1) a single prism is used as both polariser and analyser, so transmitted and reflected light through the model are along the same path; (2) when changing from a plane to a circular polariscope, only the retardation plate needs to be rotated; (3) the total cost of the optical parts is considerably lower than the transmission polariscope. However, the disadvantage of the method is that only part of the reflected light reaches the screen F due to the use of the partial mirror. Zandman and Wood (1956) gave a detailed description of the photoelastic technique. Properties of coating materials, including two types of plastic sheets and two types of liquid plastic were listed and recommendations were made according to different work pieces to be examined. They predicted that this method would permit automatic measurements. A polariscope that was mainly suitable for static testing in full-field and point-by-point analyses was employed and three case studies were given. Figure 2.5 shows the light

path through the Photo-Stress Meter LF/Z both as a crossed plane and a circular crossed polariscope. The advantage of this type of polariscope is that the analyser can be moved independently of polariser, thus allowing Tardy compensation, as well null-balance and Babinet compensators to be used for measuring fractional fringe order. The light reaching the observer is greater than that in Mindlin's polariscope. The main disadvantage is that incident light and reflected light are not normal to the plane of the coating.

Developments in coating and adhesive materials speeded up the application of the technique as a practical tool for use in the field. For example, Holister (1961) applied the technique on several different real components, such as a rocket motor case, a missile tail section, and turbine blade corrosion pits. Zandman, Redner and Post (1963) analysed several thermal stress using the coating method. Based on the work done on a wide range applications of the photoelastic technique, factors that may cause errors in the strain and stress analyses were identified. Generally speaking, errors may be caused by: (1) Poisson's ratio mismatch of the component and the coating; (2) reinforcing effect of the coating; (3) strain gradients through thickness of the coating; (4) temperature; (5) dynamic state of stress. Detailed discussions have been presented by Duffy (1961), Zandman, Redner and Riegner (1962) and Zandman, Redner and Dally (1977). The photoelastic technique has recently become less used because it is time consuming and requires an experienced analyst while on the other hand, numerical techniques has become readily available and fast. Numerical methods have become more popular in the stress analysis field, but they need to be validated by experiments particularly for complex cases. Therefore, there is a demand for automated methods of photoelasticity that can provide precise results easily and quickly.

2.1.3 Automated Photoelasticity

Automated photoelastic methods can be classified into two approaches, point-by-point analysis and full-field analysis according to Patterson (1988). Most automatic techniques that have been developed are based on transmission photoelasticity. In

the following review, automated reflection photoelasticity has been used only when it is specifically mentioned.

2.1.3.1 Point-by-point Approach

2.1.3.1.1 Acquisition of Automated Data Using Manual Polariscopes

In the early stage of automation, electronic sensors were used to make conventional photoelastic measurements. Brown and Hickson (1950) incorporated a photometer into a polariscope. The photometer consisted of a photocell and galvanometer and was used to detect the intensity of the light. They claimed that the accuracy of this method was within $\pm 1/500$ fringe compared with $\pm 1/4$ fringe for the Tardy method. Zandman and Wood (1956) used a servomotor to drive a Babinet compensator, and a photoelectric cell was used to detect the intensity of light passed through the polariscope. The variation in intensity of photoelectric current resulting from a variation of the birefringence was measured in either a static test by means of the null-balance method using a milli-ammeter and a compensator, or in dynamic tests, by means of an oscilloscope. Allison and Nurse (1971) utilised an optical system to measure both isochromatic and isoclinic fringe orders. To determine the isoclinic angle, a collimated light beam was passed through continuously rotating coupled crossed polarisers located on either side of the model. The resulting light output was modulated at a frequency corresponding to four times the rotational speed and this was converted by means of a silicon photocell into an electrical signal. A visual display of the isoclinic angle was obtained by passing the DC output from the phase computer into a suitably calibrated digital voltmeter. This isochromatic fringe order was determined by continuously rotating a circular compensator in the field of the polariscope. The colour of the light input to the optical system was changed alternatively from red to green at high frequency. With the polarisers set at the previously determined isoclinic angle, the rotation of the compensator for minimum light intensity gave a measure of the isochromatic fringe order at the point under observation. The sensitivity of the system was claimed as $\pm 0.2^\circ$ for isoclinic angle, and ± 0.1 fringes in the range -10 to $+10$ fringes compared to a commercial manual polariscope of $\pm 1^\circ$.

An automatic photoelastic system developed by Redner (1974) is based on the phase-angle difference at two different wavelengths. Direction of principal stresses was measured using a plane polariscope. With the polariser and analyser crossed rotating at a constant speed, light intensity is modulated with a frequency 4 times larger than the frequency of rotation of the polarisers. A photoelectric sensor generated an electric current proportional to the light intensity, and a reference voltage was generated using an electro-magnetic or photoelectric pickup. The phase detector generates a d-c output proportional to the phase difference between the voltage generated by the photoelectric sensor and the reference voltage. The measured angle provides a positive identification of one of the directions of principal stresses. The measurement of retardation employed a circular polariscope. The analyser was spinning at a constant speed. Using a beam splitter, the light emerging from the analyser is divided into two beams. Each of the beam is then filtered through a narrow-band filter, transmitting wavelengths λ_1 and λ_2 , respectively. The light intensity was transformed into electric currents proportional to the intensities using photoelectric sensors. The frequencies of these currents is twice that of the spinning analyser. A phase detector comparing the phase of these currents provides a d-c voltage proportional to their phase difference. The d-c output of the phase detector is proportional to the difference of principal stresses and the sign is that of the difference of principal stresses. The estimated sensitivity of the system is ± 0.01 fringes in a range of 20 fringes and 0.05° for isochromatic and isoclinic fringes respectively. The advantages of this method are that first, it measures simultaneously the direction and the difference of principal strain and stresses. Secondly, the operation is completely automatic without the intervention of the human eye. Thirdly, the results appear on digital panel meters and finally, the range of application includes the analysis of photoelastic model and coating.

2.1.3.1.2 Spectral Analysis

The optical components in the systems reviewed above need to be rotated during operation. A method proposed by Redner (1984) makes use of spectral analysis, or spectral content analysis to measure fringe orders without rotation of the optical

components. The method was based on the relationship between the intensity, retardation and wavelength of the light. The measuring system is shown schematically in Figure 2.6. Light emerging from the investigated point is channelled to the spectral analyser functioning as a conventional spectro-photometer. A prism or a diffraction grating was used to divide light into several rays, each carrying a narrow band of frequencies. The photodiode array is scanned sequentially and the data digitised and stored. The retardation was found by an error-summation method that involved substituting many values of retardation into the intensity equation and finding that which gave the smallest difference between the experimental and theoretical spectra. Sanford and Iyengar (1985) developed a similar system using a Newton-Raphson search approach to find the fringe order from the spectrum. Voloshin and Redner (1989) evaluated three methods: the error-summation method, the Newton-Raphson search and a database search method to find the retardation. It was found that all three approaches seem to give similar results, with error summation being the fastest. The data-base-search approach is more prone to errors in the measured light intensity for offsets of between 10-20 percent. The Newton-Raphson method takes into account both experimental and some systematic errors, but the search needs an initial guess for the calculation. If the initial guess was relatively far away from the actual solution, the solution will not converge. The two steps procedure, utilising results of the error-summation technique as an initial guess for the Newton-Raphson solution is capable of providing the most accurate results.

Haake and Patterson (1992) applied spectral analysis to frozen stressed 3D components containing a range of stress gradients. The matching of the theoretical data to the experimental data was performed using Brent's method and the golden section search. The retardation giving the smallest difference overall was taken to be the solution. The advantage of this method is that an expert photoelastician is not required as the fringe order is determined uniquely by the spectral signature of the point analysed. The accuracy of the technique has been found to be in the order of ± 0.005 fringe which is comparable to the method used by Allison and Nurse (1972) in their point-by-point technique (± 0.005 fringe), the technique used by Redner (1984) (± 0.01 fringe), and the spectral analyser developed by Voloshin and Redner

(1989) (± 0.017). An analysis of a single point takes appropriately 20 seconds (excluding calibration of the sample which is a lengthy procedure). The estimate of 20 seconds for the analysis of a single point consists of 8 seconds for the measurement of the spectrum and 12 seconds for the subsequent function minimization procedure. The system used for the spectral-content analysis is semi-automatic and its speed could be increased by fully automating the data collection and calibration procedures.

Pacey *et al* (1999) proposed a number of new methods for searching the fringe order from the spectrum, including the maximum entropy method combined with an evolutionary algorithm, either a genetic algorithm, or a memetic algorithm. Comparison of the methods with those discussed above showed that the maximum entropy method combined with either a genetic algorithm or a memetic algorithm was as much as 30 times faster than any of the existing methods and gave comparable accuracy. These new methods do not require seeding with an initial value for fringe order and operate with a minimum of user interaction.

The major disadvantage of the automated systems reviewed so far is that isochromatic and isoclinic fringes can only be assessed in a point-by-point manner.

2.1.3.2 Full-field Approach

2.1.3.2.1 Full-field Method Using Image Processing

A full-field automatic polariscope was developed by Mueller and Saackel in 1979. A TV camera and a computer were used to record the photoelastic picture. The information from every point of the image, called its 'grey level' was stored within an 8-bit word. Theoretically, 256 different levels of grey can be fixed in a word. However, in practical applications, a TV camera delivering 30 levels or 60 levels can be achieved if a shading corrector is inserted. The information stored was processed using a software package. Random noise was diminished by enhancing the contrast of the image. A mask was generated using a threshold process in which all parts of the picture belonging to the model were shown bright and the rest of the picture was shown dark. This mask was superimposed on the fringe pattern image by computer so that the image except the fringe pattern was blacked out. Extraction of the

isochromatic and isoclinic fringes was implemented by the fitting of circles into the fringe and expanding the circles until the fringe boundaries were reached. Isoclinic information was obtained using sixteen isoclinic pictures taken at different angles of the cross-polarisers in a range between 0 and 90 degrees. Laplace's equation was used to separate stresses. A major disadvantage of the system is that operator has to identify and assign fringe orders to the isochromatic fringes.

Seguchi *et al* (1979) developed a system similar to that of Mueller and Saackel. The technique includes three stages: fringe pre-processing; fringe recognition; and stresses separation. Positive and negative images were used for fringe multiplication. The boundary of the model was identified using a black sheet with the boundary contour. Random noise in the image was reduced using a low-pass filter. The fringes were extracted using a thinning method. The central lines of the fringes were obtained by progressively thinning each fringe through progressively removing the outer layer of points until only the centre line was left. A finite element solution of Laplace's equation was used to determine the principal stresses over the entire picture. The major disadvantage of the system is the same as in that of Mueller and Saackel.

Voloshin and Burger (1983) developed 'Half Fringe Photoelasticity'. Manual identification of isochromatic fringe order was not needed. But the maximum fringe order could not exceed 0.5 fringes. It was based on a digital grey level analyser and picture-processing system which divided its field of view into 640 by 480 picture elements and assigned to each element to an 8-bit resolution, i.e. within 256 grey levels. The system consisted of a regular polariscope in which the camera or viewing lens was replaced with a video camera. An 'EYECOM' scanner that used a special vidicon television-camera tube was used to scan the chosen image area. It was linked to a real time digitiser connected to a computer via a buffer memory. The requirement for the maximum fringe order to be lower than half made it necessary to use one or a combination of the following three factors: (1) low loads which resulting small shear stresses in the model; (2) a model with high material fringe constant; (3) a very thin model. The advantages of the system are that it does not require manual assignment of isochromatic fringe order, materials such as glass with

a high material fringe constant can be used; and thin slices mean that the strain field should not vary through the thickness of the model. However, it is not easy to control the loads to be small enough to keep the fringe order lower than a half in practical applications.

A system that does not require manual assignment of isochromatic fringe order has been developed by Umezaki *et al* (1989). The technique utilised two wavelengths of light and obtained two corresponding full-field isochromatic fringe patterns. Zero order fringes can be detected based on the fact that when the two fringe patterns were superimposed, the zero fringes matched perfectly. A search for the other fringe orders started from the position of the zero-order fringes and the nonzero fringe orders were determined from the relative locations of fringes between two fringe patterns. The disadvantage of the system is that if there are none zero order fringes within the field of view then the technique is not feasible.

The two-wavelength technique has been extended by Chen (1997). The isochromatic fringe order can be extracted without the presence of zero order fringe. The relationship between fringe order and the two wavelengths was derived in the light field circular polariscope set-up as

$$N_1 f_1 = N_2 f_2 \quad (2.13)$$

where f_1 and f_2 are the material fringe values with respect to wavelengths λ_1 and λ_2 .

Digital determination of the fringe order was performed using cross-shaped points that were equally spaced either horizontally or vertically across appropriately on fringe width. The exact fringe order N of the central point is to be determined for one wavelength. The procedure for the fringe order extraction are: (1) calculate difference function $D(N_1, N_2) = |N_1 f_1 - N_2 f_2|$ for points selected; (2) search over the function $D(N_1, N_2)$ and store three pairs of fringe orders having the smallest errors for each point; (3) fit the fringe orders of horizontal and vertical points and calculate the error between the new fringe orders and the original one $E(|N_h - N| + |N_v - N|)$, where N_h and N_v are calculated from the best-fit polynomial in all combinations of the horizontal and vertical points; (4) search for the one with minimum value of $|N_h - N| + |N_v - N|$ and designate N as the exact fringe order of the central point. The determination of the fringe orders from two 512x512 fringe patterns took 28 minutes

which included eight minutes on the image normalization and adjustment process, 15 minutes on finding an exact fringe order and five minutes for the subsequent whole field fringe order determination. The advantage of the technique is that isochromatic fringe orders can be automatically determined using the two wavelengths without a zero fringe order in the field of view. Accuracy of the technique reported was 0.05 fringe for isochromatics.

2.1.3.2.2 Phase-stepping Method

Hecker and Morche (1986) introduced a phase-stepping method into the computer aided measurement of photoelasticity. With the method, complete extraction of photoelastic information at a local element (pixel) can be done from series of related images of the same stress state. A circular ring made of polyester resin was used in the experiment. Five images were recorded when angles $\varphi = \psi$, at 0° , 60° and -60° , $\varphi = \psi - 45^\circ$ and $\varphi = \psi + 45^\circ$ where φ and ψ are angles between reference axis and slow axis of the output quarter-wave plate and analyser respectively. Fractional orders of isochromatic fringes at the local picture element were calculated using the formulae derived from the principles of the phase stepping. The accuracy is moderate, because it does not consider the inhomogeneties of the rotated optical components.

An automated full-field photoelastic system based on the principles of the phase-stepping has been developed by Patterson and Wang (1991). The configuration of the system is divided into four parts: the polariscope, the optical element controller, the image sampler and the fringe analyser/processor. A stepper motor controlled by a computer was used to drive each of the output optical elements. The image sampler includes a standard monochromatic CCTV camera and lens. The digitiser is controlled by computer and digitises a 256×256 pixel image from the camera and data were saved in 256 grey levels in the computer. Fringe analysis/processing was performed using interactive software specially written for the automated photoelastic system. Six images of the specimen were obtained by rotating the output elements. Maps of the periodic values of isochromatic and isoclinic parameters were subsequently obtained by mathematically combining the six images. An unwrapping

algorithm was employed to produce continuous isochromatic and isoclinic data. A slice from a full-scale model of a bolt loaded in axial tension was used to test the system and results showed that the system had potential for automated photoelastic analysis of complex components. The major advantage of the method is that both fractional isochromatic fringe order and the isoclinic parameter can be established at all individual points in the field without reference to their neighbouring points. It is fast and less expensive than other automated photoelastic systems. The disadvantages are that the assignment of two fringe orders is required and a relatively thin slice is needed in order to reduce the density of isochromatic fringes. There was a problem associated with the phase-stepping technique in that data generated by the method is periodic with respect to space or location, but this has been solved later by Wang and Patterson (1995) using demodulation of the intensity signals and classification of periods of data using fuzzy sets. The automated photoelastic system has been evaluated by Haake *et al* (1993). Five different models were used for analysis using the automated system and using the Tardy compensation method. Accuracy of the technique claimed is that for isochromatic fringe orders the error was ± 0.007 fringes and $\pm 0.75^\circ$ for isoclinic angle.

Carazo-Alvarez *et al* (1994) proposed a completely automated photoelastic analysis by combining spectral contents analysis and the phase-stepping technique. This method permitted the evaluation of the absolute fringe order at a point in the pattern, thus an automated identification of the fringe order in the full-field image was feasible. However, the system needed two different instruments, one to acquire the data for phase-stepping and one for the spectral analysis.

The phase-stepping technique was also reported by Sarma *et al* (1992) for whole-field determination of isoclinic and isochromatics. The formula for computing isoclinic and isochromatic parameters were derived using the Stokes parameter representation of polarised light. Images were captured with the analyser positioned at 0° , 45° and 90° respectively in a plane polariscope set-up. An RCA ultracon tube black and white camera connected to the PC-EYE frame grabber installed in the microcomputer-based image processing system was used and each image frame is represented by 512×512 pixels. The stray light was not taken into account explicitly

and the influence of the general background light was determined using an unstressed model of the same material and thickness, viewed in the crossed-analyser position. This value was subtracted from the image intensities before they were space averaged. A circular stress-frozen disk under diametrical compression was used to demonstrate the method. The accuracy achieved was of the order of ± 2 degrees for isoclinics and ± 0.05 fringe for isochromatics.

Ramesh and Ganapathy (1996) have demonstrated the principles of the phase-stepping techniques reported in papers of Patterson and Wang (1991) and Sarma *et al* (1992) using the Jones calculus. The two phase-stepping techniques were compared with the theoretical solution using a circular disk under diametrical compression. Three lines were selected from the whole field isochromatic map and two experimental results and the theoretical solution were drawn in a graph with same axes. The results from the technique proposed by Patterson and Wang (1991) were close to the theoretical solution while the results from the Sarma *et al* (1992) have shown more local oscillations in the value of the fringe order. It was concluded that the algorithm proposed by Patterson and Wang (1991) is truly a whole-field method and it can determine both fractional fringe order and the isoclinic angle.

Ramesh and Deshmukh (1997) reported three-fringe photoelasticity using white light. Images were captured using a colour CCD camera and saved as *R*, *G* and *B* planes. Comparison of the wavelength in the three planes with the wavelength defined by the International Commission on Illumination showed that the experimental by calculated wavelength in the green plane is very close to the standardised value. Therefore, data in the green plane is considered to be equivalent to an image recorded by a green filter. This three-fringe photoelasticity has used the methodology of phase-stepping developed by Patterson and Wang (1991) to obtain full-field phase-stepped maps. It has also used the idea of RGB photoelasticity proposed by Ajovalasit *et al* (1995) although this has not been mentioned by the authors. The advantage of three-fringe photoelasticity that combines phase-stepping and RGB photoelasticity is that no specialised hardware other than a general purpose colour image processing system is required. The technique is restricted to determining fringe orders up to third order.

Nurse (1997) proposed a phase-stepping method based on the use of a plane polariscope with white light source and three narrow-band filters of wavelengths corresponding to the three primary colours red, green and blue (RGB). A total of 18 intensity patterns were obtained and six patterns for each colour filter. There are four unknowns for each colour yielding a total 12 unknowns to be determined from the 18 intensity patterns. An over deterministic approach with a least squares minimization routine was used to reduce the effects of noise in the data. The advantages of the method are that it allows the photoelastic parameters to be determined without the isoclinic-isochromatic interaction problems inherent in other automated analyses, and the isoclinic angle phase map may be unwrapped to allow its definition to be more specific and refer to only one of the principal stress directions. It is fast and only four minutes are needed to attain the solution. The accuracy of the method was not reported.

Ekman and Nurse (1998) reported the development of load-stepping technique which is the technique of phase-stepping with a circular polariscope to analyse a 2D photoelastic model for three increments loads. The small value of load increment ∂P is important for reducing the possibility of highly stressed regions giving a value of $\partial\alpha \geq \pi$. The isochromatic map was obtained first, then the isoclinic map was obtained using the isochromatics. Since the relative retardation α can be found in the range $-\pi < \alpha \leq \pi$, the isoclinics can be obtained in the range $-\pi/2 < \theta \leq \pi/2$ without unwrapping. Two examples were used to demonstrate the technique. The disc in compression specimen where 'live' load were applied with a load step of 5% yielding results for the isochromatic up to 10 fringe orders. The isoclinic angles were in a full range of value $-\pi/2 < \theta \leq \pi/2$. The comparison of results from theory and experiment showed that consistent agreement was obtained for isochromatic values up to the loading point where the experimental data is likely to be affected by 3D stresses and plasticity. Reasonable agreement was obtained for the isoclinic angles. The second specimen was a single-edge-notch plate in tension and load step 10 % was employed. Comparison with other methods was not given for the plate. The advantage of the technique is that isoclinic angle can be obtained in the range

$\pi/2 < \theta \leq \pi/2$ without the need for unwrapping. The disadvantage is to assume that there is no spatial translation during the three load increments.

Almost all the automated full-field photoelastic analysis systems reported are for use with static loading conditions. Patterson and Wang (1998) have designed a novel instrument for the simultaneous observation and capture of four phase-stepped photoelastic images. The instrument was designed for reflection with dynamic loading conditions, but can be used in a transmission configuration and with static loading conditions. It has a high sensitivity, so very thin photoelastic coatings or very low loads can be used. The repeated experimental results using the instrument were close to the theoretical results and the repeatability of the instrument was good. The systems developed by Patterson and Wang will be used in the present research; the principles of the phase-stepping and the configuration of the instrument and software for image processing will be reviewed in detail in section 2.2.

In order to achieve the complete automation of photoelasticity, Patterson and Wang (1999) have proposed an integration of spectral and phase-stepping methods. In this method, the prediction of light intensities generated by half and integer fringe orders from zero to three and a half fringes were calculated using the spectral responses of source, the three filters, stress optical coefficients and wavelength. The predicted spectra were used as templates. In the two experiments (a transmission and a reflection) that demonstrate the use of the method, the locations of the half and integer fringe orders were identified manually along a line. The measured intensities at each of these points were compared with the data in the template by calculating the sum of the squared difference between the experimental and theoretical values for the intensities of red, green and blue. The fringe order at the point of interest was indicated by the theoretical fringe order giving the lowest sum. The results from the experiments have shown that maps of isoclinic angle and absolute fringe order to a maximum of approximately four can be obtained from phase-stepped images collected with a colour digital camera through close integration of the methods of phase-stepping and spectral content analysis. The spectra in the templates limit the maximum fringe order that can be evaluated to less than three, but high values can be present in the data field.

2.1.3.2.3. RGB Photoelasticity

RGB photoelasticity is a full-field method proposed by Ajovalasit *et al* in 1995. White light was used in the automatic measurement of the integral and fractional fringe orders. The isochromatic fringe pattern was acquired using a colour video camera and the colour was then decomposed in the three primary colours, *R*, *G* and *B* to give three intensity levels. The three intensities that are recorded for each point depend on the optical retardation of the point. The retardation was found by comparing the recorded values of intensity with values stored in a database. The values in the database were obtained by a calibration procedure using a specimen that was made from the same photoelastic material as the specimen under test. Due to the attenuation of the RGB levels for retardations higher than 4 to 5 orders, in practice, the maximum measurable retardation is limited to three orders. The advantages of the technique are: (1) it can determine fringe orders up to third order without need of manual assignment of the fringe order compared to half order for half fringe photoelasticity; (2) since the specimen used in the calibration is made from the same photoelastic material, the dispersion of birefringence is taken into account. (3) errors in the optical retardation from both dark and light field polariscope is taken into account. The disadvantage is that it does not provide isoclinic angle. The accuracy of the technique was claimed to be 0.02 fringes.

2.1.3.2.4. The Fast Fourier Transform Method

Morimoto *et al* (1993) proposed a method to distinguish between the isochromatics and the isoclinics using a Fourier transform of a 3D image processing. Light intensity $i(\theta)$ obtained in a dark-field plane polariscope is expressed as

$$i(\theta) = \frac{a^2}{2} [1 - \cos 4(\phi - \theta)] \sin^2(m\pi) \quad (2.14)$$

Where a is the amplitude of the incident polarised light, ϕ is the angle of the principal stress and θ is the angle of the analyser and m is the isochromatic fringe order.

The Fourier series of equation (2.14) with respect to θ was obtained and Fourier transformed in the θ direction to make a Fourier spectrum. The 2D images in the

frequency domain at $\omega = 0$ are the isochromatics and the arctangent of the ratio of the imaginary to the real part of the frequency at $\omega = -\omega_0$ (ω_0 is the fundamental frequency) gives the direction of principal stress.

A circular disk was used to demonstrate the technique. The 3D (x, y, θ) image was constructed by ninety θ sequential 2D (x, y) images obtained in a dark-field plane polariscope at 1 degree intervals of the angle θ from 0 to 89 degrees with a CCD camera. The size of the 2D image was 128x120 pixels. Following the procedure mentioned above, the extracted isoclinic fringe patterns (0° to 89° in 1° interval) were obtained by subtracting the calculated ϕ into equation (2.14) and setting $\sin^2(m\pi) = 1$. Accuracy of the method is high and it is insensitive to high frequency noise due to the use of a Fourier transform in the image processing. The major drawback of the method is that too many images are need and it is not applicable for practical implementation.

Quan *et al* (1993) proposed a carrier fringe and FFT technique. Only one image is needed to create the fringe information. Isochromatic fringes produced by a circular polariscope were modulated using photocarrier fringes. The photocarrier fringes were generated using a crystalline quartz wedge. The fringe patterns with image sizes of 512x512 pixels and resolution of each pixel 8-bit were captured by a CCD camera. The images were automatically processed by the Fourier transform technique to generate the wrapped phase map of stress fringe pattern. The principle of the method is that, for each Fourier series, there is a frequency at which the isoclinic angle has no influence upon the measured intensity and so the isochromatic fringe order can be determined. The isoclinic angle can be calculated using the ratio between the real and imaginary part of the Fourier transform. The continuous phase map of the stress fringes is produced by the phase-unwrapping procedure. A circular disk and a circular ring made of epoxy resin were used to demonstrate the technique. Accuracy of the technique was not reported. The advantage of the technique is that only one image is needed to create the fringe information. The major disadvantage of the method are that the required computational time is expensive and use of the method is restricted to the availability of high density carrier fringes.

Ng (1997) reported an object step-loading method for photoelastic stress analysis. Images were taken in dark and light field setting of a circular polariscope. For a point of interest, a series of intensity reading were made while increasing the load, each of which was calculated by subtracting the intensity obtained with the analyser axis oriented parallel to and crossed with the polariser. A Fourier transform was used to the series of the intensity data of the point. With the complex conjugate removed, the spectral distribution is inversely Fourier transformed. The real part and imaginary components were used to calculate the retardation. The basics of the method are the same as the carrier fringe and FFT technique developed by Quan (1993). The advantage of the method is the ability to compute the entire deformation phase to load history.

Ajvalasit *et al* (1998) reviewed automated methods for the collection and analysis of photoelastic data. Comparison of these methods was made on three aspects: parameters determined, ease to use; and source of errors and uncertainty. It is concluded that the phase-stepping method can provide both isochromatic and isoclinic parameters and has no limit for the maximum fringe order that can be determined. The number of necessary acquisitions depends on the method, and it varies from one frame such as half fringe photoelasticity (Voloshin and Burger, 1983) to maximum 90 frames as for the FFT method (Morimoto *et al*, 1993). The method with fewer frames is preferred but the ability to provide photoelastic information is more important than the number of frames used. The phase-stepping method requires a minimum of four frames and it was considered with limitation on static problems. However, the phase-stepping method has been used in dynamic reflection photoelasticity (Patterson and Wang, 1998). Automated photoelasticity is influenced both by the usual sources of errors common to the methods of digital image processing and by the typical sources of errors of photoelasticity such as error of quarter-wave plates and dispersion of birefringence and in general, the technical literature does not report comparative analysis of the uncertainty.

2.2 Phase-stepping Systems (Patterson and Wang)

The automated full-field stress analysis systems developed by Patterson and Wang (1991, 1998) utilised the principles of phase-stepping proposed by Hecker and Morche (1986). The system was initially constructed for transmission photoelastic analysis, and then extended to reflection photoelastic analysis with a newly designed optical instrument PSIOS. Both automated transmission and reflection polariscopes will be used in this study, so the theory and configuration of the two systems are reviewed as follows.

2.2.1. Automated Transmission Photoelasticity

2.2.1.1 Theory

Consider a standard circular polariscope with arbitrarily orientated output quarter-wave plate and polariser or analyser, with an input of unpolarized light from the source having a stokes vector, S as

$$S = \begin{bmatrix} 1 \\ 0 \\ 0 \\ 0 \end{bmatrix} \quad (2.15)$$

P_β is the Mueller matrix of an ideal linear polariser whose principal axis subtends an angle β with the reference axis such as

$$P_\beta = \frac{1}{2} \begin{bmatrix} 1 & \cos 2\beta & \sin 2\beta & 0 \\ \cos 2\beta & \cos^2 2\beta & \cos 2\beta \sin 2\beta & 0 \\ \sin 2\beta & \cos 2\beta \sin 2\beta & \sin^2 2\beta & 0 \\ 0 & 0 & 0 & 0 \end{bmatrix} \quad (2.16)$$

The reference axis is taken as being perpendicular to the principal axis of the input polariser. A quarter-wave plate with its fast axis at an angle ϕ to the reference axis is given by Mueller matrix

$$Q_\phi = \begin{bmatrix} 1 & 0 & 0 & 0 \\ 0 & \cos^2 2\phi & \cos 2\phi \sin 2\phi & -\sin 2\phi \\ 0 & \cos 2\phi \sin 2\phi & \sin^2 2\phi & \cos 2\phi \\ 0 & \sin 2\phi & -\cos 2\phi & 0 \end{bmatrix} \quad (2.17)$$

The specimen is considered as a linear retarder of retardation δ with its fast axis at an angle θ to the reference axis. The angle θ is related to the isoclinic angle and the retardation is related to the isochromatic fringe order by

$$N = \frac{\delta}{2\pi} \quad (2.18)$$

The Mueller matrix for the specimen is given by

$$R_{\theta}(\delta) = \begin{bmatrix} 1 & 0 & 0 & 0 \\ 0 & \cos^2 2\theta + \cos \delta \sin^2 2\theta & (1 - \cos \delta) \sin 2\theta \cos 2\theta & -\sin 2\theta \sin \delta \\ 0 & (1 - \cos \delta) \sin 2\theta \cos 2\theta & \sin^2 2\theta + \cos^2 2\theta \cos \delta & \sin \delta \cos 2\theta \\ 0 & \sin 2\theta \sin \delta & -\cos 2\theta \sin \delta & \cos \delta \end{bmatrix} \quad (2.19)$$

The resulting Stokes vector of the light at the output of the polariscope is obtained as

$$S' = P_{\beta} Q_{\phi} R_{\theta}(\delta) Q_{\pi/4} P_{\pi/2} S = \begin{bmatrix} s_0 \\ s_1 \\ s_2 \\ s_3 \end{bmatrix} \quad (2.20)$$

where s_0' is the light intensity emitted from the polariscope based on the physical meaning of the Stokes vector and for a dark field, circular polariscope and can be expressed as (Patterson and Wang, 1991)

$$i(x, y) = i_m + i_v (\sin 2(\beta - \phi) \cos \alpha - \sin 2(\theta - \phi) \cos 2(\beta - \phi) \sin \alpha) \quad (2.21)$$

where i_v is the intensity emerging when all the axes of the polariscope and specimen are parallel and term i_m takes account of stray light. The angles β , ϕ and θ are angles between a reference axis and the analyser, the slow axis of output quarter wave plate and specimen respectively as shown in Figure 2.7. The light intensity i_v , i_m and isochromatic angle α and the isoclinic data θ are four unknowns. In order to find the four unknowns, at least four independent equations that are determined according to the arrangement of ϕ and β are required.

In their algorithm for transmission photoelasticity, Patterson and Wang (1991) chose the six values of the angles ϕ and β given in Table 2.1. This produces an

over-deterministic system of equations derived from equation (2.21) which are as follows:

$$i_1 = i_m + i_v \cos \alpha \quad (2.22)$$

$$i_2 = i_m - i_v \cos \alpha \quad (2.23)$$

$$i_3 = i_m - i_v \sin \alpha \sin 2\theta \quad (2.24)$$

$$i_4 = i_m + i_v \sin \alpha \cos 2\theta \quad (2.25)$$

$$i_5 = i_m + i_v \sin \alpha \sin 2\theta \quad (2.26)$$

$$i_6 = i_m - i_v \sin \alpha \cos 2\theta \quad (2.27)$$

The latter four equations can be combined as shown below to yield the isoclinic parameter:

$$\theta = \frac{1}{2} \tan^{-1} \left(\frac{i_5 - i_3}{i_4 - i_6} \right) \quad (2.28)$$

and the isochromatic parameter is given by

$$\alpha = \tan^{-1} \left(\frac{i_4 - i_6}{(i_1 - i_2) \cos 2\theta} \right) = \tan^{-1} \left(\frac{i_5 - i_3}{(i_1 - i_2) \sin 2\theta} \right) \quad (2.29)$$

The isoclinic parameter and isochromatic fringe order are obtained as periodic functions, because equation (2.28) and (2.29) contain arctangent operators, the isoclinic data are not defined when $\alpha = 0$.

2.2.1.2 System Configuration

The schematic arrangement of the system is shown in Figure 2.8. In this system, a standard diffuse light polariscope is used with a 15-inch field of view and a sodium light source (Sharples Stress Engineers Ltd, Preston, England). The wavelength of the sodium light is 589.3 nm. The image acquisition system consists of a monochromatic CCD camera (Panasonic, WV-BP 100, Japan) with a resolution of 380x380 pixels, a monitor (Microvitec, UK) and a digitiser (Micro Eye TM 425, Digithurst Ltd). The fringe pattern generated by the optical system is recorded by the CCD camera that converts the optical signal to an electronic signal. The output from the camera is supplied to a Micro Eye card that is a transputer-based digitiser. The card is housed in a computer and provides an analogue signal to a monitor that

is used to position the specimen being analysed and to adjust the aperture and focus of the camera. The digitiser output can be sampled by the computer and can digitise a 720x512 pixel image from the camera. The resolution of the recorded image is 256x256 pixels saved in an 8-bit word, i.e. 256 grey levels. The image analysis is performed using a program *VIZION* written specially for the purpose. The isochromatic fringe order and isoclinic angle can be obtained using the following steps, namely, Estimate, Markfind, Background and Wrapping. In the Estimate subroutine, the fractional isoclinic and isochromatic parameters can be obtained using the image intensity data collected from the polariscope using equations (2.28) and (2.29) at individual points in the field of view without reference to neighbouring points. In the Markfind and Background subroutines, the marks on the slice, and on the input optical elements of the polariscope and also the jig used to hold the slice can be identified using a threshold applied to the first two intensity signals collected from the polariscope, i.e. i_1 and i_2 in equations (2.22) and (2.23). The background to a slice and the data that lies outside the boundary of the slice can be identified using threshold. The threshold T_1 operates on image i_1 whilst T_2 operates on image i_2 . Decreasing T_1 reduces the black areas belonging to the model, this usually means identifying some whole or half order isochromatic fringes as background as well as other parts of the slice at the edges. Increasing T_1 does the reverse and may lead to some background being identified as belonging to the model. Decreasing T_2 has a similar effect to increasing T_1 except that the effect is less on the whole and half order fringes. A relative retardation threshold T_K is used to remove areas within the slice. The T_K is defined by $\frac{d\alpha_f}{dx} \langle T_\alpha \rangle \frac{d\alpha_f}{dy}$. Hence decreasing T_K will decrease the

black/background areas.

The Wrapping subroutine extends the range of the isoclinic so that the sign and derivative of the retardation can be found correctly and then calculates a map of continuous relative retardation from the periodic value. The relative retardation K_f and isoclinic angle ϕ_f were found using an arctangent operator and this resulted in the relative retardation and isoclinic angle lying in the ranges $-\frac{\pi}{2} \leq \alpha_f \leq \frac{\pi}{2}$ and

$-\frac{\pi}{4} \leq \theta_f \leq \frac{\pi}{4}$. The procedures for extending the range of the isoclinic angle and calculating relative retardation from the periodic value was described in detail by Wang and Patterson (1995). Here, the procedures will be given briefly.

(1) Extending the range of the isoclinic angle

In equation (2.29) θ_f is required to evaluate the denominators. The periodic nature of θ_f causes the reversal of the sign of the relative retardation and its first derivative at locations where $\theta_f = \pm 45^\circ$. These reversals do not exist in stress or strain distributions to which the retardation is related. This difficulty can be overcome by extending the range of the periodic isoclinic angle to $-\frac{\pi}{2} \leq \theta_f \leq \frac{\pi}{2}$ before it is used to generate the modulate signals. The field of isoclinic data can be considered as two families of curves C_x and C_y parallel to the x and y axes respectively. Each curve is made up of a period of data values θ_f and has a discontinuity at each end of height $\pi/2$. The period extension can be easily achieved by scanning the isoclinic data continuously from any arbitrary point in the $x - y$ plane, and on searching the discontinuity at the end of a curve the data of next curve is given a $\pi/2$ translation in the z -direction so that θ , $d\theta/dx$ and $d\theta/dy$ are continuous across the period boundary. The scan is continued for the second curve until the discontinuity at its boundary with the next curve is located. This second discontinuity should be of magnitude π and should be allowed to remain, and the scan continued repeating the whole process until all the data has been considered. It should be pointed out that this procedure generates one of two fields of data depending on the location of the arbitrary starting point relative to the period of θ_f , i.e. if the starting point was in the second period described above the extended isoclinic angle would be $\pi/2$ out of phase with the one generated by the process described. Physically the two fields of extended data are related to the two principal stress directions respectively.

(2) Generating continuous isochromatic data

The field of relative retardation data can be considered as two families of curves D_x and D_y parallel to the x and y axes, respectively. Each curve is made up of data

values α_j and has a discontinuity at each end where $\tan\alpha = \pm\infty$. These curves can be identified by scanning the data from an arbitrary point, although in practice the same starting point is used as that employed when extending the isoclinic data. When a discontinuity is identified all the data already scanned is given a $\pm\pi$ translation in the z -direction. The direction of translation is dependent on achieving constant α , $d\alpha/dx$ or $d\alpha/dy$ at the location of the discontinuity. The result of this process is a continuous field of relative retardation data which may be related to $(\sigma_1 - \sigma_2)$ or $(\sigma_2 - \sigma_1)$, and these two possible fields are the inverse of each other.

The relative retardation can be converted to isochromatic fringe order by the provision of fringe order data at two calibration points. The use of a single calibration point allows the relative retardation to be converted to absolute retardation and hence isochromatic fringe order, the provision of a second calibration point allows the gradient of the $(\sigma_1 - \sigma_2)$ field to be identified so that the appropriate one of the two data fields can be selected, provided the isochromatic fringe order is not identical at the two calibration points.

(3) Fuzzy set classification

The families of curves C and D are rarely well-defined with discontinuities of height precisely $\pi/2$ and π , respectively, as a result of noise from various sources. In practice the ends of periods in the relative retardation data are defined by

$$\left| \frac{d\alpha}{dx} \text{ or } \frac{d\alpha}{dy} \right| \geq \frac{7}{8}\pi \quad (2.30)$$

and the isoclinic parameter by

$$\left| \frac{d\theta}{dx} \text{ or } \frac{d\theta}{dy} \right| \geq \frac{4}{9}\pi \quad (2.31)$$

The shape of each period of data can be described by its first derivative and value at the mid-point and ends of the period. The characteristics of both photoelastic data and the functions $\tan\alpha$ and $\tan\theta$ allow the main shapes of the curves C_x , C_y , D_x and D_y to be classified into the six fuzzy subsets. By using the fuzzy set classification,

isoclinic parameter can be extended and a continuous map of relative retardation can be obtained.

The presence of the spikes of noise in the data can disturb the classification process and so these are removed at the same time as the ends of the periods are identified. Points forming discontinuities and spikes of noise have been found to satisfy the following condition:

$$\frac{\pi}{24} < \left| \frac{dz}{dx} \right| \text{ or } \left| \frac{dz}{dy} \right| < \frac{\pi}{4} \quad (\text{per point}) \quad (2.32)$$

where z could be either the relative retardation or isoclinic angle. When the condition is satisfied the spikes can be removed and replaced by a value equal to the average of the adjacent data points.

It was found that there were two main types of error in this experimental arrangement. The errors associated with the optical apparatus present in the manual measurement, such as linear alignment, angular alignment, quarter wave plate mismatch, material inhomogeneities and partial and temporal variation of the light. And the error associated with sensor including discretization of intensity data, spatial quantization and geometric distortion (Ji and Patterson, 1998).

Figure 2.9 shows maps of light intensity data of the quadrant disc using the automated transmission polariscope. Figure 2.10 shows maps of isochromatic fringe and isoclinic angle calculated from the intensity data.

2.2.2 Automated Reflection Photoelasticity (PSIOS)

Patterson and Wang (1998) have extended their work from automated transmission photoelasticity to automated reflection photoelasticity. Figure 2.12 shows light passage in conventional transmission photoelasticity with beamsplitter inserted. A schematic diagram of the PSIOS system is shown in figure 2.13.

2.2.2.1 Theory

When orientation of the output optical elements of the polariscope are set as in Table 2.2, the intensities observed in each step can be derived from equation (2.21) as

$$i_1 = \frac{a^2}{2}(1 - \cos 2\theta \sin \delta) \quad (2.33)$$

$$i_2 = \frac{a^2}{2}(1 + \sin 2\theta \sin \delta) \quad (2.34)$$

$$i_3 = \frac{a^2}{2}(1 - \sin 2\theta \sin \delta) \quad (2.35)$$

$$i_4 = \frac{a^2}{2}(1 - \cos \delta) \quad (2.36)$$

where a is the amplitude of the light emerging from the polariser. Solving the four equations, isochromatic fringe order and isoclinic angle can be obtained by using

$$\theta = \frac{1}{2} \tan^{-1} \left(\frac{i_2 - i_3}{i_2 + i_3 - 2i_1} \right) \quad (2.37)$$

and

$$\delta = \tan^{-1} \left[\frac{i_2 - i_3}{\sin 2\theta (i_2 + i_3 - 2i_4)} \right] \quad (2.38)$$

Beamsplitters were introduced into the polariscope by Patterson and Wang to allow four images to be recorded simultaneously. The beamsplitters will be partial polarisers and so must be represented in the mathematical model of the polariscope.

The beamsplitters are aligned parallel and perpendicular to the reference system and for simplicity the transmission coefficients in the OX and OY directions have been used as k_x and k_y respectively. The Mueller matrix P_k , for a partial linear polariser is

$$P_k = \frac{1}{2} \begin{bmatrix} k_x + k_y & k_x - k_y & 0 & 0 \\ k_x - k_y & k_x + k_y & 0 & 0 \\ 0 & 0 & 2\sqrt{(k_x k_y)} & 0 \\ 0 & 0 & 0 & 2\sqrt{(k_x k_y)} \end{bmatrix} \quad (2.39)$$

The Stokes vector for the light emerging from each beam of the instrument is

$$S' = P_\beta Q_\phi P_k R_\theta(\delta) Q_{\pi/4} P_{\pi/2} S \quad (2.40)$$

The light intensity at a point (x, y) in the plane of the image emerging from an arm of the instrument can be expressed as

$$i(x, y) = \frac{a^2}{4} (A + B \sin 2\theta \sin \delta + C \cos 2\theta \sin \delta + D \cos \delta) \quad (2.41)$$

where

$$A = (k_x + k_y) + (k_x - k_y) \cos 2\phi \cos 2(\beta - \phi) \quad (2.42)$$

$$B = (k_x - k_y) + (k_x + k_y) \cos 2\phi \cos 2(\beta - \phi) \quad (2.43)$$

$$C = -2\sqrt{(k_x k_y)} \sin 2\phi \cos 2(\beta - \phi) \quad (2.44)$$

$$D = -2\sqrt{(k_x k_y)} \sin 2(\beta - \phi) \quad (2.45)$$

When the orientation of the output quarter wave plates and polarisers are as in Table 2.2 then the intensities of the images observed on each arm of the instrument are

$$i_1 = \frac{a^2}{4} \{k_{x1} + k_{y1} + (k_{x1} - k_{y1}) \sin 2\theta \sin \delta - 2\sqrt{k_{x1} k_{y1}} \cos 2\theta \sin \delta\} \quad (2.46)$$

$$i_2 = \frac{a^2}{2} k_{x2} (1 + \sin 2\theta \sin \delta) \quad (2.47)$$

$$i_3 = \frac{a^2}{2} k_{y3} (1 - \sin 2\theta \sin \delta) \quad (2.48)$$

$$i_4 = \frac{a^2}{4} \{k_{x4} + k_{y4} + (k_{x4} - k_{y4}) \sin 2\theta \sin \delta + 2\sqrt{k_{x4} k_{y4}} \cos \delta\} \quad (2.49)$$

Cubes with a transmission:reflection ratio of 53:46 were selected for the system. The assumption had been made for simple calculation, that $k_{x1} = k_{y1}$, $k_{x4} = k_{y4}$, $k_{x2} = k_{y3}$, $k_{x3} = k_{y2}$, so the values for the transmission coefficients are

$$k_{x1} = k_{y1} = k_{x4} = k_{y4} = 24.4 \quad (2.50)$$

$$k_{x2} = k_{y3} = 21.2 \quad (2.51)$$

$$k_{x3} = k_{y2} = 28.1 \quad (2.52)$$

The orientation of these beamsplitters is important for three reasons: (1) the path length for all the beams must be the same so that the four images recorded by the CCDs are identical in size. (2) the number of divisions or splits experienced by each beam must be the same so that prior to the output quarter-wave plate the intensities are identical. (3) the beamsplitters have to be arranged so that their effect on the

state of polarisation is complementary to that of output quarter-wave plate and analyser.

The isoclinic angle and fractional isochromatic fringe order can be obtained using the following expressions

$$\theta = \frac{1}{2} \tan^{-1} \left(\frac{\frac{i_2}{Rk_{x2}} - 1}{1 - \frac{i_1}{Rk_{x1}}} \right) \quad (2.53)$$

and

$$\delta = \tan^{-1} \left(\frac{Rk_{x1} - i_1}{\cos 2\theta (Rk_{x1} - i_4)} \right) \quad (2.54)$$

where

$$R = \frac{i_2 + i_3}{2k_{x3}} \quad (2.55)$$

The isoclinic parameter is not defined at $L = 0$ as in the automated transmission photoelasticity reviewed in Section 2.2.1.1.

2.2.2.2 System Configuration

In the PSIOS system, a white light 300W projector lamp (Thorn-EMI, type: ELH) was selected as the light source because it satisfies the requirements for power, portability and integration with the optical head. A cold mirror is used in front of the light source to direct the light beam and to remove the near-infrared radiation. Circularly polarised light is produced by a polariser and a quarter-wave plate positioned in front of the cold mirror. The resulting beam allows a field of diameter 25 mm to be examined at a distance of 100 mm or 250 mm from a distance of 1 m. When the circularly polarised light passes through a birefringent coating the light will be elliptically polarised. The elliptically polarised light is passed through a lens, L_1 that generates collimated light and the collimated light beam is then split into four beams of equal energy that pass through quarter wave plates and analysers before being focused by an objective lens L_2 on to a CCD chip (Pulnix, TM 526), so that each beam generates a different phase-stepped image. The hybrid cube beamsplitter

(03 BSC 007, Melles Griot) have a 53:46 transmission: reflection ratio for light within a wavelength range from 400 to 700 nm. A set of four signals from the four CCD cameras is processed by a Micro Eye 425 card, Digithurst Ltd and a multiplexer (Panasonic Quad WJ 410) to combine them into a signal composite image that can be digitised by a single frame-grabber. The composite image is displayed on a TV monitor prior to digitisation as in the automated transmission polariscope so that the instrument can be set up and aligned on the appropriate area of the object to be analysed.

The program *PECAN* is used to process the images. The composite image is divided into four phase-stepped images each of 256×256 pixels by a software operation. The processing method is almost the same as in the program *VIZION* except for a slight difference in the *Estimate* subroutine to take into account the difference in the number of images (six images for automated transmission photoelasticity and four images for the automated reflection photoelasticity). In addition, three smoothing methods named Gentle, Medium and Heavy had been added in the subroutine in order to diminish noise in the intensity data and these smoothing methods will be discussed in following section.

In order to automatically calibrate the isochromatic fringe orders, colour CCD camera (WAT-202B(PAL), Watec Co, Ltd, Japan) and a MRT card (MRT micro ASA, Norway) were used in some experiments to obtain images. The MRT card generates 24-bit image with resolution 768x574 that consists of the four phase-stepped fringe patterns. The program *BMPDAT1* is used to extract the four images to form three sets of data in the *R*, *G* and *B* planes. The RGB data was used to calibrate automatically the isochromatic fringe orders using a method developed by Patterson and Wang (1999). The data extracted in the green plane are used in the calculation of isochromatic and isoclinic parameters using the program *PECAN*. The reason for use of the data in the green plane has been reviewed in Section 2.1.3.2.2.

Figure 2.13 is a map of light intensity from a quadrant of a disc using the automated reflection polariscope, PSIOS. Figure 2.14 shows the isochromatic fringe order and the isoclinic angle maps of the disc.

Isochromatic and isoclinic maps from the automated transmission and reflection polariscopes as shown in Figures 2.10 (1), (2), 2.13 and 2.14 have demonstrated the validity of the two systems. Both two systems can provide meaningful information of photoelastic parameters for the discs under diametrical compression in static loading condition. However, noise in the maps in Figures 2.13 and 2.14 from the automated reflection polariscope is more severe than in the maps in Figures 2.10 (1) and (2) from automated transmission polariscope. The degraded maps will affect the subsequent stress and strain separation. Therefore, effect of noise should be reduced in order to improving the accuracy of the photoelastic parameter and stress and strain analysis.

2.3 Smoothing Methods in Automated Full-Field Photoelasticity

The images from all reported automated polariscope contain noise. Noise may be caused by various factors. Some of them are common to every automated photoelastic system. Mueller and Saackel (1979) reduced noise in their images by shifting or distorting the frequency levels at some points. Shifting or distorting the frequency level, causes the contrast of the picture to be intensified. ‘This is essential, e.g., to enhance the information of pictures, or to show a picture’s information not previously discernible due to noise’ (Mueller and Saackel, 1979, p.248).

Seguchi *et al* (1979) used a formula

$$b_{i,j} = 0.1(b_{i,j} + \sum_{k=-1}^1 \sum_{l=1}^1 b_{i+k} b_{j+l}) \quad (2.56)$$

to diminish random noise in the image. The value b related to intensities at pixels which are shown in Figure 2.15. The point of interest and the three adjacent points were used in the calculation.

Voloshin and Burger (1983) in their half fringe photoelastic technique, averaged the intensity of 16 consecutive pictures to remove time-varying electrical noise and in the Fourier transform method, Quan *et al* (1993) and Morimoto and Imamoto (1994) eliminated the unwanted lower frequency background and high frequency speckle noise by properly selecting the spatial cut-off frequency.

Sarma *et al* (1992) employed two smoothing methods in their phase-stepping technique. The intensity image was obtained by averaging 10 frames for the same input light in order to reduce time-dependent noise. Then the averaged images were space averaged. The spatial averaging of the pixel values with the intensities of the surrounding eight pixels has been assigned to the central point.

In the two wavelengths technique (Chen, 1997), electronic noise was reduced by averaging the intensity values of eight frames for same input light.

In the RGB photoelasticity, digitised R , G and B signals are affected by high frequency random noise. Ajovalasit *et al* (1994) applied a median filter on each R , G and B signal using a two dimensional window of square shape (3x3 or 5x5 pixels).

The Median filter is a statistical (non-linear) filter. It uses a sorting of pixels in intensity to determine the pixel's filtered value. The shape of the median filter is the same as that of the normal convolution filter kernels but instead of weighting pixels with elements of the filter kernel the elements were sorted from the least to the greatest and choosing the median(center) value. For a window about a pixel i, j , the N pixels within the neighbourhood are ranked according to value (Hussain, 1991, p. 89)

$$x_{i,j}^1 \leq x_{i,j}^2 \leq \dots \leq x_{i,j}^N \quad (2.57)$$

The output value is chosen

$$\text{median}(x) = R_{\lfloor \frac{N}{2} \rfloor}^N(x) \quad (2.58)$$

where x is the input image.

The median filter with 3x3 and 5x5 pixels have nine and twenty-five elements in the kernels respectively. The schematic diagrams of the cells or pixels used in the formulae are shown in Figures 2.16 and 2.17.

Barone and Patterson (1998) employed Liebmann's formula

$$x_{i,j} = \frac{1}{4} \{x_{i-1,j} + x_{i+1,j} + x_{i,j+1} + x_{i,j-1}\} \quad (2.59)$$

to smooth thermoelastic data. The schematic diagram of the cells or pixels used in the formulae is shown in Figure 2.18.

There are three smoothing methods called 'Gentle', 'Medium' and 'Heavy' in the program *PECAN*. The 'Gentle' smoothing method makes use of a sixth difference smoothing formula and performs the smoothing along individual lines of data. The principle of the sixth difference method is that, in the recording of data, there are often one or more isolated missing values. The common way of supplying an isolated missing value is to use an interpolation formula based on the assumption that the data locally can be described a polynomial of some odd degree. This is equivalent to the assumption that the next higher order difference is zero. For example, assume that the 6th difference is zero, we have (Frieden, 1979, p.187)

$$\Delta^6 x_{i-3} = x_{i-3} - 6x_{i-2} + 15x_{i-1} - 20x_i + 15x_{i+1} - 6x_{i+2} + x_{i+3} = 0 \quad (2.60)$$

Solving the equation for x_i gives

$$x_i = \frac{1}{20}(x_{i-3} - 6x_{i-2} + 15x_{i-1} + 15x_{i+1} - 6x_{i+2} + x_{i+3}) \quad (2.61)$$

It is illustrated in Figure 2.19.

The 'Medium' and 'Heavy' subroutines in the program *PECAN* are smoothing methods using the same formulae as the method of Median 3x3 and 5x5 pixels respectively, i.e. equations (2.57) and (2.58).

2.4 Comparison of Maps from Full-Field Experimental, Theoretical and Numerical Methods

Along with the development of computer science, many experimental techniques have been improved in recent years. Full-field stresses are now expressed intuitively by computer images. Voloshin and Burger (1983) in demonstrating half fringe photoelasticity, performed a comparison of the fringe orders for a disc under diametrical compression by showing the full-field contour maps from half fringe photoelasticity and theory. Morimoto *et al* (1993) checked the accuracy of the results from the FFT photoelasticity by positioning a map of the isoclinic distribution for a disc under diametrical compression on the left of a map from the theoretical result. Absolute differences between the two maps were obtained in a point by point subtraction and the resulting map represents the error distribution for the isoclinics. These maps are shown in Figure 2.20.

Tsai and Morton (1995) published a study of a laminated composite single-lap adhesive joint. The results from full-field moire interferometry and finite element analysis using the ABAQUS code were compared along selected lines across the maps.

Vaillancourt *et al* (1995) verified the accuracy of a finite element analysis of two-dimensional porous-coated dental implants. The maps of the maximum shear stress contours from the finite element method (ANSYS, Version 4.4A) were compared with maps from transmission photoelasticity as shown in Figure 2.21. The results from the finite element method were also compared to theoretical solutions at some points on the interface of the flat-plane rigid indenter (along a line across the maps).

Ramesh and Mangal (1997) compared the results for a disc in diametrical compression from an experiment using full-field phase shifting photoelasticity and theory. The fringe order variations were shown along three selected horizontal lines with the disc centre at the origin (see Figure 2.22).

Barone and Patterson (1998) compared the results for stresses in a tension plate with a hole from thermoelasticity with those from theory. The normalised principal stresses were plotted along the horizontal centre line of the plate.

The examples revealed above are typical of comparative studies and the methods fall into two main types. One type of method is to compare the two stress maps pixel by pixel, it is suitable for comparison of two computer images of identical size and resolution. The other type of method is to select some points along a line across the map, it can be used for maps generated from different sources. Quantitative conclusions may be drawn from either type of method.

In practice, the end result map of stress calculated from images from an experimental method is represented as a dense matrix of data which typically is dependent on the magnification used. The density may vary and the point-on-point method can only be used when two digital maps with same magnification are available as performed by Morimoto *et al* (1993). In finite element analysis the mesh density is relatively coarse and stresses are calculated at a few nodes per element. The colour contour plots generated from the finite element data use interpolation with the stress matrix, whereas the plots from experimental methods have data values for every colour dot in the plot. The interpolation may not be properly used to those non-linear elastic fracture mechanics problems. Hence, investigation of a comparison of the maps from digital experimental method and numerical method is needed.

2.5 Discussion

2.5.1 Photoelasticity

Photoelasticity is a well-known and well-documented technique. It is almost the sole technique available for determining by experiment the three-dimensional stress state in a model. Reflection photoelasticity was developed based on the principles of transmission photoelasticity with some modifications. Both transmission and reflection photoelasticity are tedious and time-consuming to perform, in order to analyse the stress and strain in a model or real component. The development of automated photoelasticity makes the work easier, faster and more precise. In point-by-point methods, optical elements need to be rotated during the experiment and this is a drawback of all the methods except spectral content analysis. Hence, spectral content analysis is best suited for use as a point-by-point method but it requires considerable computing time for each analysis. In the category of full-field methods, half fringe photoelasticity and two wavelength methods are not feasible for real component measurement due to the restrictions of the fringe order being below a half fringe or the existence of a zero fringe order respectively. RGB photoelasticity is able to perform full-field analysis in a reasonable time, but it is only able to find fringe orders up to three. The fast Fourier transform method requires a huge amount of data, so it is not suitable for fast analysis. The method based on phase-stepping can provide isochromatic and isoclinic parameters but it requires the operator to provide an isochromatic fringe order. This disadvantage has been removed by combining the phase stepping technique with spectral content analysis and it has been performed by Patterson and Wang (1999).

Most of the automated photoelastic techniques reported used transmission specimens to validate their techniques, so errors caused by the specimen such as coating in reflection photoelasticity are not specified. Moreover, errors caused by electronic instrumentation employed in the techniques are not emphasised.

As suggested by Ajovalasit *et al* (1998), uncertainty of the automated methods of photoelastic analysis is worthy of careful attention by researchers, since in general, the technical literature does not report comparative analysis of the uncertainty. It is

desirable to compare the results from automated photoelasticity with other techniques, such as theory and numerical methods.

2.5.2 Phase-stepping systems

The automated transmission polariscope designed by Patterson and Wang (1991) is capable of yielding accurate maps of isochromatic fringe order and isoclinic angle that are needed in stress and strain analysis and for the calculation of stress intensity factors. It is an easy, fast and accurate method for two and three dimensional stress and strain analysis. However, it requires a model of the component and cannot be used for dynamic loading conditions.

The automated reflection polariscope, PSIOS (Patterson and Wang, 1998) is capable of solving dynamic problems because multiple images can be obtained simultaneously. In addition, it is sufficiently sensitive that thin coatings can be applied to the real component, hence no model is needed and the component can be tested under service loading. The drawbacks of reflection photoelasticity also exist in the PSIOS system. The noise in the light intensity images is more severe than in transmission photoelasticity. The degraded intensity images will cause error in the Wrapping process and this will affect the quality of isoclinic and isochromatic parameters, and the subsequently calculated stress and strain, as well as stress intensity factors from the photoelastic parameters. Therefore, it is necessary to identify the sources of noise and to select suitable methods to eliminate or reduce effect of noise.

2.5.3 Smoothing Methods in Automated Full-Field Photoelasticity

The averaging of the 16 consecutive pictures as used by Voloshin and Burger (1983), 10 pictures by Sarma *et al* (1992) and eight pictures by Chen (1997) would be an effective way to reduce the time-varying electrical noise because of the character of the noise in the images; but this method cannot remove the noise caused by other sources. The method for reducing noise in the image by shifting or distorting the frequency levels at some points (Mueller and Saackel, 1979) is not

applicable for images from the PSIOS system, because the isochromatic and isoclinic parameters are calculated using intensity data from four images which must be treated in an identical manner. One or more of the images may look smoother after the threshold method, but simply changing the intensity values of the images will result in false photoelastic parameters calculated based on these modified intensity data.

The method used by Seguchi *et al* (1979) uses the point of interest and three points after the current point, so the adjacent points before the current point that may have influence on the current point are neglected.

The median method is based on the fact that characteristic of very dissimilar pixel values is a probable indication of noise. Pixels that are not similar in value to their neighbours will be truncated using the method. Sarma's (1992) space averaging method is the same as the median 3x3. When a 5x5 pixels array is used there are two tiers of surrounding points — 25 points in total. There is no doubt that this method can smooth the image but the disadvantage of the method is obvious. It may significantly change the original distribution of intensity in the image, so that the subsequent stress and strain values are not reliable.

In the Fourier transform method, Quan *et al* (1993) and Morimoto and Imamoto (1994) eliminated the unwanted lower frequency background and high frequency speckle noise by properly selecting the spatial cut-off frequency. The image reported in the paper is not as smooth as desired. Moreover, in the Fourier transform method, intensities are transformed from the spatial domain to the frequency domain. Unwanted signals are removed and the remaining signals are then transformed back to the spatial domain. Processing time for the transform is not a problem because the Fourier transform is part of the procedure of the method. However, for the phase stepping method, using the Fourier transform method to smooth the data would be computational expensive.

The Liebmann smoothing method (Barone and Patterson, 1998) is an approximation method due to the truncation of the terms and error of the expression (2.59) is

$$O(h^2) \tag{2.62}$$

which is an error of order h^2 , the second order truncation error (Ames, 1977, p.17). The values of the edge points (neighbouring points) are used in the calculation of the value of the central point. The effects of the corner points on the central point are neglected.

The sixth difference formula gives different weightings to the points according to the distances of the points from the current point. The method takes into account the influence of distance between the point interest and other points used in the calculation but it only provides one set of coefficient for different applications in which noise may vary for those methods.

The above methods have been used in images from automated full-field polariscopes. They are effective for a particular application such as transmission photoelasticity, and thermoelasticity as reported. However, it may not be very effective with images obtained from the PSIOS system for reflection applications because the noise in the automated reflection photoelasticity is more severe than in automated transmission photoelasticity as shown in Figures 2.13 and 2.14. It is appropriate to assess the following methods: sixth difference method; Liebmann smoothing method; the median 3x3 and 5x5 pixels methods; and to investigate attractive smoothing methods that may effectively reduce noise in images from different applications according to the user's requirement.

2.5.4 Comparison of Maps from Full-Field Experimental, Theoretical and Numerical Methods

Methods that compare maps from experimental, theoretical and numerical techniques have been reviewed and can be classified into two main types. In the first type maps are obtained using different techniques when the specimen is loaded in the same condition. A map of difference of the two maps is used to present the error between the two methods (Morimoto *et al*, 1993); or it is left to readers to judge the difference using their common sense (Vaillancourt, 1995). In the second type some points are selected on a line across the maps from the different methods and they are plotted on the same axes (Barone and Patterson, 1998, Scalea, Hong and Cloud,

1997; Tsai, Chiu and Hsu, 1997; Olofsson and Lindgren, 1993). The latter is used widely and usually a reasonable, quantitative conclusion can be made. However, comparison of the full-field maps will give more information than a single line about the relationship between assumptions, boundary conditions and errors involved in the techniques being compared. The comparison of two computer images can be done using a pixel-by-pixel comparison for corresponding points as performed by Morimoto *et al* (1993). However, maps from finite element method cannot be simply compared with maps from experimental or theoretical method in the same way without approximation using interpolation of adjacent nodal points, due to the lack of one-on-one correspondence of the respective stress matrices. In practice, it is quite common to compare hot spots on experimental maps to the numerical maps for validation of numerical models. If the hot spots on the two maps match well, the numerical method is considered valid. However, when designs are being optimised for weight or crack paths are being investigated, comparison of the positions of the hot spots alone will not be enough and the correlation elsewhere in the data field should be taken into account. Hence, it is desirable to find a correlation method for comparison of maps from full-field experimental techniques and numerical method.

2.6 Conclusions

It is concluded that

- (1) The development of manual transmission and reflection photoelasticity is well established.
- (2) The combination of phase-stepping photoelasticity with spectral content analysis allows the automatic production of full-field maps of absolute fringe order and isoclinic angle.
- (3) Noise in the images obtained from the automated reflection polariscope, PSIOS is more severe than those from automated transmission photoelasticity. Therefore, a method should be found to minimise the effect of noise in the intensity images.
- (4) Development of a quantitative method for the comparison of full-field maps from experimental method and numerical analysis is desirable.

Table 2.1 Orientations of quarter-wave plate ϕ and analyser β in the automated transmission polariscope.

Image number	Orientation of quarter-wave plate ϕ	Orientation of analyser β
1	0	$\pi/4$
2	0	$-\pi/4$
3	0	0
4	$\pi/4$	$\pi/4$
5	$\pi/2$	$\pi/2$
6	$3\pi/4$	$3\pi/4$

Table 2.2 Orientations of quarter-wave plate ϕ and analyser β in the automated reflection polariscope

Image number	Orientation of quarter-wave plate ϕ	Orientation of analyser β
1	$\pi/4$	$\pi/4$
2	0	0
3	$\pi/2$	$\pi/2$
4	0	$\pi/4$

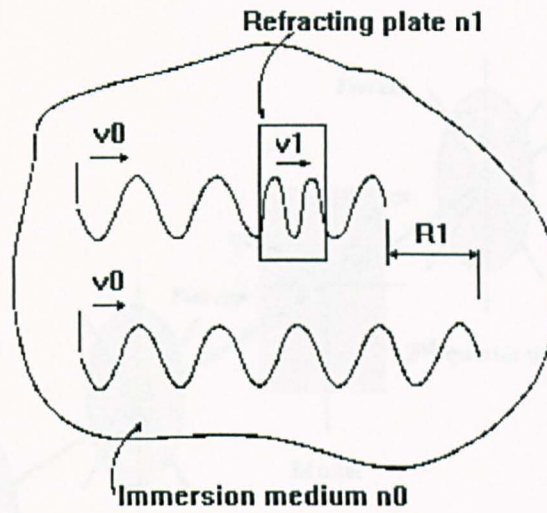


Figure 2.1 Absolute retardation by a refracting plate in an immersion medium.

(from Cloud, 1995, p.59, Fig. 4.1)

Figure 2.2 Passage of light through a plane polariscope.

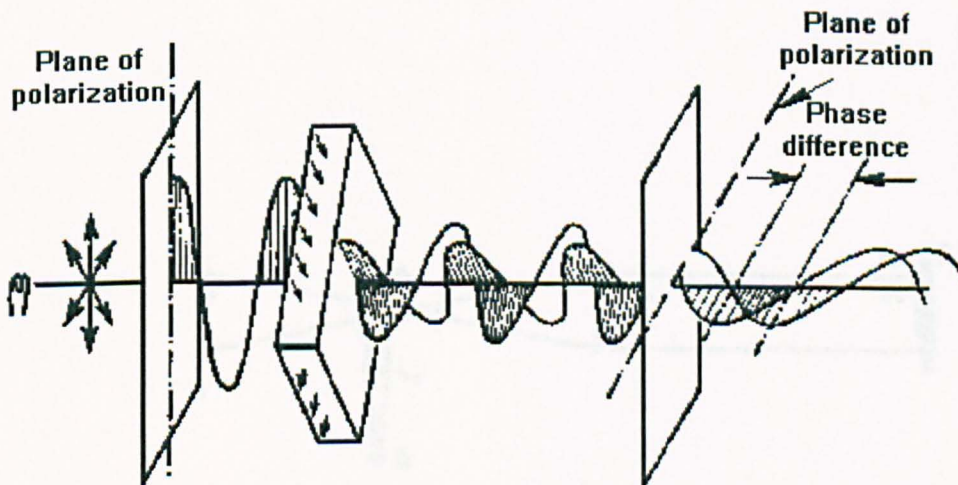


Figure 2.2 Passage of light through a plane polariscope.

(from Heywood, 1952, p.13, Fig. 1.6)

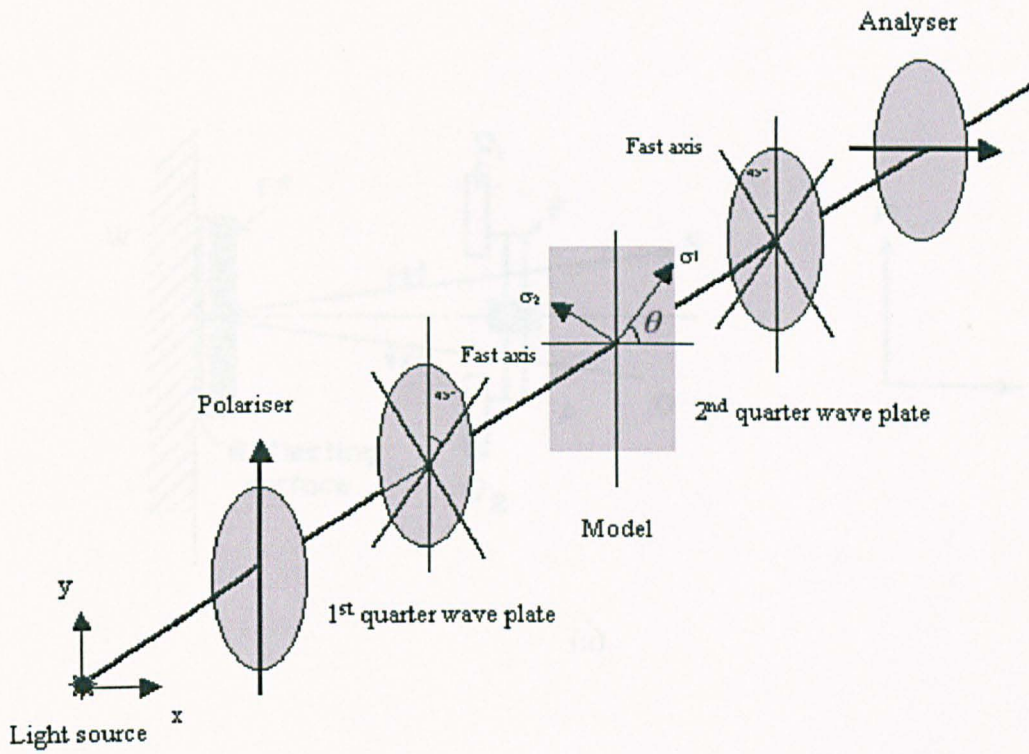


Figure 2.3 Schematic illustration of a circular polariscope.

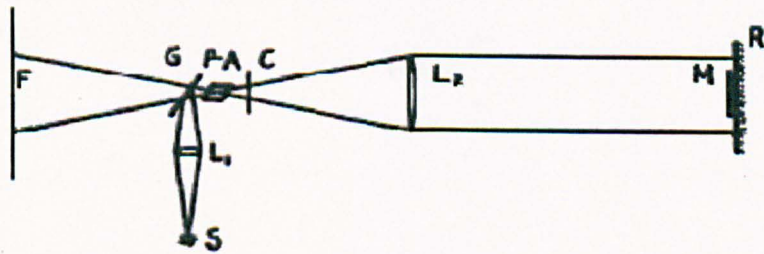
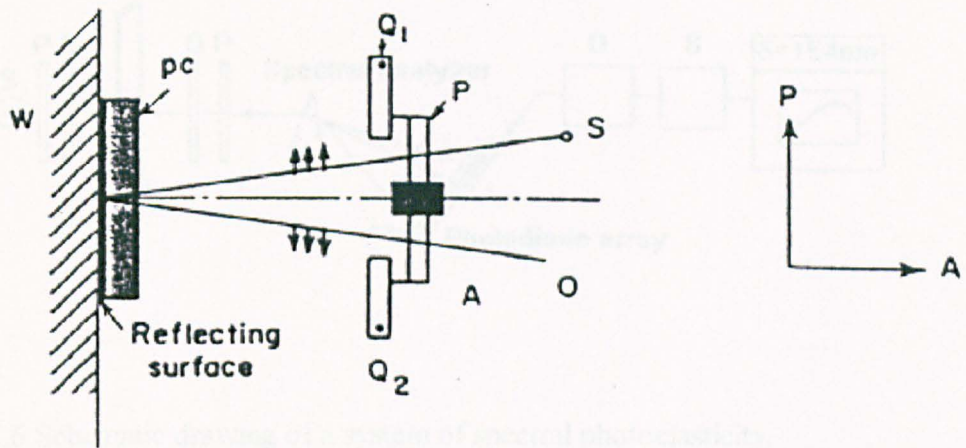
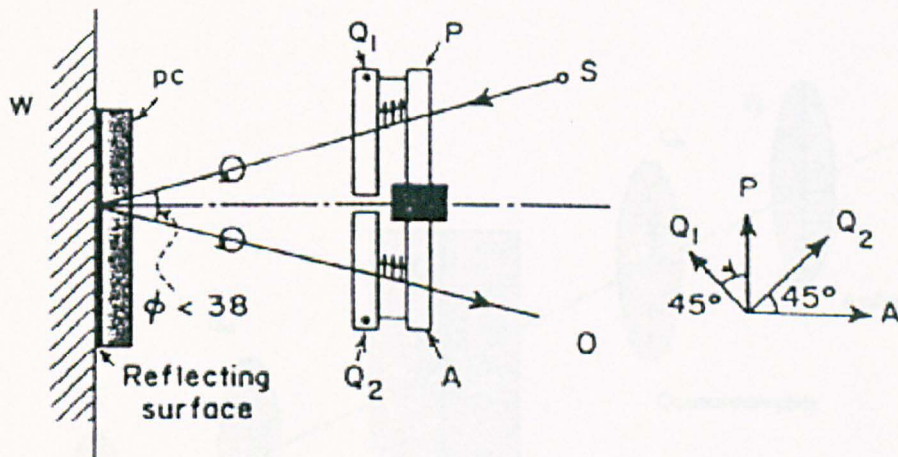


Figure 2.4 Reflection Polariscope.
(from Mindlin, 1934, p.225, Fig. 1)



(a)



(b)

Figure 2.5 Diagrams of light paths through Photo-Stress Meter LF/2 as a crossed (a) plane polariscope; (b) a circular polariscope.
(from Zandman and Wood, 1956, p.173, Fig. 7)

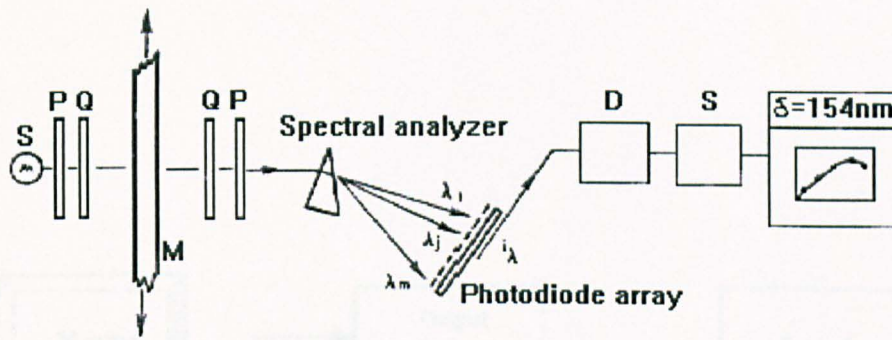


Figure 2.6 Schematic drawing of a system of spectral photoelasticity.

(from Redner, 1984, p. 150, Fig. 2)

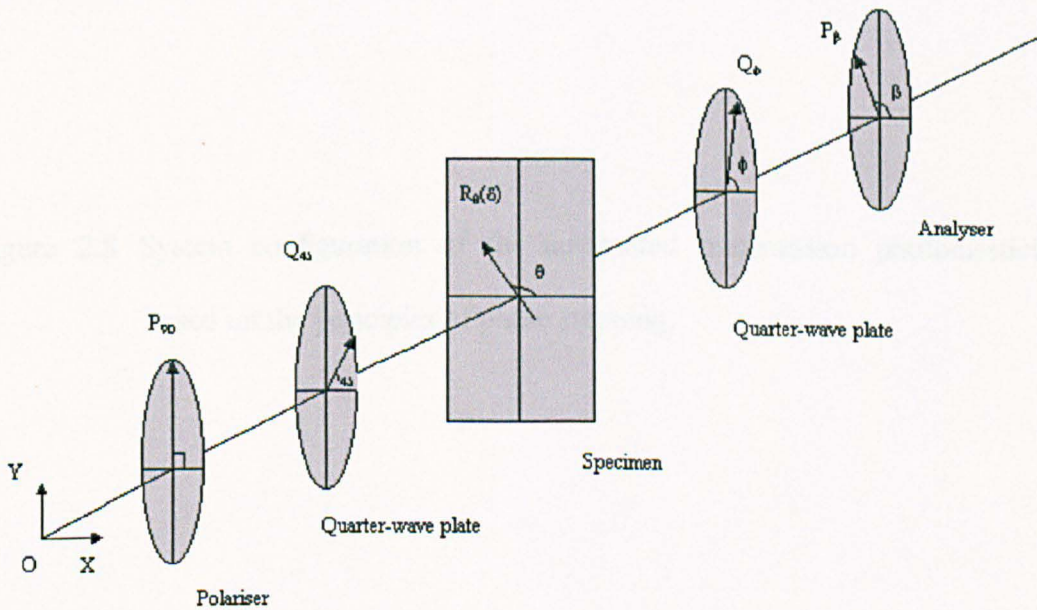


Figure 2.7 The phase-stepping method in automated transmission photoelasticity.

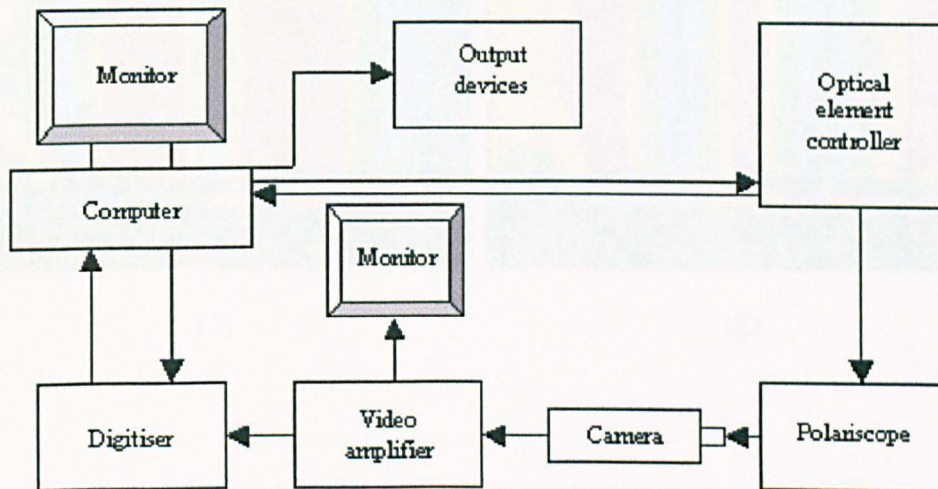
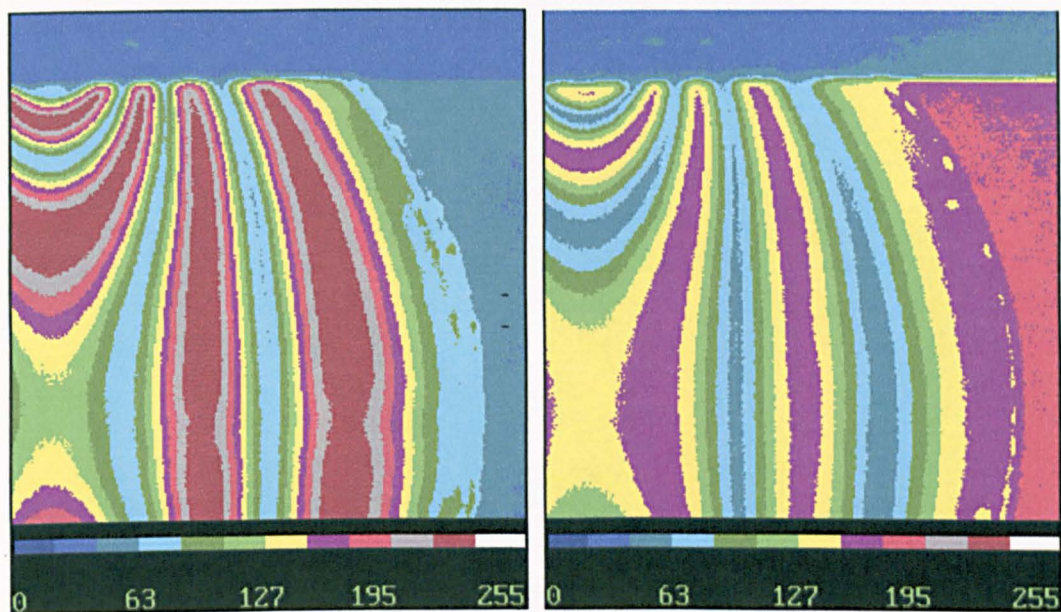
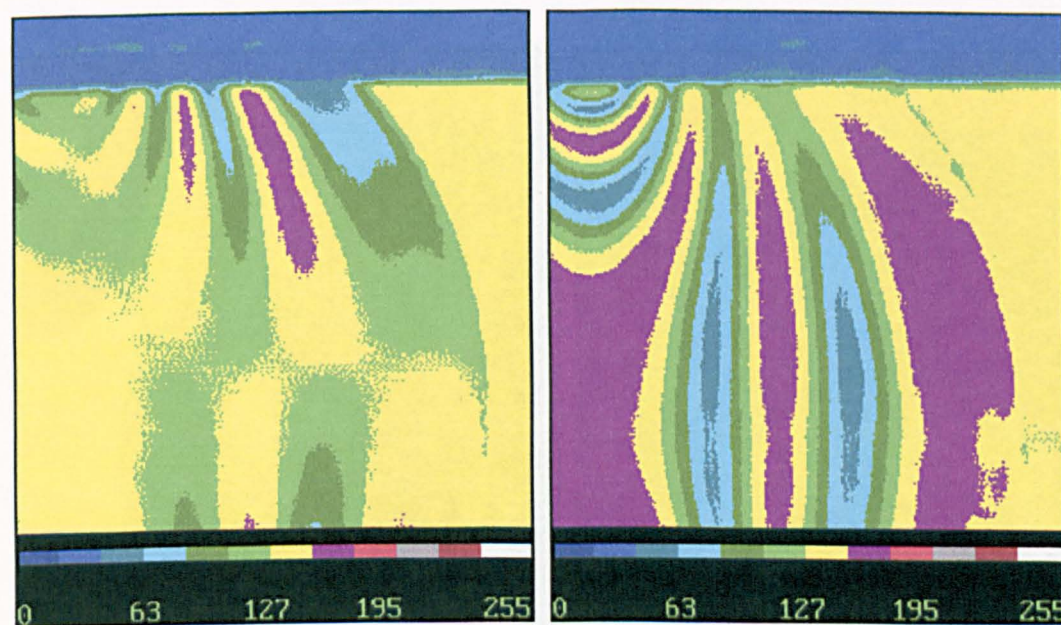


Figure 2.8 System configuration of the automated transmission photoelasticity based on the principles of phase stepping.



(1)

(2)



(3)

(4)

Figure 2.9 Maps of six phase stepped light intensity data recorded using the automated transmission polariscope. The quadrant of a stress frozen disc was under diametrical compression. Images from phase step 1 to 6 are shown in (1) to (6). The colour bar shows scale of intensity. (Continued)

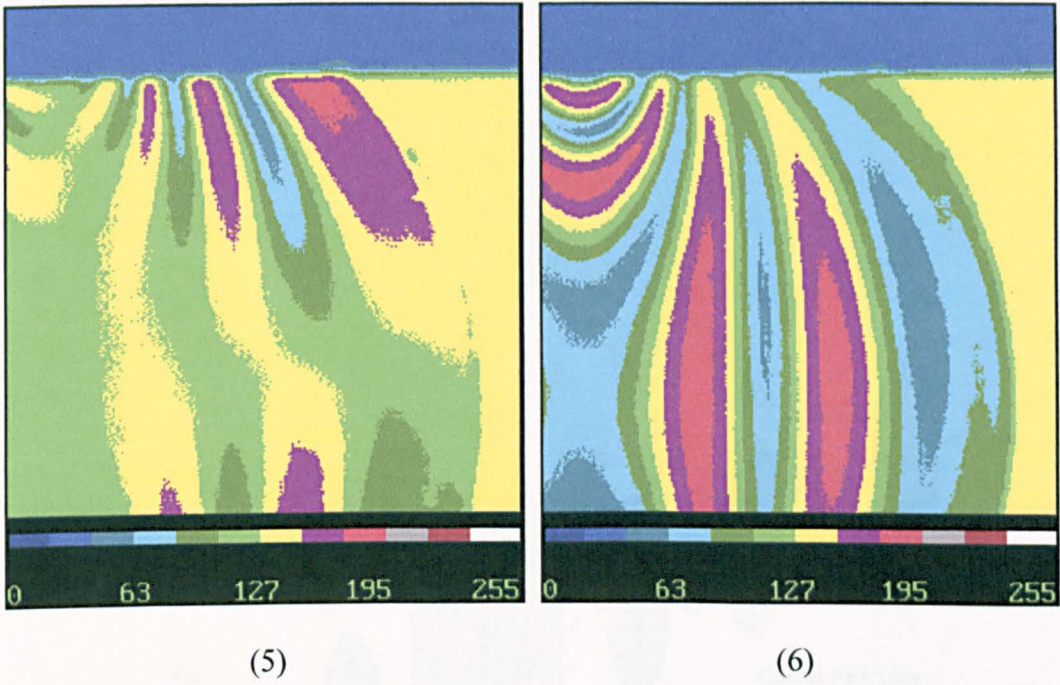


Figure 2.9 Continue from page 51.

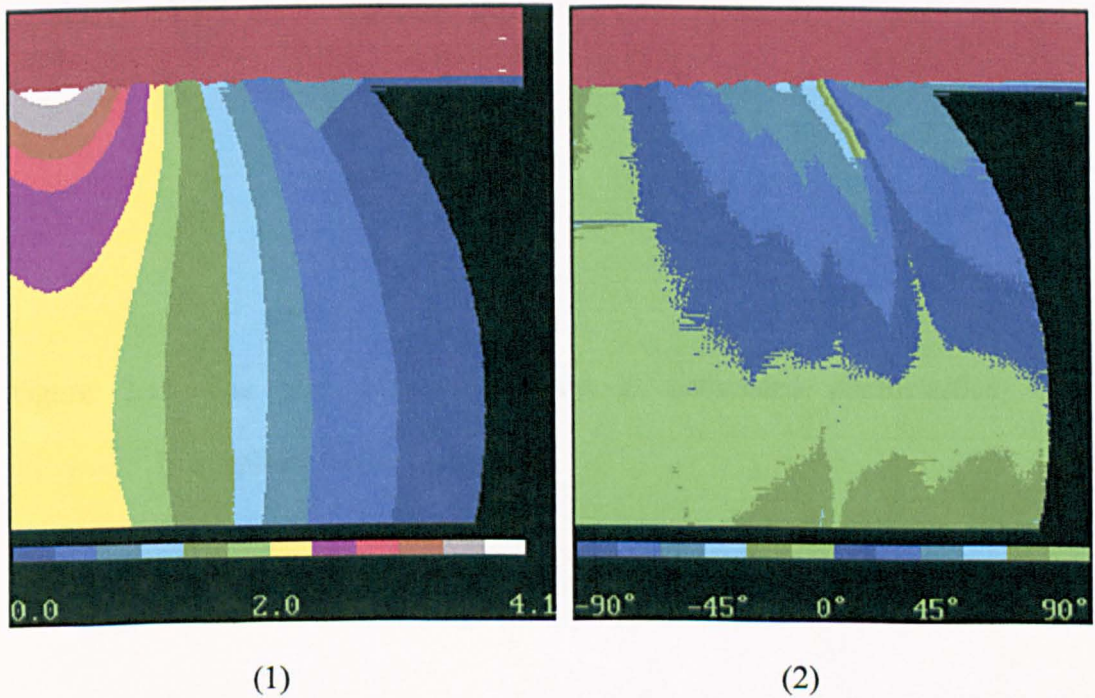


Figure 2.10 The isochromatic and isoclinic parameters of the disc processed using the program *VIZION*. The colour bar shows scale of (1) isochromatic fringe order and (2) isoclinic angle.

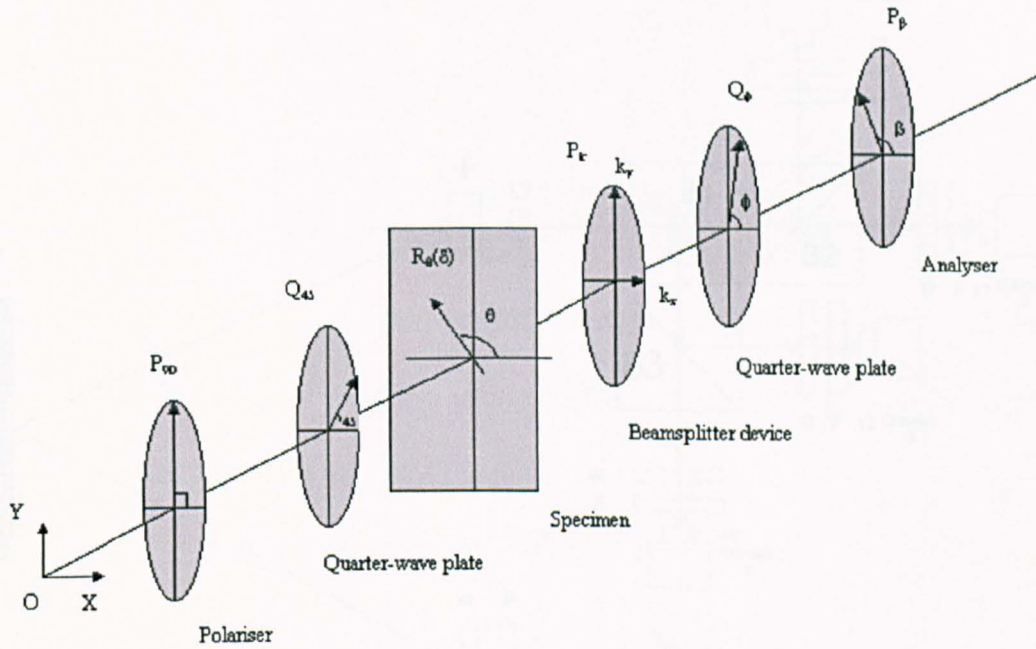


Figure 2.11 The phase-stepping method in automated photoelasticity with beamsplitter device inserted.

Figure 2.12 Scherwin's design of an ARPS system.

A: Analyser, B_1, B_2, B_3 : Beam splitters, F: Focal lens

L: Lenticular lens, M: Collimator, P: Polariser, S: Light source

Q: Quarter-wave plate, T: Thin specimen with coating

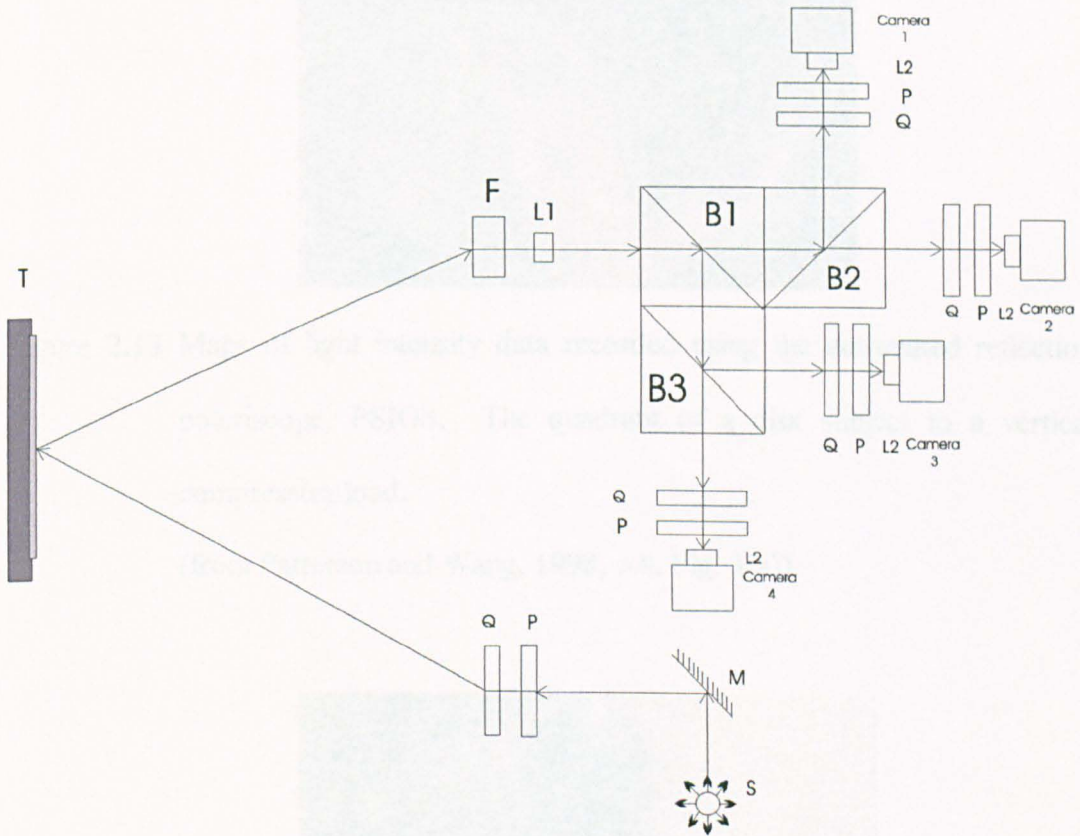


Figure 2.12 Schematic diagram of the PSIOS system.

A: Analyser; B₁, B₂, B₃: Beamsplitters; F: Focal lens;

L₁, L₂: Objective lens; M: Cold mirror; P: Polariser; S: Light source;

Q: Quarter-wave plate; T: Test specimen with coating



Figure 2.13 Maps of light intensity data recorded using the automated reflection polariscope, PSIOS. The quadrant of a disk subject to a vertical compressive load.

(from Patterson and Wang, 1998, p.6, Fig. 3(a))

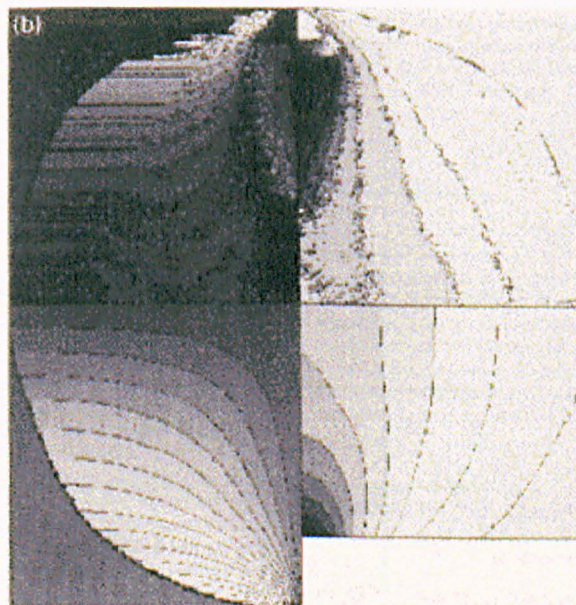


Figure 2.14 Isochromatic and isoclinic parameters of the disc using the program PECAN.

(from Patterson and Wang, 1998, p.6, Fig. 3(b))

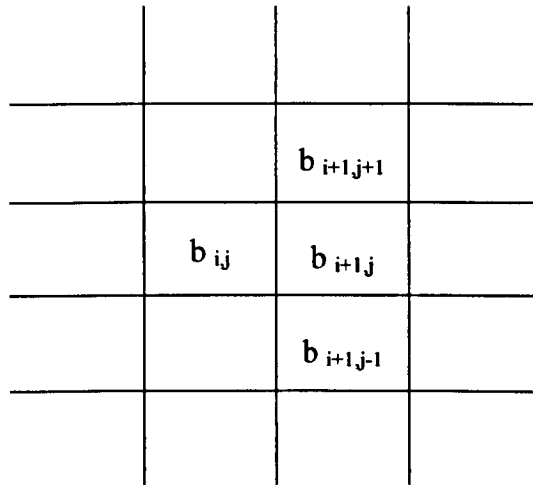


Figure 2.15 Schematic diagram of the Seguchi *et al* formula.

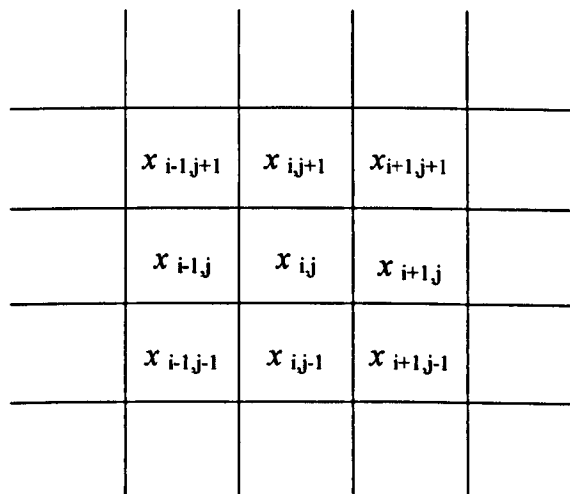


Figure 2.16 Kernel of the median filter 3x3 pixels.

	$x_{i-2,j+2}$	$x_{i-1,j+2}$	x_{ij+2}	$x_{i+1,j+2}$	$x_{i+2,j+2}$
	$x_{i-2,j+1}$	$x_{i-1,j+1}$	x_{ij+1}	$x_{i+1,j+1}$	$x_{i+2,j+1}$
	$x_{i-2,j}$	$x_{i-1,j}$	x_{ij}	$x_{i+1,j}$	$x_{i+2,j}$
	$x_{i-2,j-1}$	$x_{i-1,j-1}$	x_{ij-1}	$x_{i+1,j-1}$	$x_{i+2,j-1}$
	$x_{i-2,j-2}$	$x_{i-1,j-2}$	x_{ij-2}	$x_{i+1,j-2}$	$x_{i+2,j-2}$

Figure 2.17 Kernel of the median filter 5x5 pixels.

		$\frac{1}{4}$ x_{ij+1}	
$\frac{1}{4}$ $x_{i-1,j}$	x_{ij}	$\frac{1}{4}$ $x_{i+1,j}$	
	$\frac{1}{4}$ x_{ij-1}		

Figure 2.18 Schematic diagram of the Liebmann's formula.

	$1/20$	$-6/20$	$15/20$		$15/20$	$-6/20$	$1/20$	
	x_{i-3}	x_{i-2}	x_{i-1}	x_i	x_{i+1}	x_{i+2}	x_{i+3}	

Figure 2.19 Schematic diagram of the Sixth difference method.

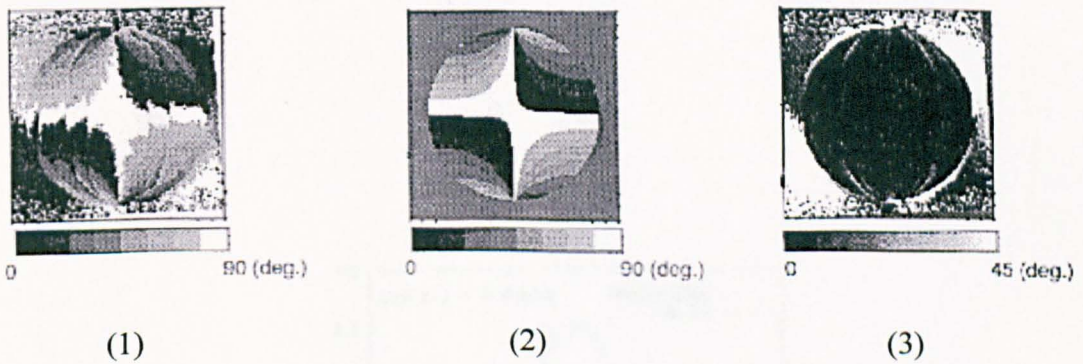


Figure 2.20 Distribution of principal stress direction using FFT photoelastic method

- (1) from the FFT photoelastic method;
- (2) from theoretical calculation;
- (3) difference of the maps in (1) and (2).

(from *Morimoto et al*, 1993, pp. 1156, 1158, Fig. 8, Fig. 9 and Fig.11)

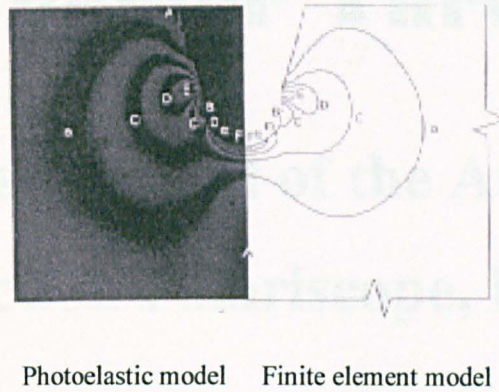


Figure 2.21 Maximum shear stress contours.

(from Vaillancourt *et al*, 1995, p.53, Fig. 6(b))

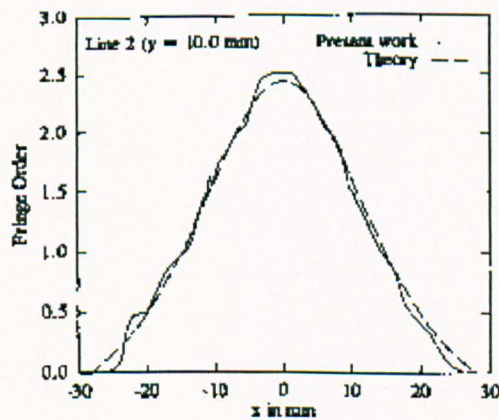


Figure 2.22 Comparison of fringe orders for a circular disc under diametrical compression.

(from Ramesh and Mangal, 1997, p.100, Fig.7)

Chapter Three

Initial Assessment of the Automated Reflection Polariscopes, PSIOS

3.1 Introduction

3.2 Formulae of Stress Intensity Factor K_I for Strain Gauge and
Photoelastic methods

3.3 Experiments

3.4 Discussion

3.5 Conclusion

3.1 Introduction

The design and principles of the PSIOS instrument have been reviewed in section 2.2.2. It is necessary to assess the capabilities of the PSIOS instrument using real engineering components. The determination of the stress intensity factors for a plate with cracks is a difficult task due to the presence of steep changes in the stress gradient; thus it was selected for the assessment.

Stress intensity factor (SIF) is a parameter that characterises the redistribution of the stress in a body due to the introduction of a crack. In brittle materials, the stress intensity factor K_I can be compared with the fracture toughness of the material, K_{IC} to predict whether the crack will be stable under an applied load or will become unstable and cause abrupt failure. In ductile materials the amplitude of K_I in cyclic loading can be used to predict the rate of crack growth using the Paris law.

Many methods have been developed to determine stress intensity factors by experiment. However, the accuracy of individual methods is quite different when they are applied directly to a structure rather than a model. Previous investigations have revealed that the accuracy depends on a number of factors, such as the selection of the experimental methods, the instrumentation, the specimen preparation and the algorithms employed. Photoelasticity is one of the available techniques and has been applied in the field for more than forty years. In the present study, results for the SIF from three different procedures using reflection photoelasticity are compared with those from strain gauges and from Newman's (1971) numerical solutions for the stress intensity factor for a tensile plate with double cracks from the edge of a central hole (Murakami 1990). The three photoelastic procedures involve (a) point-by-point readings from a conventional reflection polariscope; (b) extracting data from a colour photograph obtained using a conventional polariscope (Nurse & Patterson 1990, 1992 and 1993(a)), and (c) digital data from the automated polariscope PSIOS (Patterson & Wang, 1998). The different instruments and algorithms used are described in the following sections.

3.2 Formulae of Stress Intensity Factor K_I for Strain Gauge and Photoelastic Methods

Consider a crack in a component, the area adjacent to the crack tip is divided into three regions as shown in Figure 3.1. The region *I* (very near-field region) which is close to the crack tip is very small and extends only a distance of $0.02a$ from the tip of the crack. Since the stress distribution in this region is three-dimensional, neither plane stress nor plane strain assumptions are valid. This region is not a valid region for data acquisition. The region *II* (near-field region) is a valid area where the strain field can be represented within a specified accuracy by a multiparameter theory containing K_I and coefficients of higher order terms as unknowns. The region *III* (far-field region) is avoided in measuring field quantities in an attempt to determine the stress intensity factor, because the large number of unknown coefficients in the series require that large amounts of data be taken with very high accuracy. The stress field near a single-ended crack tip loaded in opening mode can be expressed as Westgaard equations (Dally and Riley, 1991, p.94)

$$\sigma_{xx} = \operatorname{Re} Z - y \operatorname{Im} Z' \quad (3.1)$$

$$\sigma_{yy} = \operatorname{Re} Z + y \operatorname{Im} Z' \quad (3.2)$$

$$\tau_{xy} = -y \operatorname{Re} Z' \quad (3.3)$$

where $Z(z)$ is a complex stress function and z is defined as

$$z = x + jy = re^{j\theta} \quad (3.4)$$

The stress function Z which is applied to solve the problem of an infinite plate with a central crack of length $2a$ is

$$Z = \frac{\sigma_0(z+a)}{\sqrt{z(z+2a)}} \quad (3.5)$$

where the origin of the coordinate system is placed at the tip of the crack.

Consider a small region near the crack tip where $z \ll a$, equation (3.5) reduces to

$$Z = \sqrt{\frac{a}{2}} \sigma_0 z^{-1/2} \quad (3.6)$$

Substituting equation (3.4) and

$$e^{\pm j\theta} = \cos \theta \pm j \sin \theta \quad (3.7)$$

into equation (3.6) shows that the real part of Z is

$$\text{Re } Z = \sqrt{\frac{a}{2r}} \sigma_0 \cos \frac{\theta}{2} \quad (3.8)$$

Along the crack line where θ and y are both equal to zero, equations (3.8) and (3.2) give

$$\sigma_{yy} = \text{Re } Z = \sqrt{\frac{a}{2r}} \sigma_0 \quad (3.9)$$

When the stress $\sigma_{yy} \rightarrow \infty$ and is singular with order $1/\sqrt{r}$ as one approaches the crack tip along the x axis, the stress intensity factor K_I can be expressed as

$$K_I = \lim_{r \rightarrow 0} (\sqrt{2\pi r} \sigma_{yy}) = \sqrt{\pi a} \sigma_0 \quad (3.10)$$

This result shows that the stress intensity factor K_I varies as a linear function of the applied stress N_0 and increases with crack length as a function of the \sqrt{a} .

3.2.1 Strain gauge method

The modified Westgaard equations (Dally and Riley, 1991, p.107) are

$$\sigma_{xx} = \text{Re } Z - y \text{Im } Z' - y \text{Im } Y' + 2 \text{Re } Y \quad (3.11)$$

$$\sigma_{yy} = \text{Re } Z + y \text{Im } Z' + y \text{Im } Y' \quad (3.12)$$

$$\tau_{xy} = -y \text{Re } Z' - y \text{Re } Y' - \text{Im } Y \quad (3.13)$$

where the stress functions are given as series relations in terms of z as

$$Z(z) = \sum_{n=0}^N A_n z^{(n-1/2)} \quad (3.14)$$

$$Y(z) = \sum_{m=0}^M B_m z^m \quad (3.15)$$

By substituting equations (3.11), (3.12) and (3.13) into the plane stress-strain relations:

$$\varepsilon_{xx} = \frac{1}{E} (\sigma_{xx} - \nu \sigma_{yy}) \quad (3.16)$$

$$\varepsilon_{yy} = \frac{1}{E} (\sigma_{yy} - \nu \sigma_{xx}) \quad (3.17)$$

$$\gamma_{xy} = \frac{1}{\mu} \tau_{xy} \quad (3.18)$$

where E and ν are elastic modulus and Poisson's ratio of the material respectively.

The generalised equations can be obtained for the strain field.

$$E\varepsilon_{xx} = (1-\nu)\text{Re } Z - (1+\nu)y\text{Im } Z' - (1+\nu)y\text{Im } Y' + 2\text{Re } Y \quad (3.19)$$

$$E\varepsilon_{yy} = (1-\nu)\text{Re } Z + (1+\nu)y\text{Im } Z' + (1+\nu)y\text{Im } Y' - 2\nu\text{Re } Y \quad (3.20)$$

$$\mu\gamma_{xy} = -y\text{Re } Z' - y\text{Re } Y' - \text{Im } Y \quad (3.21)$$

The strain fields can be expressed exactly by using the infinite series representation of the stress functions Z and Y . This exact approach cannot be utilised in practice due to the infinite number of unknown coefficients A_n and B_m .

Dally and Sanford (1987) described a four-term representation where the first two terms of each of the series for Z and Y have been retained. The strains relative to a rotated coordinate system (x', y') with its origin at an arbitrary point $P(r, \theta)$ as defined in Figure 3.2 is determined from the first invariant of strain,

$$\varepsilon_{x'x'} + \varepsilon_{y'y'} = \varepsilon_{xx} + \varepsilon_{yy} \quad (3.22)$$

and the complex form of the strain-transformation equations,

$$\varepsilon_{y'y'} - \varepsilon_{x'x'} + i\gamma_{x'y'} = (\varepsilon_{yy} - \varepsilon_{xx} + i\gamma_{xy})e^{2i\alpha} \quad (3.23)$$

Substituting equations (3.19), (3.20) and (3.21) into equation (3.23) and letting $n = 0, 1$ and $m = 0, 1$ in equations (3.14) and (3.15), one obtains the following equations,

$$\begin{aligned}
2\mu\varepsilon_{x'x'} = & A_0 r^{-\frac{1}{2}} \left[k \cos\left(\frac{\theta}{2}\right) - \frac{1}{2} \sin \theta \sin\left(\frac{3\theta}{2}\right) \cos 2\alpha + \frac{1}{2} \sin \theta \cos\left(\frac{3\theta}{2}\right) \sin 2\alpha \right] \\
& + B_0 (k + \cos 2\alpha) + A_1 r^{\frac{1}{2}} \cos\left(\frac{\theta}{2}\right) \left[k + \sin^2 \frac{\theta}{2} \cos 2\alpha - \frac{1}{2} \sin \theta \sin 2\alpha \right] \\
& + B_1 r \left[(k + \cos 2\alpha) \cos \theta - 2 \sin \theta \sin 2\alpha \right]
\end{aligned} \tag{3.24}$$

$$\begin{aligned}
\mu(\varepsilon_{y'y'} - \varepsilon_{x'x'}) = & \frac{A_0}{2} r^{-\frac{1}{2}} \sin \theta \left[\sin \frac{3\theta}{2} \cos 2\alpha - \cos \frac{3\theta}{2} \sin 2\alpha \right] \\
& - B_0 \cos 2\alpha + \frac{A_1}{2} r^{\frac{1}{2}} \sin \theta \left[\cos \frac{\theta}{2} \sin 2\alpha - \sin \frac{\theta}{2} \cos 2\alpha \right] \\
& + B_1 r \left[a \sin \theta \sin 2\alpha - \cos \theta \cos 2\alpha \right]
\end{aligned} \tag{3.25}$$

where r is the distance from the gauge to the crack tip and

$$k = (1 - @)/(1 + @) \tag{3.26}$$

In region II, A_0 is related to K_I by

$$K_I = \sqrt{2\pi} A_0 \tag{3.27}$$

The unknown coefficients could be determined if four or more strain gauges are placed at appropriate position in the region II.

Single gauge with three-parameter solution

For a single gauge, three-parameters is used and the coefficient of the B_0 is eliminated by selecting the angle K as

$$\cos 2K = -k = -(1 - @)/(1 + @) \tag{3.28}$$

The coefficient A_1 vanishes if the angle δ is selected as

$$\tan \frac{\theta}{2} = -\cot 2\alpha \tag{3.29}$$

Therefore, the stress intensity factor K_I is related to the strain as

$$K_I = \left(\frac{E}{1+\nu} \varepsilon_{x'x'} \sqrt{2\pi r_c} \right) / \left(\frac{1-\nu}{1+\nu} \cos \frac{\theta}{2} - \frac{1}{2} \sin \theta \sin \frac{3\theta}{2} \cos 2\alpha + \frac{1}{2} \sin \theta \cos \frac{3\theta}{2} \sin 2\alpha \right) \tag{3.30}$$

Rectangular rosette strain gauge with two-parameter solution

For a stacked rectangular rosette strain gauge, a two-parameter solution is used. The output from the Wheatstone bridge gives the measurement of $\varepsilon_{y'y'} - \varepsilon_{x'x'}$. The coefficients of the B_0 term will vanish if

$$\cos 2K = 0 \text{ or } K = \pi/4 \quad (3.31)$$

When $\delta = \pi/2$, equation (3.25) gives

$$K_I = \frac{2E}{1+\nu} (\varepsilon_{y'y'} - \varepsilon_{x'x'}) \sqrt{\pi r} \quad (3.32)$$

3.2.2 Conventional photoelastic method

For opening mode, modified Westgaard stress equations are (Dally and Riley, 1991, p.509)

$$\sigma_x = \frac{K_I}{\sqrt{2\pi r}} \cos \frac{\theta}{2} \left(1 - \sin \frac{\theta}{2} \sin \frac{3\theta}{2} \right) + \sigma_{ox} \quad (3.33)$$

$$\sigma_y = \frac{K_I}{\sqrt{2\pi r}} \cos \frac{\theta}{2} \left(1 + \sin \frac{\theta}{2} \sin \frac{3\theta}{2} \right) \quad (3.34)$$

$$\tau_{xy} = \frac{K_I}{\sqrt{2\pi r}} \sin \frac{\theta}{2} \cos \frac{\theta}{2} \cos \frac{3\theta}{2} \quad (3.35)$$

where σ_{ox} is a non-singular term appearing only in the σ_x component to take account of far-field effect.

The maximum shear stress O_m is expressed in terms of the cartesian stress components as

$$(2\tau_m)^2 = (\sigma_{yy} - \sigma_{xx})^2 + (2\tau_{xy})^2 \quad (3.36)$$

From equations (3.33), (3.34) and (3.35), the equation (3.36) can be expressed as

$$(2\tau_m)^2 = \frac{K_I^2}{2\pi r} \sin^2 \theta + \frac{2\sigma_{ox} K_I}{\sqrt{2\pi r}} \sin \theta \sin \frac{3\theta}{2} + \sigma_{ox}^2 \quad (3.37)$$

When $\delta = 90^\circ$, equation (3.37) can be written as

$$\tau_{\max} = \frac{K_1}{\sqrt{8\pi r}} + f(\sigma_{ij}^o) \quad (3.38)$$

where $f(\sigma_{ij}^o)$ is a set of constants which account for the contribution of the non-singular stress field.

Re-arranging expression (3.38) gives

$$\frac{K_{AP}}{\sigma\sqrt{\pi a}} = \frac{K_1}{\sigma\sqrt{\pi a}} + \frac{f(\sigma_{ij}^o)}{\sigma} \left(\frac{r}{a}\right)^{\frac{1}{2}} \quad (3.39)$$

where σ is the nominal applied stress and K_{AP} the apparent stress intensity factor

$$K_{AP} = \tau_{\max} (8\pi r)^{\frac{1}{2}} \quad (3.40)$$

Linear elastic fracture mechanics is considered to be valid when the measurement is carried out in an annular region of inner radius of 10ρ and outer radius of $0.4a$ where ρ is crack tip radius and a is crack length (Gdoutos, 1985, p.191). For reflection photoelasticity, data points must be taken $4t$ (where t is coating thickness) away from the edge of the coating in order to take into account the influence of the Poisson's ratio mismatch between the specimen and the coating (Dally and Riley, 1991, p.558). The normalised apparent K_{AP} varies linearly with the square root of the normalised distance of the measured data from the crack tip. The intercept on the normalised K_{AP} axis provides the value of the geometric factor, Y . The stress intensity factor is readily obtained from the relationship

$$K_1 = Y\sigma_0\sqrt{\pi a} \quad (3.41)$$

where N_0 is applied stress.

3.2.3 Photographic and automated photoelastic methods

The determination of the stress intensity factor in automated photoelastic method is the same as in the photographic photoelastic method. The stress field around the crack tip is defined using the Muskhelishvili approach in which the in-plane stresses are represented by two analytical functions of the complex variable. The in-plane

rectangular components of stress in a stressed body in the absence of body forces can be written as (Nurse and Patterson, 1993(b))

$$\sigma_x + \sigma_y = \Phi(z) + \overline{\Phi(z)} \quad (3.42)$$

and

$$\sigma_y - \sigma_x + i\tau_{xy} = \bar{z}\Phi'(z) + \Psi(z) \quad (3.43)$$

where the prime denotes differentiation and the overbar denotes complex conjugate.

Conformal mapping was used and in the mapping plane the complex stress functions $J(z)$ and $\Psi(z)$ are given in the complex Fourier series form

$$\Phi(\zeta) = \sum_{N=0}^{\infty} A_n \zeta^{2N} + \sum_{m=1}^{\infty} \frac{a_m}{\zeta^{2m}} \quad (3.44)$$

$$\Psi(\zeta) = \sum_{N=0}^{\infty} B_n \zeta^{2N} + \sum_{n=1}^{\infty} \frac{b_n}{\zeta^{2n}} \quad (3.45)$$

assuming the stress field is symmetrical about the imaginary axis. The series parameters, A_n , B_n , a_m and b_n ($n = 1, \dots, \infty$) are generally complex and are used to describe different states of stress.

To satisfy the crack boundary conditions the series parameters a_m and b_n are

$$a_m = A_0 + \bar{A}_0 + \bar{B}_0 + \sum_{j=1}^m (4j)\bar{A}_j - (2m+1)\bar{A}_m - \bar{B}_m \quad (3.46)$$

$$b_n = A_0 + \bar{A}_0 + \bar{B}_0 + \sum_{k=1}^n (4k)a_k - (2n+1)a_n - \bar{A}_n \quad (3.47)$$

The complex stress functions are determined by inserting expressions (3.46) and (3.47) into expressions (3.44) and (3.45) which after re-arranging gives

$$\Phi(\zeta) = A_0 + \frac{A_0 + \bar{A}_0 + \bar{B}_0}{(\zeta^2 - 1)} + \sum \left[\left(\frac{2N}{\zeta^{2N}} \right) \left(\frac{\zeta^2 + 1}{\zeta^2 - 1} \right) \bar{A}_N - \frac{\bar{A}_N}{\zeta^{2N}} - \frac{\bar{B}_N}{\zeta^{2N}} + A_N \zeta^{2N} \right] \quad (4.48)$$

and

$$\Psi(\zeta) = B_0 + \frac{B_0 - \bar{B}_0}{(\zeta^2 - 1)} + a(A_0 + \bar{A}_0 + \bar{B}_0) \frac{\zeta^2(\zeta^2 - 1)}{(\zeta^2 - 1)^3}$$

$$\begin{aligned}
& + \sum_{N=1}^{\infty} \left[\left(\frac{4N^2}{\zeta^{2N}} \right) \frac{(\zeta^4 - 1)(\zeta^2 + 1)}{(\zeta^2 - 1)^3} \bar{A}_N + \left(\frac{8N}{\zeta^{2N}} \right) \frac{\zeta^{24}(\zeta^2 + 1)}{(\zeta^2 - 1)^3} \bar{A}_N \right] \\
& - \left(\frac{4N}{\zeta^{2N}} \right) \frac{(\zeta^2 + 1)}{(\zeta^2 - 1)} \bar{A}_N - \left(\frac{2N}{\zeta^{2N}} \right) \frac{(\zeta^2 + 1)}{(\zeta^2 - 1)^3} \bar{B}_N + \frac{\bar{B}_N}{\zeta^{2N}} + B_N \zeta^{2N}
\end{aligned} \quad (3.49)$$

The complex stress intensity factor $K_I + iK_{II}$ is calculated using the limiting value of $J(4)$ as $\zeta \rightarrow \pm 1$, i.e.

$$K_I + iK_{II} = A_0 + \bar{A}_0 + B_0 + 2 \sum_{N=1}^{\infty} (A_N + \bar{A}_N) \quad (3.50)$$

The best-fit solution of the unknown series parameters A_n and B_n can be determined by using an over-deterministic solution procedure, i.e. more data points than variables solved to reduce the effect of data collection errors and it utilises a least squares minimisations process to produce a best-fit solution. The number of terms can be chosen by the operator, and the iteration procedure will stop when the SIFs converge.

3.3 Experiments

3.3.1 Specimens

Two aluminium-alloy plates each with cracks originating from a central hole were used in the experiment. The artificial cracks were machined from the edges of the hole and were perpendicular to the loading direction, as shown in Figure 3.3. The aluminium plates were 120 mm wide and 6.6 mm thick. The elastic modulus of the plate was 73 GPa and the Poisson's ratio was 0.32. The radius of the central hole was 15 mm. The length of the crack from the edge of the central hole in specimen *A* was 15 mm and in specimen *B* is 9 mm. The crack was machined using a jeweller's saw which resulted in a crack thickness of 0.2 mm, with a semi-circular profile at its tip. Pieces of photoelastic coating (PS-1B) were cut to fit the geometry of the plate and cracks, and was bonded to the plates but not over the cracks using PC-1 adhesive. (Both PS-1B and PC-1 were supplied by Measurement Group Inc. Raleigh, N. C. USA). The pieces of coating were 120x80 mm and glued to the plates symmetrical to the crack surface. The thickness of the photoelastic coating was 2 mm, strain optical coefficient 0.15, elastic modulus 2.5 GPa, Poisson's ratio 0.36 and material fringe constant 200 N/fringe/mm. Strain gauges (Tokyo Sokki Kenkyujo Co. Ltd.) were bonded to the back of the specimens *A* and *B* in the region near the crack tip.

The specimens were subjected to tensile loads of 1, 1.5, 2, 2.5 and 3 tonnes respectively on a large dead-weight loading rig. Several different methods were employed to obtain data for the subsequent calculation of the SIF of the specimens as described below.

3.3.2 Strain Gauge Method

A linear, two-element stacked rosette, electrical-resistance strain gauge (gauge factor $f = 2.12$, gauge length $l = 5$ mm, Tokyo Sokki Kenkyujo Co. Ltd.) was bonded on to specimen *A*. The distance from the geometric centre of the gauge to the crack tip was 7.6 mm on a line through the crack tip and perpendicular to the

crack plane. The strain gauge was connected to a Switch & Balance Unit and a Strain Indicator of Model P-3500 (Vishay Instrument Measurement Group, USA). The stress intensity factor was obtained by calculating data from strain gauge reading using equation (3.32).

A linear, one element, flat strain gauge (gauge factor $f = 2.09$, gauge length $l = 2$ mm, Tokyo Sokki Kenkyujo Co. Ltd.) was bonded on to specimen *B*. The position and orientation of the gauge are shown in Figure 3.2. The distance from the geometrical centre of the gauge to the crack tip was 3.75 mm. The instrumentation in this experiment was same as for specimen *A*, but the results were obtained using equation (3.30) when angles of α and θ equal to 60.5° and 62° .

The results are plotted in Figures 3.6 and 3.7.

3.3.3 Conventional Reflection Photoelasticity Method

A reflection polariscope Model 031 (Vishay Instruments Measurement Group, USA) with a white light source ($\lambda = 575$ nm) and a Null-Balance Compensator Model 232 (Vishay Instruments Measurement Group, USA) and a colour CCTV camera Model WV-CP210/B (Panasonic, Japan) were used in the experiment. The experimental set up is shown in Figure 3.4.

Data points were taken in an annular ring of inner radius of 8 mm and outer radius of 12 mm and in a line from the crack tip and perpendicular to the crack. The reading from the null-balance compensator was divided by 47 as suggested by the manufacturer of the instrument to obtain the absolute fringe order of the point. The fringe order N can be related to the maximum in-plane shear stress in the coating, O_m ,

$$\tau_{\max} = \frac{Nf}{2h_c} = \frac{E_s N \lambda}{(1 + \nu) 4h_c k} \quad (3.51)$$

where f and k are material constants, h_c is the coating thickness, E_s is the elastic modulus and ν is the Poisson's ratio of the plate respectively. The apparent stress intensity factor K_{AP} can be calculated using equation (3.40). The normalised apparent K_{AP} varies linearly with the square root of the normalised distance of the

measured data from the crack tip. The intercept on the normalised K_{AP} axis provides the value of the geometric factor, Y . The stress intensity factor K_I can be obtained using equation (3.41). The results are plotted in Figures 3.6 and 3.7.

3.3.4 Photographic Method (Nurse & Patterson, 1991)

Colour photographs were taken in the dark field, circular setting of the reflection polariscope, using a SLR camera (Pentax K1000, Japan) and a colour film (Fuji, Japan). The colour photographs were produced as 5×3 inch prints and then enlarged using a colour photocopier to three times their original size. A colour calibration chart supplied with the reflection polariscope was used to assign the isochromatic fringe order on the colour photocopies. About 70 points were identified along the fringe loops in an annular region as defined in section 3.3.3. In order to digitise this information, each photocopy was placed on a digitising tablet connected to a personal computer. In conjunction with *AUTOCAD* software, a puck on the tablet was used to define an axis system centred on the crack tip and to identify the location of the data points on the fringe loops. This information, together with the fringe order associated with each loop was stored in a data file. The file was subsequently used as input to a purpose-written program known as *CHOPIN*, which used the data to determine the stress intensity factors. The program *CHOPIN* employs the modified Multi-Point Over-Deterministic Method (MPODM) in which the Westergaard stress field equations are replaced by those of Muskhelishvili to allow a non-uniform passing stress field through the use of Fourier series to describe the stress field. The resulting stress field equations are fitted to the experimental data using an iterative, least square approach. The number of terms used in the calculation was 10. The results are plotted in Figures 3.6 and 3.7.

3.3.5 Automated Reflection Photoelastic Method (PSIOS)

The experimental set up of the PSIOS system is shown in Figure 3.5. Intensity data were processed using the program *PECAN*. The periodic distributions generated by expressions (2.53) and (2.54) are unwrapped using the algorithms

discussed by Wang and Patterson (1995). The operator has to seed a calibration of the full-field map of isochromatic parameter. In order to perform analyses of the fringe pattern around a crack tip, the location of the tip has to be identified in the image. The program creates an array of points within the annular region defined in section 3.3.3 and creates a data file in a similar way to that described in the section 3.3.4. This program and the program *CHOPIN* are linked together, so that the solution procedure is identical to that used in section 3.3.4. The results are plotted in Figures 3.6 and 3.7.

3.3.6 Newman's numerical solution (Newman, 1971)

The solution of stress intensity factor was based on the complex variable method of Muskhelishvili and a modified boundary-collocation method. The numerical values of the SIF were found for the cracks emanating from a circular hole in a rectangular plate subjected to uniaxial stress. The geometric factor for $2R/w = 0.25$, $2a/w = 0.5$ is $Y=1.2853$ and for $2R/w = 0.25$, $2a/w = 0.4$ is $Y=1.2156$. The results are plotted in Figures 3.6 and 3.7.

3.4 Discussion

According to Figures 3.6 and 3.7, results using the PSIOS are closer to the numerical results than those from the other methods used in this experiment. The relative errors for the automated method compared with the numerical results are in a range of 2.25 percent to 3.38 percent for specimen *A* and of 0.54 percent to 6.28 percent for specimen *B*. Errors arise from both systematic and random causes. The latter includes defects in the photoelastic coating which affected the quality of images and so caused some errors in the image processing, in the automated method. Whereas errors were avoided in the manual and photographic method, almost sub-consciously through the selection of data points by the operator; in the automated method the array of selected points is chosen based on geometry relative to the crack tip and length and without regard to imperfections in the data field. These imperfections cause errors in the results, and increase the sensitivity of the MPODM to the initial estimate, tolerance of the fit, and the number of terms in the series describing the stress field. Consequently, the solution must be repeated with a number of increments of these parameters to ensure that a stable solution has been achieved.

The results using the conventional reflection polariscope with a null-balance compensator are close to the numerical results although the difference becomes bigger at smaller loads. The relative errors are in a range of 1.16 percent to 13.5 percent for specimen *A* and of 1.16 percent to 8.92 percent for specimen *B* (there is no result for 1 tonne loading because the fringe (colour) on the specimen *B* is too faint to recognise). The method is considered to be suitable for the clearly defined fringes, which means the larger loads in this experiment. At the small loads the fringes within the valid annulus were less than 0.5 order so that the recognition of fringes was difficult.

The photographic method yielded results with relative errors in a range of 1.23 percent to 11.19 percent for specimen *A* and of 12.97 percent to 14.51 percent for specimen *B* (there are no results for 1 tonne loading because the fringe on the photocopies were too indistinct) compared with the numerical results. The errors

are considered to be caused by poor data collection. The large error occurred at smaller loads because there were no integer fringes on the picture, and all points were selected by comparing the colour with the calibration chart, therefore the accuracy of the fringe order assigned was small. The truncation of the series terms and the initial estimated value of SIF in the MPODM are also potential sources of error in this method.

The results using the rosette strain gauge on specimen *A* are consistently lower than the numerical results (i.e. 8.25 percent to 10.91 percent). The results from single strain gauge on specimen *B* are higher than the numerical results with a relative error from 3.38 percent to 5.5 percent. The errors may be caused by geometry (width, tip radius) and strain gradient effect as reported by Dally and Sanford (1987). The comparison of results from the two gauges showed that the error increased with the length of the gauge. The results are consistent with the theory on strain gauges that the absolute error is directly proportional to square of the length of the strain gauge (Dally & Riley 1991). Although the strain gauge yielded good results for specimen *B* in this experiment, the use of strain gauges is constrained by many factors. For example, a tiny deviation of the position of the gauge from the correct place will cause large errors.

The stress field equations employed in different experimental methods have influence on the results. Because the crack originates from the edge of the hole, so the passing field is non-uniform. The Muskhelishvili stress function describes a non-uniform passing stress field through the use of Fourier series and the Westgaard stress function describes a uniform stress field. In the strain gauge method, the Westgaard stress function was modified with additional terms added to account for all of the non-singular terms. However in practice, only three and two parameters were used for the single strain gauge and rectangular rosette strain gauge respectively. The truncation of terms in the stress function causes error.

3.5 Conclusion

The assessment of capability of the automated reflection polariscope, PSIOS has been performed by comparison of several different experimental techniques for the determination of the stress intensity factors in a component. Among the experimental processes employed, the strain gauge method and photographic method are inexpensive, but the two methods are limited by their ability to achieve the desired accuracy. Since the evaluation of the photoelastic patterns can be time-consuming and tedious, and particularly for those specimens with low fringe order, the conventional reflection polariscope is not considered practicable. However, for high stresses, it yielded accurate results in this experiment. By comparison, the automatic reflection polariscope has yielded the value of the SIFs with a smaller relative error and was less time-consuming, and may be the easiest technique to use.

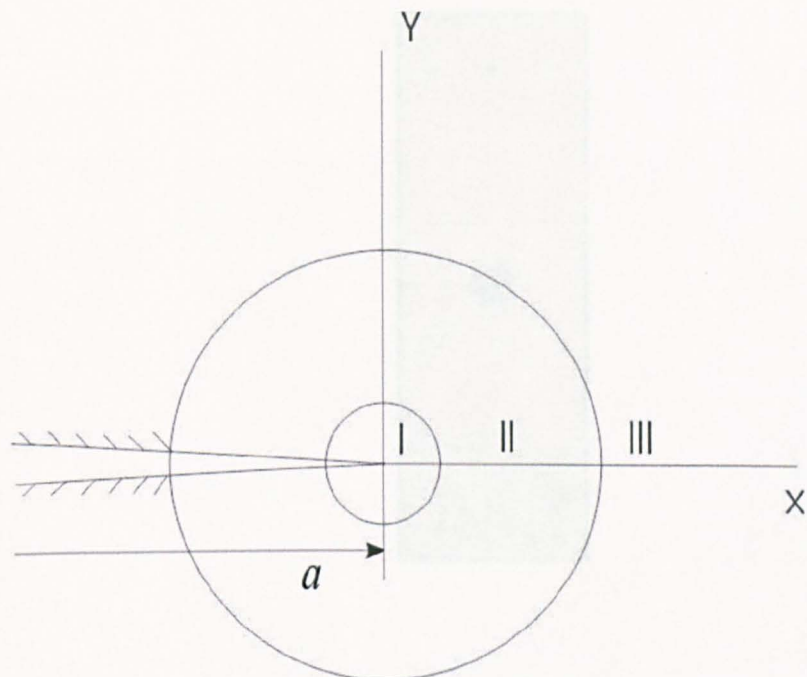


Figure 3.1 Specimen A, an aluminum plate with crack, mounted by brass tie rods.

Figure 3.1 Field adjacent to the crack tip is divided into three regions. The region *I* is the very near field, region *II* is the near field and region *III* is the far field.

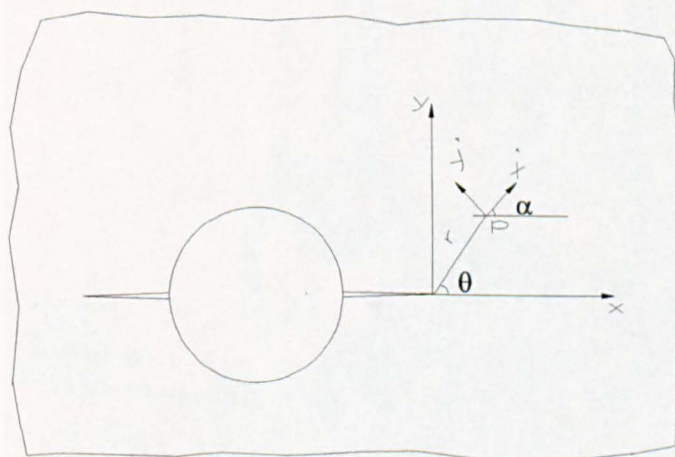


Figure 3.2 Orientation of single element strain gauge on specimen B (not to scale), with loading applied in the Y-direction.

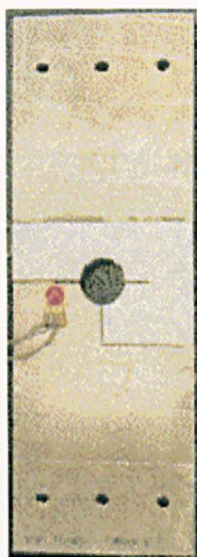


Figure 3.3 Specimen A, an aluminium plate with cracks emanating from the central hole.

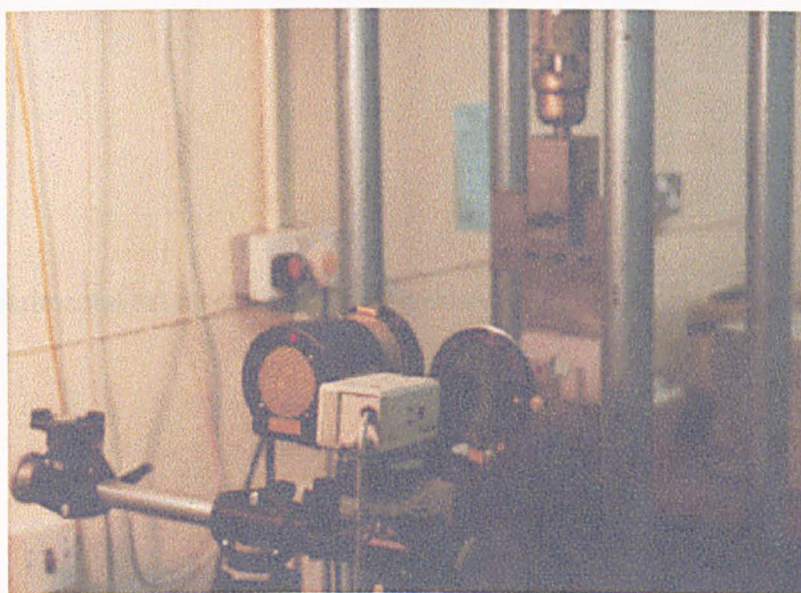


Figure 3.4 Experimental set up of the conventional reflection photoelasticity.

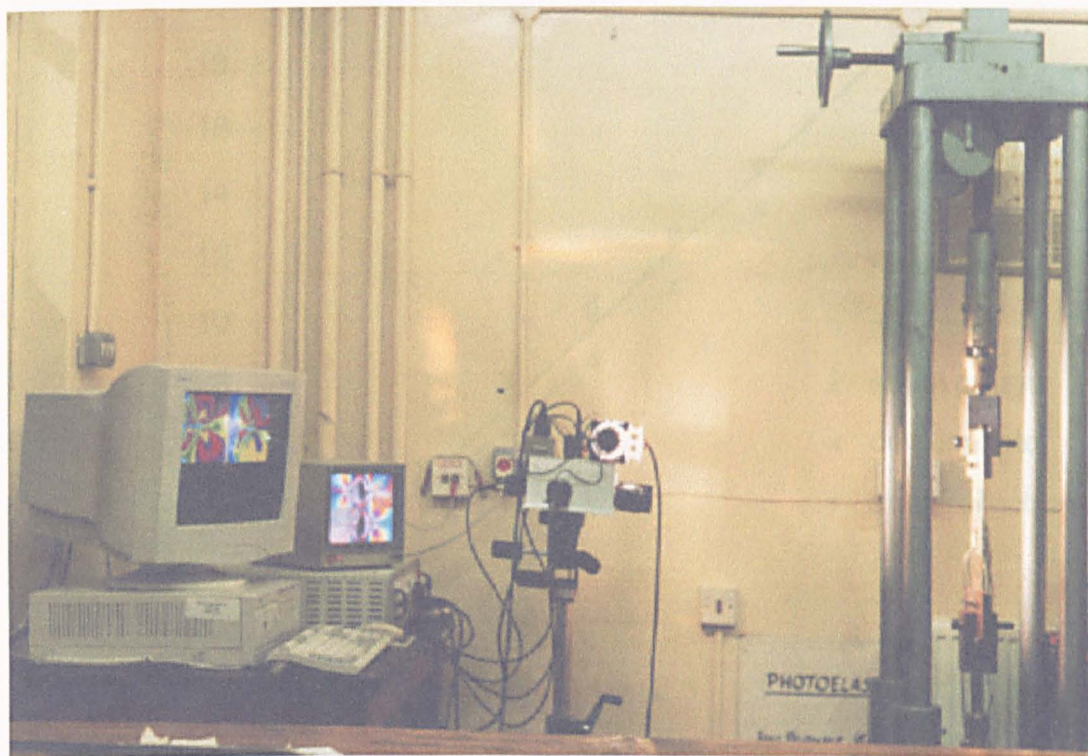


Figure 3.5 Stress intensity factors found by five methods for various loads on specimen A

Figure 3.5 Experimental set up of the PSIOS system.

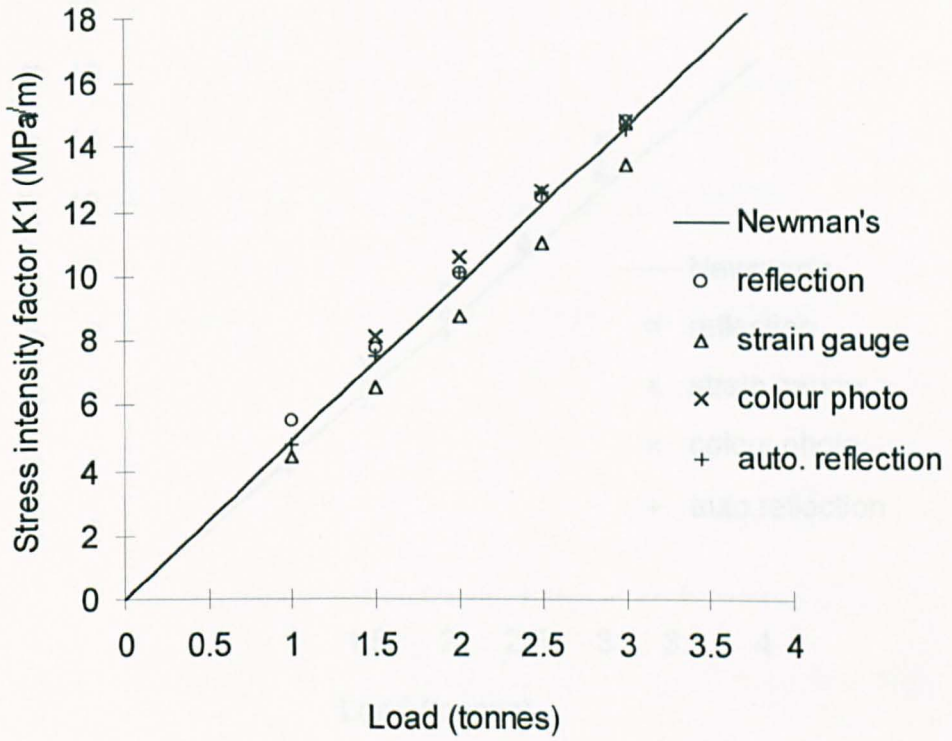


Figure 3.6 Stress intensity factors found by five methods for various loads on specimen A.

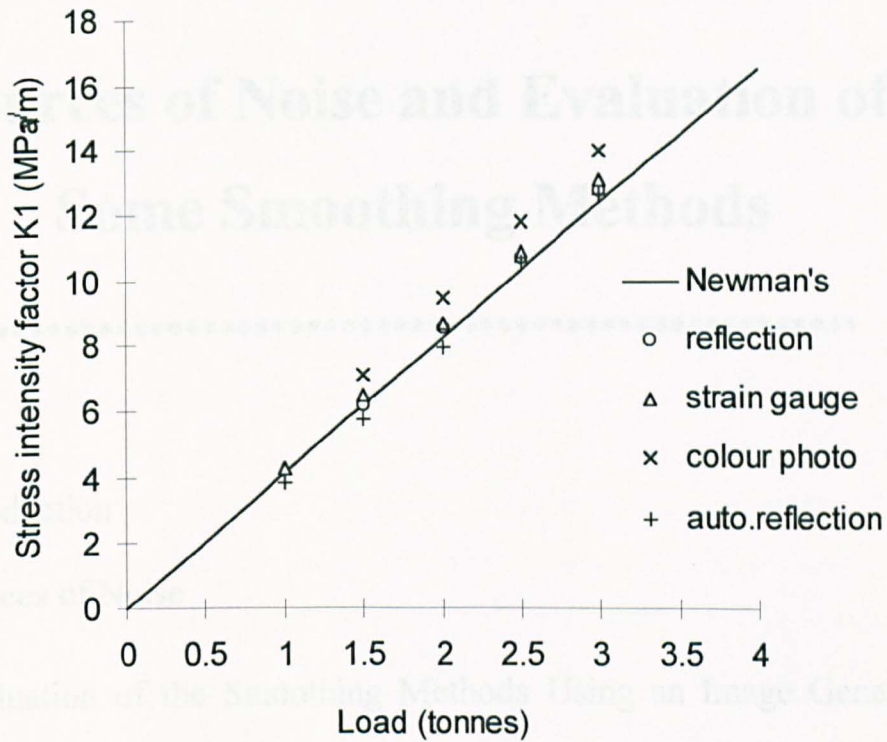


Figure 3.7 Stress intensity factors found by five methods for various loads on specimen B.

Chapter Four

Sources of Noise and Evaluation of Some Smoothing Methods

4.1 Introduction

4.2 Sources of Noise

4.3 Evaluation of the Smoothing Methods Using an Image Generated
by a Computer Program

4.4 Evaluation of the Smoothing Methods Using an Image Obtained
from the PSIOS

4.5 Discussion

4.6 Conclusion

4.1. Introduction

In practice, images obtained from the PSIOS instrument using a specimen with a photoelastic coating look fuzzy. Figure 4.1 shows a typical intensity image collected during the determination of stress intensity factors described in the previous chapter. It is image number 1 from the PSIOS instrument and was obtained using a monochromatic camera (Pulnix, TM 526, Japan). Curves using the intensity data plotted in Figure 4.2 show that the noise mixes with the meaningful data.

Error may be caused by a variety of sources. The errors caused by the use of a white light source, an oblique angle of incidence and the mis-alignment of the optical elements have been discussed by Ji (1998) for the automated transmission polariscope that is based on the principle of phase-stepping. The same principle of phase-stepping is used in the automated reflection polariscope and the discussion of the sources of error in the automated transmission polariscope hold for the automated reflection polariscope. However, the additional errors caused by the use of the photoelastic coating and the electronic instrumentation in the PSIOS system cannot be considered to be the same as the effect of the transmission specimen and the instrumentation in the automated transmission polariscope. In this chapter, the results of several experiments carried out in order to find the major sources of noise when using the PSIOS and the assessment of different smoothing methods for reducing the effect of the noise are reported.

4.2. Sources of Noise

4.2.1 Experiments

The main sources of noise in the intensity images from the PSIOS instrument were assumed to be the photoelastic coating (due to the statistically distributed aluminium particles generating a diffuse reflection), the electrical noise of the automated instrument and the quantization errors of the analogue/digital (A/D) converter. In order to validate this assumption, four experiments were carried out. The specimens and instruments used in the four experiments are listed in Table 4.1.

Table 4.1 Specimens and instruments used in the four experiments.

	Transmission specimen	Reflection specimen
Transmission polariscope	Experiment No. 1	Experiment No. 2
PSIOS	Experiment No. 3	Experiment No. 4

The purpose of experiments No.1 and No.2 is to qualify the noise caused by the reflection specimen. Since noise can be caused by both the reflection specimen and the transmission instrument, it is necessary to assess the noise caused by the transmission instrument first. This was done by using a transmission specimen with the transmission instrument. The transparent disc and a conventional transmission polariscope with manual operation using an automated data acquisition device, a CCTV camera (Panasonic, WV-BP100/B, Germany), a computer, an A/D converter and a monitor were used in the first experiment. The specimen was a disc made of epoxy resin and was 6 mm thick and 76 mm in diameter and has been stress frozen whilst subject to a diametrical compressive load. The system set up is shown in Figure 4.3. The program *VIZION* was used to control the data acquisition and six images were obtained. Figure 4.7(a) shows the intensity data in the first image along a line.

In the second experiment, a disc made of photoelastic coating (PS1-B, Measurement Group, Inc. USA) was used in the experiment. The disc is 2 mm thick and 80 mm in diameter and was subjected to a compressive load of 65.6 N. The conventional reflection polariscope (Model 03, Measurement Group, Inc. USA) was

used to illuminate the specimen and the ray of reflected light was passed through a quarter-wave plate and an analyser before entering the CCTV camera. The data acquisition program and the instrument were the same as in the first experiment. The system set up is shown in Figure 4.4. The intensity data from the first image along a line are plotted in Figure 4.7(b). Comparison of the results of the two experiments showed that the transparent disc causes noise due to scattering of the light. However this is very small compared with noise caused by the photoelastic coating.

The purpose of the third experiment is to quantify noise caused by the PSIOS instrument. The photoelastic coating has been considered to be a source of the noise, so a transmission specimen (used in experiment No. 1) that could be assumed to be noise free was used in this experiment. The polariscope was a combination of a conventional transmission polariscope and the optical head of the PSIOS. The optical head was connected to a computer (Compaq, Deskpro XL 5100), an A/D converter and a monitor (Micro Vitec). The program *PECAN* was used to control the data acquisition and four images were obtained.

In the fourth experiment, the PSIOS instrument and the coating disc were used. System setup for the third and fourth experiments are illustrated in Figures 4.5 and 4.6 respectively. The intensity data from first image of the third and fourth experiments along lines are plotted in Figures 4.7(c) and (d).

The highest fringe order on the transmission specimen is larger than that on the reflection specimen, and the data points chosen from the two specimens in the four experiments were not at same location.

4.2.2. Discussion

The results of the first and second experiments indicated that the photoelastic coating does cause noise. The noise in images from the third experiment is mainly caused by the electronic instrumentation of PSIOS. The results from the fourth experiment are the combination of the meaningful signal and noise of electrical and quantization noise and noise caused by the diffusely reflected light. From analysis

of the results of the experiments, noise caused is mainly in the higher spatial frequency domain.

The noise caused by the electronic instrumentation is complicated whilst the quantization noise is straightforward to understand. When an analogue signal $x(n)$ is converted into digital signal $x_q(n)$, a error $e(n)$ is introduced as illustrated in Figure 4.8. The error $e(n)$ can be written as

$$e(n) = x_q(n) - x(n) \quad (4.1)$$

and

$$|e(n)| \leq \frac{q}{2} \quad (4.2)$$

where

$$q = 2^{-B+1} \quad (4.3)$$

where B is the word length (Ahmed and Natarajan, 1983, p.320).

The quantization of $x(n)$ can be regarded as the addition of the meaningful signal and a noise signal.

$$x_q(n) = e(n) + x(n) \quad (4.4)$$

The noise signal $e(n)$ is called quantization noise and is a random variable. The effect of the $e(n)$ can be assessed in terms of its variance

$$\sigma_e^2 = \frac{2^{-2B}}{3} \quad (4.5)$$

It is obvious that the variance will be very small and may be neglected because the word length used is 8 bits. Figure 4.7(a) shows that quantization noise is small and acceptable.

Noise is caused by the PSIOS instrumentation because of the use of the CCD camera (Pulnix, TM 526, Japan). The CCD camera is equipped with electronic circuits, noise will occur when the camera is in operation. The quad video system will cause noise because a set of four signals from the four CCD cameras is processed by a multiplexer (Panasonic Quad WJ 410) to combine them into a signal

composite image that can be digitised by a single frame-grabber which will also cause noise.

Noise is also caused by the photoelastic coating because statistically distributed aluminium particles generating a diffuse reflection. The photoelastic coating has two layers. One is made of transparent material and another is aluminium powder with adhesive compressed on the transparent plate. Most aluminium particles in the lower layer of the photoelastic coating are small in size and can be considered identical except that a few of them may be bigger than the usual size. The aluminium particles are thought to be spherical and compressed on to the one surface of the transparent plate. Speckle noise will occur due to the imperfection of the reflective surface of the aluminium layer.

The noise caused by the camera and the photoelastic coating cannot be removed in the experiment, therefore it is necessary to filter or smooth the data collected so that the effect of noise is not propagated to the stress pattern that is calculated from the intensity data.

The noise in the high spatial frequency domain caused by the photoelastic coating can be eliminated using a low pass filter and at the same time noise caused by the electronic instrumentation and the quantization noise will be removed. Noise cannot be completely eliminated even in theory, but it can be suppressed to an acceptable degree. In the following sections, a smoothing method will be selected according to its effectiveness in reducing effect of the noise.

4.3. Evaluation of Some Smoothing Methods

4.3.1 Evaluation of the Smoothing Methods Using an Image Generated by a Computer Program

The sixth difference method, Liebmann's method and the median method using 3x3 and 5x5 arrays which were reviewed in section 2.3 are evaluated using an image of a quadrant of a compression disk generated by a computer program. Speckel noise was added to the original computer generated image and the reason for adding 'speckle' noise rather than the 'salt and pepper' noise is based on the conclusion of the experiment in the last section. The smoothing methods were used on the image with speckle noise. The original, the one with added speckle noise and smoothed images using these smoothing methods, one and twice to the image are shown in figures 4.9 to 4.18. Plots consisting of selected lines from the original image and image with speckle noise and those smoothed using the methods are shown in figures 4.19 to 4.22. The Liebmann's formula was further processed in order to achieve higher accuracy and the deduced expression is called the 'nine-point' formula. The nine-point formula and a filtering method (Butterworth filter) used in the signal processing are introduced as following.

4.3.2 The Nine-point Smoothing Method

The Nine-point method is a bilinear method that is based on a numerical solution to Laplace's classical equation

$$\nabla^2 \Phi = \frac{\partial^2 \Phi}{\partial x^2} + \frac{\partial^2 \Phi}{\partial y^2} = \Phi_{xx} + \Phi_{yy} = 0 \quad (4.6)$$

Suppose that region R is covered by a net mesh of squares with sides parallel to the x - y axes, the second differentiation gives

$$(\Phi_{xx})_{ij} \approx \frac{\Phi_{i-1,j} - 2\Phi_{i,j} + \Phi_{i+1,j}}{h^2} \quad (4.7)$$

$$(\Phi_{yy})_{ij} \approx \frac{\Phi_{i,j-1} - 2\Phi_{i,j} + \Phi_{i,j+1}}{h^2} \quad (4.8)$$

where h is the distance between the two adjacent points.

Adding together expressions (4.7) and (4.8), gives

$$(\Phi_{xx})_{i,j} + (\Phi_{yy})_{i,j} \approx \frac{1}{h^2} (\Phi_{i-1,j} + \Phi_{i+1,j} + \Phi_{i,j+1} + \Phi_{i,j-1} - 4\Phi_{i,j}) \quad (4.9)$$

hence

$$\Phi_{i,j} = \frac{1}{4} (\Phi_{i-1,j} + \Phi_{i+1,j} + \Phi_{i,j+1} + \Phi_{i,j-1}) \quad (4.10)$$

Equation (4.10) is known as standard five point formula (James, *et al* 1993, p.673) or Liebmann's formula (Baron and Patterson, 1998). The expression states that the value of Φ at (i, j) is the mean of the values of Φ at the four neighbouring points $(i-1, j)$, $(i+1, j)$, $(i, j+1)$ and $(i, j-1)$. Liebmann's formula makes use of the four edge points in a square of eight points around the point of interest.

The Liebmann's formula can be used to deduce the Nine-point formula (Ames, 1977, p.18) which has the form

$$\Phi_{i,j} = \frac{1}{20} [\Phi_{i-1,j-1} + \Phi_{i+1,j+1} + \Phi_{i-1,j+1} + \Phi_{i+1,j-1} + 4(\Phi_{i-1,j} + \Phi_{i+1,j} + \Phi_{i,j+1} + \Phi_{i,j-1} - 4\Phi_{i,j})] \quad (4.11)$$

The Nine-point smoothing method takes into account the influence from both the edge and corner points with different weighting according to the result derived from the Laplace equation. The error in expression (4.11) is of the order h^6 , provided that Φ is sufficiently smooth. A schematic diagram of the Nine-point smoothing method is shown in figure 4.23. The smoothed intensity data using the Nine-point formula to the image in figure 4.10 are shown in figures 4.28 and 4.29. The comparison of data selected from the original, speckle noised and smoothed images is shown in figure 4.26.

4.3.3 The Low-Pass Butterworth Filter

Noise in images from the PSIOS instrument is mainly in the high spatial frequency domain. This provides an opportunity to use a low-pass filter to reduce the noise. The Butterworth filter is commonly used in signal processing and in this section it is introduced to remove noise in the images.

Suppose the digitized 2-D data is the input and can be represented by $x(n_1, n_2)$. The output, $y(n_1, n_2)$ is (Lu, 1992, p.32)

$$y(n_1, n_2) = \sum_{i=-\infty}^{\infty} \sum_{j=-\infty}^{\infty} h_1(i)h_2(j)x(n_1 - i, n_2 - j) = \sum_{i=-\infty}^{\infty} h_1(i) \sum_{j=-\infty}^{\infty} h_2(j)x(n_1 - i, n_2 - j) \quad (4.16)$$

where

$$h(i, j) = h_1(n_1)h_2(n_2) \quad (4.17)$$

where $h(i, j)$ is a separable function and $h_1(n_1)$ and $h_2(n_2)$ is independent of n_2 and n_1 .

The expression (4.16) can be written as

$$y(n_1, n_2) = \sum_{i=-\infty}^{\infty} h_1(i)w(n_1 - i, n_2) \quad (4.18)$$

where

$$w(n_1 - i, n_2) = \sum_{j=-\infty}^{\infty} h_2(j)x(n_1, n_2 - j) \quad (4.19)$$

Once $w(n_1, n_2)$ is computed, the output $y(n_1, n_2)$ can be computed from expression (4.18). Therefore, $w(n_1, n_2)$ and $y(n_1, n_2)$ can be regarded as the responses of the two 1-D digital filters with impulse responses $h_2(n_2)$ and $h_1(n_1)$ and inputs $x(n_1, n_2)$ and $w(n_1, n_2)$. The separability is of practical importance since it allows the design of a 2-D digital filter to be carried out by two 1-D digital filters and then to be connected in a cascade.

The frequency domain characterization of the filter can be obtained by assuming the initial conditions are zero, which yields the filter transfer function

$$H(z_1, z_2) = \frac{Y(z_1, z_2)}{X(z_1, z_2)} \quad (4.20)$$

The steady-state frequency domain response of the digital filter can be obtained by evaluating $H(z)$ on the unit circle of the z -plane:

$$H(z_1, z_2) \Big|_{z_1=e^{j\omega_1 T}, z_2=e^{j\omega_2 T}} = H(e^{j\omega_1 T}, e^{j\omega_2 T}) = \left| H(e^{j\omega_1 T}, e^{j\omega_2 T}) \right| \text{Arg}H(e^{j\omega_1 T}, e^{j\omega_2 T}) \quad (4.21)$$

where T is the sampling period.

The transfer function can be expressed as a ratio of two polynomials

$$H(z_1, z_2) = \frac{\sum_{i=0}^{N1} \sum_{j=0}^{N2} a_{i,j} z_1^{-i} z_2^{-j}}{1 + \sum_{i=0}^{N1} \sum_{j=0}^{N2} b_{i,j} z_1^{-i} z_2^{-j}} \quad (4.22)$$

A time domain characterization of equation (4.22) as a recursive difference equation is given by (Lu, 1992, p.13)

$$y(n_1, n_2) = \sum_{i=0}^{N1} \sum_{j=0}^{N2} a_{i,j} x(n_1 - i, n_2 - j) - \sum_{i=0}^{N1} \sum_{j=0}^{N2} b_{i,j} y(n_1 - i, n_2 - j) \quad (4.23)$$

The output of the filter is a weighted sum of past outputs and inputs and the present input.

The impulse response of discrete-time linear time-invariant digital filters is either of infinite duration or of finite duration. Thus, from the point of view of the impulse response duration, filters can be classified as infinite-duration impulse response (IIR), or finite-duration impulse response (FIR) digital filters. In the design of a 2-D digital filter, the major concerns are the efficiency of the computation and the stability of the filter. Finite-duration impulse response (FIR) filters are always stable, but for the same characteristic of the filter in the transition zone, the FIR filter needs to be of higher order than the infinite-duration impulse response (IIR) filter which means that more computation time is required. Therefore, a stable, IIR filter should be designed in the present study.

The design of a digital filter involves several steps, namely approximation, realisation, implementation and analysis of quantization effects. In order to solve the problem encountered, design of a low pass filter was carried out following the four steps.

Approximation

Approximation is a process of generating a rational transfer function that satisfies the required specification. The design started from the selection of a transfer function. The Butterworth, Chebyshev type I and II and Ellipse filters were used in the selection. The Butterworth type of response is known as a maximally flat response because it is the response that is flattest at $\omega = 0$. Frequency response is monotonic overall, decreasing smoothly from zero to infinite. The characteristic of

the Chebyshev type I filter is that there is equal ripple in the passband and the stopband response is maximally flat. In contrast, the Chebyshev type II filter has a maximum flat response in the passband and equal ripple in the stopband. The elliptic filter has equal ripple in both the passband and the stopband. The transition width of the Chebyshev type I, II and elliptic filters are narrower than the Butterworth filter. The Butterworth filter was selected in the present study due to its maximum flat and non-ripple characteristic. The disadvantage of the Butterworth filter on the wider transition zone will be improved by increasing the order of the filter.

The Butterworth low pass amplitude-squared function of order n is defined by (Pashtoon, 1987, p.306)

$$|H(f)|^2 = \frac{1}{1 + \left(\frac{w}{w_c}\right)^{2n}} = \frac{1}{1 + \left(\frac{f}{f_c}\right)^{2n}} \quad (4.24)$$

where f_c is the cut-off frequency and $w_c = 2\pi f_c$. The amplitude response of the Butterworth filter can be considered to be approximately constant in the passband and the phase response over the frequency band representing the spectrum of the desired signal are approximately linear. The phase response of the filter beyond the cut-off frequency is usually unimportant. In the design of a filter, a lower order is preferred because the amount of computation tends to increase as the square of the order of the filter. The stability of the low pass Butterworth filter can be determined by analysing the poles of the transfer function. Since all the poles (transfer function is infinite at such points) of the Butterworth filter with the particular condition are inside the circle in the z -plane, the filter is stable.

Realisation

Realisation is a process of converting the transfer function obtained through the approximation step into a state-space representation. For example, consider a low pass third-order Butterworth filter, the equation (4.23) has the form

$$y(n) = \sum_{k=0}^3 a_k x(n-k) - \sum_{k=1}^3 b_k y(n-k) \quad (4.25)$$

where a_k and b_k are coefficients. The coefficients can be calculated according to the procedures proposed by Ahmed and Natarajan (1983, p.236) as illustrated in Appendix A.

Implementation

The algorithm of the third-order Butterworth filter can be represented by the following expression for implementation in 2-D data.

$$y(i, j) = \sum_{i,j=0}^3 a_{i,j} x(i, j) - \sum_{i,j=1}^3 b_{i,j} y(i, j) \quad (4.26)$$

where $b_{i,j}$ and a_{ij} are coefficients,

Since the Butterworth filter is not symmetric, the phase relation between the input and output signals is not the same for all frequencies. This can be solved in processing the data in both forward and backward directions. For example, there is a phase shift at a given frequency in the first pass through the data, there is the same phase shift of the opposite sign at this same frequency in the second pass in the opposite direction. Because the output of the first and second passes are in the reverse direction, the two phase shifts must exactly cancel. It is called zero-phase. The double use of the filter results in an effective transfer function which is the square of the absolute value of the transfer function hence in this case, the effective transfer function is equal to a sixth order filter. Frequency responses of Butterworth filter of 3rd and 6th order are plotted in figure 4.27. The zero-phase low pass Butterworth filter can be used along both row and column directions.

Analysis of quantization effects

The effect of quantization that is introduced in the application of the filter should be taken into account. The quantization error in the A/D converter has been discussed in the section 4.22 and the overall effect of $e(n)$ is assessed by expression (4.5). Quantization of the filter coefficients will have an effect on the system. When the approximation step is carried out, the transfer function coefficients are calculated to a high degree of precision. The coefficients must be quantized before the implementation of the digital filter. When coefficients of a filter are quantized, the corresponding frequency response of the filter is altered. The change can be

considerable, such that after quantization the filter no longer meets the specification on which the calculation of the non-quantized coefficients was based. The effect is dependent upon the word length of the computer used. When the word length is 8 bits, the effect of the quantization of the filter coefficients is insignificant. Since the quantized signal $x_q(n)$ is the input to the discrete signal processing system whose transfer function is $H(z)$, the output signal will consist of two parts due to $x(n)$ and $e(n)$. The component of the output signal $\varepsilon(n)$ due to the input $e(n)$ is a random variable and can be assessed in terms of variance (Ahmed and Natarajan, 1983, p.321)

$$\sigma_\varepsilon^2 = \sigma_e^2 \frac{1}{2\pi j} \oint_{|z|=1} z^{-1} H(z) H(z^{-1}) dz \quad (4.27)$$

where \oint denotes integration around the unit circle $|z|=1$ in the counter-clockwise direction. According to the discussion in section 4.22, when the word length equals 8 bits the effect of the quantization of the input signal and the filter coefficients is small.

An experiment was done in order to find a suitable order for the Butterworth filter. The intensity data in Figure 4.9 was used and the order of the Butterworth filter was changed from two to six in unit increments. It was found that the difference between the results when the order was changed from three to six is small. As mentioned above, computation time of the filter will increase as the square of the order, so an adequate Butterworth filter for the problem should have a small order. So, the order of the Butterworth filter was chosen as three in this study but the effective order of the Butterworth filter is six due to the double use of the filter in both the forward and reverse directions.

The ratio of cut off to Nyquist frequency is required to calculate the coefficients a and b . The ratio, such as 0.1, 0.2, 0.3 and 0.4 were used in the intensity data filtering. The smoothed intensity data using the low pass, zero-phase, third order Butterworth filter when the ratio of cut off to Nyquist frequency is 0.15 on the image in figure 4.10 is shown in figure 4.28 and the comparison of data selected from the original, speckle noised and smoothed images is shown in figure 4.29. More investigation on the selection of the ratio will be done in next chapter.

4.4 Evaluation of the Smoothing Methods Using an Image Obtained from the PSIOS

The smoothing methods also have been evaluated using the intensity data extracted from the rectangular area in figure 4.1. The size of the extracted image is 130x70 pixels. The raw and smoothed intensity data using the smoothing methods are shown from figures 4.30 through 4.36.

4.5 Discussion

The sources of noise in images using the PSIOS instrument have been recognised as mainly caused by the photoelastic coating and the electronic instrumentation of the system. The sources of noise cannot be removed in the experiment, so smoothing and filtering methods were investigated to reduce the effect of noise.

The comparison of the smoothed intensity data of computer generated image using different smoothing methods showed that the sixth difference smoothing method is not good. The median 3x3, the Liebmann and Nine-point methods do have some effects on the intensity images; however, the results are not as good as desired. The smoothed image of double use of the median 5x5 seems similar to the smoothed image using the Butterworth filter. However, from the comparison of selected lines from the smoothed images, it is found that the Butterworth filter is better than the median 5x5 smoothing method, see figures 4.20 and 4.29. This is because noise in high spatial frequency domain has been removed as shown in the frequency response of the Butterworth filter. It is noted that noise mixed with the meaningful signal in the low spatial frequency domain remains in the smoothed image after the use of the Butterworth filter and the meaningful signal in the high spatial frequency domain has been truncated. In addition, the weighting in equation (4.23) varies according to the ratio of cut-off to Nyquist frequency in the Butterworth filter. When the ratio is close to 1, most of the noise will be remained in the outputs, the reverse effect will be obtained when the ratio is close to 0. Therefore, the effect of the filtering can be controlled by properly selecting the ratio of cut off to Nyquist frequency in range 0 – 1 in order to meet the user's requirement for different applications.

4.6 Conclusion

Comparison of the results from the four experiments has shown that noise is caused by the photoelastic coating and the electronic instrumentation. The images obtained from the automated reflection polariscope, PSIOS can be considered as a two-dimensional (2-D) signal that is a function of two real independent variables. Several smoothing methods including the low-pass Butterworth filter have been applied to two sets of intensity data, one set was generated using a computer program and another set was extracted from the image obtained from the PSIOS. Because the noise is severe and mainly in high spatial frequency domain, the low pass, zero-phase Butterworth filter is the most effective and flexible one amongst the smoothing methods reviewed and evaluated in the present study. The 3rd order is considered an adequate order for the problem encountered here and the desired ratio of cut off to Nyquist frequency for the Butterworth filter should be selected for different applications.

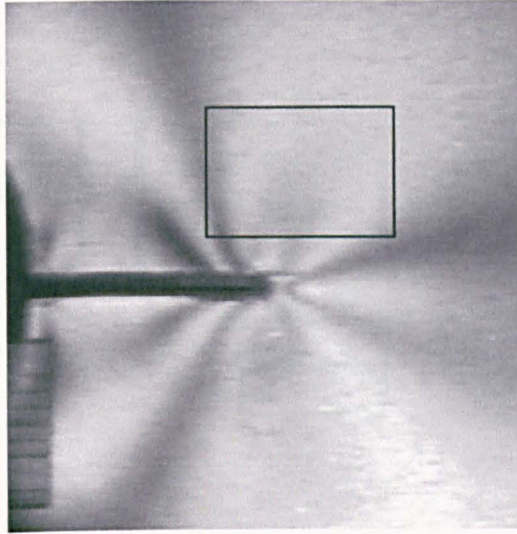


Figure 4.1 First image of the four images of a plate with cracks from the central hole under tensile load obtained using the PSIOS instrument.

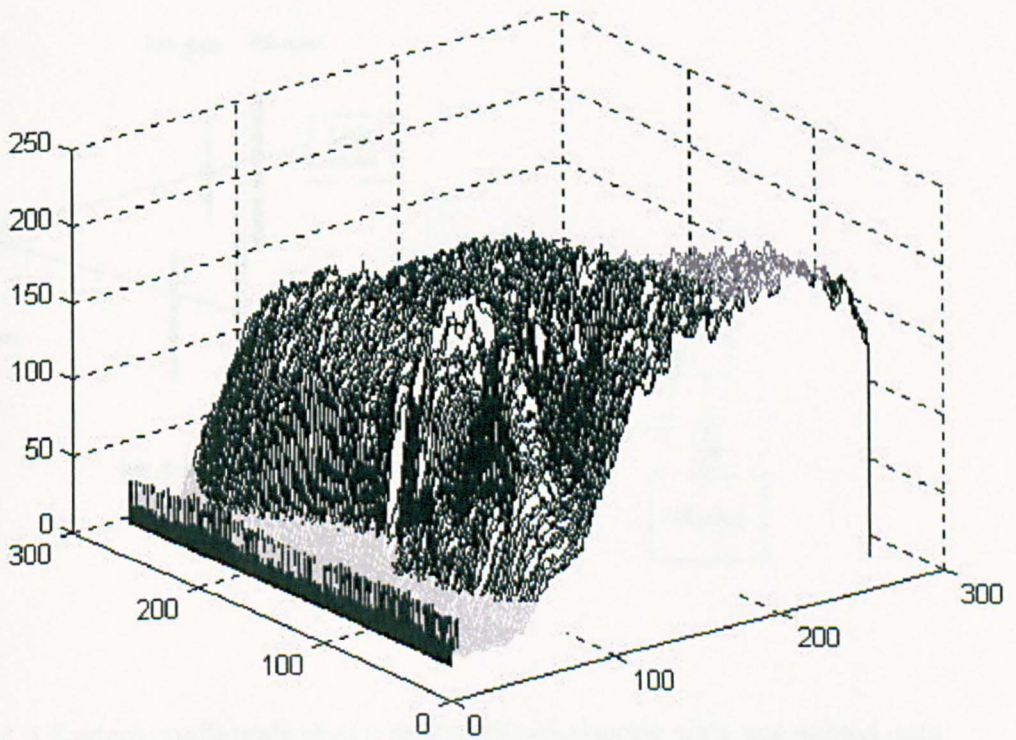


Figure 4.2 The intensity data of the image in Figure 4.1.

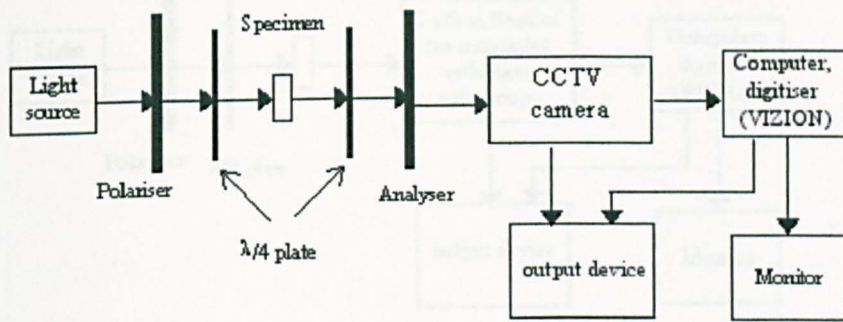


Figure 4.3 System configuration of a transmission polariscope with automated data acquisition (Experiment No.1).

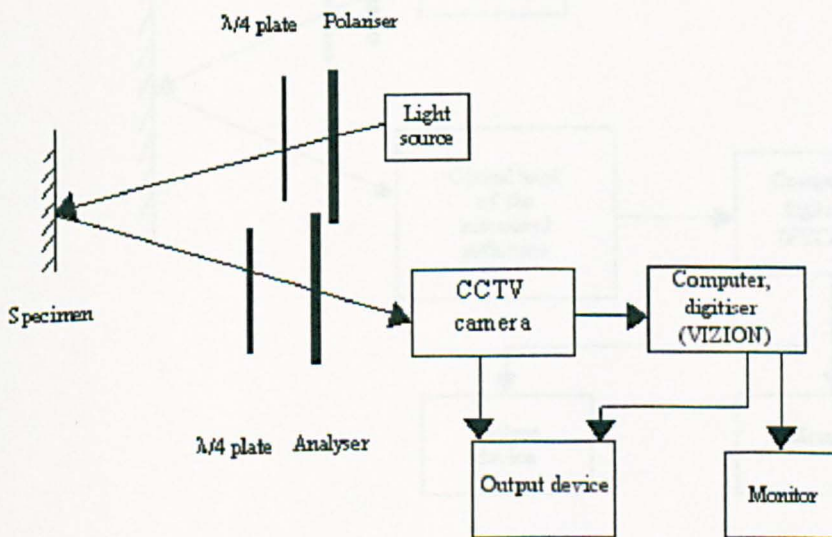


Figure 4.4 System configuration of a reflection polariscope with automated data acquisition (Experiment No. 2).

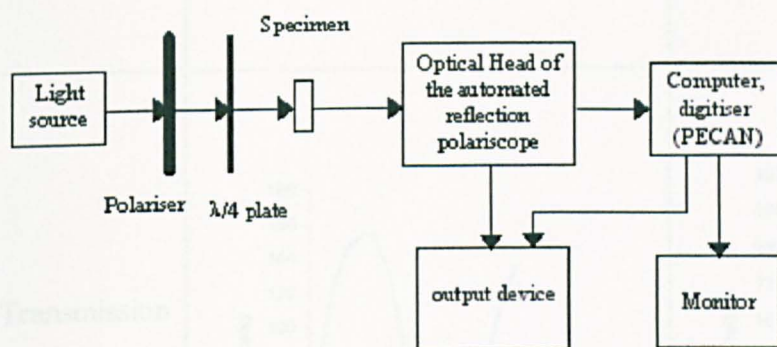


Figure 4.5 System configuration of an automated transmission polariscope using the PSOS optical head (Experiment No.3).

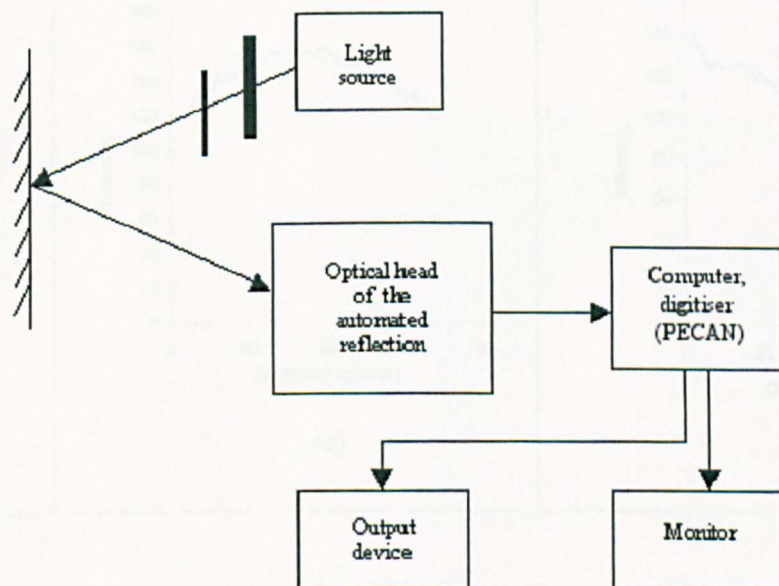


Figure 4.6 System configuration of an automated reflection polariscope, PSIOS (Experiment No. 4).

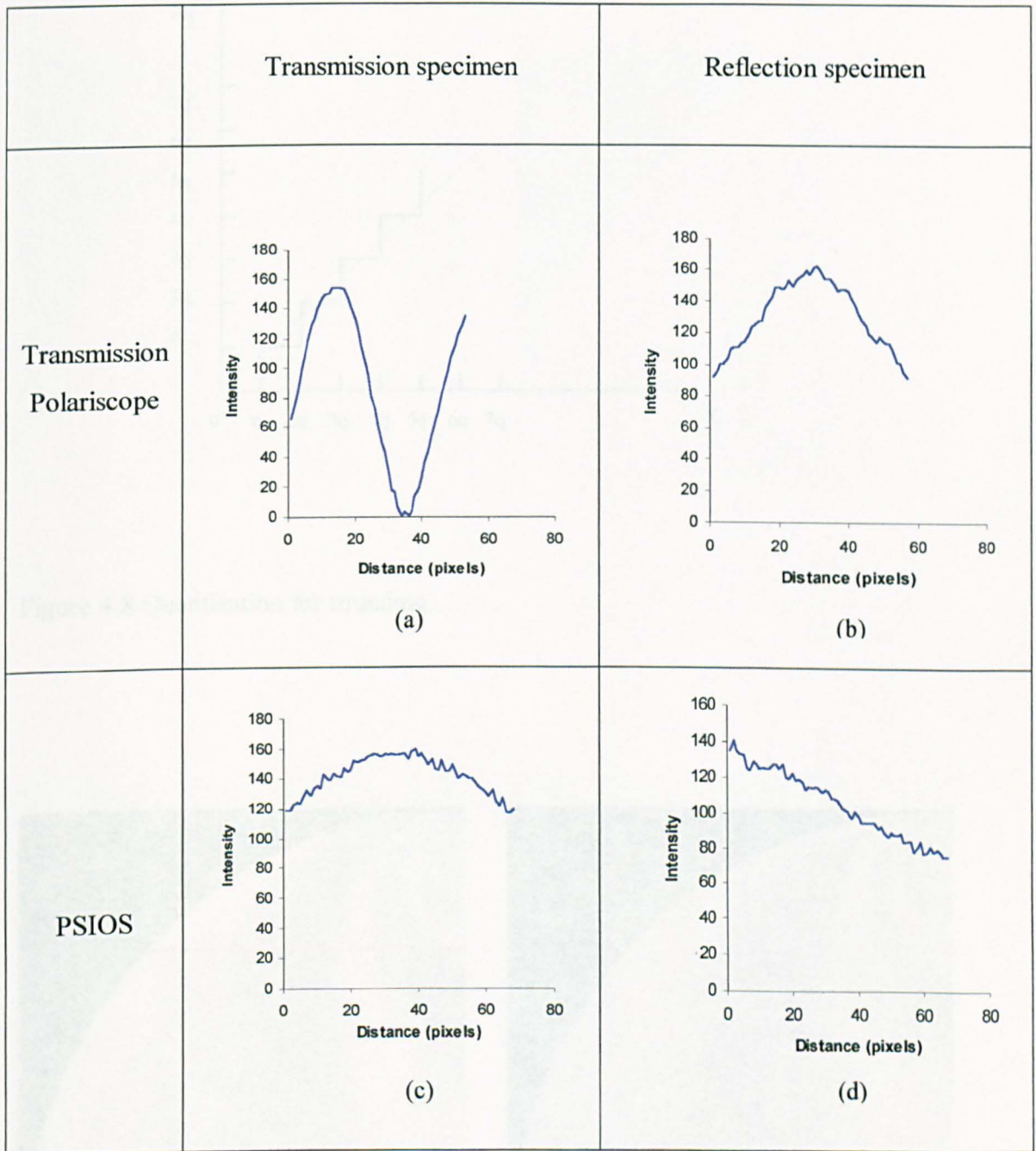


Figure 4.7 The intensity data from the four experiments (a) experiment No. 1 (b) experiment No. 2 (c) experiment No. 3 (d) experiment No. 4.

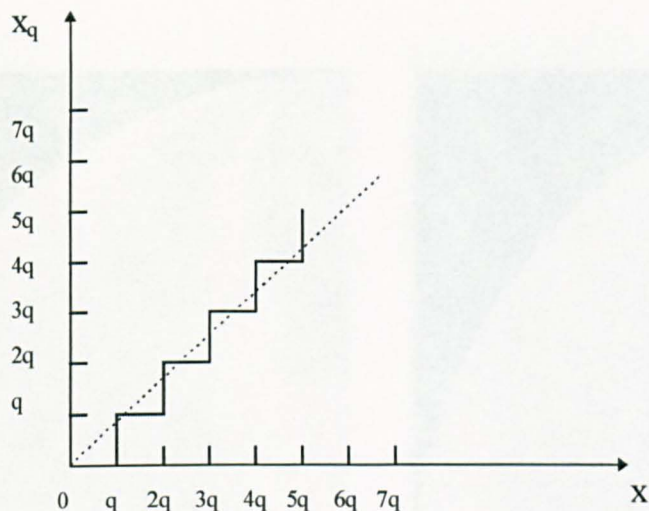


Figure 4.8 Quantization for rounding.

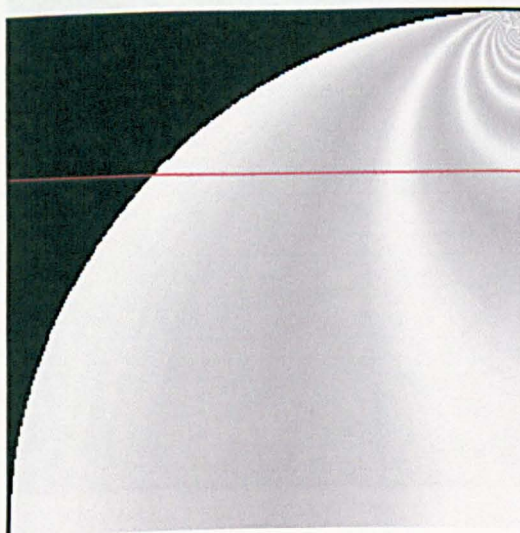


Figure 4.9 An image generated using a computer program.

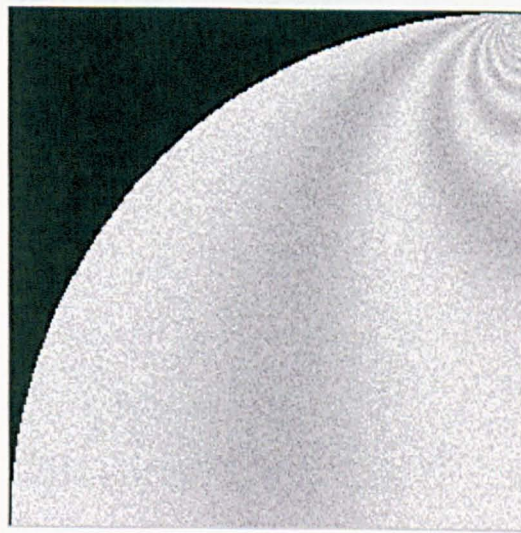


Figure 4.10 The image in Fig. 4.9 with added speckle noise.



Figure 4.11 The smoothed image of Fig. 4.10 using Median filter 3x3

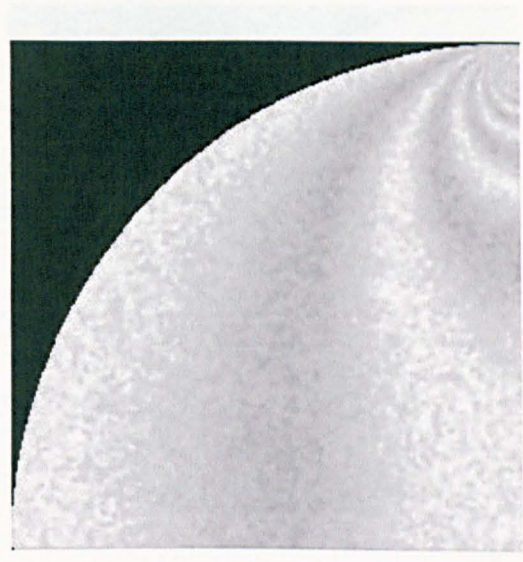


Figure 4.12 The smoothed image of Fig. 4.10 using Median filter 3x3, double used

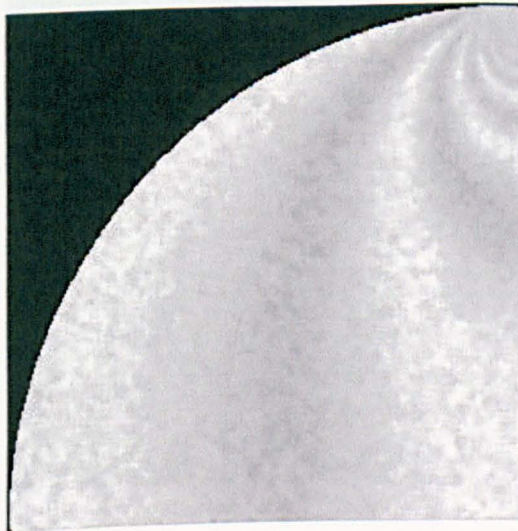


Figure 4.13 The smoothed image of Fig. 4.10 using Median filter 5x5



Figure 4.14 The smoothed image of Fig. 4.10 using Median filter 5x5, double used

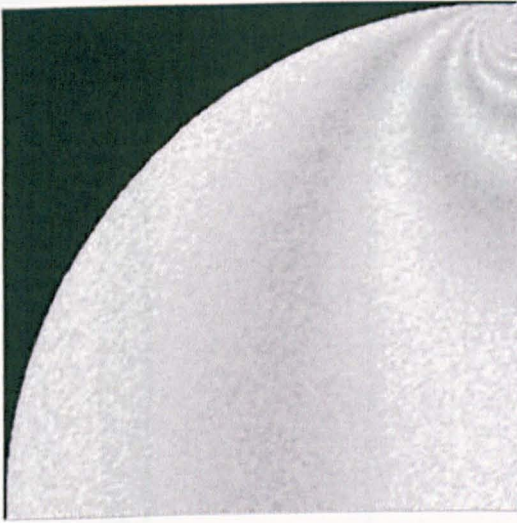


Figure 4.15 The smoothed image of Fig. 4.10 using Liebmann method

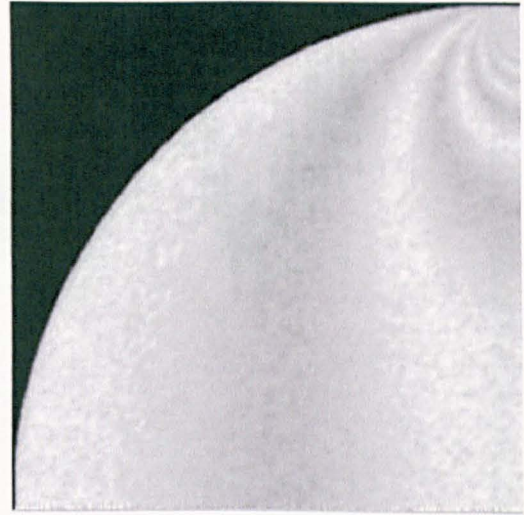


Figure 4.16 The smoothed image of Fig. 4.10 using Liebmann method, double used

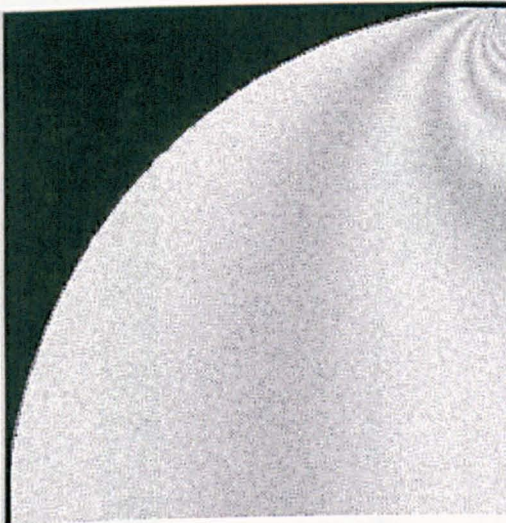


Figure 4.17 The smoothed image of Fig. 4.10 using Sixth difference method

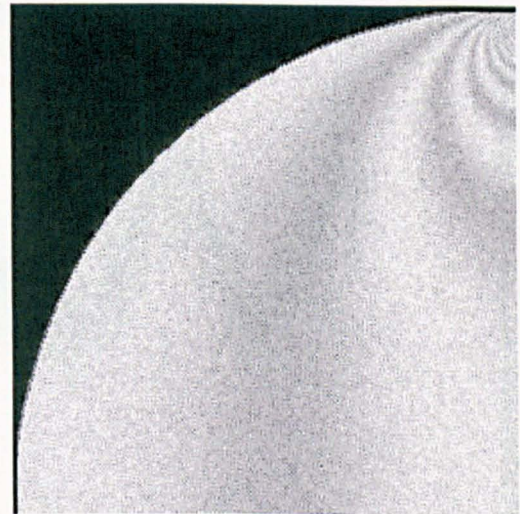


Figure 4.18 The smoothed image of Fig. 4.10 using Sixth difference method, double used

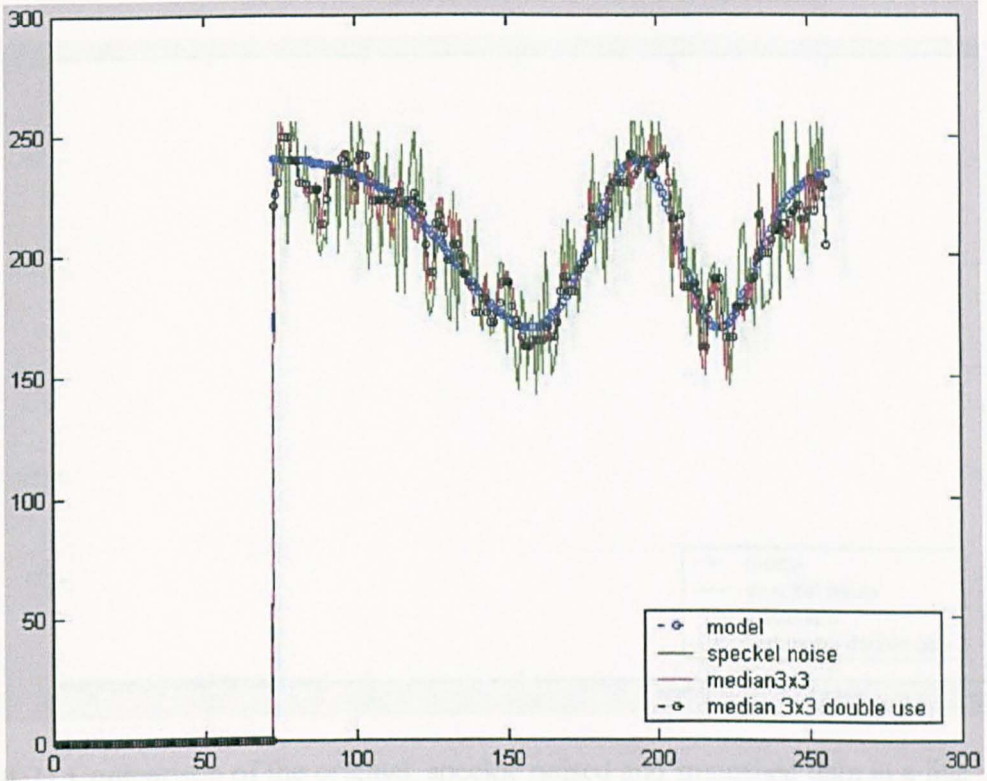


Figure 4.19 Comparison of the original, speckle noised and smoothed data in a line row 80, median 3x3.

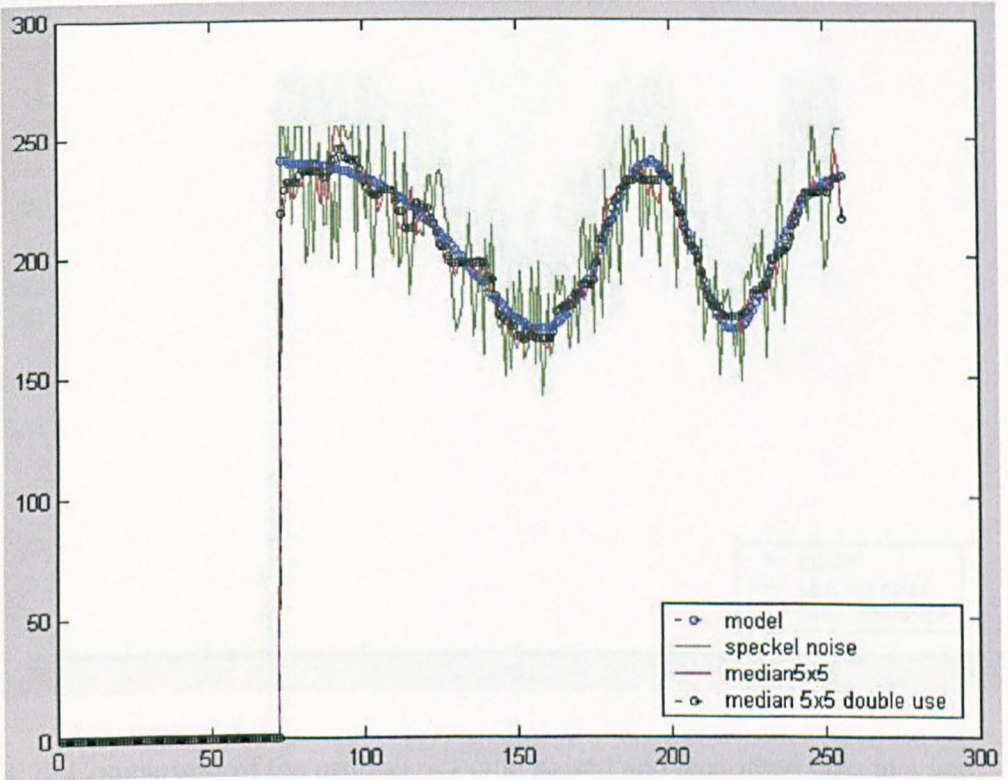


Figure 4.20 Comparison of the original, speckle noised and smoothed data in a line row 80, median5x5.

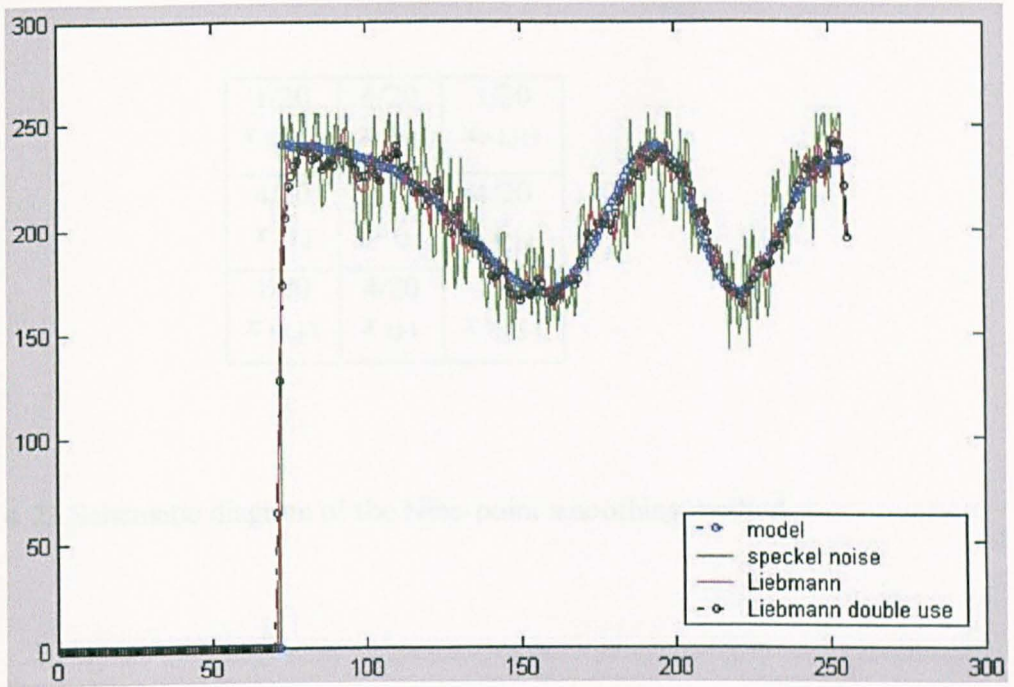


Figure 4.21 Comparison of the original, speckle noised and smoothed data in a line row 80, Liebmann method.

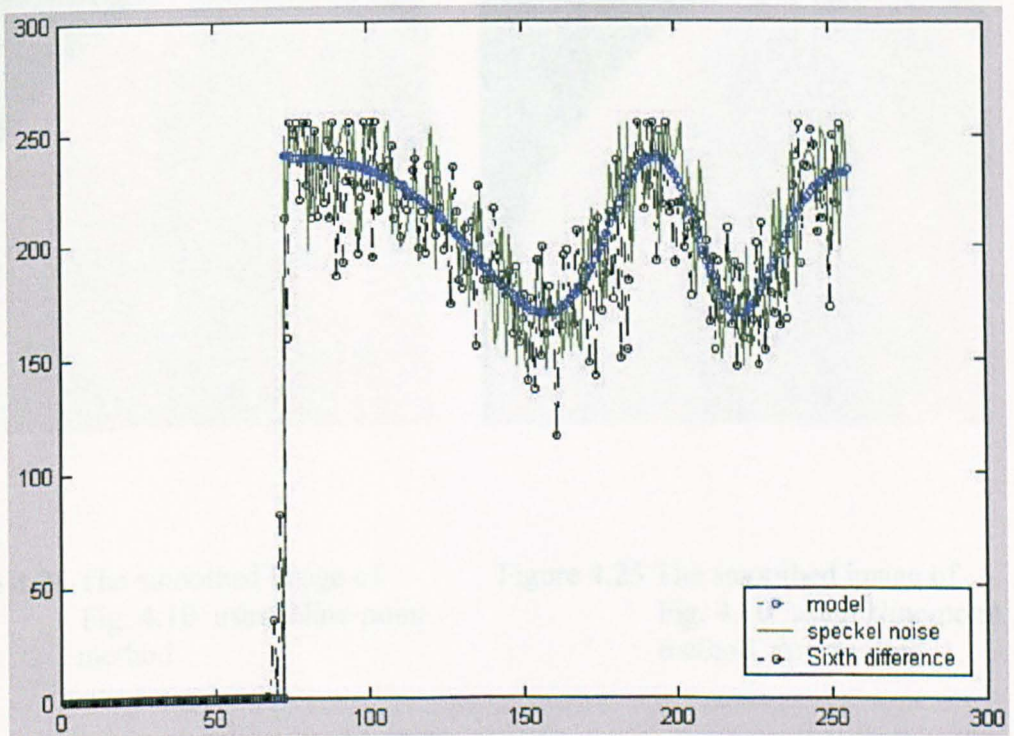


Figure 4.22 Comparison of the original, speckle noised and smoothed data in a line row 80, sixth difference method.

$1/20$ $x_{i-1,j+1}$	$4/20$ x_{ij+1}	$1/20$ $x_{i+1,j+1}$
$4/20$ $x_{i-1,j}$	x_{ij}	$4/20$ $x_{i+1,j}$
$1/20$ $x_{i-1,j-1}$	$4/20$ x_{ij-1}	$1/20$ $x_{i+1,j-1}$

Figure 4.23 Schematic diagram of the Nine-point smoothing method.

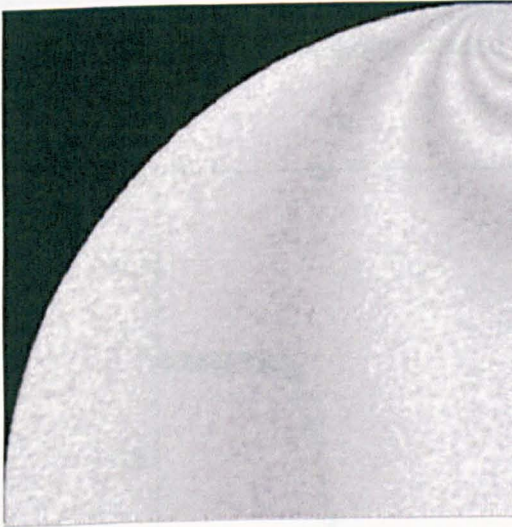


Figure 4.24 The smoothed image of Fig. 4.10 using Nine-point method



Figure 4.25 The smoothed image of Fig. 4.10 using Nine-point method, double used

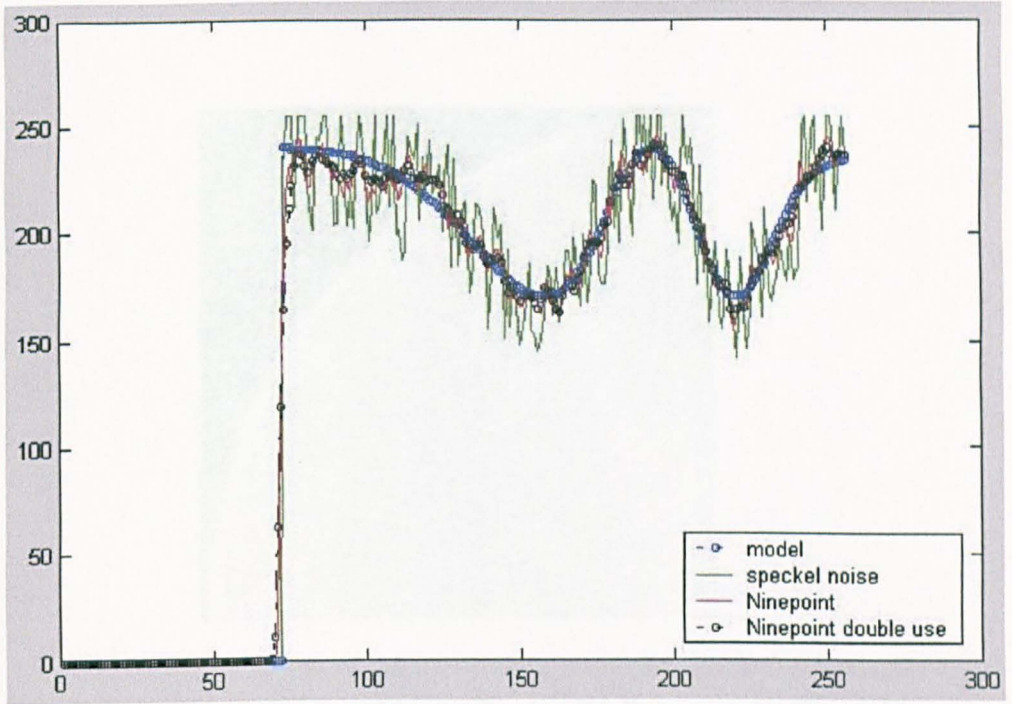


Figure 4.26 Comparison of the original, speckle noised and smoothed data in a line row 80, Nine-point method.

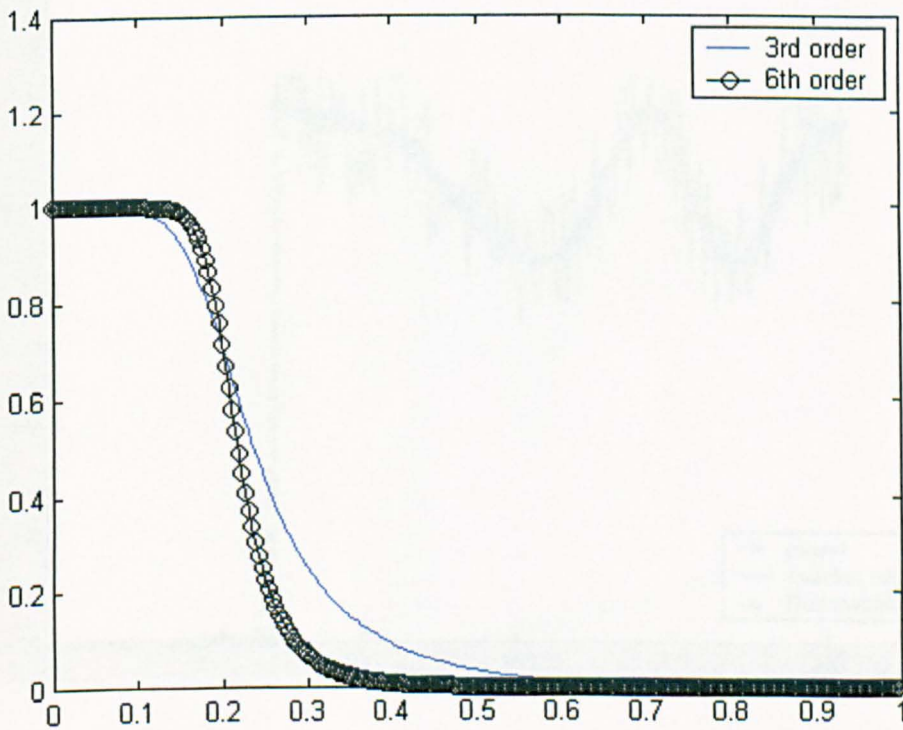


Figure 4.27 Frequency response of the Butterworth filter.

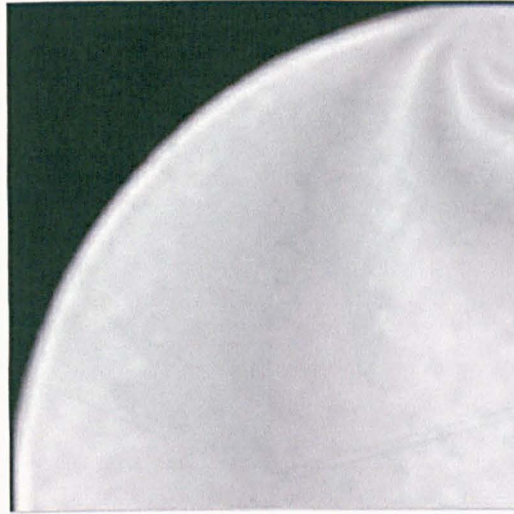


Figure 4.28 The smoothed image of Fig. 4.10 using the Butterworth filter with normalised cut off ratio 0.15.

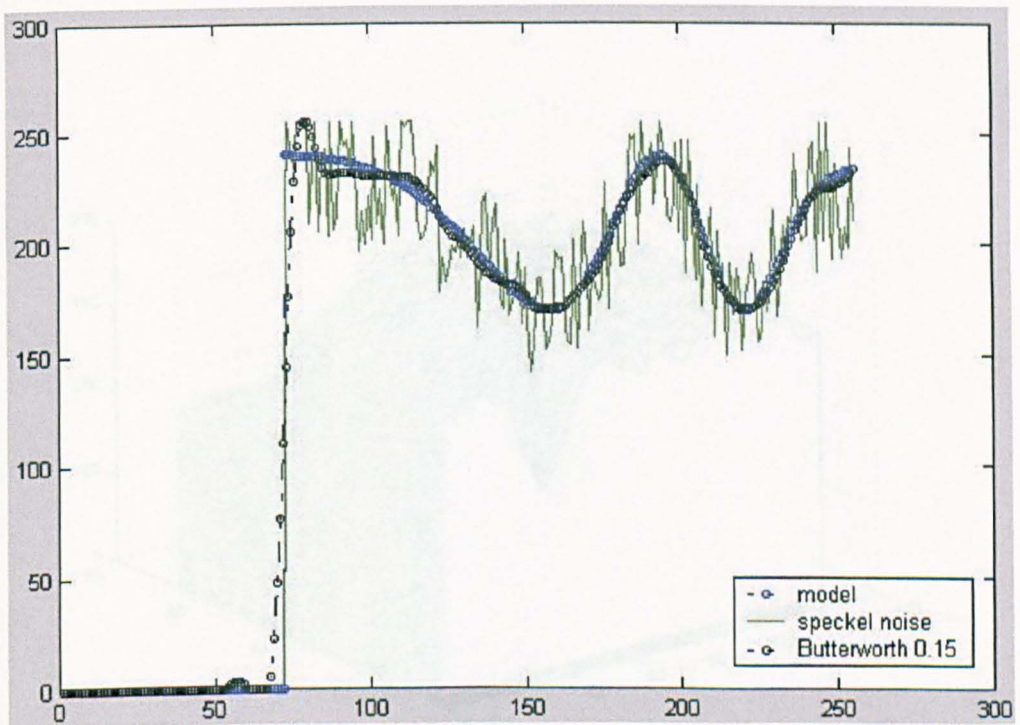


Figure 4.29 Comparison of the original, speckle noised and smoothed data in a line row 80, the Butterworth filter with normalised cut off ratio 0.15.

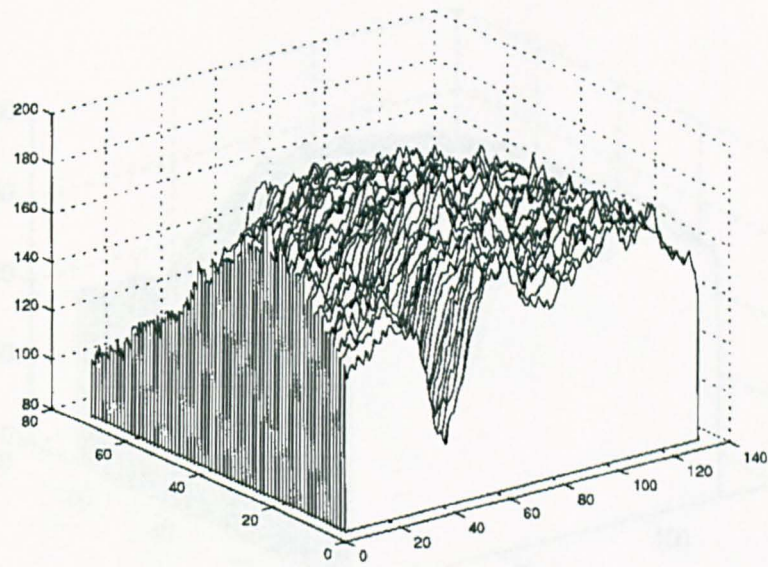


Figure 4.30 The intensity data of the image inside the rectangular area in Fig. 4.1.

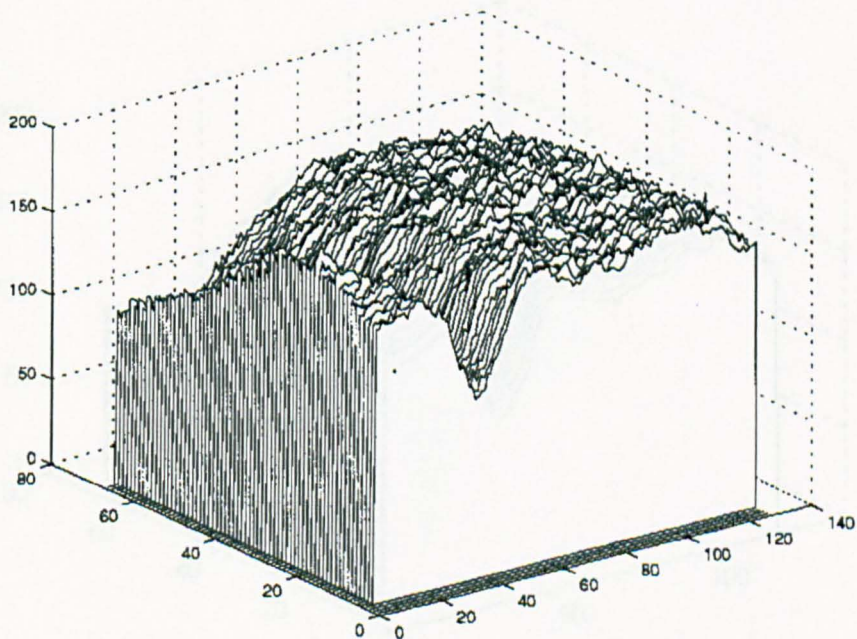


Figure 4.31 Smoothed intensity data using the Sixth difference method.

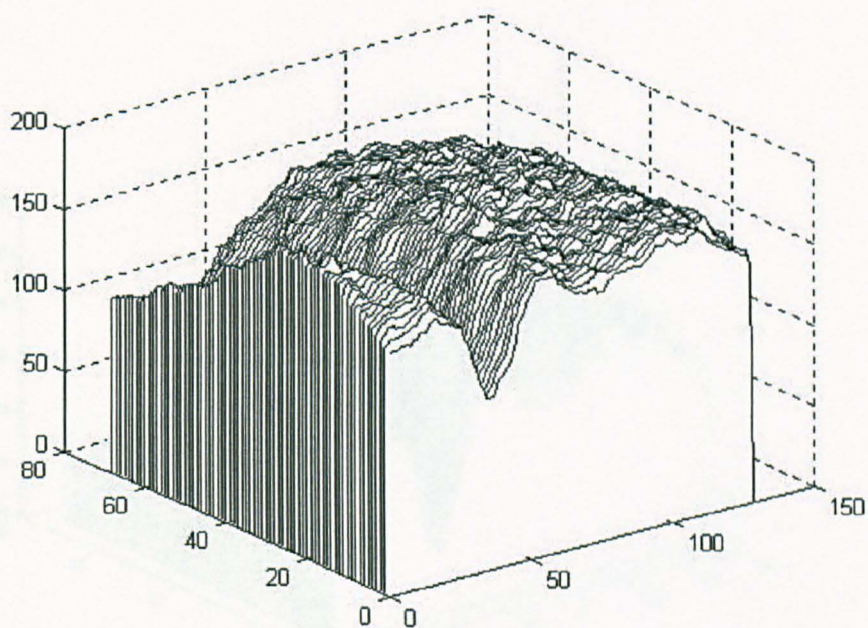


Figure 4.32 Smoothed intensity data using the Median method 3x3.

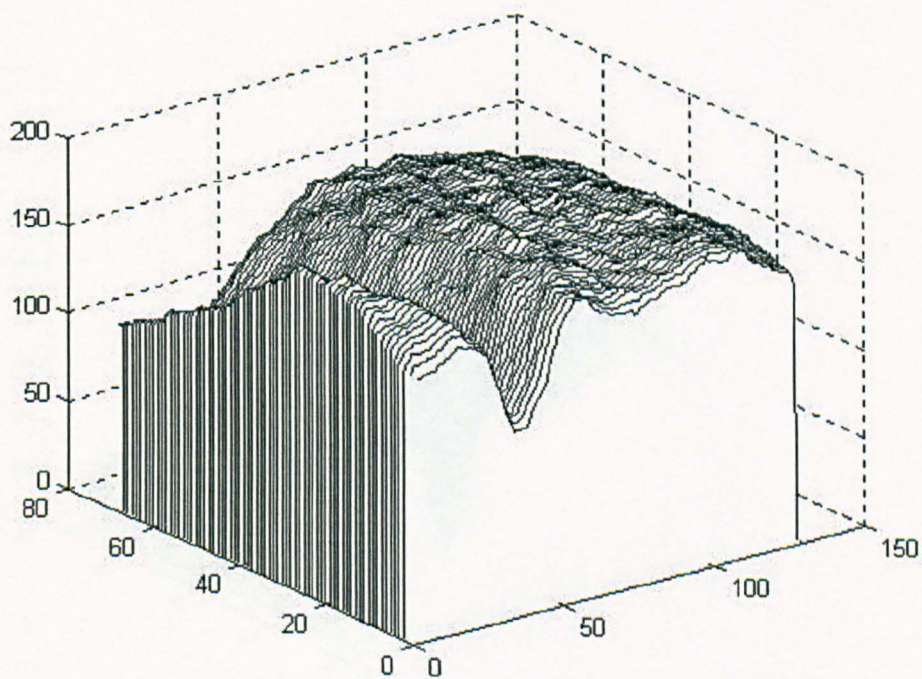


Figure 4.33 Smoothed intensity data using the Median method 5x5.

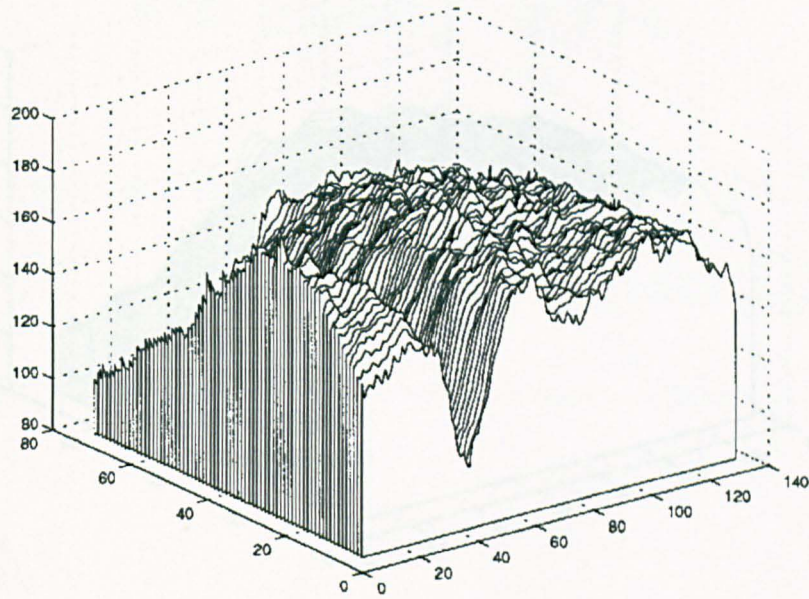


Figure 4.34 Smoothed intensity data using the Liebmann smoothing method.

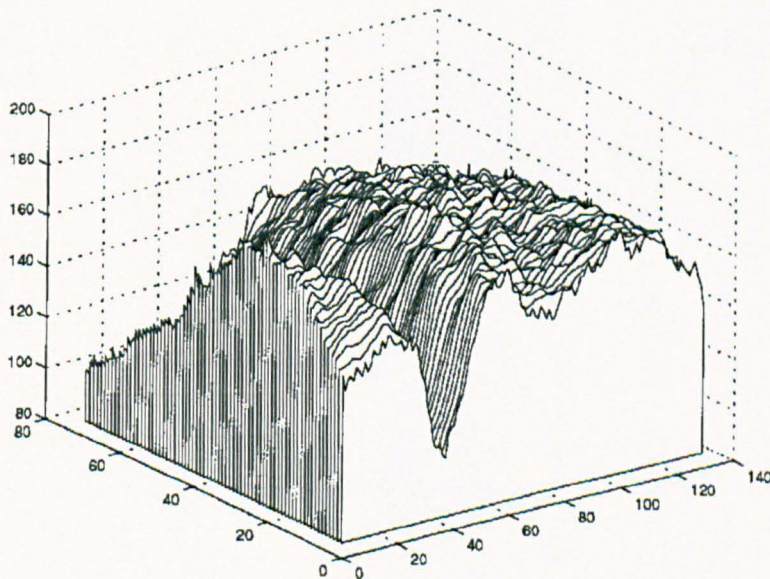


Figure 4.35 Smoothed intensity data using the Nine-point method.

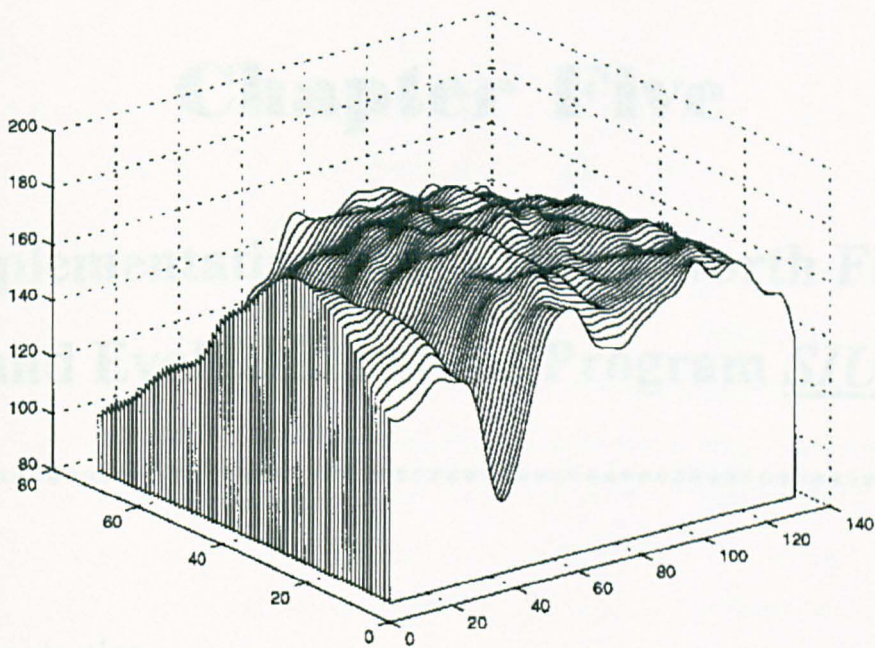


Figure 4.36 Smoothed intensity data using the low pass, zero phase, 3rd order Butterworth filter with ratio of cut off to Nyquist frequency 0.2.

Chapter Five

Implementation of the Butterworth Filter and Evaluation of the Program SIUP

5.1 Introduction

5.2 Selection of Ratio of the Cut-off to Nyquist Frequency in the
Butterworth Filter

5.3 Description of the Program SIUP

5.4 Validation of the Subroutine Butterworth Filter in the Program
SIUP

5.5 Evaluation of the Butterworth Filter in the Program SIUP

5.6 Discussion

5.7 Conclusion

5.1. Introduction

A low pass Butterworth filter has been selected for smoothing intensity images obtained from PSIOS. The Butterworth filter used in chapter 4 was a function in *MATLAB* program, in which the 'Butterworth filter' function was written for an image whose size is not large than 256x256 pixels. In addition, it is not available for data saved in 24-bit .bmp format. In the present study, an MRT card (*MRT* Micro, Inc. USA) and four colour CCD (WAT-202B(PAL), Watec Co, Ltd, Japan) cameras were used to acquire intensity images. The advantage of the use of the colour CCD camera is that the isochromatic parameter in the fringe pattern could be automatically assigned. The image acquired using an *MRT* card is of size 768x574 pixels, and consists of four phase-stepped images from the four CCD colour cameras in the PSIOS head which are saved as a single 24-bit .bmp file. Therefore, the program including a Butterworth filter function for a large image in 24-bit .bmp format is required. A Windows program *SIUP* (Soothing Method for Images Using PSIOS) was written using *Microsoft Visual C++*, version 5.0. There are some related functions in the program *SIUP*, such as the 'Butterworth filter', 'Liebmann's smoothing' method and 'data separation' function. These functions will operate separately on the Red, Green and Blue signals in a 24-bit .bmp image.

In order to obtain the desired smooth image, the user needs to supply a appropriate value of the ratio of cut-off to Nyquist frequency (called cut-off ratio in the present study) for the Butterworth filter. The cut-off frequency is a value in the frequency domain above which data are considered as noise. The Nyquist frequency is defined as half the sampling frequency. The random property of the noise means that information on its statistical behaviour is required. For the problems presented in this study, the cut-off ratio for a particular set of data could be found by using an estimate of the power spectrum. However, since the signal and noise are mixed together, it is difficult for users to choose a suitable cut-off frequency from the power spectrum. Two methods were tested in order to find a suitable cut-off ratio for images obtained from PSIOS. The first is a method that counts the number of turning points along a selected line. If the number of turning points is small, the cut-off ratio should be small. The result of the experiment showed that this method is not feasible and an empirical method was performed.

Verification of the subroutine 'Butterworth filter' in the program SIUP was done by comparing the smoothed intensity data from the SIUP and from the MATLAB programs.

Two specimens were used in the evaluation of the 'Butterworth filter' in the program SIUP. The first specimen is a plate with a right angle fillet subjected to static loading and the second is a compressor blade from an aeroplane engine undergoing vibration. The images of the two specimens were smoothed using the subroutine 'Butterworth filter' before employing the program PECAN.

5.2 Selection of Ratio of Cut-off to Nyquist Frequencies in the Butterworth Filter

5.2.1. Method One (Counting the Number of Turning points)

A consideration in design of the program *SIUP* was that a suitable cut-off ratio should be chosen automatically according to the data in different images. For example, for images with dense fringes, the cut-off ratio should be slightly larger than for images with sparse fringes. The proposed implementation of this idea was to use the density of the turning points in the fringe image. A program *CTP* (Counting Turning Points) was written to count the number of turning points along a selected line chosen by the user. The gradient of a series of straight lines, each passing through the intensity values at five consecutive pixels were calculated. The first passing through points 1-5, the second through points 2-6 and so on until the end point of the line. If the gradient was found to change from positive to negative or from negative to positive, a turning point had been found. According to the density of turning points, an estimate of cut-off ratio will be given after the calculation. A flow chart for the algorithm of the program *CTP* is given in Figure 5.1.

Five images were used in the experiment in order to find a cut-off ratio that can be used in a wide range of applications. Three of the five images were from vibration tests at different energy levels for the compressor blade. Another two images were obtained from the static loading of two plane specimens, but one has more dense fringes than the other. A description of each image is listed below.

Hcaul1: is the first of four images of the specimen *A* used in determination of the stress intensity factor in chapter 3 subjected to tensile load of three tonnes, as shown in Figure 5.2.

Diskm4: is the second of four images of the upper-right of the circular disk quadrant in compression used in the second experiment in section 4.21, as shown in Figure 5.3.

Anl31: is the first of four images of the lower part of a compressor blade in tension as shown in Figure 5.4. Vibration is first mode, frequency is

257 Hz and energy level is 1 g.

Anh11: is the first of four images from the upper part of a compressor blade in tension as shown in Figure 5.5. Vibration is first mode, frequency is 257 Hz and energy level is 2 g.

Enl21: is the first of four images of the lower part of a compressor blade in tension as shown in Figure 5.6. Vibration is third mode, frequency is 1029 Hz and energy level is 12.66 g.

In each image in Figures 5.2 to 5.6, a horizontal and vertical line are shown and the x and y coordinates of the lines are identified in the caption in terms of the row or column number measured from the top left corner of the image. Data along these lines were used in the comparisons described below.

An experiment was carried out, first with two images, *Hcau1* and *Anl31*. Because the high spatial frequency noise in the images will affect the results for the number of turning points along the selected line, a filter should be applied before the program *CTP*. A low pass Butterworth filter is considered as the pre-count filter and again the problem of selecting a suitable cut-off ratio presents itself.

In order to find a suitable cut-off ratio for the pre-count filter, low pass zero-phase Butterworth filters with cut-off ratios 0.1, 0.2, 0.3, 0.4, 0.5, 0.6 were applied to the selected lines respectively. The number of turning points along the lines for the different cut-off ratios are plotted in Figure 5.7. By examining the plot, it is clear that when the cut-off ratios are 0.3, 0.4, and 0.5, the number of turning points tend to be unchanged. Information about the fringes in the images should be kept as far as possible after pre-count filtering, therefore, the cut-off ratio 0.5 is considered to be most appropriate for the pre-count filter. A comparison of the raw and smoothed intensity data using the low pass, zero-phase, 3rd order Butterworth filter with cut-off ratio 0.5 and original intensity data is shown in Figures 5.8 through 5.11 for horizontal and vertical lines through the two images.

The above assumption is made on the results of a selected line with 256 data points. In practice, it is likely that user may choose a line with less than 256 points. On the other hand, the estimation is a statistical process, so a large amount of data

points are required. Thus, it is necessary to verify that the method can be used for less than 256 data points. Hence, a further experiment was carried out.

The concept of a number of turning points within a sample of pixels was used in the program *CTP*. The total number of turning points obtained by using the program *CTP* is divided by the number of point on the selected line times 10, so that the number of turning points per 10 pixels can be obtained. Using the same lines as defined in Figure 5.2 to 5.6, 128 data points and 80 data points were tested and results are listed in Table 5.1. The number of turning points found in row 50 of *Disk4* are 15, 7 and 1 respectively using 256, 128 and 80 pixels where as in fact only 5, 2 and 1 turning points are presented on the line. Similarly, there are 32, 19 and 9 turning points counted by the program *CTP* in column 180 compared to 2, 1, and 0 turning points actually presented for 256, 128 and 80 pixels in the line respectively. Hence, the results from the method cannot be used to estimate cut-off ratio automatically because there is a big difference in the number of turning points obtained by counting automatically and the correct answer. The results from analysis of the data from the image *Hcaul* in Table 5.1 are similar to those of the *Disk4*. The same procedure has been applied to the images of *Anl31*, *Anh11* and *Enl21* and the results are listed in Table 5.1.

To sum up, the purpose of this experiment was to find a suitable cut-off ratio for proper use of the Butterworth filter. It was assumed that the more turning points along a selected line, the more fringes were present in the image. Therefore, a larger cut-off ratio should be chosen. However, it was found that the image smoothed using the pre-count filter still contains considerable noise and the noise has been counted as fringes by the program *CTP*. Hence, the method of counting the number of turning points using data after using a Butterworth filter with cut-off ratio 0.5 to automatically estimate cut-off ratio in Butterworth filter is not feasible for this application.

5.2.2 Method Two (Empirical Method)

The cut-off ratio cannot be chosen automatically using the program *CTP* but it is possible to find a range of cut-off ratios for images obtained from the PSIOS by

performing a large number of experiments using different images. Testing cut-off ratios from 0 to 1 in a small interval is time-consuming, so a power spectrum method was employed to find an approximate range for the cut-off ratio. The power spectrum or power spectral density is the Fourier transform of the autocorrelation function of the process for varying time lag,

Power spectrum estimation is a process that determines the frequency content of the power of a signal or random process. The power spectral density of $x(n)$ is defined as (Stanley, *et al*, 1984, p.301)

$$P_x(\omega) = \sum_{k=-\infty}^{\infty} r_{xx}(k) \exp(-j\omega k) \quad (5.1)$$

over the range $-\pi \leq \omega \leq \pi$, $r_{xx}(k)$ is the autocorrelation function

$$r_{xx}(k) = E[x(n)x^*(n-k)] \quad (5.2)$$

where k is shift index and $x(n)$ is discrete-time sequence.

The Signal Processing Toolbox in the program *MATLAB* was used to analyse the five images described in the section 5.2.1 and to estimate the power spectrum in each case. The plots of the power spectrum along the rows and columns defined in Figure 5.2 to 5.6 are shown in Figures 5.12 through 5.21. Since noises are not correlated to each other, noise in high the frequency domain in the power spectrum approaches a line (Golten, 1997, p67), so that the cut-off ratio could be estimated from the turning position of the curve. By analysis of the power spectrums, the cut-off ratio for these particular lines is proposed in a range of 0.06 to 0.2. The raw data and smoothed data for images *Diskm4*, *Hcaul* and *Anl31* using cut-off ratios of 0.06, 0.13 (midpoint of 0.06 and 0.2), 0.15 0.2 and two extended values 0.25 and 0.3 are shown in Figures 5.22 through 5.27.

The simplest of the three images is *Diskm4* and it was examined first, because the intensity distribution for a circular disk in compression is well known, thus, the intensity distribution of the raw image and smoothed images can be compared with experience. The curve is smoothest when cut-off ratio is 0.06 as shown in Figures 5.22 and 5.23, but the peak near the right edge in Figure 5.22(a) was eliminated. Peaks of shapes similar to this are common in photoelastic images, and thus we

should look for a cut-off ratio higher than 0.06 to avoid its elimination. Figures 5.22(a) to (e) show that using a cut-off ratio of 0.15 and 0.2, the noise was diminished to a certain degree and the smoothed intensity data are closer to the raw intensity data than for other cut-off values. The smoothed intensity data with cut-off ratio 0.2 as shown in Figure 5.22(d) retains more detail of the peak. Figure 5.23(a) to (e) show that when the cut-off ratio is 0.15, the smoothed intensity data is reasonably close to the raw intensity data and the majority of the noise was eliminated. Since the fringe pattern of a circular disk in compression is typical, we could say that the cut-off ratio of 0.2 is a proper value for decreasing the noise in the images caused by use of the PSIOS. The cut-off ratio, 0.2 could be used for those images with complicated fringe patterns due to complicated geometrical shape or loading.

Figures 5.24(a) to (e) are the raw and smoothed intensity data for the plate with two cracks. The smoothed intensity data using cut-off ratios of 0.15, 0.2 and 0.25 are closer to the raw data than the results obtained with other cut-off ratio values. The results in Figures 5.25(a) to (e) for the vertical direction are similar to those in Figure 5.24. Finally, a more complicated case (*Anl31*) was considered. There is no large difference between smoothed intensity data using cut-off ratios of 0.13, 0.15, 0.2, 0.25 and 0.3 (see Figure 5.26). However, for data in the vertical direction (see Figure 5.27) the smoothed data is smoothest when the cut-off ratio is 0.06 compared to other cut off ratio values. It is a trade off of cost of losing detailed information against smoothness. From observation of the remaining curves in Figures 5.26 and 5.27, the curves obtained using cut-off ratios of 0.13, 0.15 and 0.2 are acceptable (here, the criteria employed in analysing the plot of the *Diskm4* was used).

To sum up, there is no universal cut-off ratio that is suitable for every application. Estimation of the cut-off ratio depends on the experience of the user. However, for the applications discussed in this section, a cut-off ratio between 0.15 and 0.25 is suggested and the results seem insensitive to the ratio within this range. The examples were chosen to represent the fringe patterns likely to be encountered in practical applications. Hence the cut-off ratio of 0.2 was used as the default value in the program *SIUP*.

5.3 Description of the Program SIUP

The program SIUP was written using *Microsoft Visual C++*, version 5.0. In the program, there are three subroutines, namely, Processing, Filter (Butterworth filter) and Filter-1 (Liebmann smoothing). The features of the program are shown in Figure 5.28. Each of these two filter subroutines can be applied to the Red, Green or Blue data in an RGB image. A function of the Butterworth filter for automatically processing RGB data on three planes rather than for each individual R, G and B data is also available. The subroutine Processing can be used to extract either the red, green or blue data from the RGB image and display it on screen. Alternatively, the subroutine Processing can be used after the Butterworth filter and the Liebmann smoothing to check the effect of the filter on individual planes. There are two more options within the Butterworth filter subroutine, i.e., *H* and *V*. *H* and *V* denote that the smoothing will be performed in horizontal or vertical directions respectively.

A flow chart of the subroutine Butterworth filter is shown in Figure 5.29. When the program is required to process a displayed image, it first checks the format of the image to ensure that it is a 24-bit .bmp file. If it is not, a dialog box appears to remind the user to open a 24-bit .bmp file instead. Then another dialog box pops up, and asks the user to provide a cut-off ratio in the edit box. In the edit box, 0.2 is set as the default value. When the value is confirmed, coefficients a_i and b_i will be calculated using the input value. The smoothing procedure is carried out and the modified image will be displayed to replace the original image on screen.

Instructions and source code for the program SIUP are given in Appendix B.

5.4 Validation of the Subroutine Butterworth Filter in the Program SIUP

In order to validate the subroutine Butterworth Filter in the program SIUP, smoothed data from the program SIUP were compared with those from the program MATLAB. Two images obtained using two plates with cracks originating from the central hole (the plate was the specimen *A* used in the determination of stress intensity factor in chapter 3) and a plate with a right angle fillet (detailed description of the specimen is in section 5.41) were used in the comparison, as shown in Figures 5.30 and 5.31. Two lines, one horizontal (line AB) and another vertical (line CD) were chosen in each of the images. Smoothed data are shown in Figures 5.32, 5.33, 5.34 and 5.35.

It is found from the plots that smoothed data using the Butterworth filter in the two different programs match each other very well. Small differences between them is likely to be caused by round off error because in the program MATLAB, data were calculated using 'double' precision (64-bits) and in the program SIUP, the data were in 'BYTE' format (8-bit). In MATLAB, the Butterworth filter is only capable of smoothing images of size 256x256 pixels or smaller due to the need for a large computer memory and a long processing time when calculating in 'double' precision. In contrast, using the Butterworth filter in the SIUP, a large image can be smoothed in one second and results are similar to those from the MATLAB program.

5.5 Evaluation of the Subroutine Butterworth Filter in the Program SIUP

5.5.1 The Plate with a Right Angle Fillet

5.5.1.1 Specimen

The specimen was a plate made of photoelastic coating (PS1, The Measurement Group, USA). The geometry of the specimen is shown in Figure 5.36. The elastic modulus and Poisson's ratio of the plate were 2.5 *GPa* and 0.38 respectively. Its strain optical coefficient was 0.15.

5.5.1.2 Experimental Procedure

The specimen was subjected to a tensile load of 258 *N*. The *MRT* card connected to the PSIOS system was used to acquire data. The image is of size 768x574 and is saved in 24-bit .bmp format. The set up of switches on the colour CCD camera is given in Table 5.3. The Butterworth filter was used upon the green data from the images, because the central wavelength for the green spectrum of the camera was closest to the wavelength of the quarter wave plates (560nm) in PSIOS. Smoothed intensity data were processed using the program PECAN which is specially written for the automated reflection polariscope and was described in chapter 2.

The data from the red and blue images are useful in this application only for the automatic calibration of fringe orders. There is no need to smooth the red and blue data in this experiment because automatic calibration function was not available in the program PECAN. Calibration of the fringe was performed manually.

5.5.1.3 Results and Discussion

The raw and smoothed version of the first of the four images are shown in Figures 5.37(a) and (b). The retardation, isochromatic fringe order and isoclinic angle maps from the raw images and smoothed images are shown in Figures 5.38, 5.39 and 5.40. The isochromatic fringe order and isoclinic angle maps from the filtered

images (in Figures 5.39(b) and 5.40(b)) are smoother than those from the raw image (in Figures 5.39(a) and 5.40(a)) and this is demonstrated by comparing of the isochromatic fringe orders and isoclinic angles from the raw image and smoothed image along the lines shown in Figures 5.41 and 5.42.

5.5.2 The Compressor Blade

When compressor blades are operating they will experience not only high temperatures and direct stress, but also rapid temperature transients at various points in the flight cycle (Driver, *et al*, 1981, p.23). High cycle fatigue problems can arise if the excitations coincide with the natural frequency of the blade in the flight speed range. Theoretical calculations, experiments and the finite element method have been used to aid the design of the blade. However, experimental methods have an intrinsic value and provide the required stimulus towards more realistic modelling. The photoelastic instrument PSIOS has the potential to be used in dynamic applications since the four images needed to produce stress distribution maps for the object can be obtained simultaneously. Noise in images from a dynamic object is severe; hence it is a good example for testing the capability of the Butterworth filter. In this experiment, a single compressor blade with aspect ratio 1.8, thickness ratio 130 and free end twist angle 30° was used in vibration without rotation. The first four modes of vibration with natural frequencies 257 Hz, 617 Hz, 1029 Hz and 1876 Hz have been used for a 1 mm thick blade with a 2 mm thick PL coating on both sides. The root of the turbine blade was mounted on the vibration isolation table and other edges were free. For the compressor blade used in the experiment, three levels of energy corresponding to acceleration levels of 1 g, 1.5 g and 2 g, where g is the acceleration of gravity were applied when blade was in vibrating at $f = 257$ Hz. Data were taken for the blade in both tension and compression at each energy level. The experimental work was done in the laboratories of SNECMA in Paris.

5.5.2.1 Apparatus

(1) PSIOS system:

Optical head

(The University of Sheffield, UK, Patterson and Wang, 1998)

8440 Slip Sync Strobex and 270D light head

(Chadwick - Helmuth Company Inc. California, USA)

Four Wattec Wat - 202B CCD colour cameras (Japan)

One Standard TV lens(Cosmicar/Pentax, Japan)

A computer Desk station V Model No.PA2712E (Toshiba, Japan)

(2) System for vibration:

Vibration equipment: vibrator Model A300BP series No. 1014,

(Pye - Ling Ltd. Royston Herts - England)

Vibration isolation table K1 No. K4371, P/N SP60, 18ST36 - 2

(Kimball Industries, Inc. Monrovia, California)

Spectral dynamics: 2552B vibration control system

Fluke 45 dual display multimeter

Digital data storage package mounted on a Sun Microsystem computer

Conditioning Amplifier Type 2626 Bruel & Kjr

465B Tektronix Oscilloscope

(Tiroir DE Surveillance, France)

(3) Specimen:

A pre-twisted blade with length $a = 230 \text{ mm}$, width $b = 130 \text{ mm}$ and thickness $h = 1 \text{ mm}$ was used in the experiment. The edges were pre-twisted through an angle of 30° . The root of the blade is 140 mm long and 60 mm wide. There is a relatively thick and complex shape to the root structure and the blade has thin edges. The 2 mm PL coating was shaped and bonded onto the whole surface of the blade. The geometry of the blade is shown in Figure 5.43.

5.5.2.2 Experimental Procedures

5.5.2.2.1 Data Acquisition

The specimen was clamped in a holding fixture and the holding fixture was bolted to the vibration isolation table. The blade was excited to resonance using a piezoelectric crystal stack embedded in the holding fixture. The frequency of the blade and the energy level can be controlled by the vibration control system and the control signal was used as a trigger to control the flash of the strobe mounted on the PSIOS head. The slew control alters the phase between the strobe and the vibration signal, thus allowing the collection of data at any selected point in the deformation cycle of the blade. Figure 5.46 shows a schematic diagram of the blade in tension and compression. The optical head and the strobe light source of PSIOS were positioned about 1.5 meters in front of the specimen. The experimental set-up of the apparatus and the blade are shown in Figures 5.44 and 5.45.

The vibration frequency for the fundamental mode of the blade is 257 Hz. Three energy levels, i.e. 2 g, 1.58 g and 1 g were applied to the blade and images were collected in both tension and compression respectively. The vibration frequency for the second and third modes were 617 Hz and 1029 Hz respectively and the energy level used 5.01 g and 12.6 g respectively. In the vibration experiment, a total of 22 data sets were obtained including two sets of data taken in the static state for the purpose of alignment of the images. Since the lens available at the site did not allow us to obtain the full image of the blade, images were taken separately for the upper and lower parts of the blade. Among the 20 data sets listed in Table 5.2, 10 data sets are images for the upper part of the blade and remaining data sets are for the lower part of the blade.

5.5.2.2.2 Data Processing

The procedure for data processing is the same as for the plate with right angle fillet in section 5.5.1.

5.5.2.3 Results and Discussions

Figures 5.47 and 5.48 show the first of the four images for the upper and lower parts of the blade before and after use of the Butterworth filter. It is obvious that information relating to the stress has been kept in the smoothed image and that most of the noise has been removed. It was found that the performance of the edge detection function in the program *PECAN* was not as good as expected, because part of the area at the edge of the blade was removed as background using the Automatic background function (the Automatic background function is the same as the function *Markfind* in transmission). This was probably due to the blurred boundary of the blade and background. In addition there is a reflective plate behind the blade as shown in Figure 5.45 which would exhibit birefringence arising from the reflection. Manual background detection, although available in *PECAN*, is not suitable for a blade with such complex shape. The Manual background function was used and the edge of irregular shape of the blade was removed and the central part of the blade retained for further processing. A suggestion for solving this problem in further experiment is to use a black blanket to provide a matt black screen and to increase the difference in intensity between the background and the specimen. Since the experiment was done on site at *SNECMA*, Paris, it is not possible to repeat the experiment with the reflective background object covered.

The images of the lower part of the blade are not good because the intensity data overflowed in the centre of the image and this may affect the implementation of the phase-stepping functions in the program *PECAN*.

The retardation, isochromatic and isoclinic maps for the upper part of the blade in the first mode with energy level 1 g and in the second mode with energy level 5.01 g calculated both from the raw images and the smoothed images are shown in Figures 5.49, 5.50, 5.51, 5.52, 5.53 and 5.54.

The comparison was done qualitatively. The problems occurred in the unwrapping process due to the noise in the raw images (see Figure 5.50). The retardation, isochromatic fringe order and isoclinic angle maps calculated from the smoothed intensity data are clear and more acceptable than those from the raw intensity data.

5.6. Discussion

Automatic estimation of the cut-off ratio for use in the low pass Butterworth filter is a good idea, but it is not feasible using the method based on counting the turning points to assess the fringe density. The experiment using five images was used to assess the assumption that the more turning points along a selected line, implied more fringes in the image, therefore, a larger cut-off ratio should be chosen. It was found that the image smoothed using the pre-count filter still contains considerable noise and the noise has been counted as fringes by the program *CTP*. Hence, the method of counting the number of turning points cannot be used to provide the estimated cut-off ratio automatically for images obtained from the PSIOS system.

The experiment of the empirical method was carried out. Three images from different specimens in different loading condition were used. Six cut-off ratios (0.06, 0.13, 0.15, 0.2, 0.25 and 0.3) were applied to the selected lines in the images on the horizontal and vertical directions. Results from the experiment showed that a cut-off ratio in the range 0.15 to 0.25 is considered suitable to eliminate the noise in the images from PSIOS.

The colour CCD cameras and the MRT card are introduced in the experiment using the PSIOS system to automatically determine the isochromatic fringe order. Since the Butterworth filter function in the program *MATLAB* was not designed for larger data set with .bmp format, a program *SIUP* consists of a Butterworth filter function for smoothing images of any size, in 24-bit .bmp format from the MRT card written using *Microsoft Visual C++*, version 5. In the program *SIUP*, the default cut-off ratio was set as 0.2. Although the default cut-off ratio was given, it is recommended that the cut-off ratio should be chosen according to the particular application in order to obtain the desired result.

Results of the smoothed intensity data from the experiment showed that the *SIUP* and *MATLAB* programs are in good agreement (see Figures 5.32 to 5.35), so the Butterworth filter in the *SIUP* is assumed to be a valid function. The computing time for performing the Butterworth filter using the program *SIUP* is considerably shorter than using the *MATLAB* program for the same image, because in *MATLAB* the calculation is done using *double* precision and in *SIUP* it is in 'BYTE'.

The evaluation of the Butterworth filter using a vibration compressor blade and a plate with a right angle fillet indicated that isochromatic and isoclinic maps using the smoothed intensity data are better than those without smoothing (see Figures 5.49 to 5.54).

5.7 Conclusion

Based on the experiments described in previous sections, it is concluded that the low pass, zero-phase, 3rd order Butterworth filter in the program *SIUP* is a valid function and is an effective, flexible smoothing tool for the images obtained from PSIOS. The recommended range of the cut-off ratio in the Butterworth filter is 0.15 to 0.25.

The Butterworth filter algorithm has been incorporated into software to be used routinely by SNECMA , and will shortly also be used by BAe system.

Table 5.1 Number of turning point of different images for different number data points

Filename	selected line	No. of pixels on the selected line	Location of data point on the line	Turning points per 10 pixels after pre-filtering	Number of turning points of raw data	Number of turning points counted after pre-filtering	Number of turning points counted from image
Anl31	row 100	256	1 - 256	0.59			
Anl31	row 100	128	50 - 178	0.5			
Anl31	row 100	80	150 - 230	0.63			
Anl31	column 160	256	1 - 256	1.6			
Anl31	column 160	128	50 - 178	1.8			
Anl31	column 160	80	150 - 230	1.38			
Anh11	row 128	256	1 - 256	1.02			
Anh11	row 128	128	50 - 178	0.7			
Anh11	row 128	80	100 - 180	0.5			
Anh11	column 128	256	1 - 256	1.87			
Anh11	column 128	128	50 - 178	1.3			
Anh11	column 128	80	100 - 180	1.75			
Hcaul	row 125	256	1 - 256	1.05	31	27	10
Hcaul	row 125	128	50 - 178	1.1	20	11	8
Hcaul	row 125	80	100 - 180	0.25	10	3	7
Hcaul	column 160	256	1 - 256	1.68	75	43	10
Hcaul	column 160	128	50 - 178	1.8	20	13	8
Hcaul	column 160	80	100 - 180	1.63	11	5	7
Diskm4	row 50	256	1 - 256	0.59	39	15	5
Diskm4	row 50	128	50 - 178	0.7	19	7	2
Diskm4	row 50	80	100 - 180	0.25	3	1	1
Diskm4	column 180	256	1 - 256	1.25	62	32	2
Diskm4	column 180	128	50 - 178	1.9	34	19	1
Diskm4	column 180	80	100 - 180	1.25	20	9	0
Enl21	row 80	256	1 - 256	0.66			
Enl21	row 80	128	50 - 178	0.8			
Enl21	row 80	80	100 - 180	0.63			
Enl21	column 80	256	1 - 256	1.84			
Enl21	column 80	128	50 - 178	2.4			
Enl21	column 80	80	100 - 180	2.13			

Table 5.2 Filenames for specimen under different mode and energy levels

Mode	Frequency (Hz)	Energy level (g)	Tension -		Compression -	
			upper	lower	upper	lower
1	257	2	snh1	snl1	snh4	snl4
1	257	1.58	snh2	snl2	snh5	snl5
1	257	1	snh3	snl3	snh6	snl6
2	617	5.01	nnh1	nnl1	nnh2	nnl2
3	1029	12.66	enh1	enl1	enh2	enl2
4	1876	28.2	mnh1	mdl1	mnh2	mdl2

Reference file:

For joining two parts of the blade	For aligning four images of the blade	
join11.dar	ref11.dar	refh1.dar
join12.dar	ref12.dar	refh2.dar

Table 5.3 Switch position of the CCD colour camera in the PSIOS instrument

White balance volume:	Middle
White balance switch:	Incandescent light
Electronic shutter:	OFF
AGC(on/off):	OFF
AGC(gain):	OFF

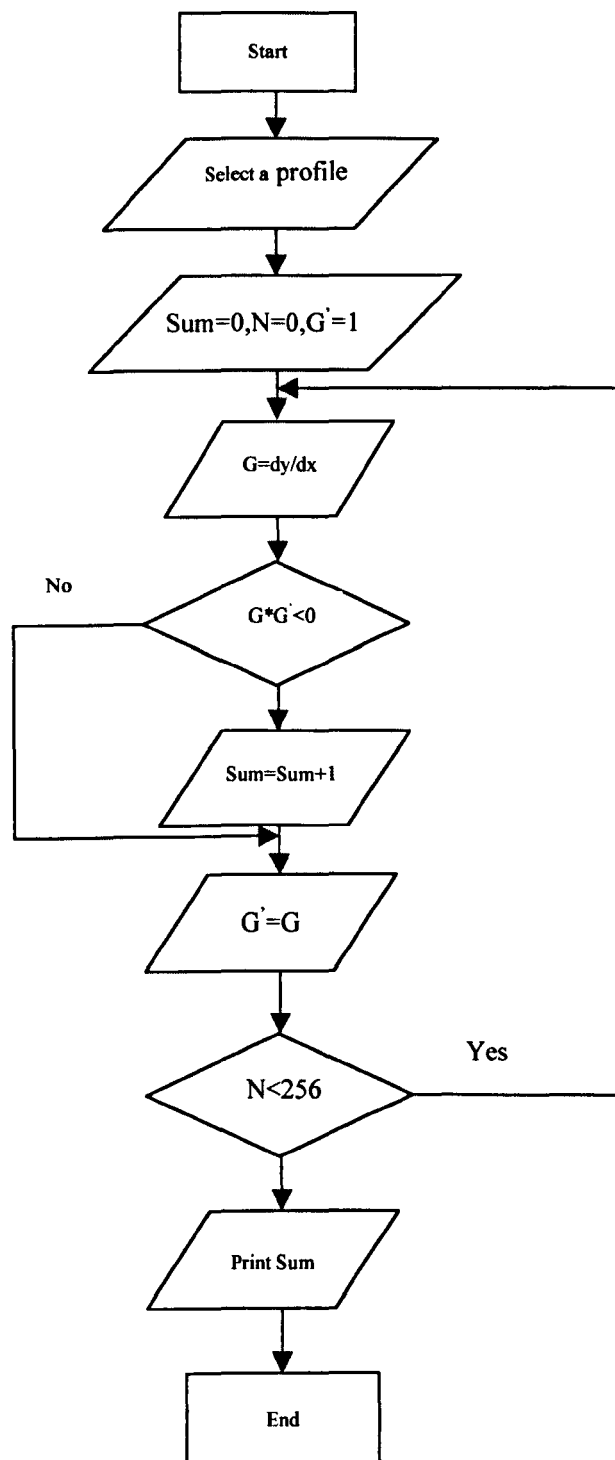


Figure 5.1 Flow chart of the algorithm of the program *CTP*.

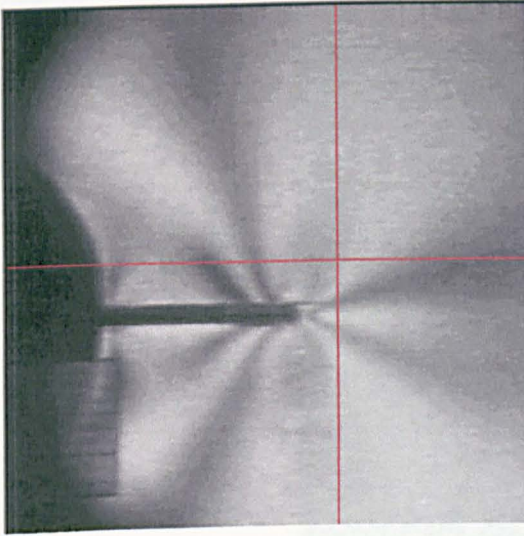


Figure 5.2 Image of HCAU1

the selected lines are
column: 160, row: 125

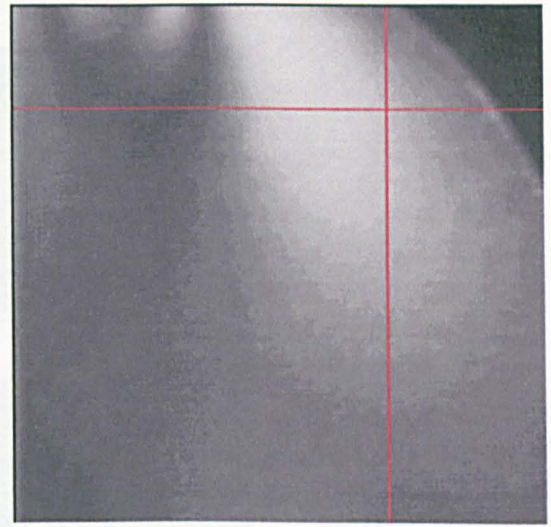


Figure 5.3 Image of DISKM4

the selected lines are
column: 180, row: 50

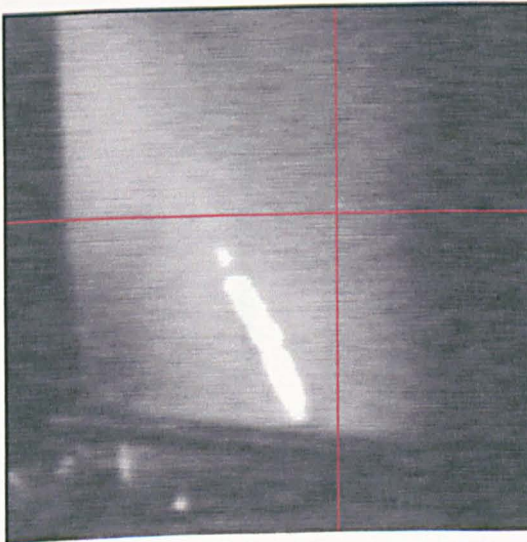


Figure 5.4 Image of ANL31

the selected lines are
column: 160, row: 100

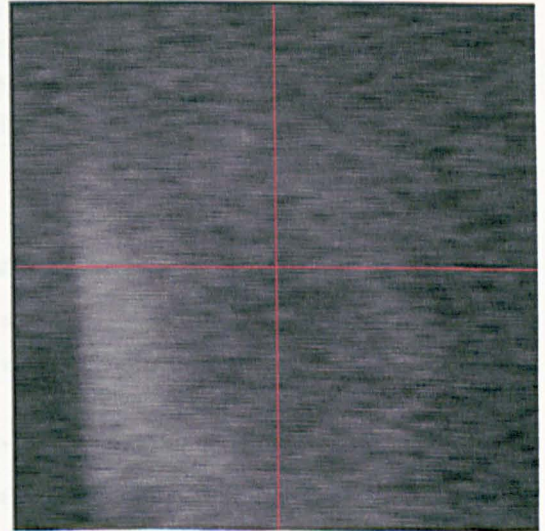


Figure 5.5 Image of ANH11

the selected lines are
column: 128, row: 128

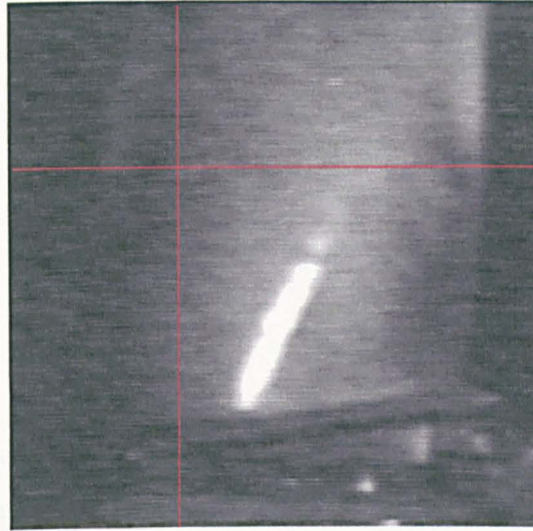


Figure 5.6 Image of ENL21, the selected lines are column: 80, row: 80

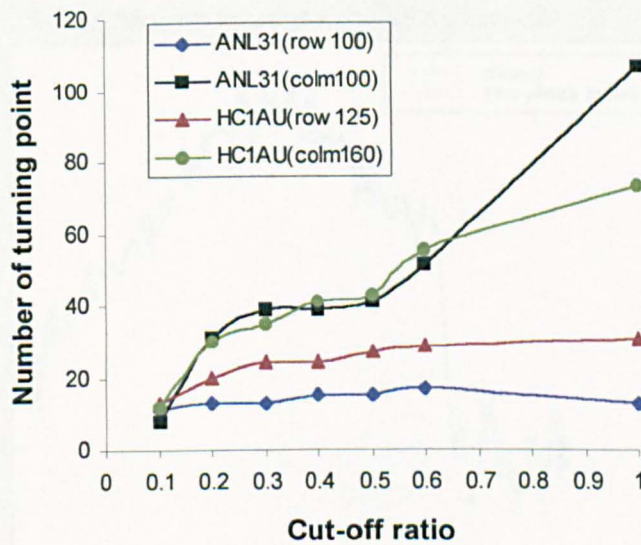


Figure 5.7 Relationship of number of turning point and cut-off ratios used in the Butterworth filter.

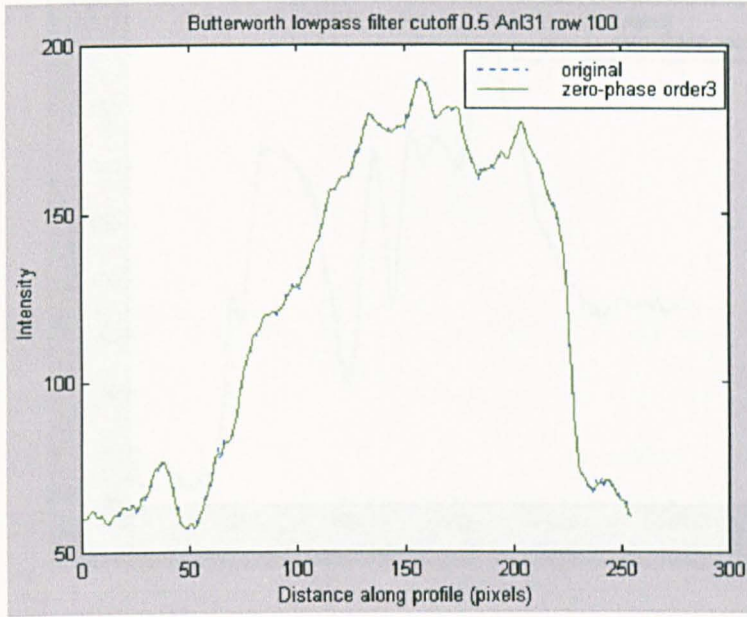


Figure 5.8 Original data and filtered data ANL31 row:100

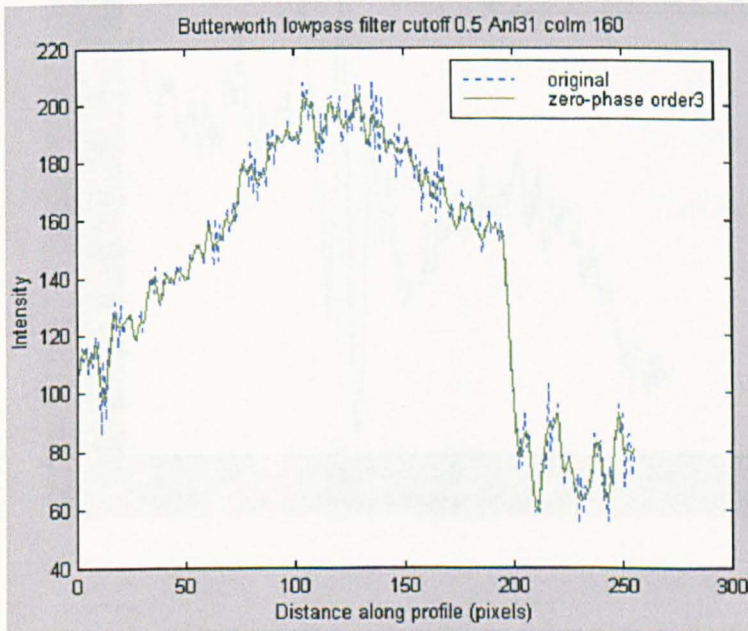


Figure 5.9 Original data and filtered data ANL31 column:160

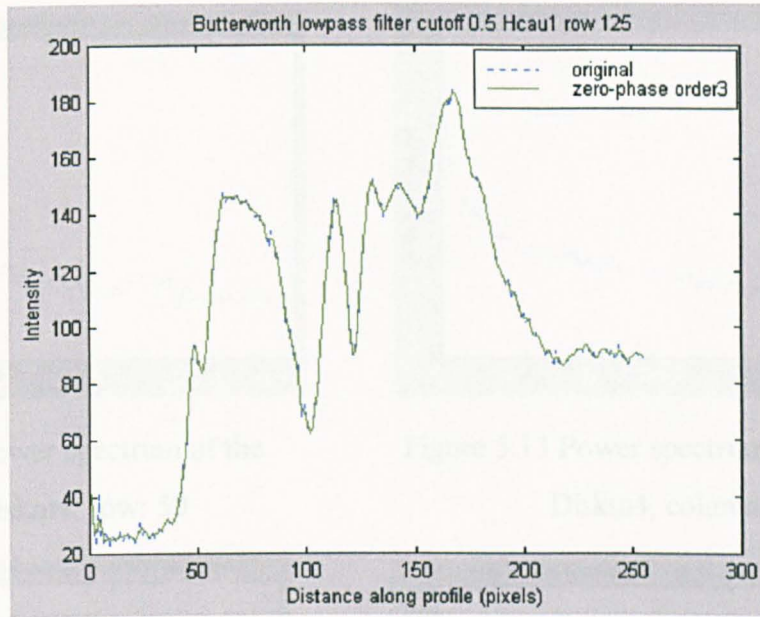


Figure 5.10 Original data and filtered data HCAU1 row:125

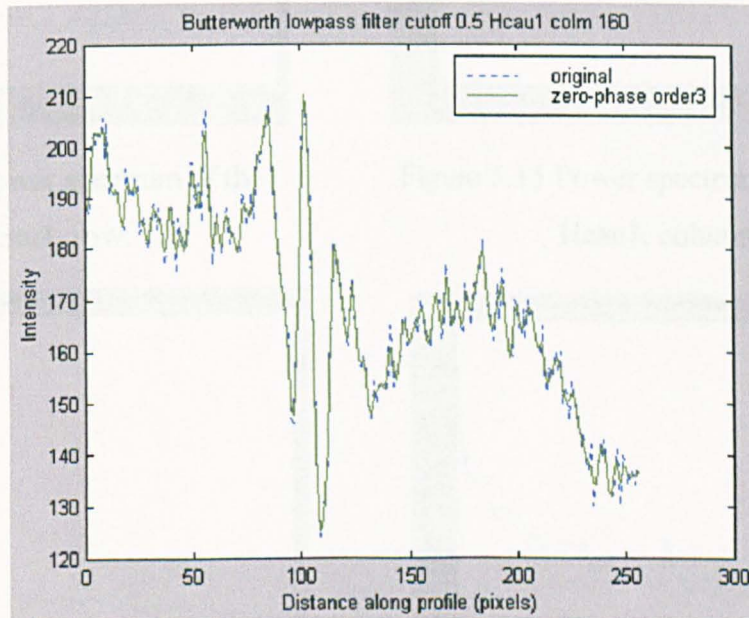


Figure 5.11 Original data and filtered data HCAU1 column:160

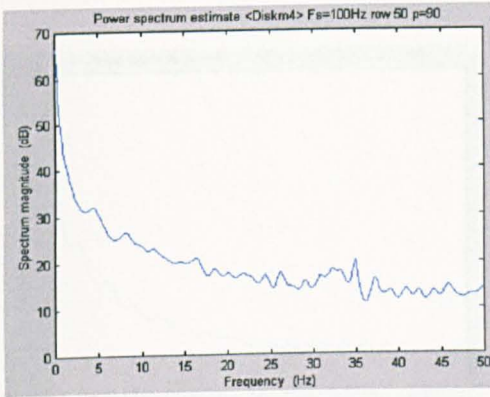


Figure 5.12 Power spectrum of the
Diskm4, row: 50

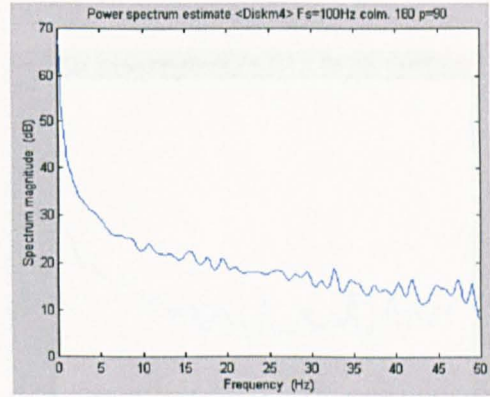


Figure 5.13 Power spectrum of the
Diskm4, column: 180

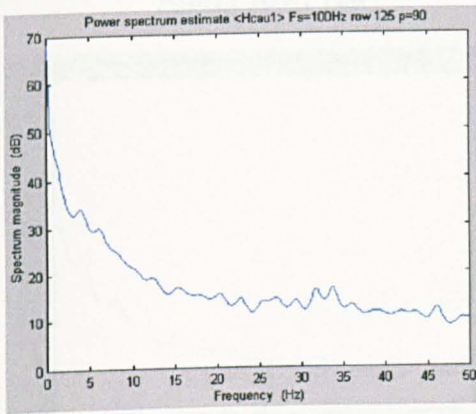


Figure 5.14 Power spectrum of the
Hcau1, row: 125

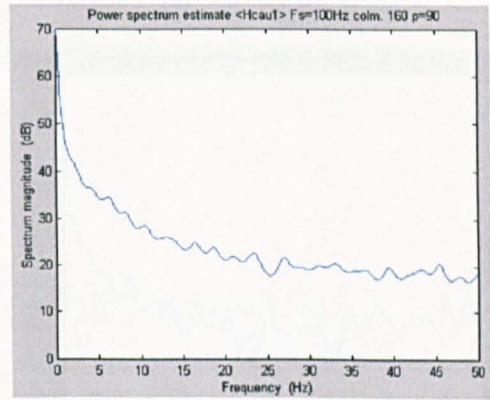


Figure 5.15 Power spectrum of the
Hcau1, column: 160

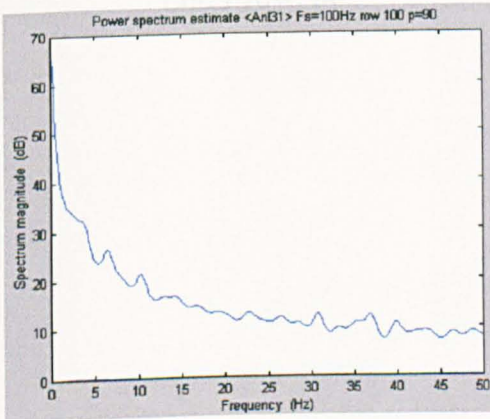


Figure 5.16 Power spectrum of the
Anl31, row: 100

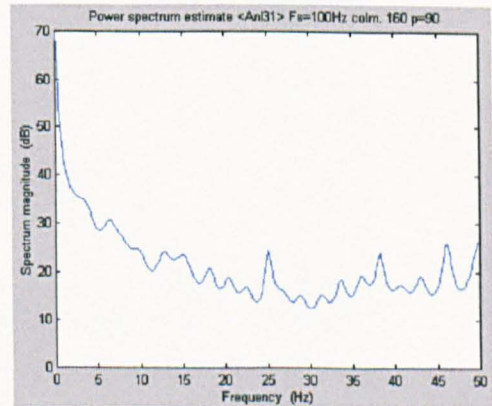


Figure 5.17 Power spectrum of the
Anl31, column: 160

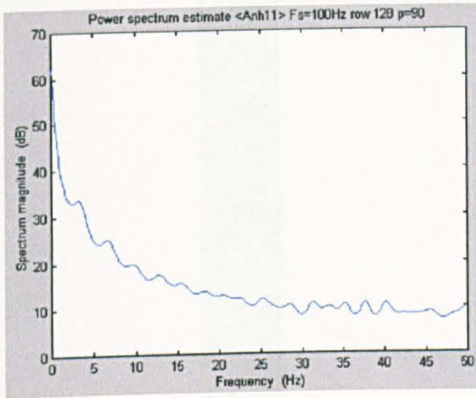


Figure 5.18 Power spectrum of the
Anh11 row: 128

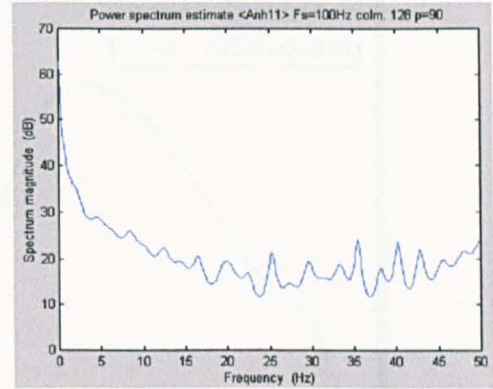


Figure 5.19 Power spectrum of the
Anh11 column: 128

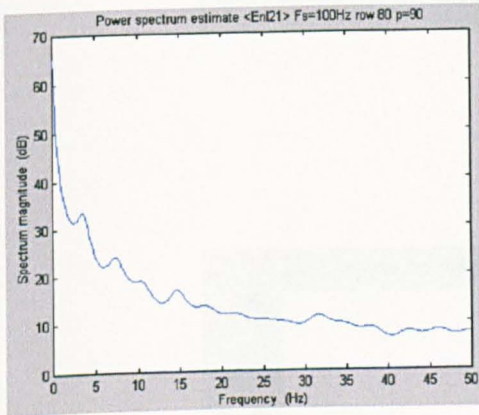


Figure 5.20 Power spectrum of the
Enl21 row: 80

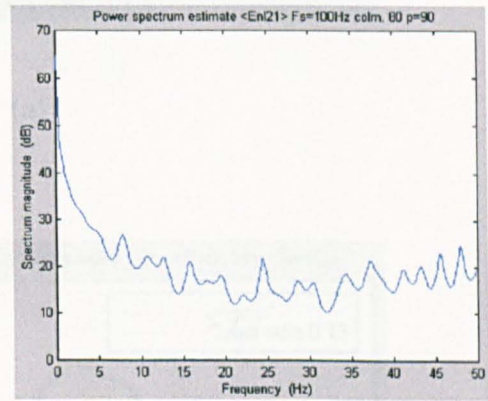
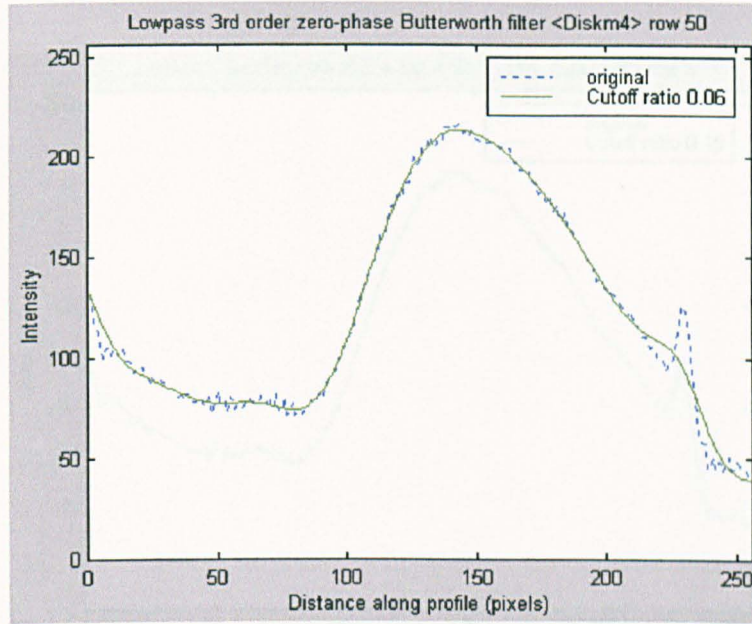
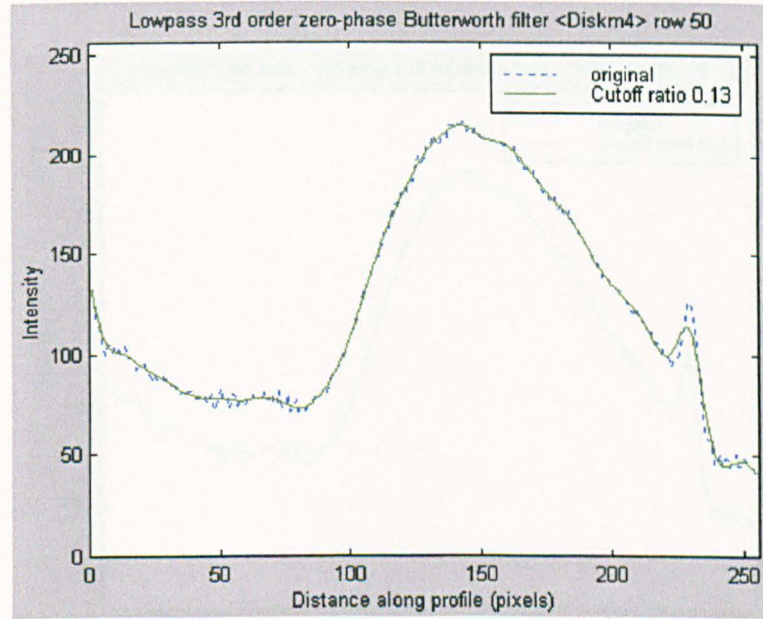


Figure 5.21 Power spectrum of the
Enl21 column: 80

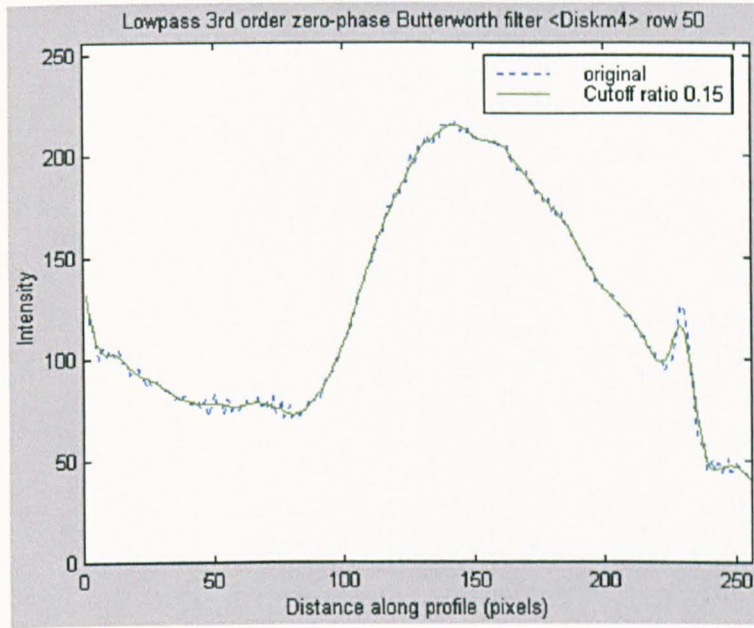


(a)

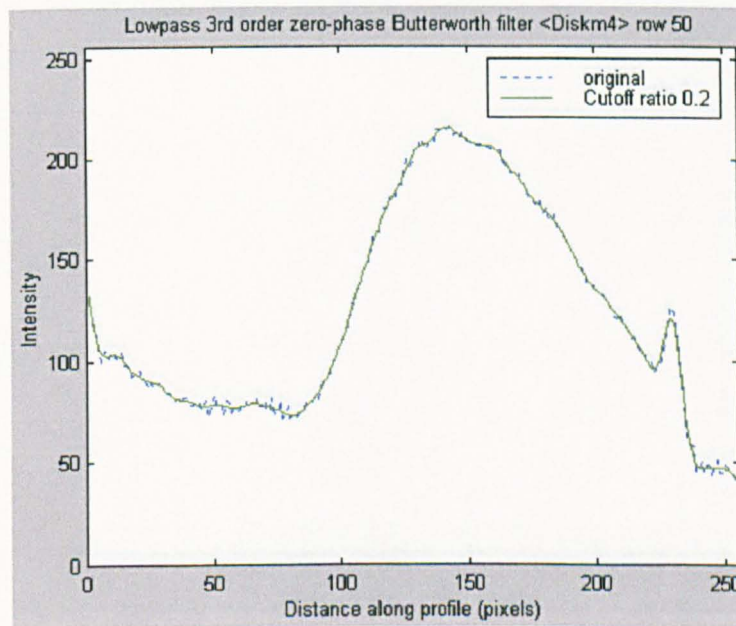


(b)

Figure 5.22 The comparison of the raw and smoothed intensity data. Diskm4, row: 50
(continued)



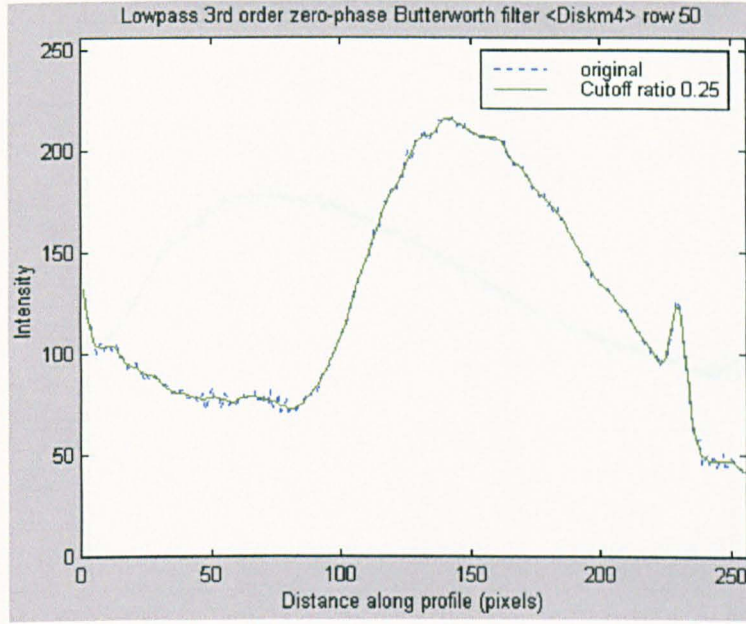
(c)



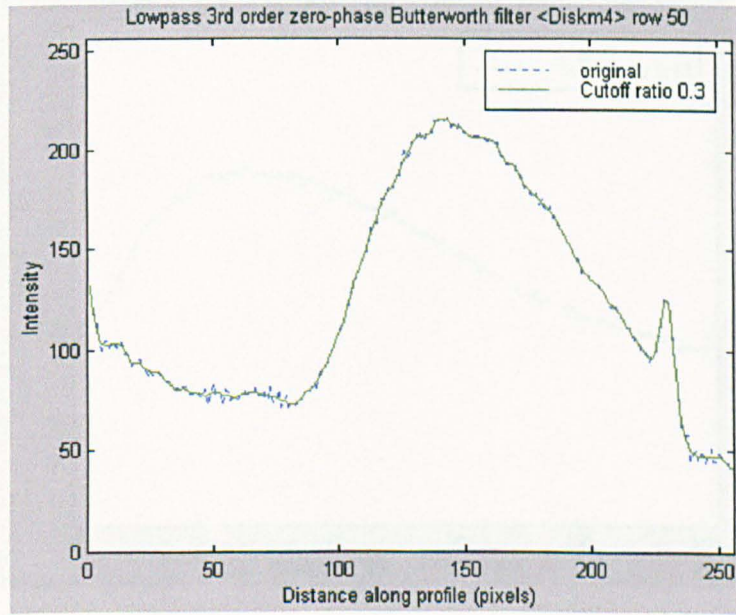
(d)

Figure 5.22 The comparison of the raw and smoothed intensity data. Diskm4, row: 50

(continued)

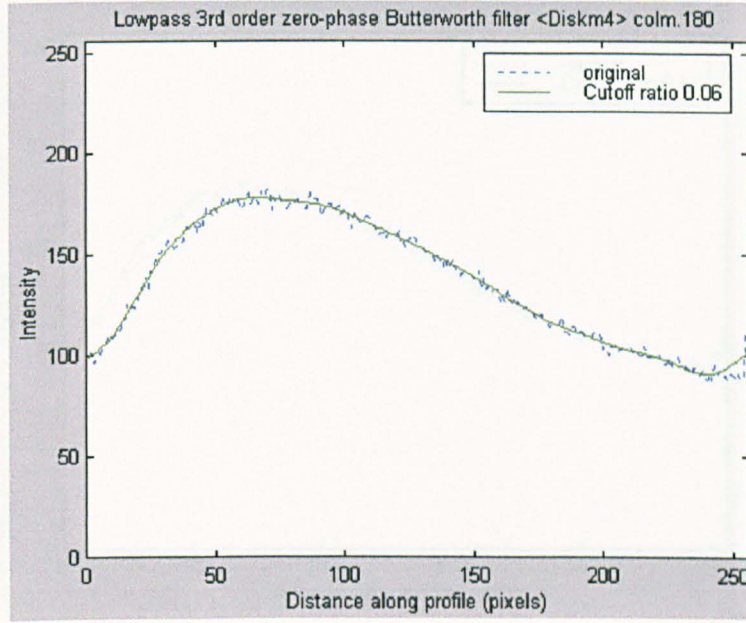


(e)

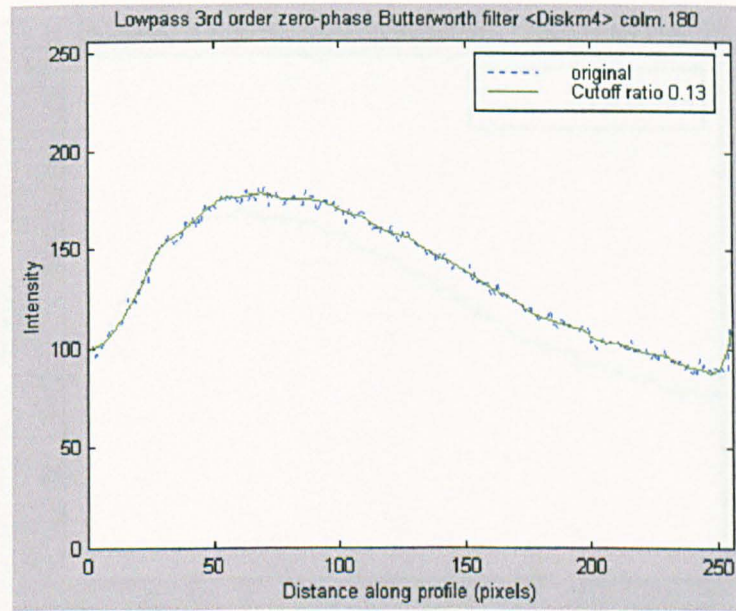


(f)

Figure 5.22 The comparison of the raw and smoothed intensity data. Diskm4, row: 50

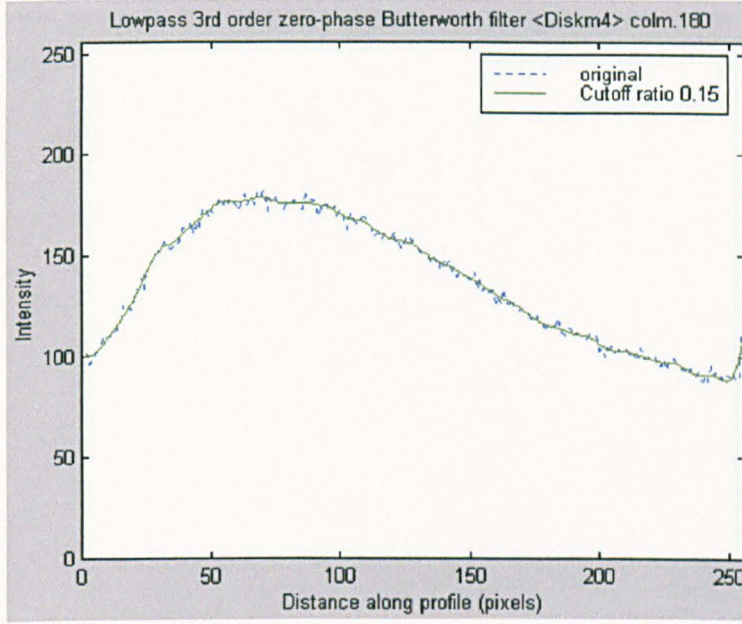


(a)

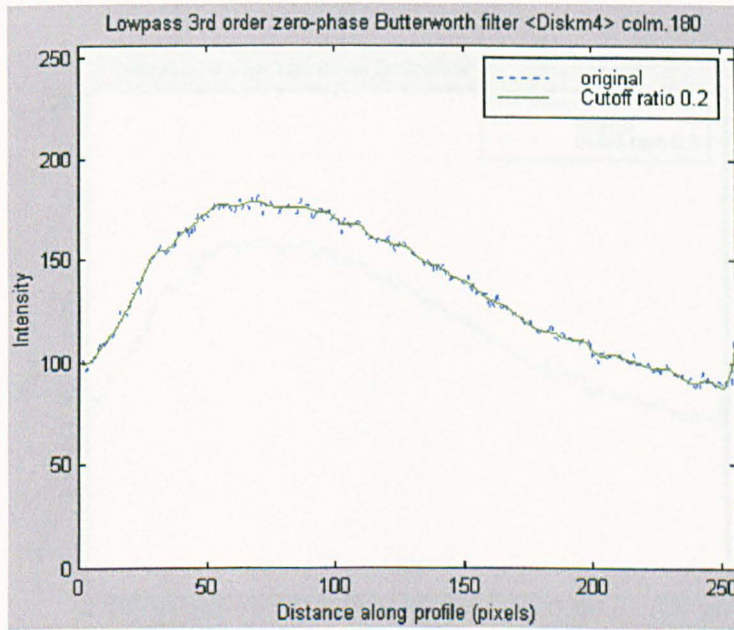


(b)

Figure 5.23 The comparison of the raw and smoothed intensity data. Diskm4, column:180 (continued)

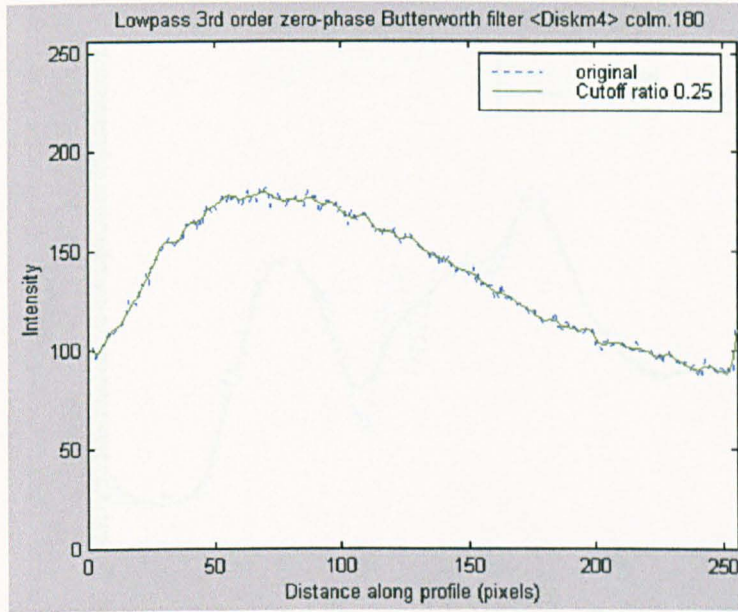


(c)

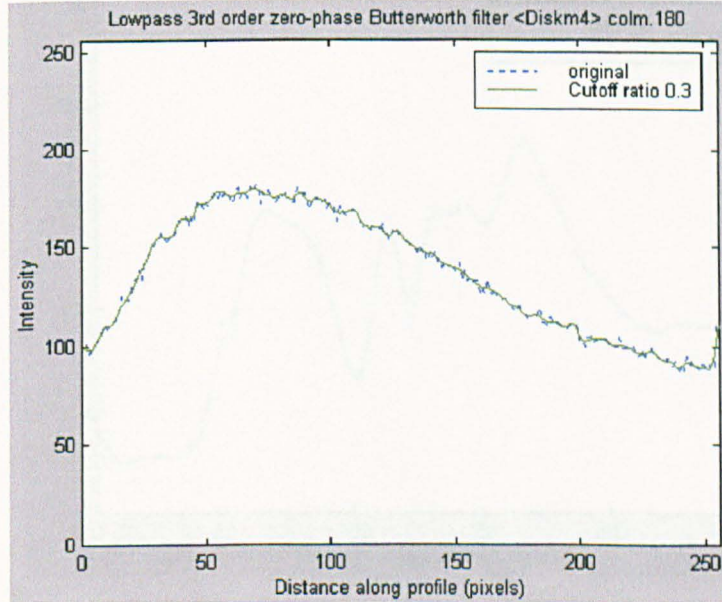


(d)

Figure 5.23 The comparison of the raw and smoothed intensity data. Diskm4, column:180 (continued)

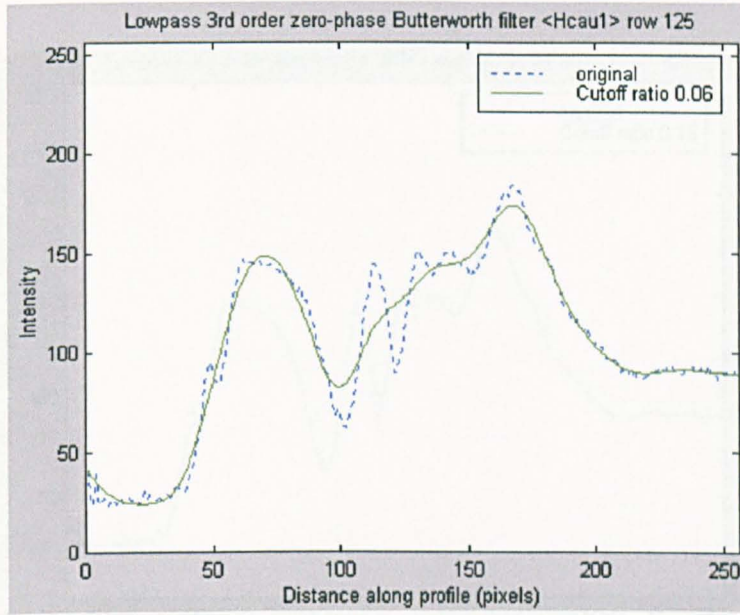


(e)

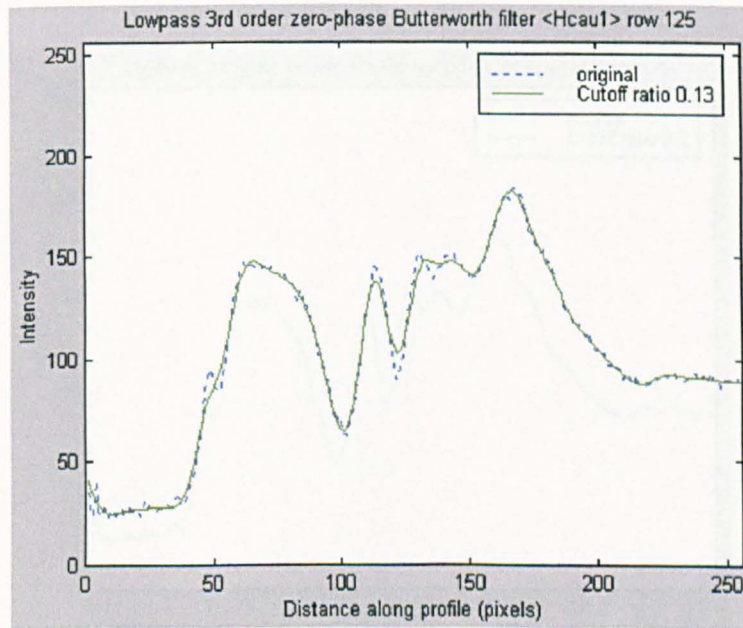


(f)

Figure 5.23 The comparison of the raw and smoothed intensity data. Diskm4, column:180

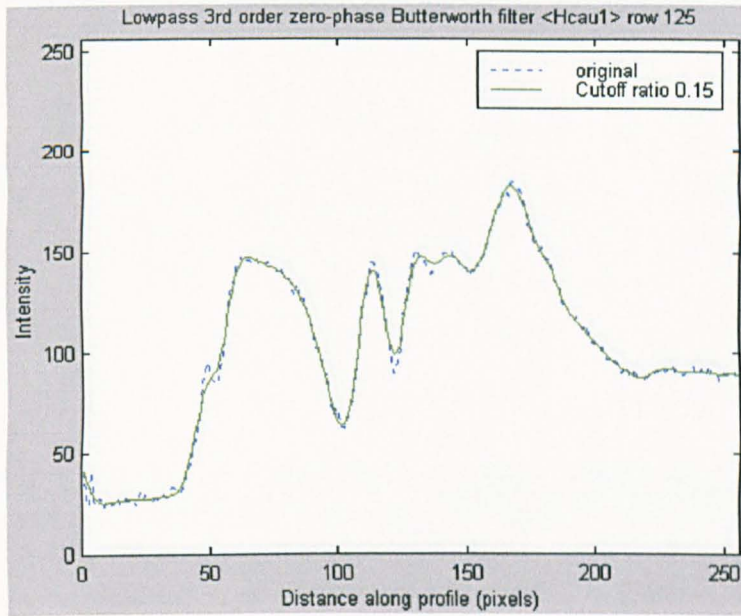


(a)

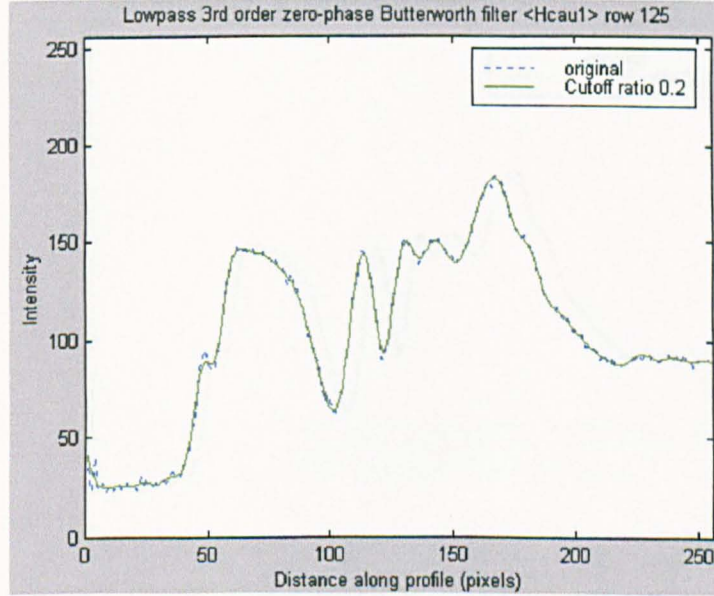


(b)

Figure 5.24 The comparison of the raw and smoothed intensity data.
Hcau1, column: 125 (continued)

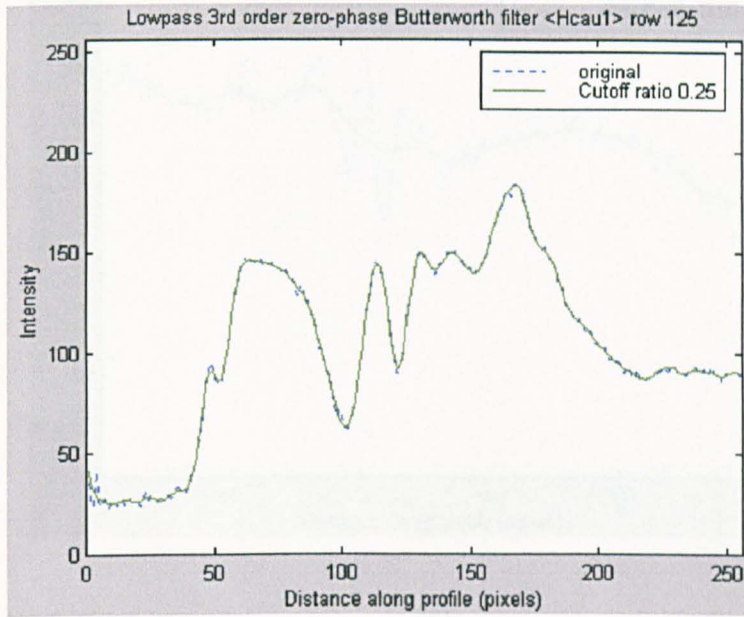


(c)

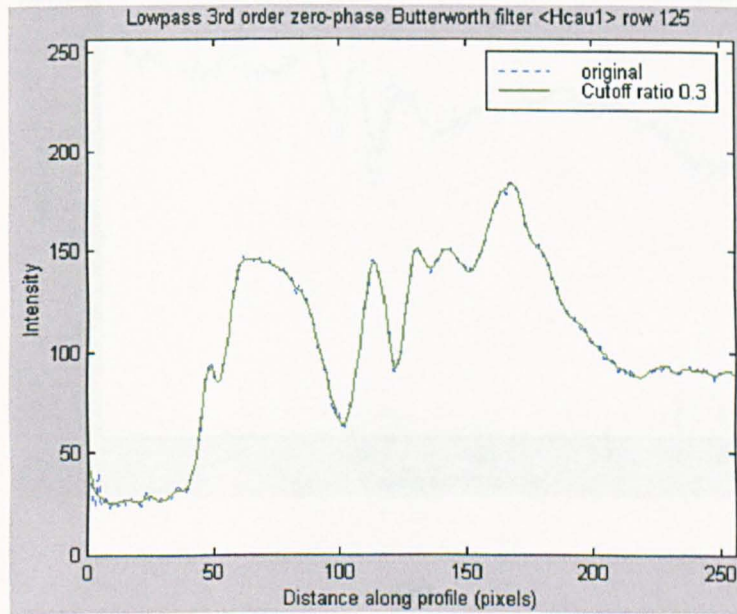


(d)

Figure 5.24 The comparison of the raw and smoothed intensity data.
Hcau1, column: 125 (continued)

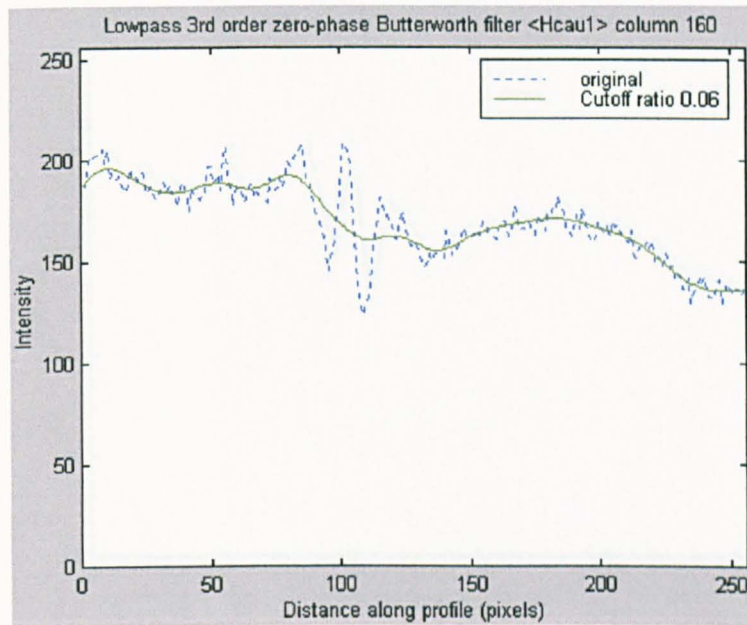


(e)

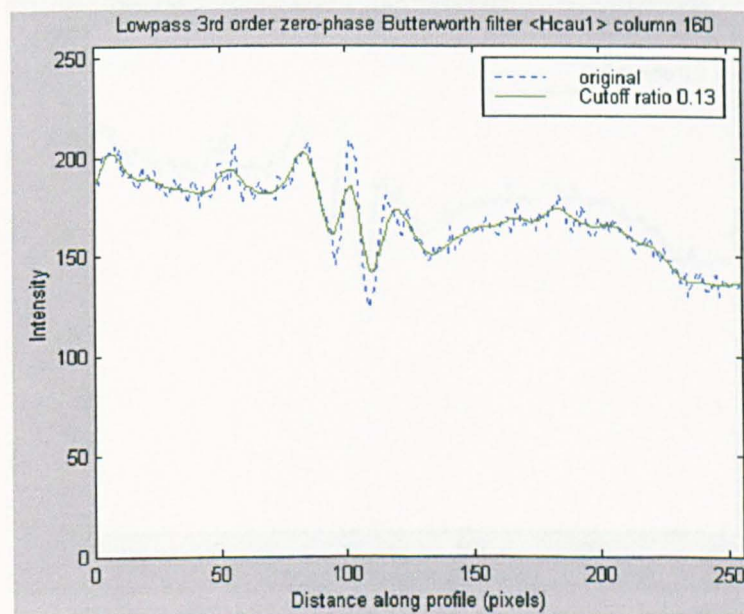


(f)

Figure 5.24 The comparison of the raw and smoothed intensity data. Hcau1, row: 125

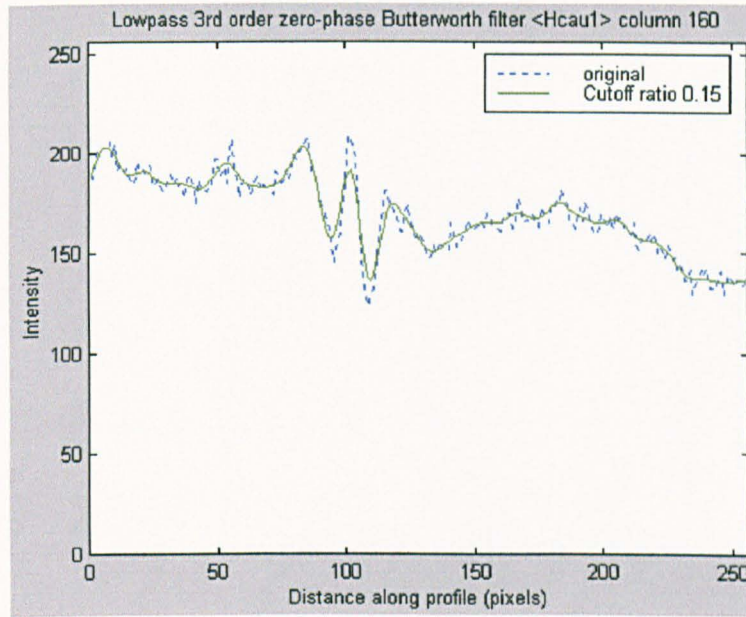


(a)

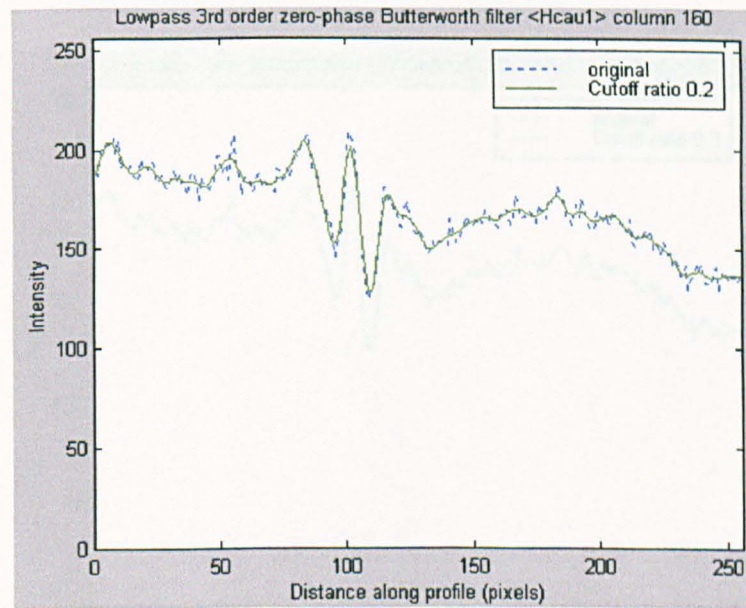


(b)

Figure 5.25 The comparison of the raw and smoothed intensity data. Hcau1, column: 125 (continued)

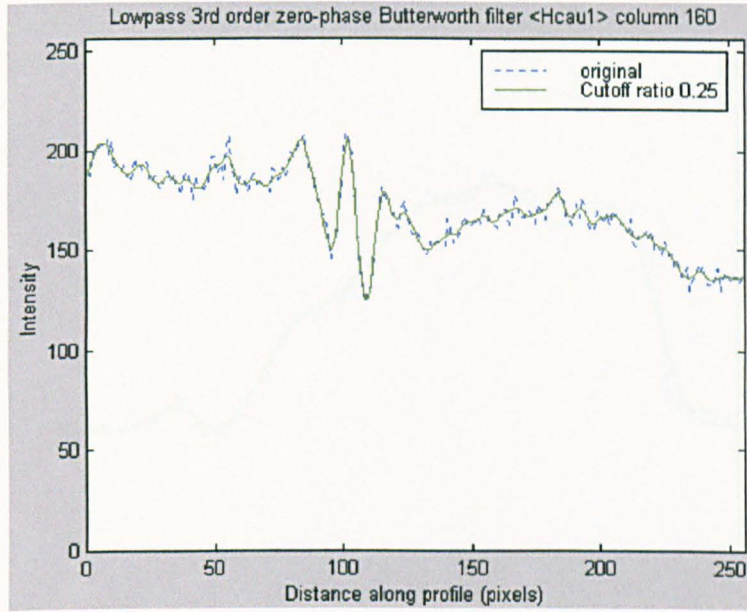


(c)

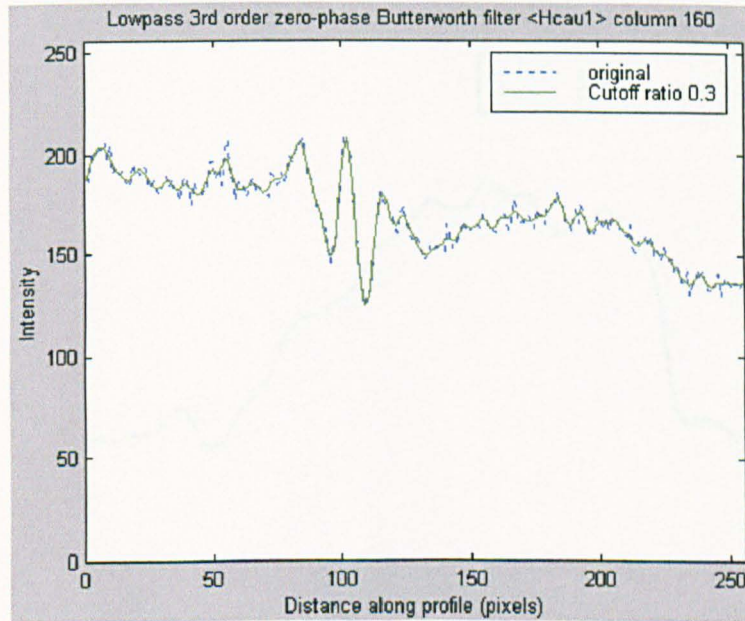


(d)

Figure 5.25 The comparison of the raw and smoothed intensity data.
Hcau1, column: 125 (continued)

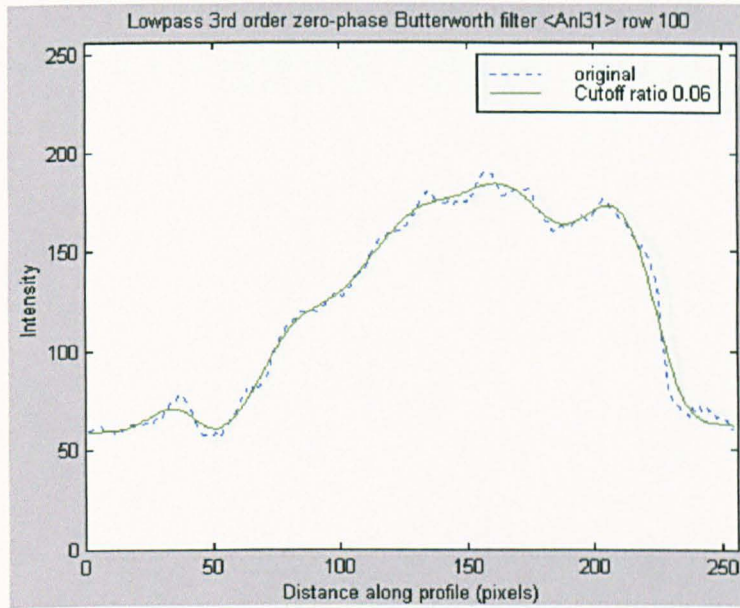


(e)

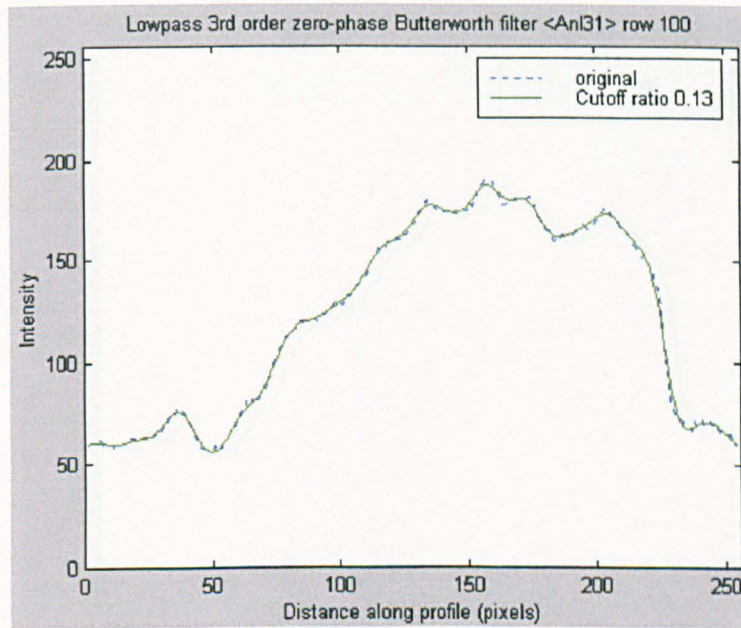


(f)

Figure 5.25 The comparison of the raw and smoothed intensity data. Hcau1, column: 125

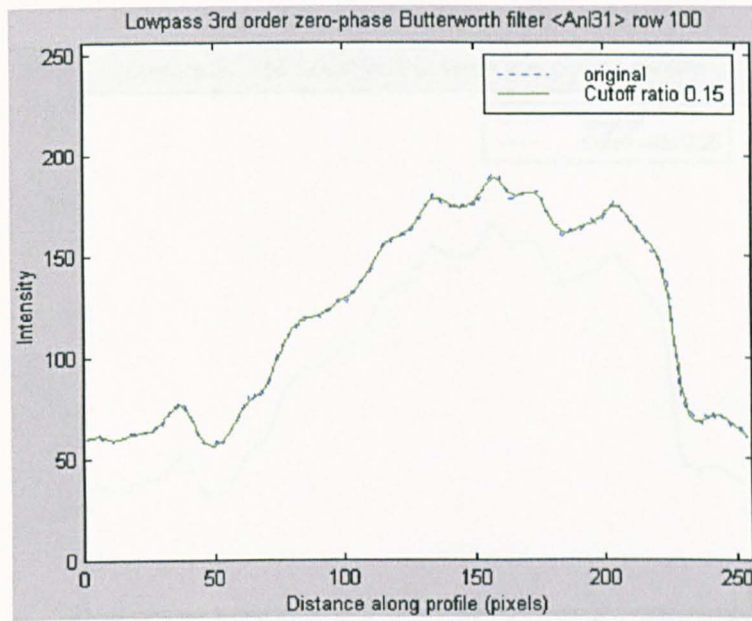


(a)

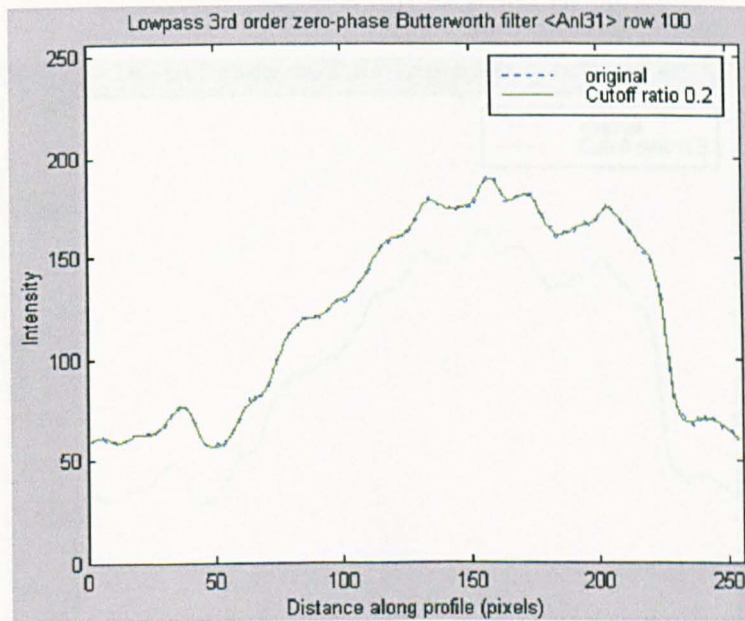


(b)

Figure 5.26 The comparison of the raw and smoothed intensity data. AnI31 row: 100
(continued)

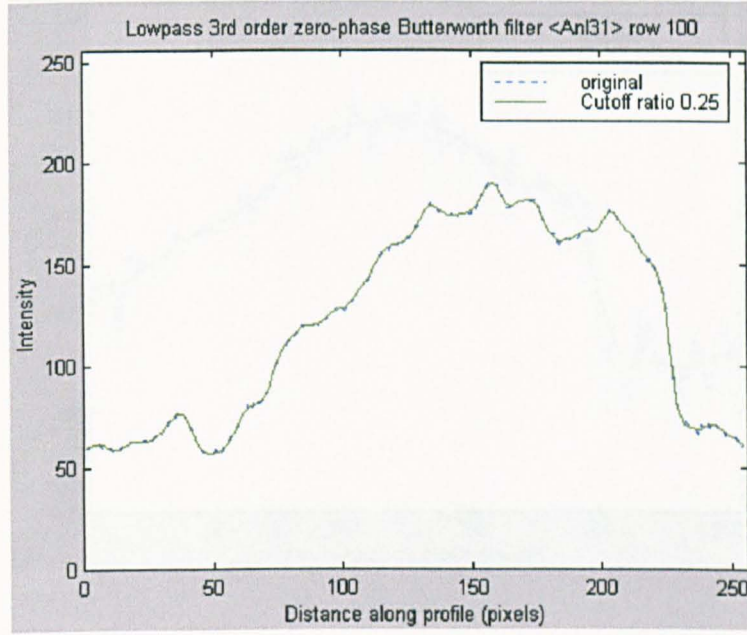


(c)

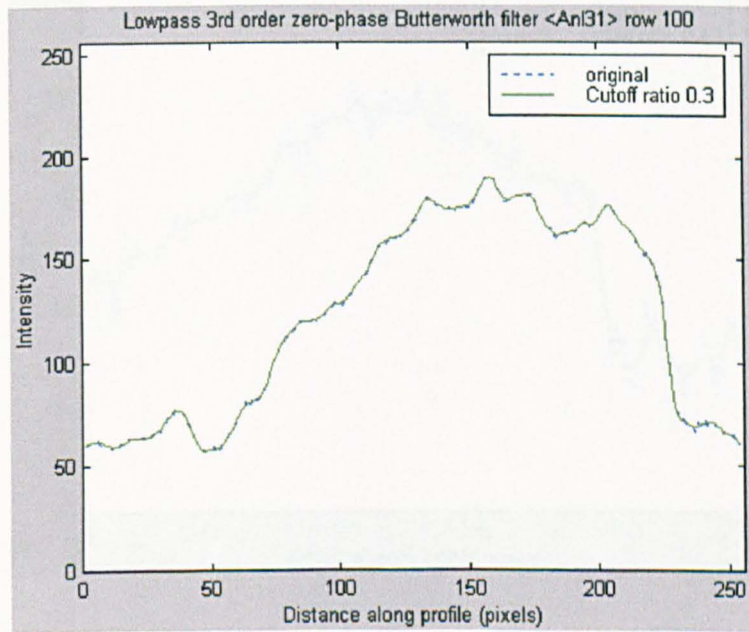


(d)

Figure 5.26 The comparison of the raw and smoothed intensity data. AnI31 row: 100
(continued)

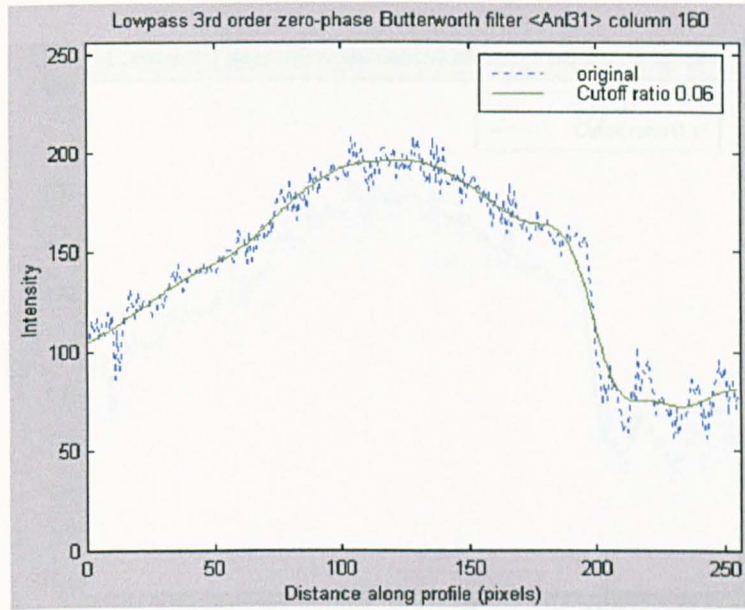


(e)

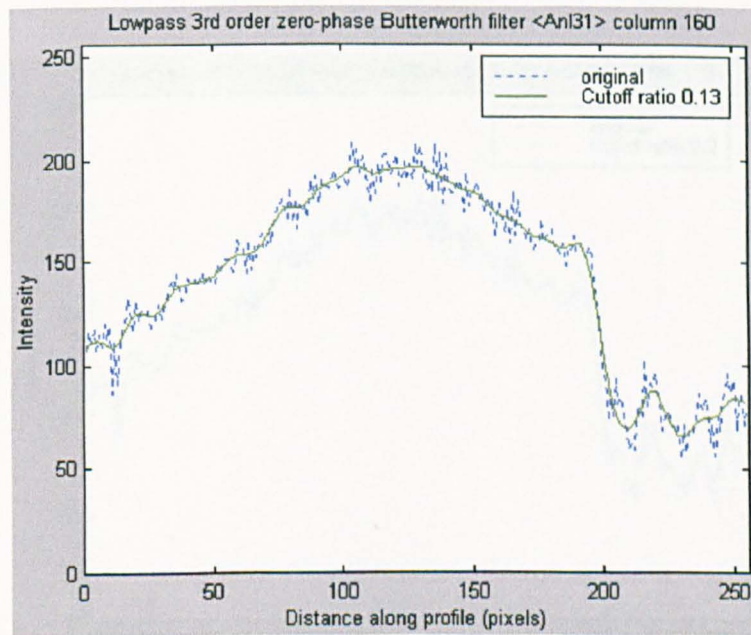


(f)

Figure 5.26 The comparison of the raw and smoothed intensity data. AnI31 row: 100

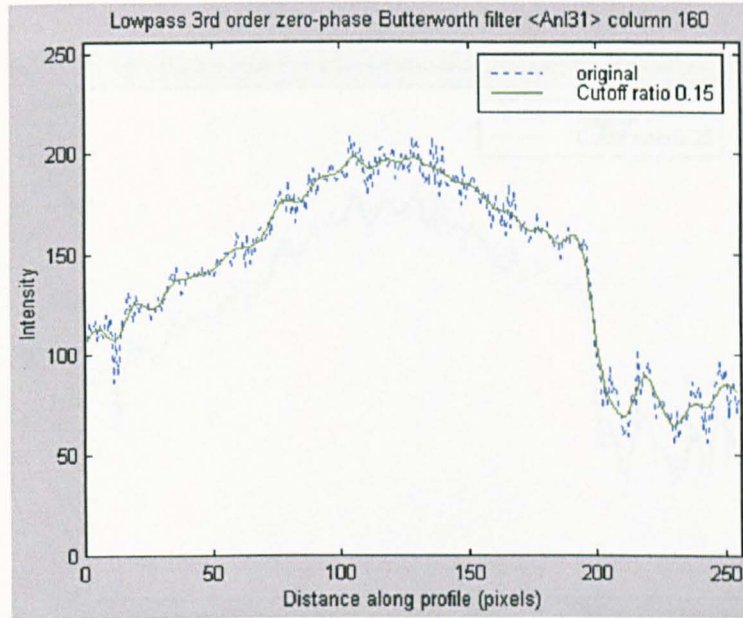


(a)

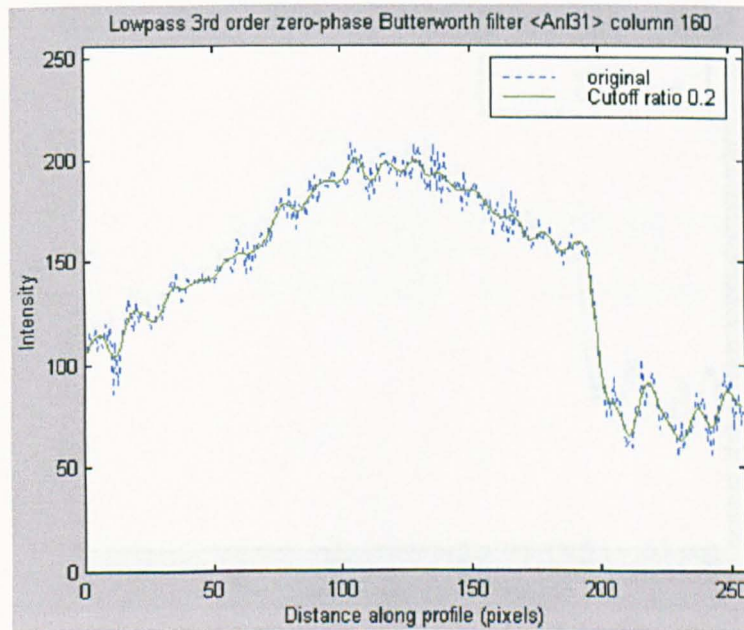


(b)

Figure 5.27 The comparison of the raw and smoothed intensity data. AnI31, column:160 (continued)

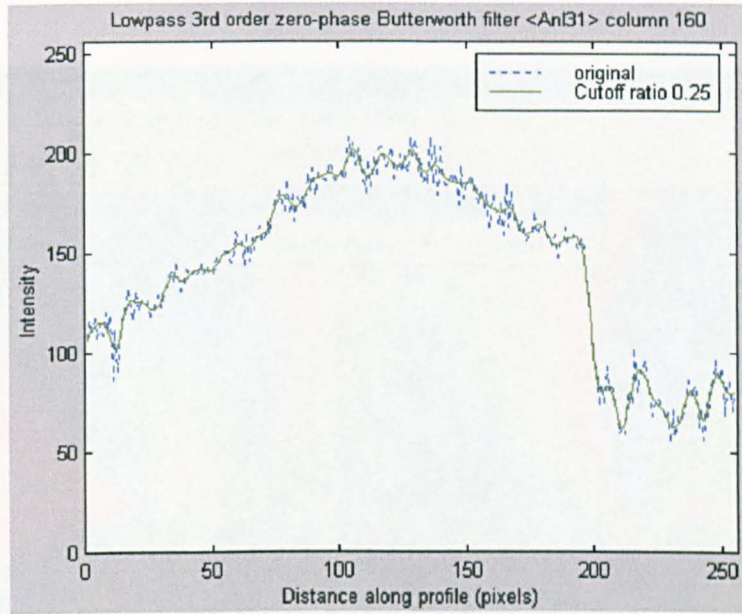


(c)

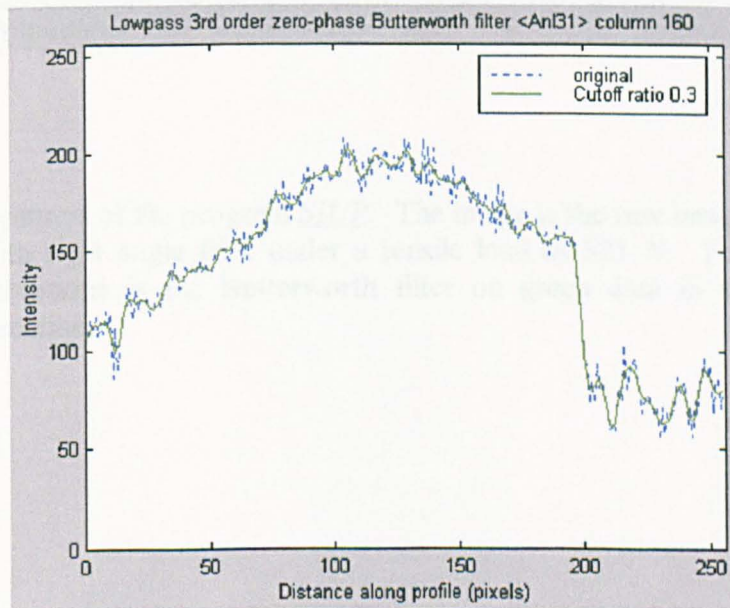


(d)

Figure 5.27 The comparison of the raw and smoothed intensity data. AnI31, column:160 (continued)



(e)



(f)

Figure 5.27 The comparison of the raw and smoothed intensity data. AnI31, column:160

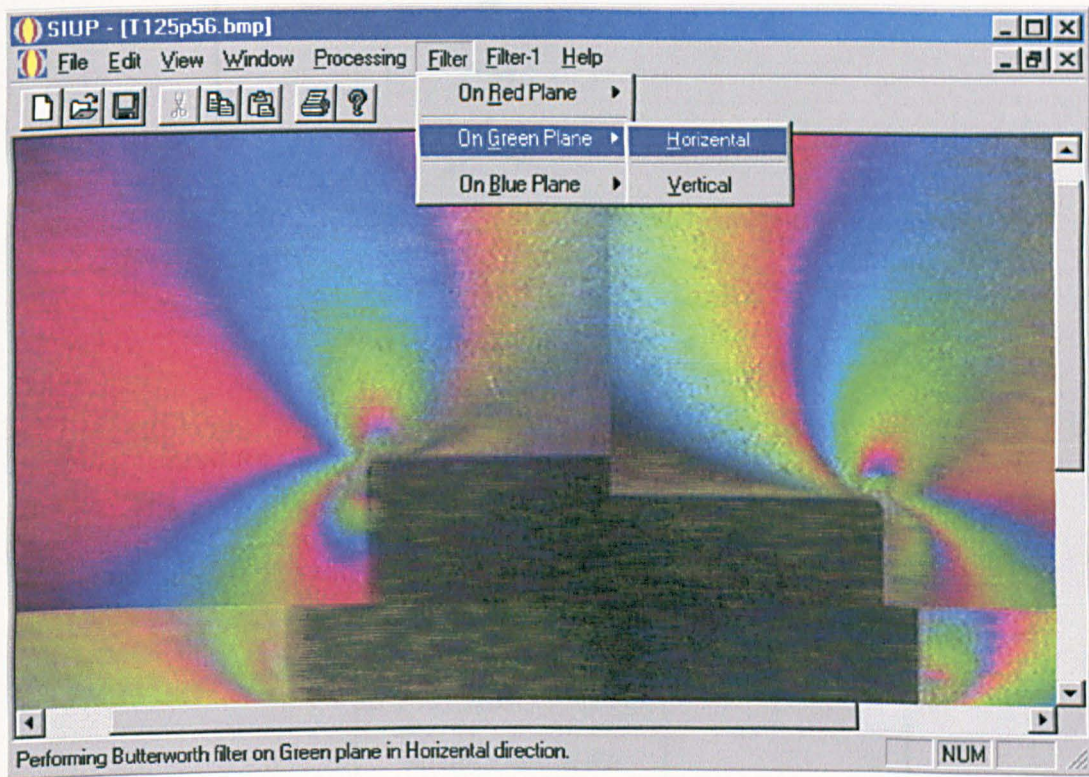


Figure 5.28 Features of the program *SIUP*. The image is the raw image of the plate with right angle fillet under a tensile load of 521 N. The highlighted subroutine is the Butterworth filter on green data in the horizontal direction.

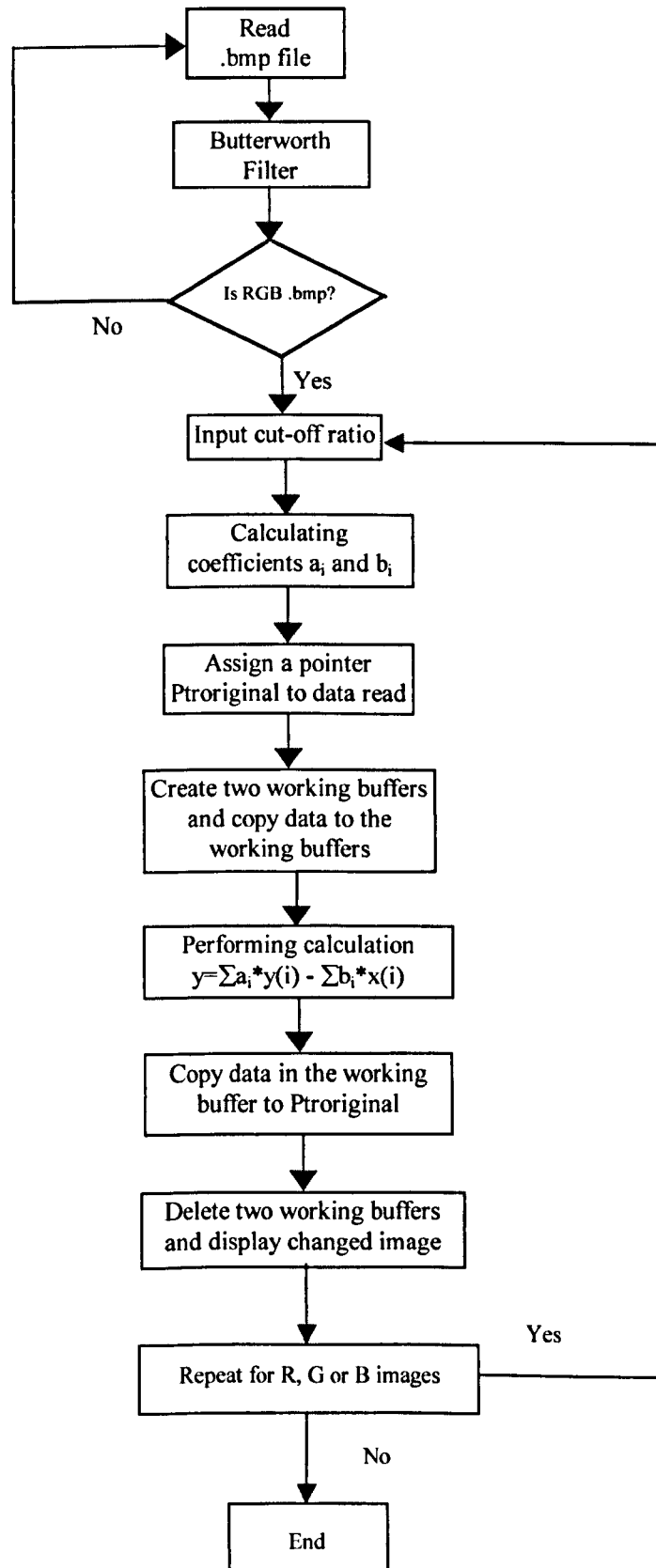


Figure 5.29 Flow chart of the Butterworth filter in the program *SIUP*.

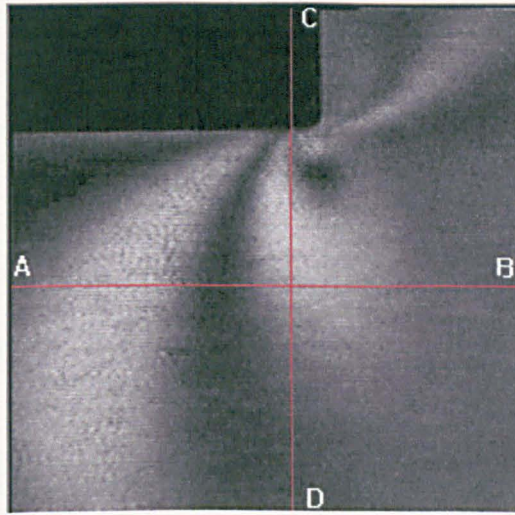


Figure 5.30 Image of a plate with right angle fillet.

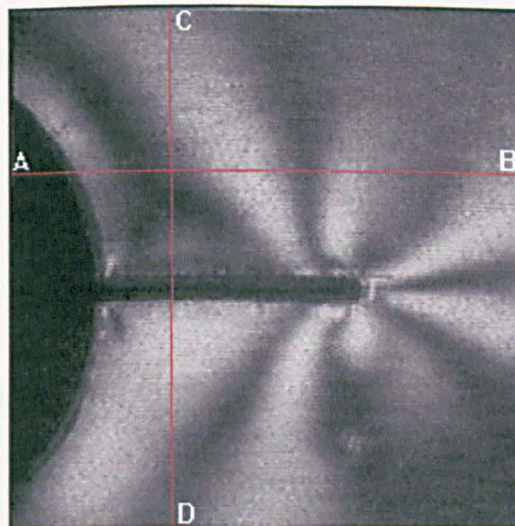


Figure 5.31 Image of a plate with cracks from the central hole.

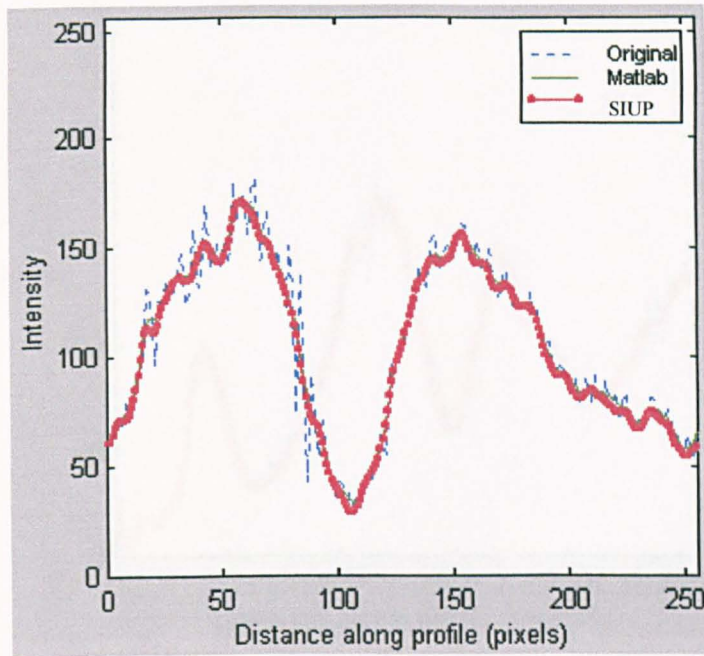


Figure 5.32 The raw and smoothed intensity data in Fig. 5.31 along the line AB.

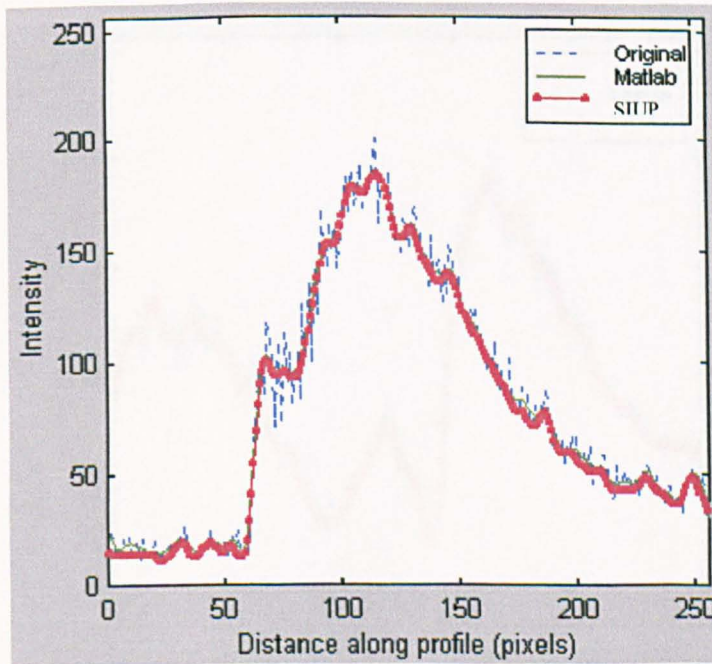


Figure 5.33 The raw and smoothed intensity data in Fig 5.31 along the line CD.

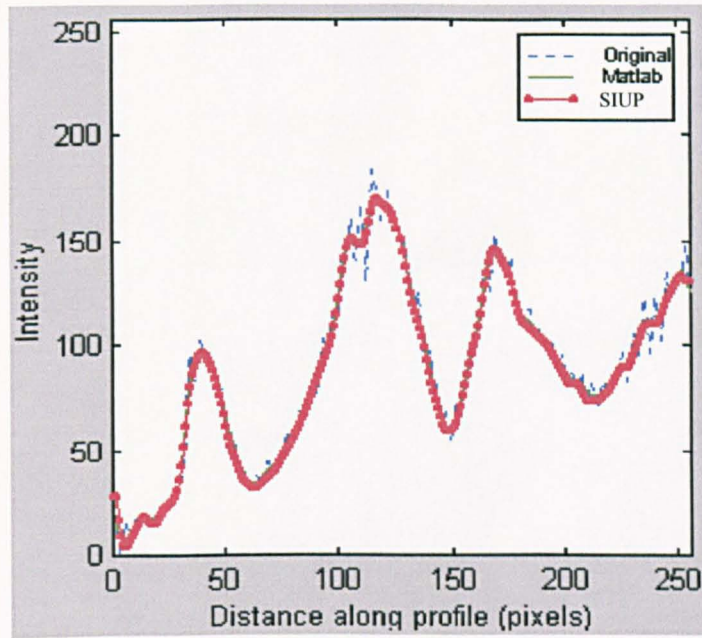


Figure 5.34 The raw and smoothed intensity data in Fig. 5.32 along the line AB.

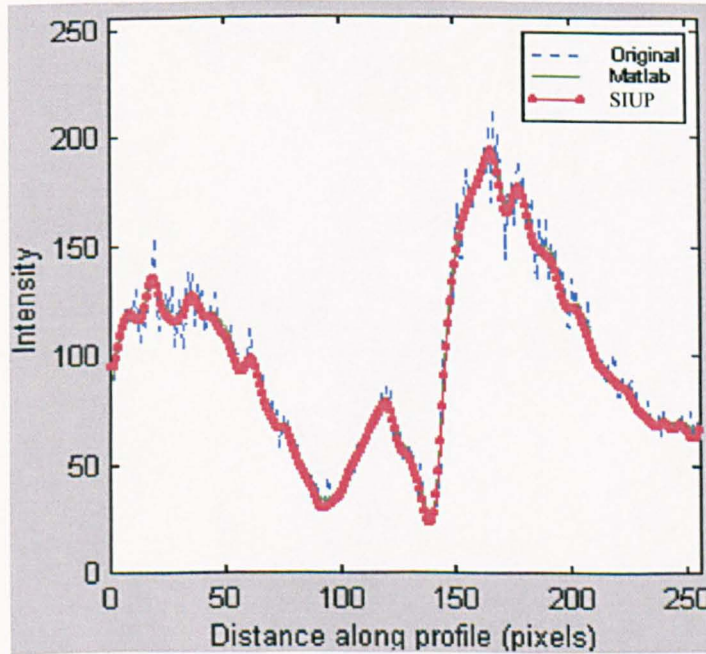


Figure 5.35 The raw and smoothed intensity data in Fig. 5.32 along the line CD.

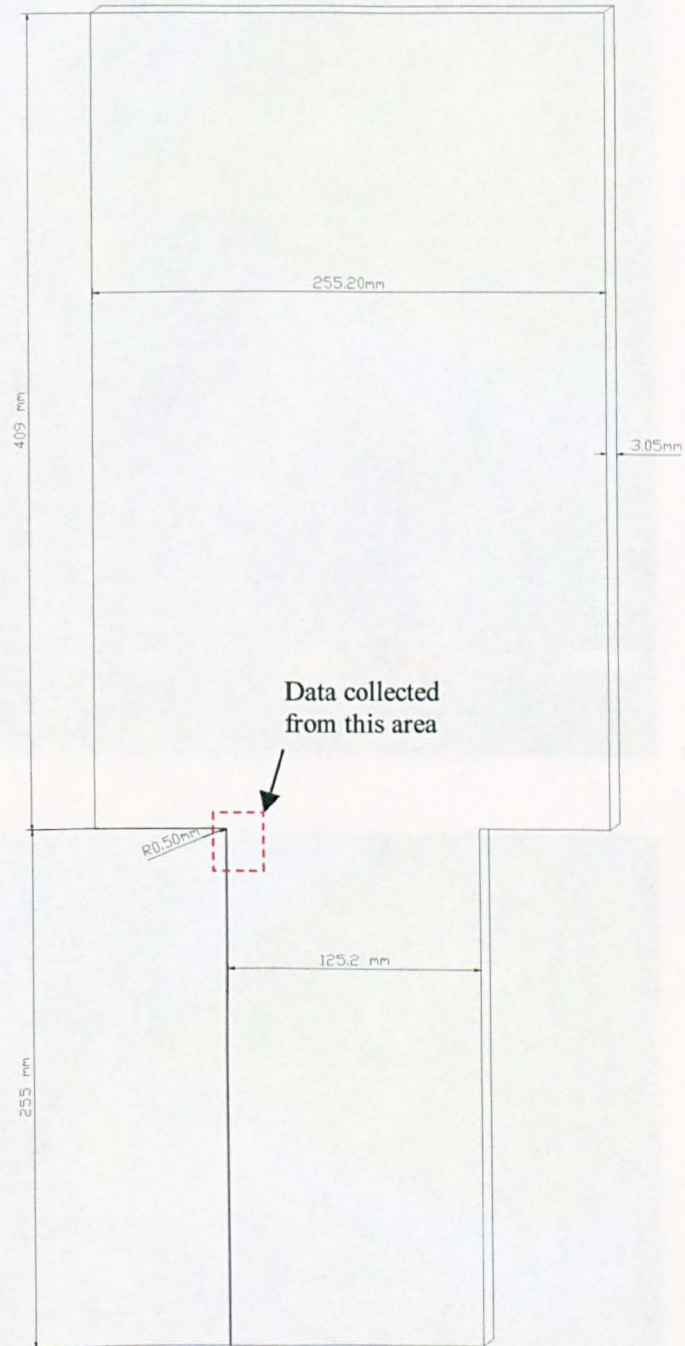


Figure 5.36 Geometry and dimensions of the plate with right-angle fillet.

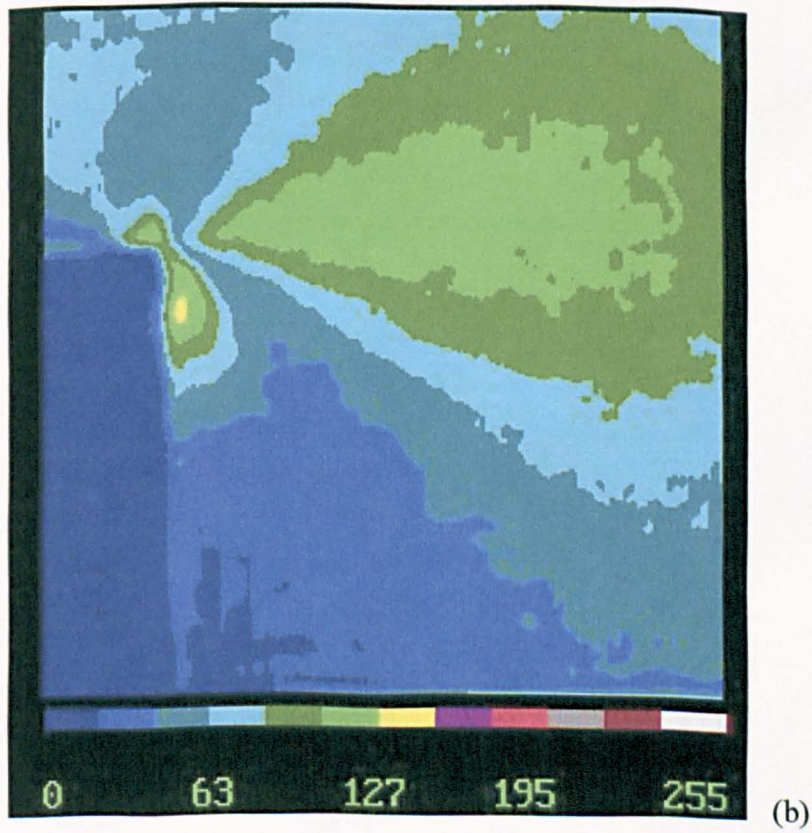
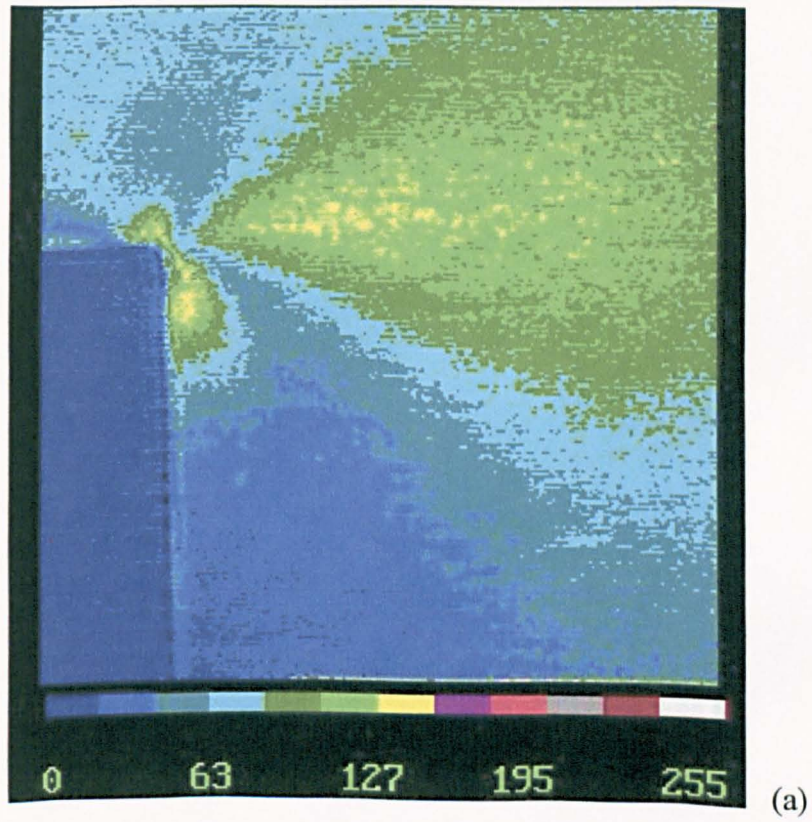


Figure 5.37 First (a) raw image and (b) smoothed image of the four images of the plate with right-angle fillet.

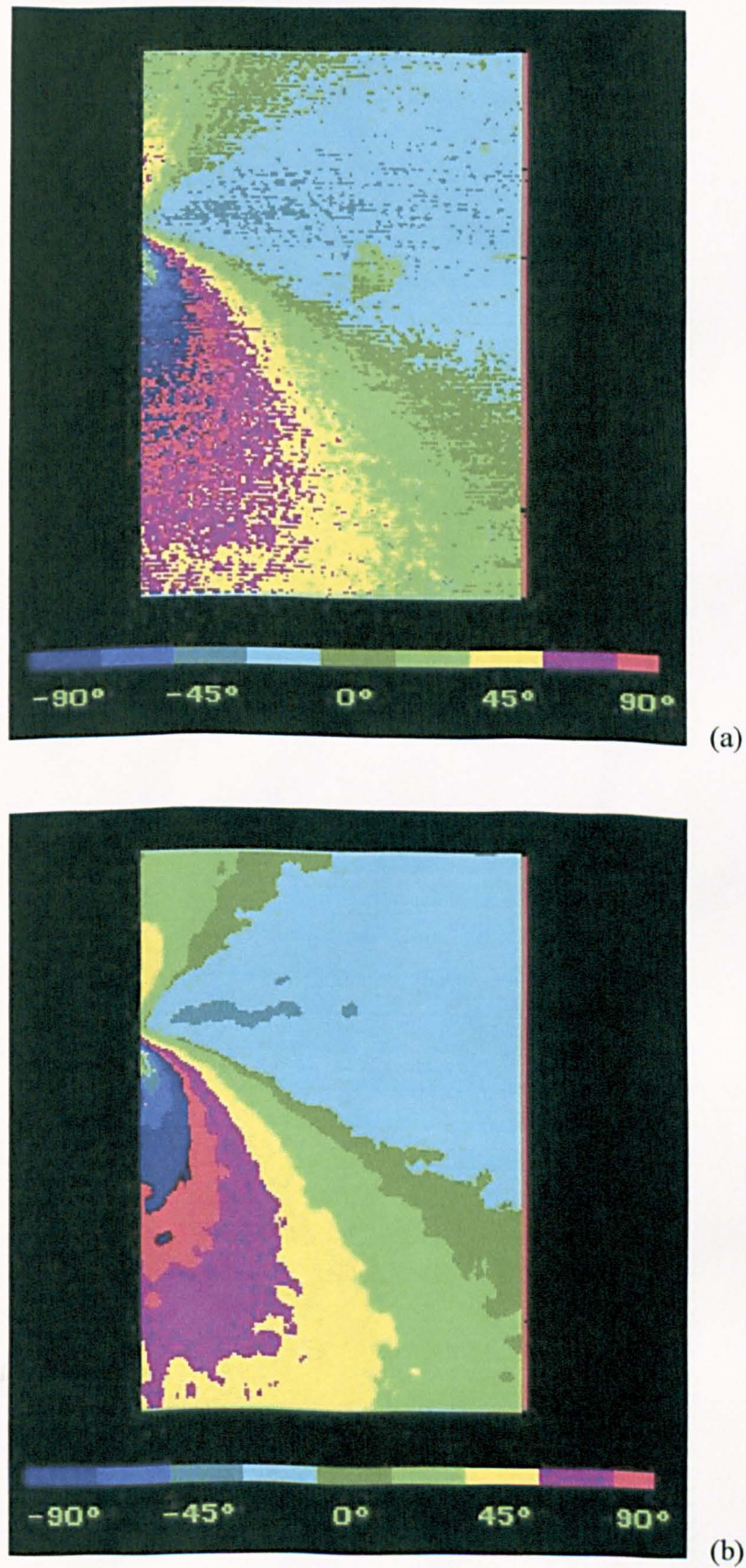


Figure 5.38 The retardation maps from the (a) raw image and (b) smoothed image of the plate.

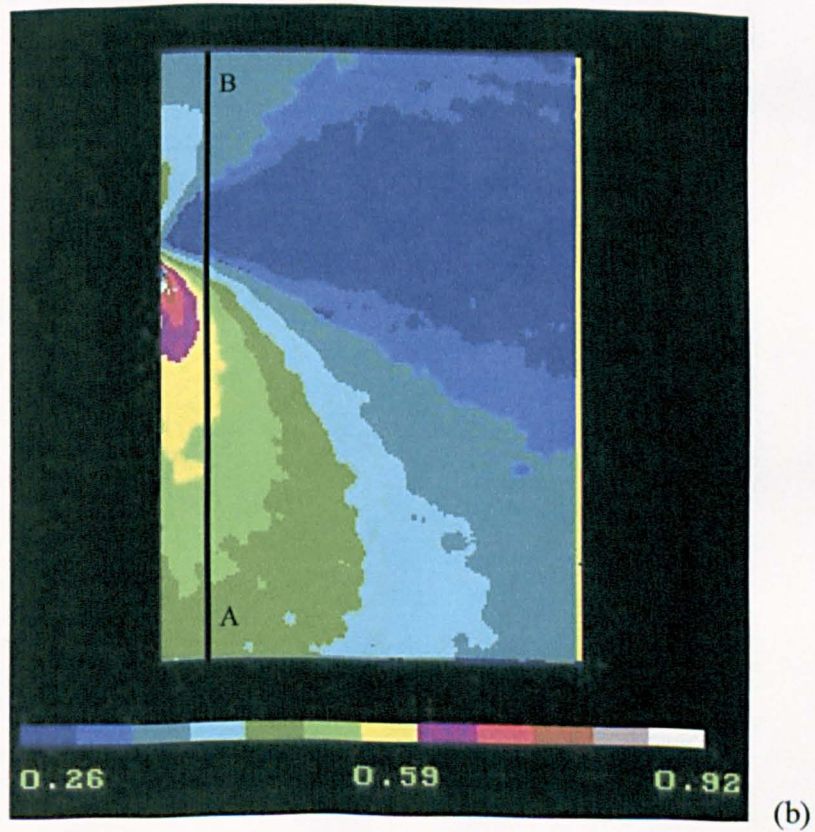
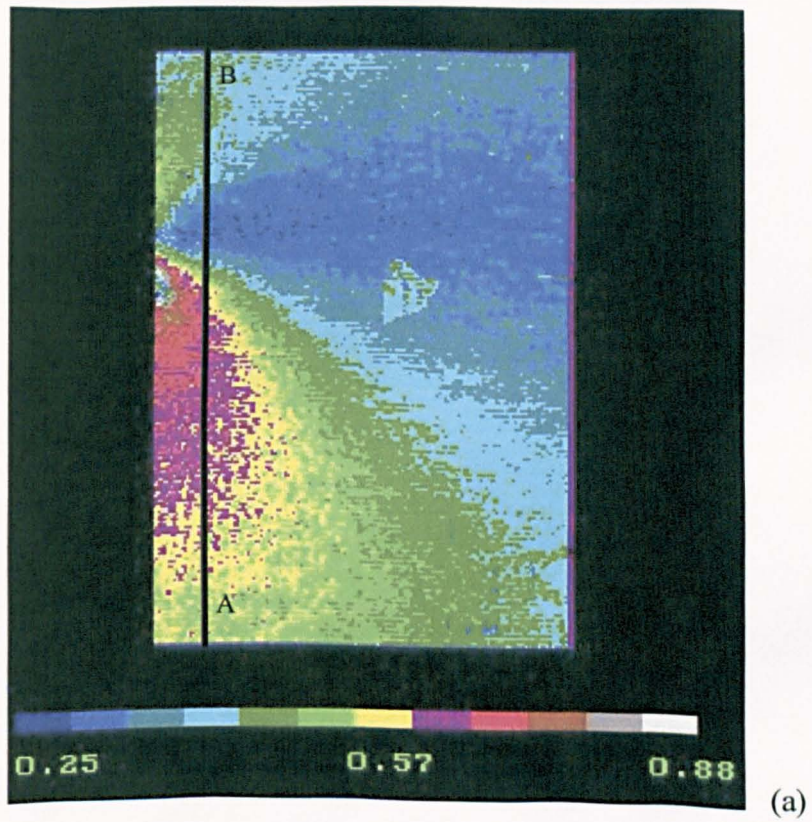


Figure 5.39 The isochromatic maps from the (a) raw image and (b) smoothed image of the plate.

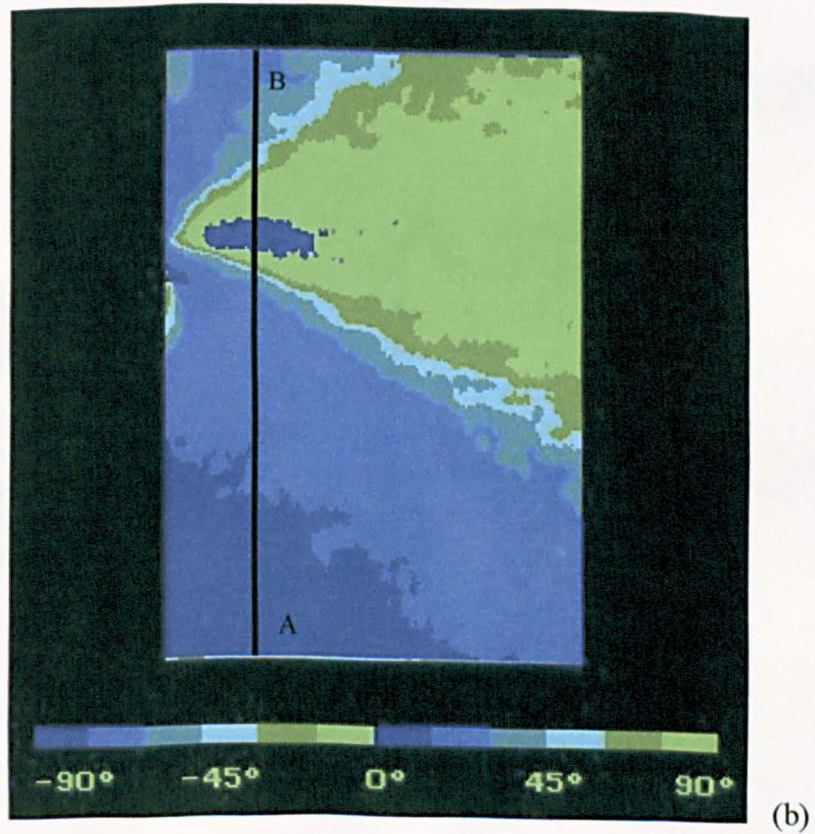
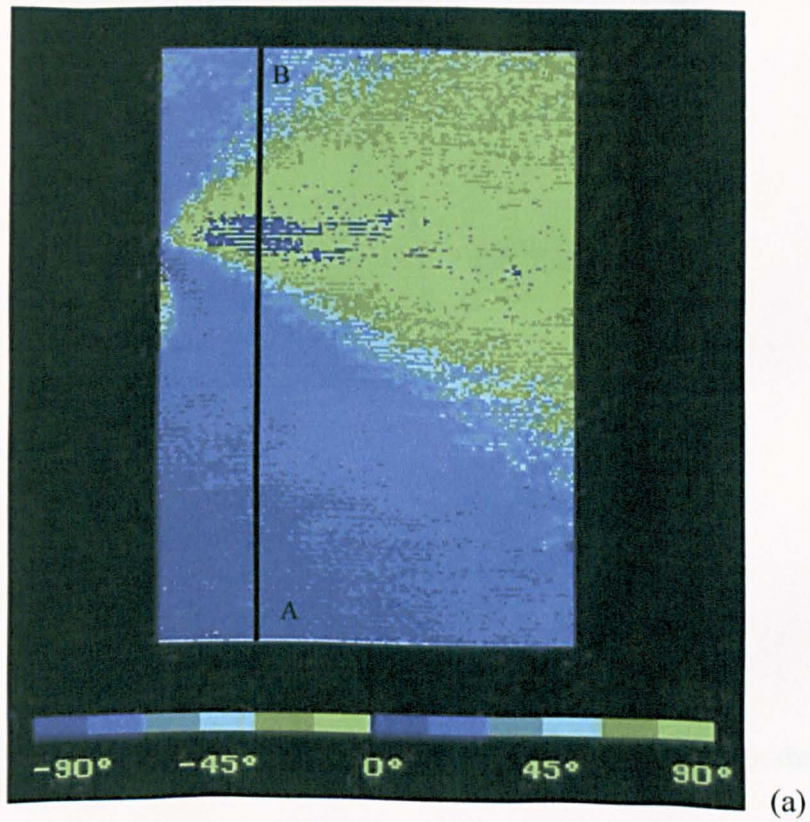


Figure 5.40 The isoclinic maps from the (a) raw image and (b) smoothed image of the plate.

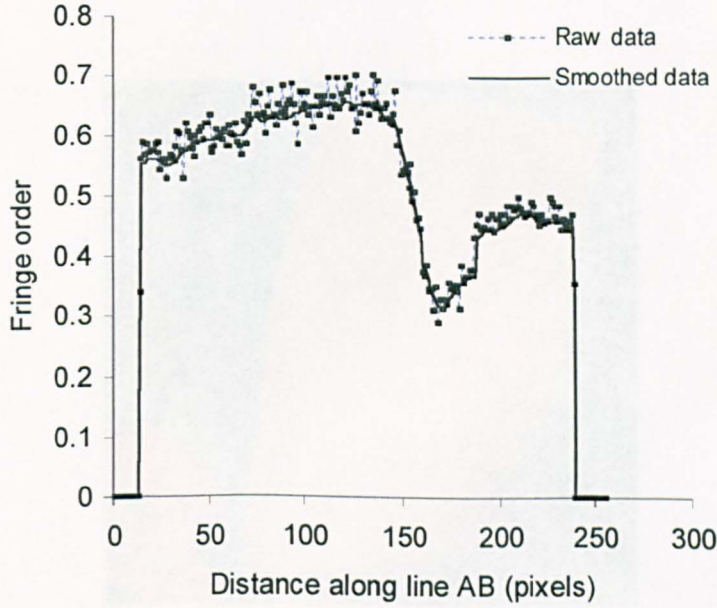


Figure 5.41 The comparison of the fringe orders from raw image and smoothed image of the plate.

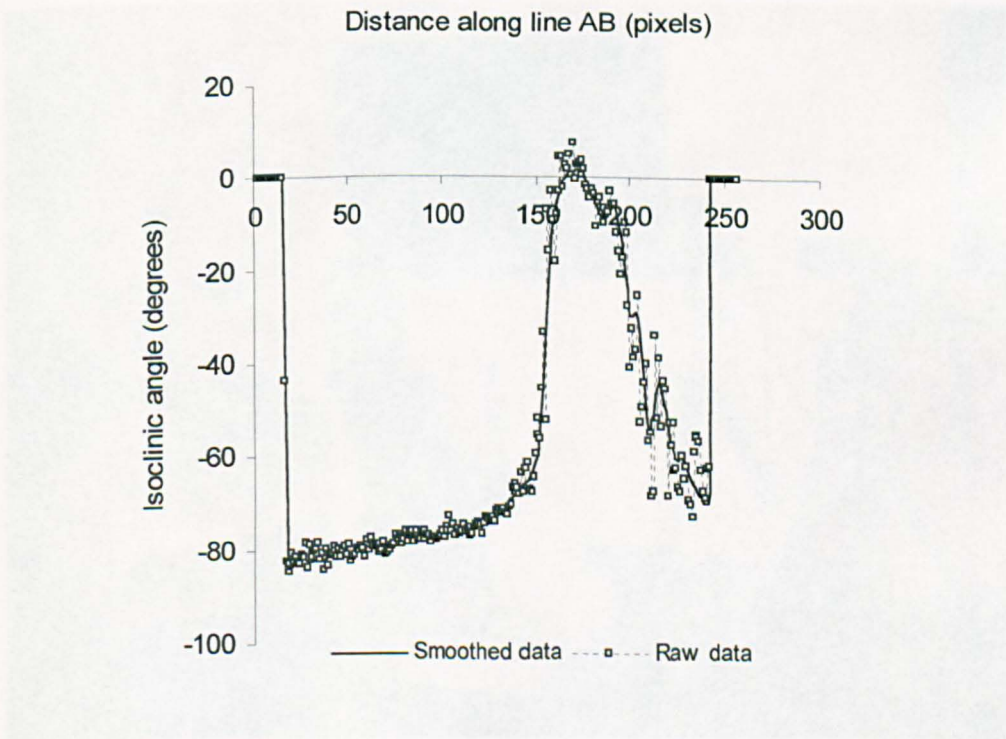


Figure 5.42 The comparison of the isoclinic angles from raw image and smoothed image of the plate.

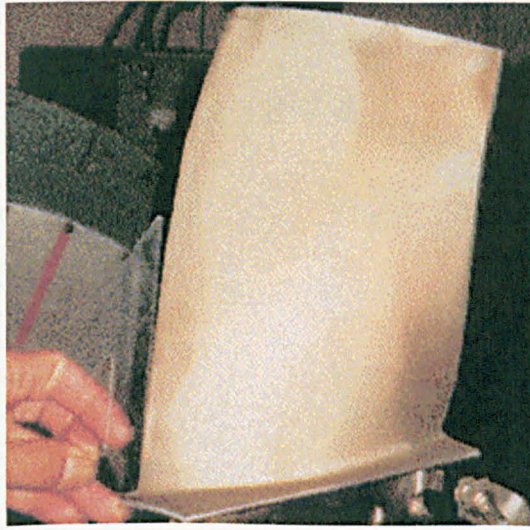


Figure 5.43 The compressor blade.

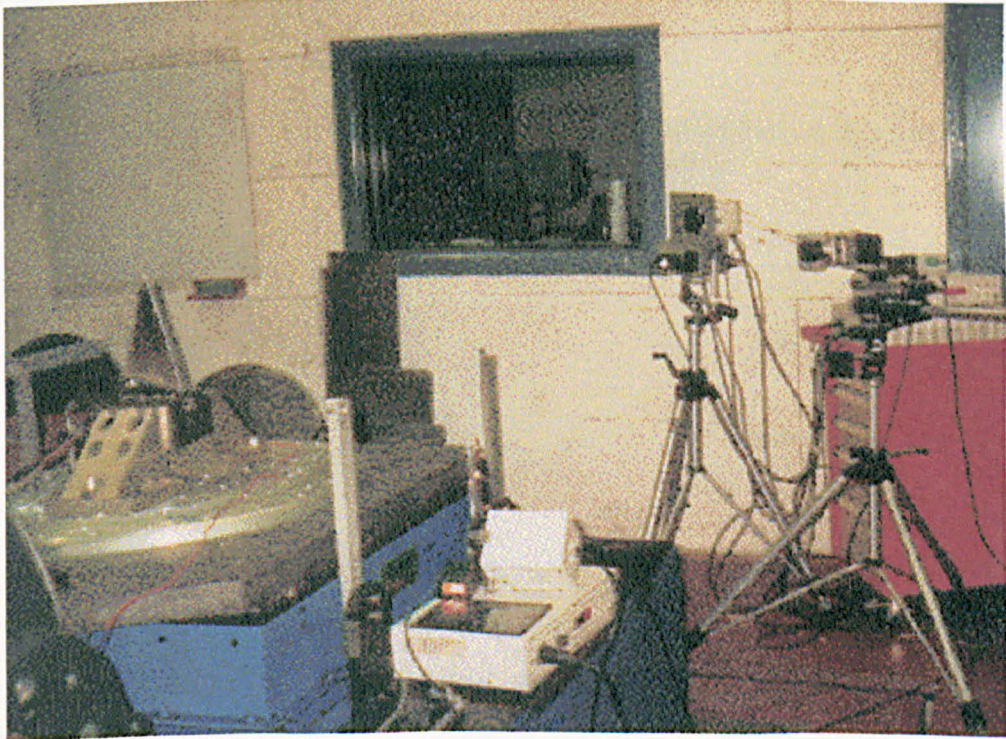


Figure 5.44 Experimental set-up.

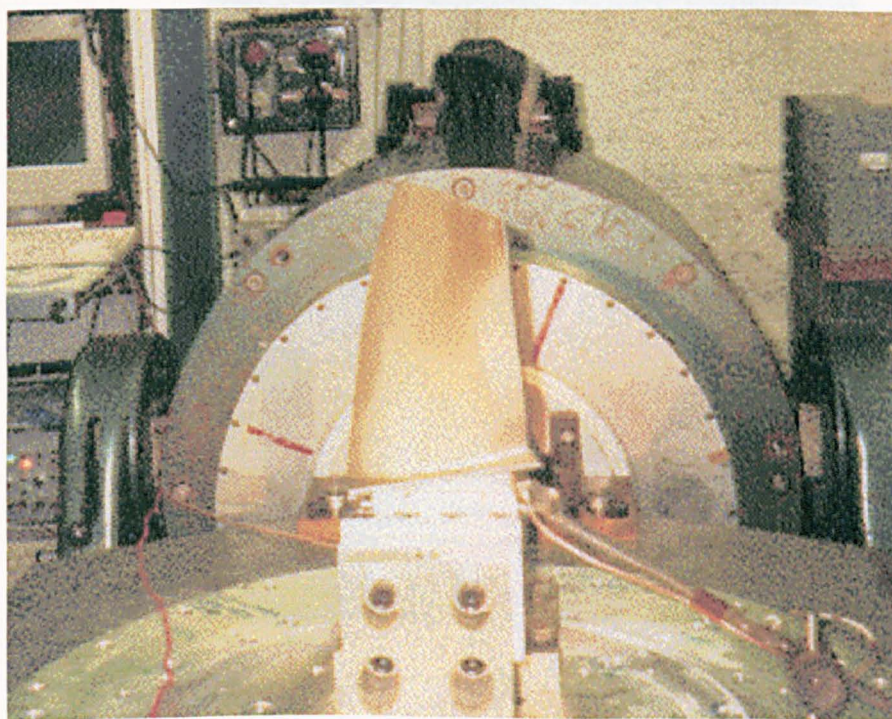


Figure 5.45 Set-up of the compressor blade.

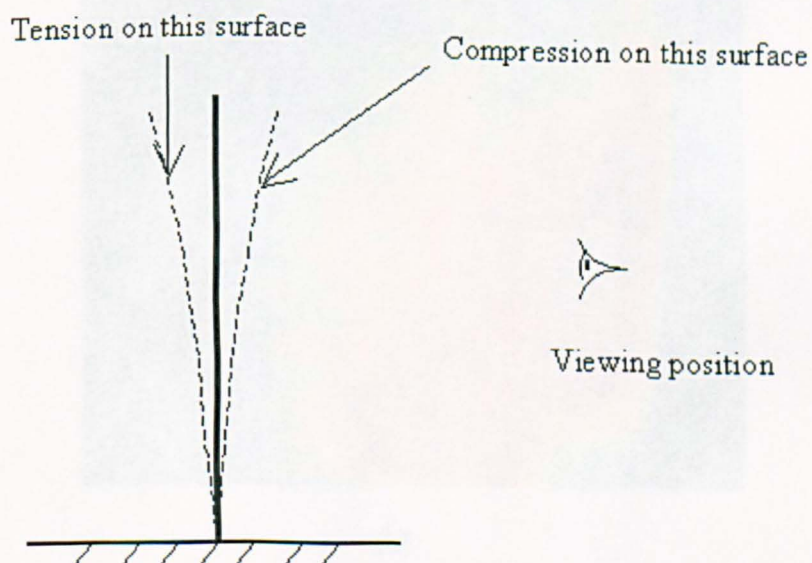
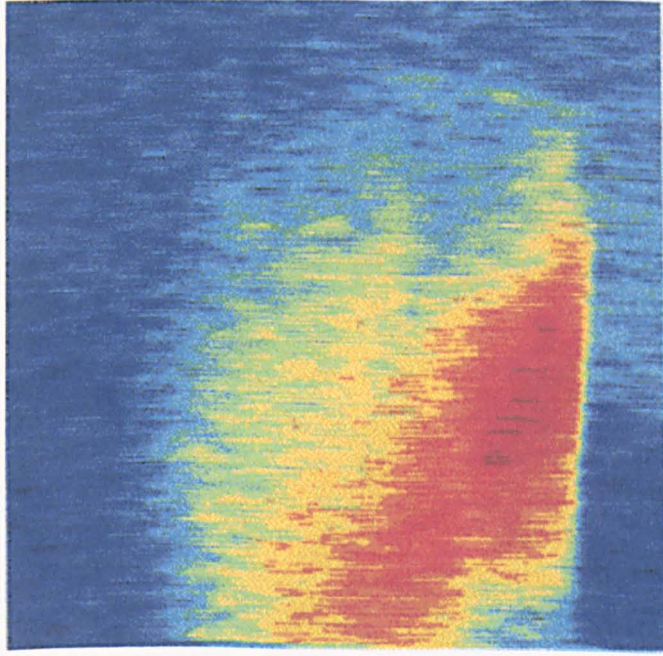
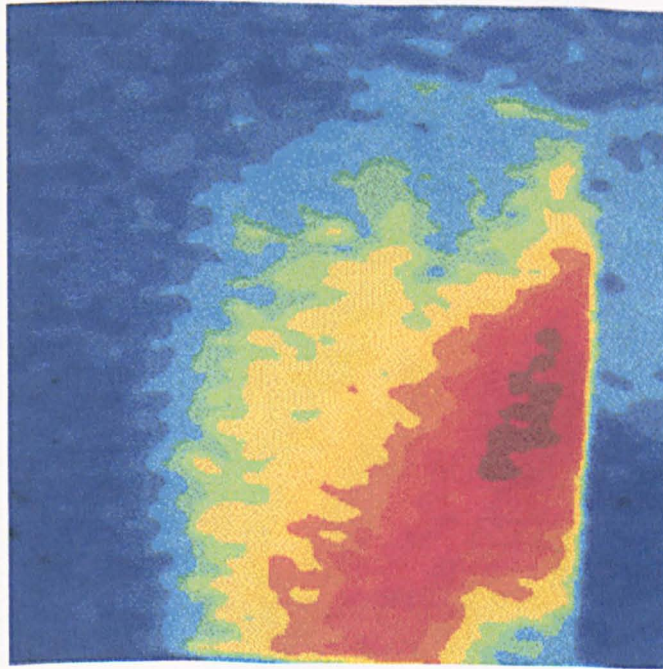


Figure 5.46 Schematic diagram of the compressor blade in tension and compression.

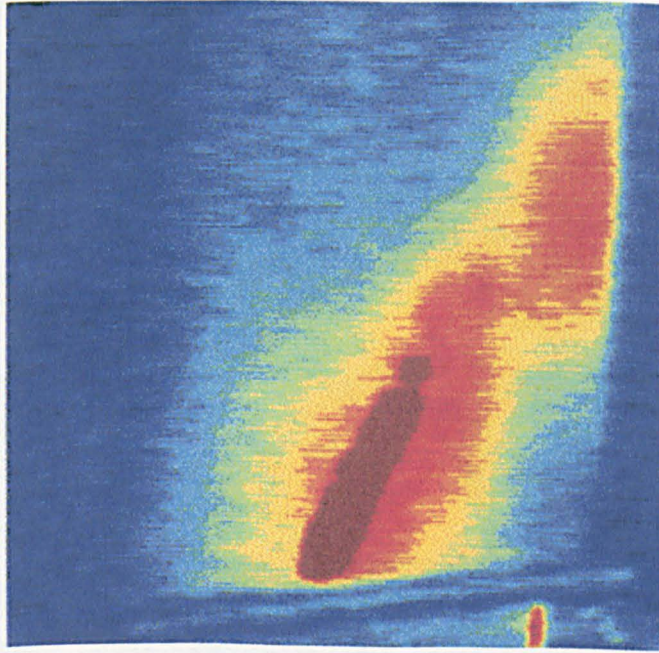


(a)

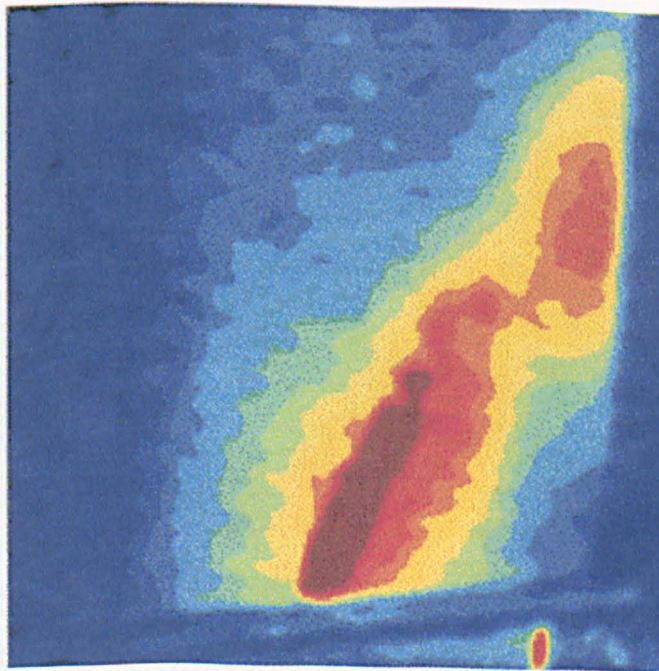


(b)

Figure 5.47 (a) Raw and (b) smoothed intensity data for first of the four images using the Butterworth filter. The cut-off ratio is 0.2. The compressor blade (upper part) is in tension at the first mode of vibration, frequency 257 Hz and energy level 1 g.



(a)



(b)

Figure 5.48 (a) Raw and (b) smoothed intensity data for first of the four images using the Butterworth filter. The cut-off ratio is 0.2. The compressor blade (lower part) is in tension at the first mode of vibration, frequency 257 Hz and energy level 1 g.

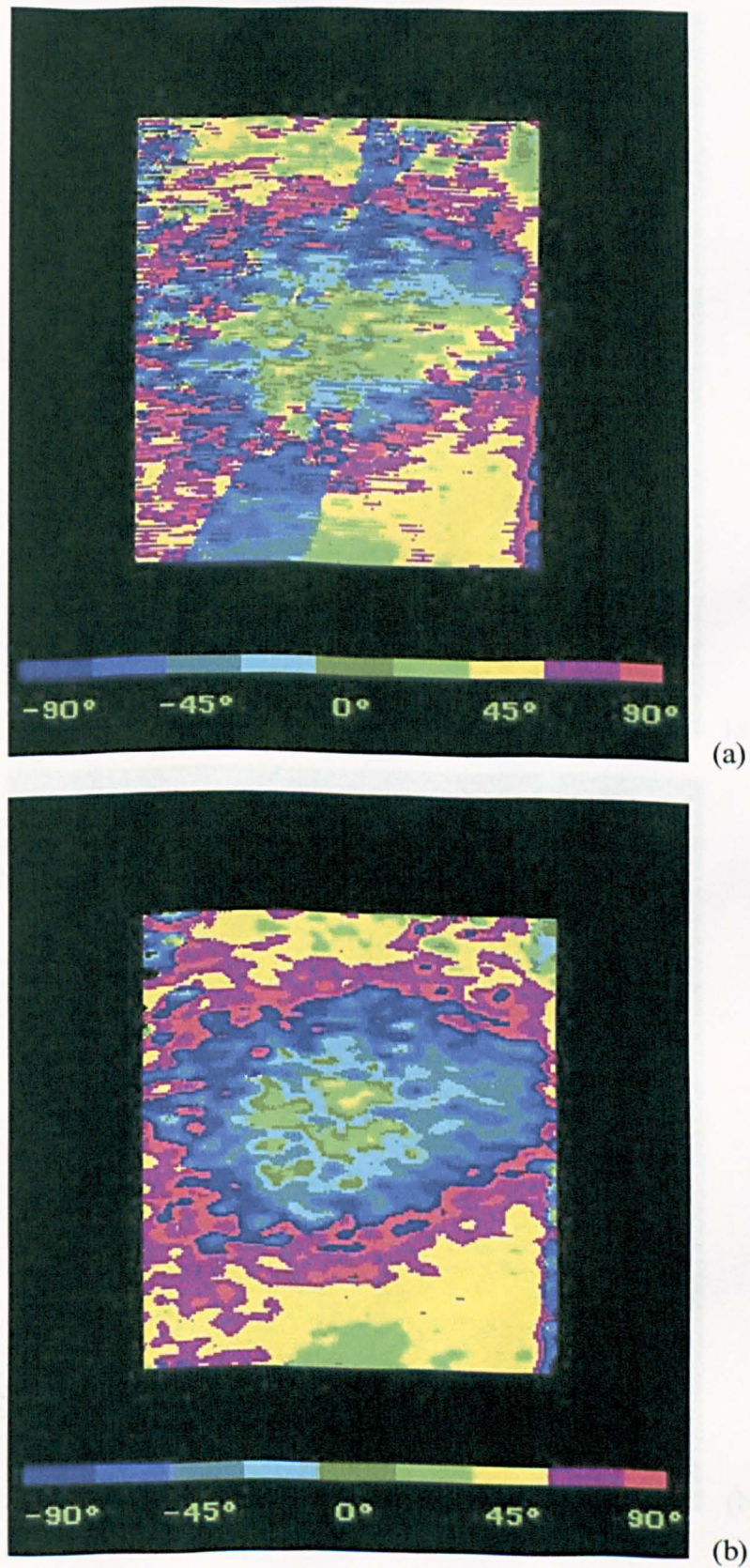


Figure 5.49 The comparison of the retardation maps, from (a) raw (b) smoothed intensity data. (Upper part of the compression blade in tension, mode 2, frequency 617 Hz and energy level 5.01 g)

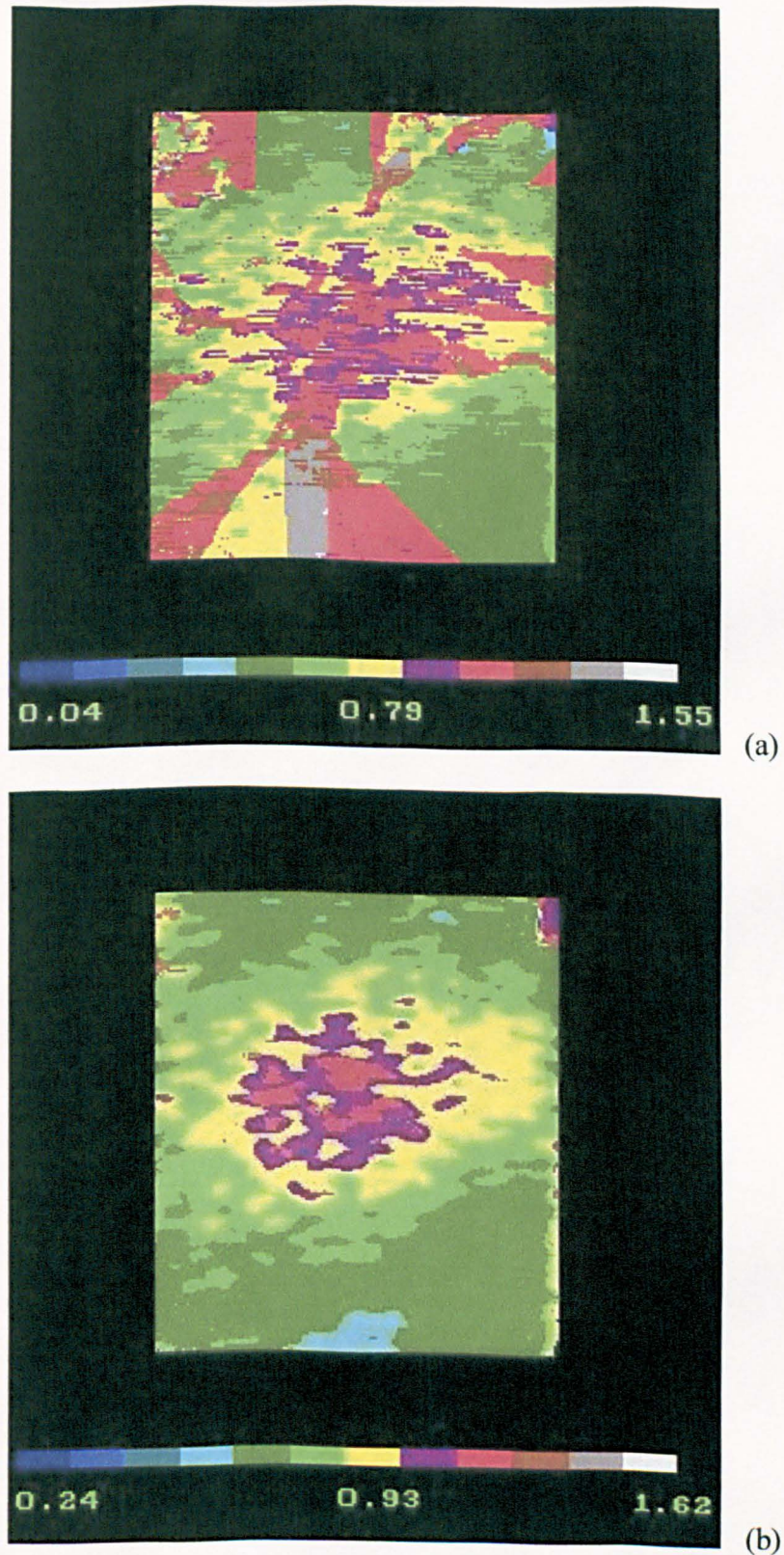


Figure 5.50 The comparison of the fringe order maps from (1) raw (2) smoothed intensity data. (Upper part of the compression blade in tension, mode 2, frequency 617 Hz and energy level 5.01 g)

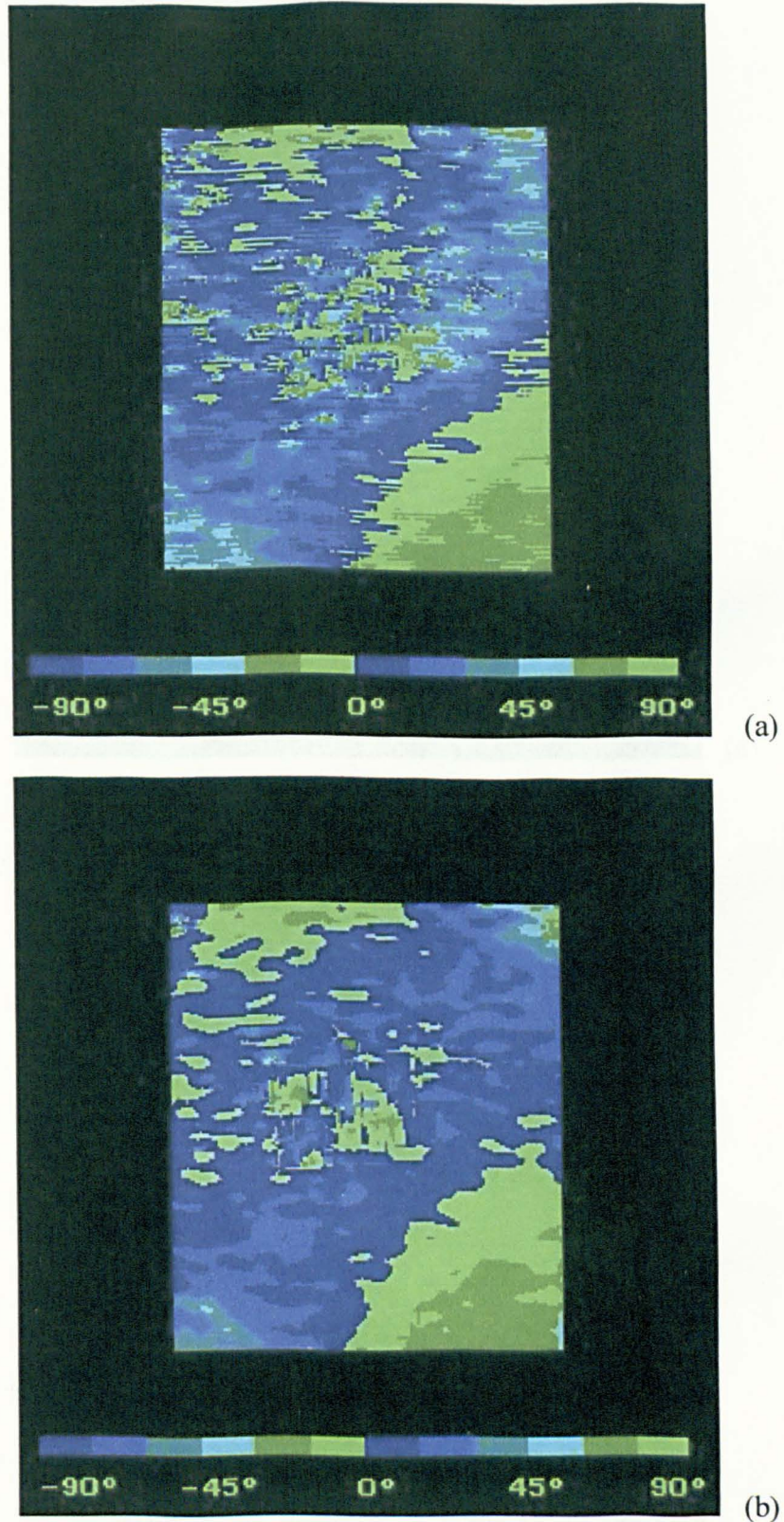


Figure 5.51 The comparison of the isoclinic maps from (a) raw (b) smoothed intensity data. (Upper part of the compression blade in tension, mode 2, frequency 617 Hz and energy level 5.01 g)

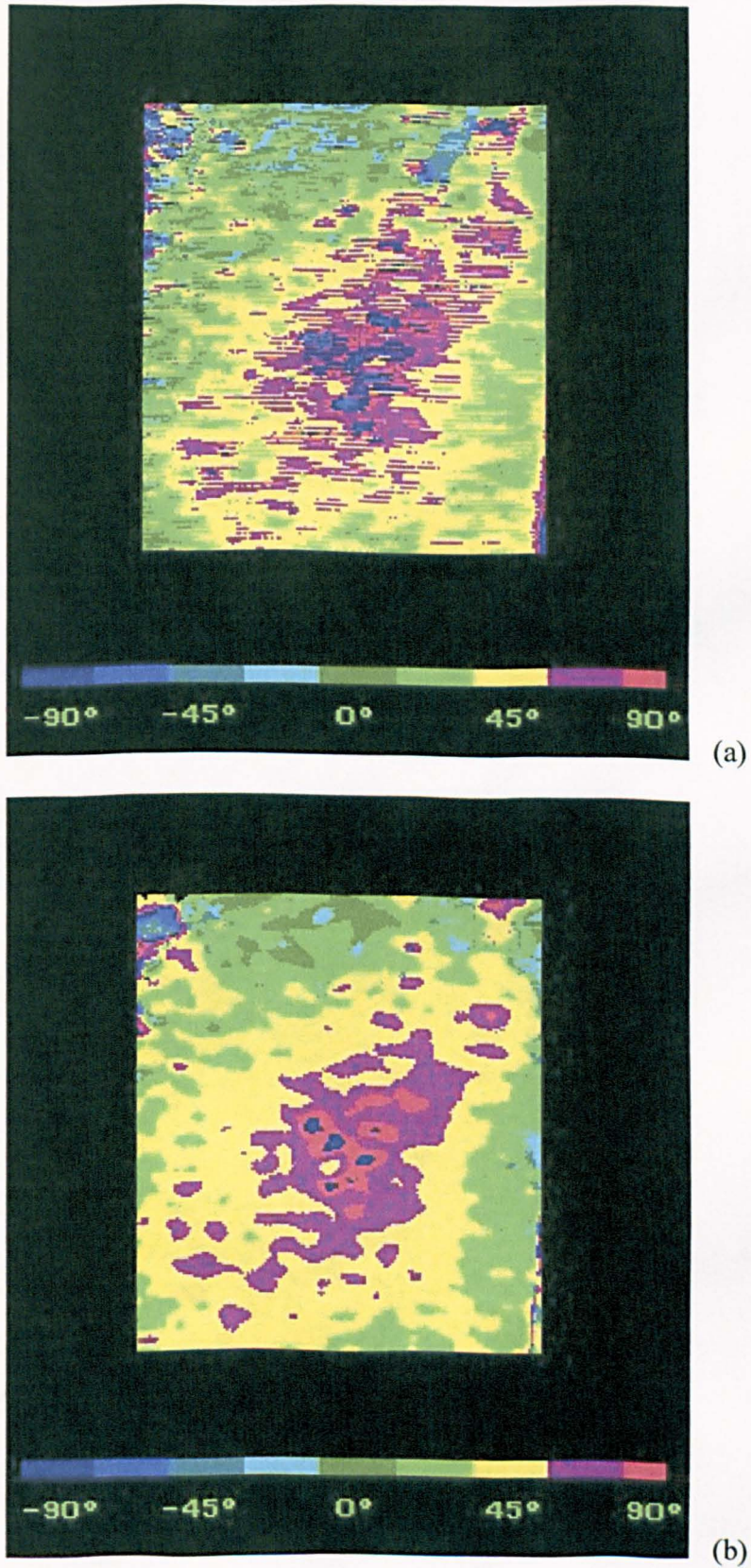


Figure 5.52 The comparison of the retardation maps from (a) raw (b) smoothed intensity data. (Upper part of the compression blade in tension, mode 1, frequency 257 Hz and energy level 1 g)

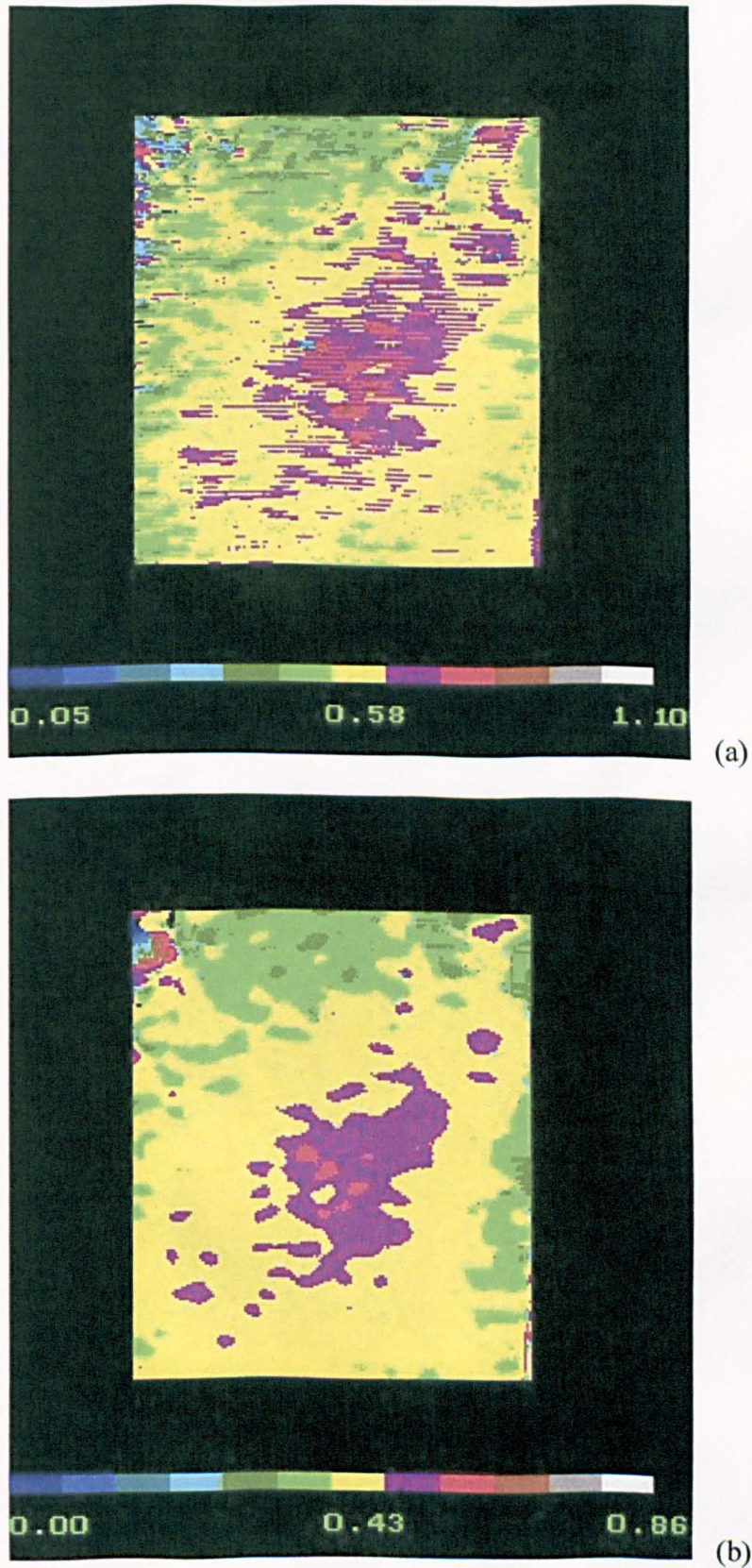


Figure 5.53 The comparison of the fringe order maps from (a) raw (b) smoothed intensity data. (Upper part of the compression blade in tension, mode 1, frequency 257 Hz and energy level 1 g)

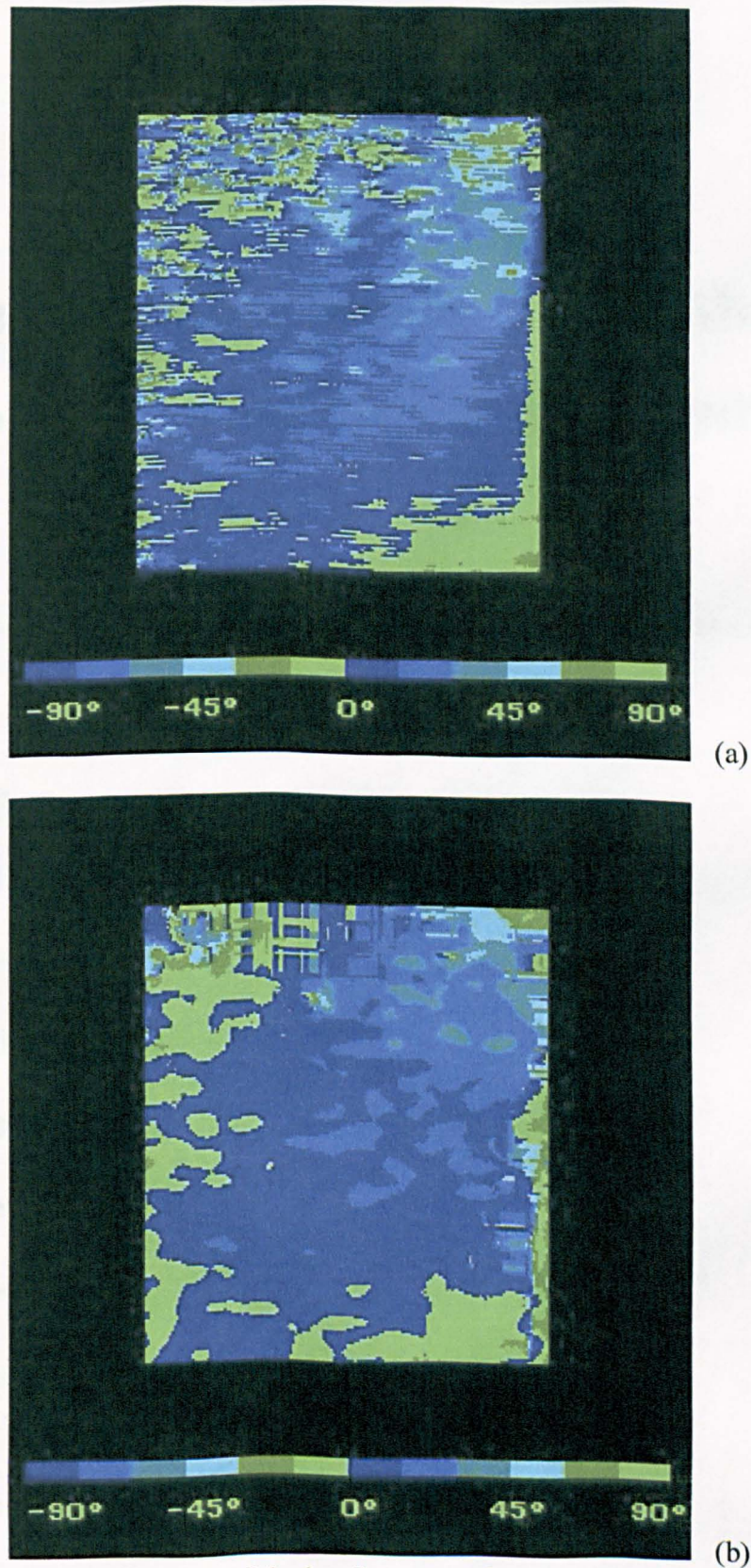


Figure 5.54 The comparison of the isoclinic maps from (a) raw (b) smoothed intensity data. (Upper part of the compression blade in tension, mode 1, frequency 257 Hz and energy level 1 g)

Chapter Six

Comparative method for Stress Maps from Experimental Method and Numerical Analysis

6.1 Introduction

6.2 Description of the Problem

6.3 Sampling Procedure

6.4 Correlation Method

6.5 Implementation of the Correlation Method

6.6 Experiments

6.7 Discussion

6.8 Conclusion

6.1 Introduction

As reviewed in section 2.5.4, the comparison of two digital images can be performed using a pixel-by-pixel comparison for corresponding points. However, for stress maps obtained from numerical analysis and experimental or theoretical methods, the pixel-by-pixel comparison is not always applicable because the data in the stress map from numerical analysis do not correspond to data in a digital image in a one on one manner except using interpolation and this may be restricted for the linear elastic fracture mechanics. Hence it is necessary to find a method of comparison for the stress maps from full-field experimental methods and numerical analysis.

In regression problems, the fit of the regression curve to the observed data is evaluated by goodness of fit statistics and, for the problem encountered here, the stress maps from full-field experimental method and numerical analysis can be assigned to the observed data and the regression surface respectively. Therefore, goodness of fit statistics may be used to compare the stress maps. In this chapter, methodologies for comparing stress maps from full-field experimental methods of stress analysis and numerical stress analysis is proposed and the correlation method is evaluated using automated photoelasticity, thermoelasticity and finite element method (FEM) as examples. Since the size of the data sets is very large, data used in the comparison were selected with reference to the sampling theory. Based on the assumption that correlation of the data in the two samples represents correlation of the full-field stress populations, comparison of the stress maps becomes a comparison of samples that were selected randomly from the stress maps. A parameter called the coefficient of determination, R^2 that is used in statistics in assessing the goodness-of-fit of regression models was calculated and then converted to a correlation coefficient r (Unwin, 1981). Hence, a conclusion could be drawn about the relationship between the values in the stress maps obtained from full-field experimental method and FEM.

In a strict sense, this type of regression analysis should not be applied to non-linear problems, such as the stress field in the vicinity of stress raisers. Stresses and strains around a crack tip can be described by Westgaard functions. Stresses and strains are functions of the inverse of the square root of distance from a crack tip.

The stress gradient near the crack tip increases exponentially but away from that area, the stress gradient changes gradually. In an area that is away from region *I* defined in section 3.2, stresses can be considered as a close-to-linear regression line. A close-to-linear non-linear regression model is one whose parameter estimators are close to being unbiased, normally distributed, minimum variance estimators, a condition that always applies in linear regression models but is approximated to a great or lesser degree in non-linear regression models depending on the model and the sample size. If the stress curve is considered as a close-to-linear regression model and increasing the sample size, linear regression properties should be used on it, that is, the correlation formula of the linear regression model may be applied to the stress and strain curves.

The method was applied to stress maps obtained from the transmission photoelastic method and from FEM for a curved bar in tension and a circular ring in diametrical compression; and to stress maps from thermoelastic and photoelastic methods and from FEM for a racing car hub carrier. Results from the experiments showed that the correlation method is not reliable for real engineering non-linear problems. The scaled standard deviation has shown to be a parameter, more reliable than the correlation coefficient r for measuring fitness of stress maps from full-field experimental methods and the numerical method.

6.2 Description of the Problem

We have two stress maps available. The first map (type 1) arises from the full-field experimental method and is a digital image. The second map (type 2) arises from the numerical method and in this study, a commercial package *ANSYS* has been used. A map of type 1 originates from an image or a series of images recorded with a CCD camera, and hence consists of an array of pixels for each of which a stress value has been evaluated, whereas a map of the type 2 consists of values of stress at nodal points within a finite element model. The location of pixels and nodes need not coincide and usually will not do so.

6.3 Sampling Procedure

Suppose that a map of type 1 is of size 256x256 pixels and hence the total numbers of data values in the digital image is 65536. If we want to compare two such images, we may want to compare the corresponding values of stress for every position in the two images, pixel by pixel; or we may chose some points randomly and use the corresponding values of stress in the two images as a pair of samples (sample 1 and sample 2). A correlation coefficient can be obtained and a conclusion about the relationship between the two samples can be drawn. The random sampling method is often used for large data sets, particularly in psychological, educational, agricultural, sociological and economical studies. The randomly selected sample is taken to represent the population, since no other better information is available. If the sample size is large, the difference between the sample standard deviation and population standard deviation should be small. Caulcott (1973, p.47) suggested that for practical purposes, the sample standard deviation is sufficiently close to the population standard deviation, when the sample size is larger than 30.

To use the random sampling theory in the present study, we can compare the stress maps of type 1 and type 2, rather than comparing a pair of stress maps of the type 1 as mentioned above. The stress maps of type 2 tend to be more sparsely populated than those of type 1 so it is easy to find a point in a map of type 1 that corresponds to a nodal point in a map of type 2, and hence the corresponding values of the stress in the two maps can be found. It is not difficult to find over 30 nodal points in a map of type 2, and their corresponding values in the map of type 1. When the two sets of sample data have been obtained, a calculation of the correlation of the samples can be carried out.

6.4 Correlation Method

Much work has been done on the comparison of observed data and data from the corresponding regression curve. Goodness of fit is a statistic that is used to measure how well a mathematical surface describes the average trend of the data and is widely used for comparison purposes. In regression theory, the coefficient of determination, R^2 is used in determining the goodness of fit of a model. Since the relationship between the coefficient of determination and the correlation coefficient is straightforward, the correlation coefficient can be easily obtained and may be used to quantify the fit between the stress maps from experiments and numerical analysis.

6.4.1 Coefficient of Determination, R^2

A typical scatter plot with a regression line fitted to the points is shown in Figure 6.1. For a particular value X_I , the regression line predicts that the dependent variable Y_I is equal to \hat{Y}_I . The deviation of Y_I from the mean can be grouped into the following components:

$$\begin{aligned} (Y_I - \bar{Y}) &= \text{total deviation of } Y_I \text{ from the mean, } \bar{Y} \\ (\hat{Y}_I - \bar{Y}) &= \text{explained deviation of } Y_I \text{ from } \bar{Y} \\ (Y_I - \hat{Y}_I) &= \text{unexplained deviation of } Y_I \text{ from } \bar{Y}. \end{aligned} \quad (6.1)$$

Let us square and sum the deviations, so that the complete components of variation for the dependent variable are obtained

$$\begin{aligned} \sum (Y_i - \bar{Y})^2 &= \text{total sum of squared deviations (TSS)} \\ \sum (\hat{Y}_i - \bar{Y})^2 &= \text{regression (explained) sum of squared deviations (RSS)} \\ \sum (Y_i - \hat{Y}_i)^2 &= \text{error (unexplained) sum of squared deviations (ESS)}. \end{aligned} \quad (6.2)$$

Hence, we get

$$TSS = RSS + ESS. \quad (6.3)$$

A large RSS relative to TSS , indicates a better fit of the regression model to the data, that is

$$R^2 = RSS / TSS. \quad (6.4)$$

The possible values of the R^2 range from 0 to 1. In one extreme case where the regression line fits the data perfectly, $ESS = 0$ and $R^2 = 1$. In the other extreme case where the regression line provides no information about the response, the $ESS = 1$ and $R^2 = 0$.

The parameter R^2 can be used to check how close the regression line is to the data points (Lewis-Beck, 1993, p.16). For example, there are two samples as shown in Figure 6.2. The R^2 for sample 1 could differ from the R^2 for sample 2, even though the estimates of the parameters, a and b for each were exactly the same. The large R^2 indicates the tight fit of the regression line in the sample 1 and small R^2 indicates loose fit in the sample 2.

The coefficient of determination, R^2 adjusted for degrees of freedom k , can be written as (Frees, 1996, p.153)

$$R_a^2 = 1 - \frac{\sum_{i=1}^n (Y_i - \hat{Y}_i)^2 / (n - k - 1)}{\sum_{i=1}^n (Y_i - \bar{Y})^2 / (n - 1)} \quad (6.5)$$

when $k = 2$, and use of a total uncorrected sum of squares $\sum_{i=1}^n Y_i$ and correction

factor $\left(\sum_{i=1}^n Y_i\right)^2 / n$ the denominator can be written as the following (Kleinbaum, Kupper and Muller, 1988, p. 99)

$$\sum_{i=1}^n (Y_i - \bar{Y})^2 = \sum_{i=1}^n Y_i^2 - \left(\sum_{i=1}^n Y_i\right)^2 / n \quad (6.6)$$

gives

$$R_a^2 = 1 - \frac{n(n-1)}{n-3} \left(\frac{\sum_{i=1}^n (\hat{Y}_i - Y_i)^2}{n \sum_{i=1}^n Y_i^2 - \left(\sum_{i=1}^n Y_i\right)^2} \right) \quad (6.7)$$

The relationship between the coefficient of determination, R^2 and the estimate of the correlation coefficient r is straightforward (Lewis-Beck, 1993, p.17)

$$R^2 = r^2. \quad (6.8)$$

hence, the estimated correlation coefficient r can be obtained from the positive value of the square root of the coefficient of determination R^2 .

For $k = 2$, the correlation coefficient can be written as

$$r = \sqrt{1 - \frac{n(n-1)}{n-3} \frac{\sum_{i=1}^n [Z_B(x,y) - Z_A(x,y)]^2}{n \sum_{i=1}^n [Z_A(x,y)]^2 - \left(\sum_{i=1}^n Z_A(x,y)\right)^2}} \quad (6.9)$$

where Z_A or Z_B are functions of coordinates x and y and represent values of the data points on the maps A and B respectively.

The correlation coefficient r will vary from 0 to 1. Values of r between 0.9 and 1 are thought to show a significant fit in the data and values of r between 0 and 0.2 suggest that the fit is not well established.

6.4.2 Comparison of the stress maps using the correlation coefficient r

In geophysics, there are many situations for which the observations are irregularly scattered over the map area. For example, for subsurface geological data, where observations are confined to wells that have been drilled, supplemented by data from scattered outcrops. (Krumbein, 1959). Trend surface analysis has been employed by scientists to obtain contour-type maps based on the irregular points. In order to find how well the surface fits the original observed data, the goodness of fit statistic has been applied. It was called 'percentage reduction in sums of squares %RSS' (Unwin, 1981, p. 178) and was written as

$$\%RSS = \frac{\sum_{i=1}^n z_{ti}^2 - \left(\sum_{i=1}^n z_{ti}\right)^2 / n}{\sum_{i=1}^n z_{obsi}^2 - \left(\sum_{i=1}^n z_{obsi}\right)^2 / n} \times 100 \quad (6.10)$$

where z_{ti} denotes the computed value of the trend at the i_{th} observation.

Draper (1984) argued the use of the R^2 . Generally, the square of the multiple correlation coefficient in a regression fit, R^2 can be increased by increasing the number of data points because the additional data will help to locate the true mean

values at each location more precisely. Draper argued that in his study the R^2 is lower when he increases the number of repeat data points. He warned that R^2 can be made to look “too bad” by increasing the number of data points to extremely high levels.

It is noted that Draper drew his conclusion from an experiment in which the increased data points were repeated at a few fixed values of the independent variable, see Figure 6.3. In contrast, in the present study, data points would be increased by using new and different values of the independent variable.

The above discussion about the coefficient of determination is for linear problems and most stress distributions are non-linear. However, stress fields can be approximately described as close-to-linear problems when data are taken away from the very near field of stress raisers. The estimators of a close-to-linear regression model come close to being unbiased, normally distributed, minimum variance estimators — a condition that always applies in linear regression models but is approximated to a great or lesser degree in non-linear regression models depending on the model and the sample size (Ratkowsky, 1990). Hence, the correlation formula for a linear regression model may be used for the stress maps obtained from full-field techniques.

In the present study, the values of stress can be considered as a function of the coordinates x and y

$$z_i = f(x_i, y_i) \quad (6.11)$$

The values in the two samples can be represented by z_{1i} and z_{2i} , where subscript 1 denotes the experimental method and 2 denotes the numerical method.

We wish to know the fitness of the data from the two samples that have been extracted from a pair of maps of types 1 and 2. We could assign the points in the sample of type 1 as being from the original observed data and assign the points in the sample of the type 2 as being from the regression surface. Hence, $Z_B(x, y)$ and $Z_A(x, y)$ in the expression (6.9) can be replaced by z_{1i} and z_{2i} respectively, as

$$r = \sqrt{1 - \frac{n(n-1)}{n-3} \frac{\sum_{i=1}^n [z_{1i} - z_{2i}]^2}{n \sum_{i=1}^n z_{2i}^2 - \left(\sum_{i=1}^n z_{2i}\right)^2}} \quad (6.12)$$

The correlation coefficient r for the samples from the maps of type 1 and 2 calculated using the above expression can be used to draw conclusions about the fitness between the two stress maps.

6.4.3 Residual Analysis

The correlation coefficient discussed in the last two sections is the positive square root of the coefficient of determination. It may be able to indicate the fit of the observed data and the regression surface, because the trends of the regression surface should be similar to the trends in the observed data. However, in engineering practice, stress maps may be complicated, so it is possible for the correlation coefficient, r to be close to the unity whilst the maps are very different. For example, stress distribution in the maps may look similar, but the location of the hot spots is in different part of the maps. It can be caused by improper loading conditions in the experiment and the numerical analysis. Identifying the difference is easy for an experienced engineer, but it is difficult using only one statistical parameter. A residual analysis can be used to solve this problem. The mean square error for regression analysis is (Frees, 1996, p.152)

$$s^2 = \frac{\sum_{i=1}^n \hat{e}_i^2}{n - (k + 1)} \quad (6.13)$$

where $\hat{e}_i = y_i - \hat{y}_i$ is the i_{th} residual. The scaled residual standard deviation is defined as

$$d_s = \frac{s}{\max[\{y_i\}, \{\hat{y}_i\}]} \quad (6.14)$$

If the scaled standard deviation is smaller than 0.1, the two stress maps are considered to have similar trends and it may indicate a good fit of the two maps.

6.5. Implementation of the Correlation Method

A Window program *COCIMS* (COrelation Coefficient of Image MapS) was written based on expression (6.13), using *Microsoft Visual C++*, Version 5. The flow chart of the algorithm and screen window of the program are shown in Figures 6.4 and 6.5.

Three files are needed in the calculation. By using the program *PECAN* or *VIZION*, phase stepped data from a polariscope can be processed and information on the photoelastic parameters, such as isochromatic and isoclinic fringes can be obtained. The information on photoelastic parameters is saved in two files. Isochromatic fringe order can be calculated using data in the first file and two factors in the second file using the following formula

$$[N] = Factor_1 \times ([V] + Factor_2) \quad (6.15)$$

where N is fringe order and V is value from the first file. $Factor_1$ and $Factor_2$ are the first and second values in the second file and related to data format of the first file.

Information on the isochromatic fringe order can also be obtained using numerical methods. When the principal stresses are available, the fringe order can be easily obtained using the following formula

$$N = \frac{(\sigma_1 - \sigma_2) \times t}{2\pi f} \quad (6.16)$$

where N is the fringe order, σ_1 and σ_2 are the principal stresses, t is the thickness of the specimen and f is the stress optical constant.

To use the program *COCIMS*, you need to provide three files – two files from photoelastic analysis using *VIZION* or *PECAN* and a file from the Finite Element Method (FEM). The file from FEM can be in either *.txt* or *.prn* format. Data obtained from FEM can be processed in the program *EXCEL* using the procedure described in Appendix C. The source code of the program *COCIMS* is listed in Appendix D.

6.6 Experiments

6.6.1 Comparison of the Stress Maps from Automatic Photoelasticity and Finite Element Analysis

The elastic modulus of the two specimens was 2.5 *GPa*, the Poisson's ratio was 0.38 and photoelastic fringe constant was 7 *N/fringe/mm*. The shape and dimensions of the specimens are shown in Figure 6.6 and Figure 6.7.

The first specimen was a curved tie-bar and the second is an annular ring. The tie-bar was set up in a conventional transmission polariscope and subjected to a tensile load of 103 *N*. A CCTV camera was used and six phase-stepped images were obtained and processed to generate an isochromatic fringe map using the program *VIZION*.

The commercial program package *ANSYS* 5.4 was used to calculate the isochromatic maps. The isochromatic map was obtained by multiplying the difference of two principal stresses with some known parameters using expression (6.16). The element type used in the model was plane 82. The total number of elements and nodes in the model were 887 and 2790 respectively for the tie-bar (Model 1). Validation of the finite element model was done by checking its convergence. The load applied on the model was the same as in the experiment. Another model of the specimen with 1355 elements and 4216 nodes was also generated to obtain another isochromatic map (Model 2).

Five sets of data were randomly selected from the Model 1. The number of data points selected for each set was 32, 100, 200, 300 and 600 respectively. The reason for selecting five sets of fringe order is to check whether or not the correlation coefficient r varies directly with the number of data points selected. The coordinates of the data points and corresponding fringe orders were recorded. Fringe orders in the photoelastic maps were extracted using the recorded spatial coordinates. The sets of fringe order from the FEM maps and the photoelastic map were used to calculate the correlation coefficient r using the program *COCIMS*. The results for the correlation coefficient r for different numbers of data points are

listed in Table 6.1 and plotted in Figure 6.8. The analysis was repeated for data samples containing 100 and 200 data points and was listed in Table 6.2.

The second specimen was an annular ring and was subjected to a compressive load of 46 *N*. The correlation coefficient for the specimen was obtained using the same procedure as for the curved tie-bar. The results are listed in Table 6.3 and plotted in Figure 6.9.

Maps of fringes of the bar and the ring from both photoelasticity and finite element analysis are shown in Figure 6.10 and Figure 6.11, respectively. Relationship of the fringe orders from selected 100 data points for the tie-bar and the ring are shown in Figure 6.12 and Figure 6.13. The scaled residuals for the bar and the ring are 0.019 and 0.102 respectively.

6.6.2 Comparison of the Stress Maps from Thermoelasticity and Finite Element Analysis

6.6.2.1 Theory

Any substance in nature, whether solid, liquid or gas become slightly warmer or slightly cooler when its volume is changed by a force. This phenomenon is called the thermoelastic effect. The thermoelastic effect can be induced either by compressive load, which heats the stressed substance or by tensile load which causes it to cool. The relationship between the small temperature change caused by the change in the stress state of a linear elastic, homogeneous material can be derived in the form

$$\Delta T = -\frac{\alpha T}{\rho C_p} \sum_{i=1,2} \sigma_{i,i} \quad (6.17)$$

where T is the absolute temperature of the material,

C_p is the specific heat at constant pressure,

ρ is the density of the material,

α is the linear coefficient of thermal expansion of the material.

σ_{ij} is the stress change tensor.

The equation (6.18) can be rewritten as

$$\Delta T = -KT(\sigma_1 + \sigma_2) \quad (6.18)$$

where $K = \frac{\alpha}{\rho C_p}$ and σ_1, σ_2 are the changes in the principal stresses.

The experimental technique of thermoelastic stress analysis allows the direct measurement of the change in the sum of the principal stresses on the surface of a component which is experiencing a cyclic stress regime. An infrared detector is employed which generates a two dimensional spatial record of the thermoelastic signal from the surface of an isotropic component which can be related to the surface stress by the expression

$$(\sigma_1 + \sigma_2) = AS \quad (6.19)$$

where A is a calibration constant, S is the thermoelastic signal (Dulieu-Barton, 1999).

6.6.2.2 Experiment

Specimen

The hub carrier of a racing car is a lightweight alloy casting and the geometry of the hub carrier is shown in Figure 6.14. A thin coating of matt black paint was applied to both the flat plate specimen and the hub carrier to ensure a uniform emissivity in the infrared region. The same paint was applied to the loading frame of the hub carrier to reduce reflection effects and problems associated with signal overload of the thermoelastic detectors. A strain gauge rosette was applied to both specimens in a region of moderate surface stress and low stress gradient to allow the calibration of each material for thermoelastic response. The specimen was subjected to a sinusoidal load with a maximum of 15 kN and minimum of 2 kN at operating frequency 10 Hz. Images were taken from the rectangular area highlighted in the Figure 6.14 using two thermoelastic instruments, namely SPATE and Delta-Therm.

Instruments

(a) SPATE 4000 series (SPATE Manual, 1996. p. 2.2)

The SPATE (Stress Pattern Analysis by Thermal Emission) system is a instrument for measuring vibration components and structures. It uses a pair of mirror to build a two-dimensional raster scan of a surface, bringing a single detector to bear on each point of the scan. The VPI sensor incorporates scanning mirrors to permit movement of the measuring position across a structure. In the VPI sensor a laser beam is divided into reference and signal beams. The signal beam is directed onto a vibrating test surface and back-reflected light is recombined with the internal reference beam. When the test surface moves, the path difference between the routes followed by the reference and signal beams changes, resulting in intensity modulation of the re-combined beam due to interference between the reference and signal beams. The re-combined beam is shared between two independent detection channels in such a way that the interferometric path difference presented to one channel is effectively one quarter of a wavelength longer than that presented to the other. This configuration results in a 90° phase shift between the signals from the two channels, the direction of motion of the surface determining which signal leads the other in phase. The two signals at frequency F_d (the Doppler frequency associated with a surface velocity v) are fed to a dual channel balanced modulator where they are respectively modulated by internally generated two signals at a carrier frequency F_c . Summation of the two modulated outputs yields a single, frequency shifted output at F_c+F_d , F_c-F_d , depending on the direction of motion of the surface. In this way, electronic mixing results in essentially the same frequency shifted Doppler signals as those obtained using optical frequency-shifting techniques, and established frequency tracking methods can be used to drive an analog voltage representing the instantaneous velocity of the moving surface. The primary instrument output is an analog voltage proportional to surface velocity which can be fed to external signal analysis equipment, or linked to any one of a range of Ometron scan control and display systems to map the full-field vibrational deflection shapes of a test piece under conditions of single frequency excitation or random/service loading.

The SPATE 4000 detector (Ometron Limited, UK) was used in the experiment. It takes about 4 hours to capture one image.

(b) Delta-Therm

The Delta-Therm is an instrument suited to the measurement of cyclically changing temperatures. It uses an array-style infrared detector and high-speed image-processing electronics that acquire, process and deliver data in just seconds. The Delta-Therm (Model No. H1450, imager: DT1500, resolution 320x256, Stress Photonics Inc. USA) was used in the experiment. The array of 320x256 can be captured in 30 seconds.

Results

The maps of sum of two principal stresses were obtained using the thermoelastic technique*. A map of the sum of the principal stresses was also obtained using ANSYS*. There are 51418 elements and 11850 nodes. The type of element is solid 72, 3D 4-node tetrahedral structural solid with rotations. A sinusoidal displacement distribution was applied to half of the central hole with the direction towards the symmetry axis of the hub. The maps from SPATE, Delta-Therm and FEM are shown in Figures 6.15 (a), (b) and (c). Figure 6.16 shows the relationship between the sum of the principal stresses from Figure 6.15(a) and the data inside the dashed rectangle in Figure 6.15(c) for selected points. The correlation coefficient r calculated from the selected 82 data points is 0.3615 and scaled deviation is 0.332. Figure 6.17 shows the relationship between the sum of the principal stresses from the data in Figure 6.15(b) and corresponding area inside the rectangle in Figure 6.15(b) for selected 87 data points. The correlation coefficient, r calculated from selected data points is 0.8464 and scaled deviation is 0.4908.

* The author is grateful to Mr. Richard J. Greene (University of Sheffield) for providing thermoelastic data and Dr. Sandro Barone (University of Pisa, Italy) for providing the FE data. The work of design of the model and stress maps from the FEM was done by Professor Conti in the University of Perugia, Italy.

6.7 Discussion

Results from the curved tie-bar and the circular ring (Figures 6.8 and 6.9) showed that correlation coefficient tends to increase with the size of the sample. This contradicts Draper's findings. The proximity of the correlation coefficient to unity in the case of the curved bar (0.966) suggests very close agreement between the FE and the photoelastic data. The correlation coefficient for the SPATE and FEA data from the hub carrier is very low (0.36) and indicates a very poor correlation between the thermoelastic (SPATE) and the FE data. The difference can be observed in the maps in Figures 6.10 and 6.15.

The results from the experiments using photoelasticity applied to the circular ring and the Delta-Therm system applied to hub carrier are interesting. The correlation coefficients for the two specimens were in the range 0.8 to 0.9. The stress maps for the circular ring from the photoelastic method and FEM are similar (Figure 6.11), but the stress maps for the hub carrier from the Delta-Therm instrument and FEM are quite different (Figure 6.15). By examination of Figure 6.15 (b) and (c), it is found that in the rectangle area of the FE map, stress values are large at some area but are small in the corresponding area in the Delta-Therm map. It is noted that the scaled standard deviation of the two specimens are quite different. For the circular ring, the scaled standard deviation is 0.102 and for the hub carrier using the Delta-Therm it is 0.4908.

By comparing the correlation coefficient r , and scaled standard deviation d_s (Curved bar: $r = 0.996$, $d_s = 0.019$, circular ring: $r = 0.837$, $d_s = 0.102$, SPATE: $r = 0.362$, $d_s = 0.332$, DeltTherm: $r = 0.846$, $d_s = 0.491$), it is found that the correlation coefficient r indicated the fit of two stress maps for the examples of curved bar, circular ring and race car hub carrier (SPATE), but it does not give a right answer for the race car hub carrier (DeltTherm). Therefore it is not reliable for measuring the fitness of stress maps. It is also found that the scaled standard deviation does indicate the fitness of two stress maps for all the examples in this experiment, Hence, it can be used as a reliable measure to quantify the fitness of stress maps from experimental methods and numerical analysis.

The difference between the thermoelastic data and the FE data was found caused by improper loading. Two metal plates were used to hold the hub carrier. The plates have a central hole with six small holes around it. The central hole has the same diameter as the hub carrier. When load was applied, the load was put on the edge of the hole of the plate rather than the edge of the hole of the hub carrier. Because the plates were fastened to the hub carrier on the six small holes, the load was transmitted to the small holes. This resulted in stress maps with hot spots near the two small holes in the area examined and no hot spot appears in area where the load should apply.

6.8 Conclusions

The following conclusions can be made based on the discussions.

Comparison of two stress maps from a full-field experimental method and a numerical method can be done by comparison of samples selected randomly from the two stress maps. It is found that correlation coefficient r calculated from the coefficient of determination, R^2 is not reliable in practice, but the scaled standard deviation has shown its capability for the task. If the scaled standard deviation is smaller than 0.1 the full-field experimental data and the FE data can be considered in good agreement.

Tables

Table 6.1 Correlation coefficient of stress maps (curved tie-bar)

Photoelastic maps	Model 1					Model 2
	32	100	200	300	600	600
Correlation coefficient r	0.964	0.956	0.969	0.975	0.967	0.983

Table 6.2 Correlation coefficient of stress maps (curved tie-bar, 100 and 200 points)

Data set	1	2	3	4	Average
Correlation coefficient r (100)	0.957	0.959	0.975	0.884	0.944
Correlation coefficient r (200)	0.969	0.95	0.973	0.96	0.963

Table 6.3 Correlation coefficient of stress maps (circular ring)

Number of data points	32	100	200	300	600
Correlation coefficient r	0.855	0.812	0.847	0.781	0.889

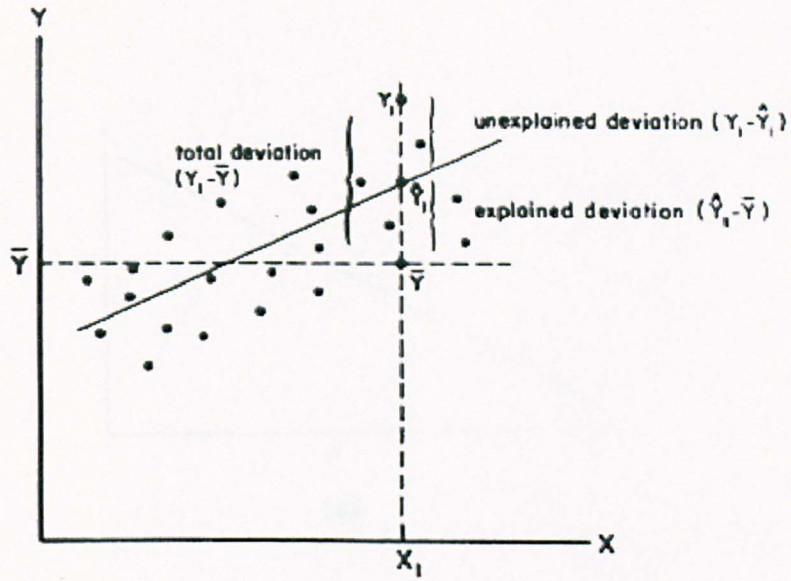


Figure 6.1 Components of variation in Y.
(Lewis-Beck, 1993, p.14, Fig.5)

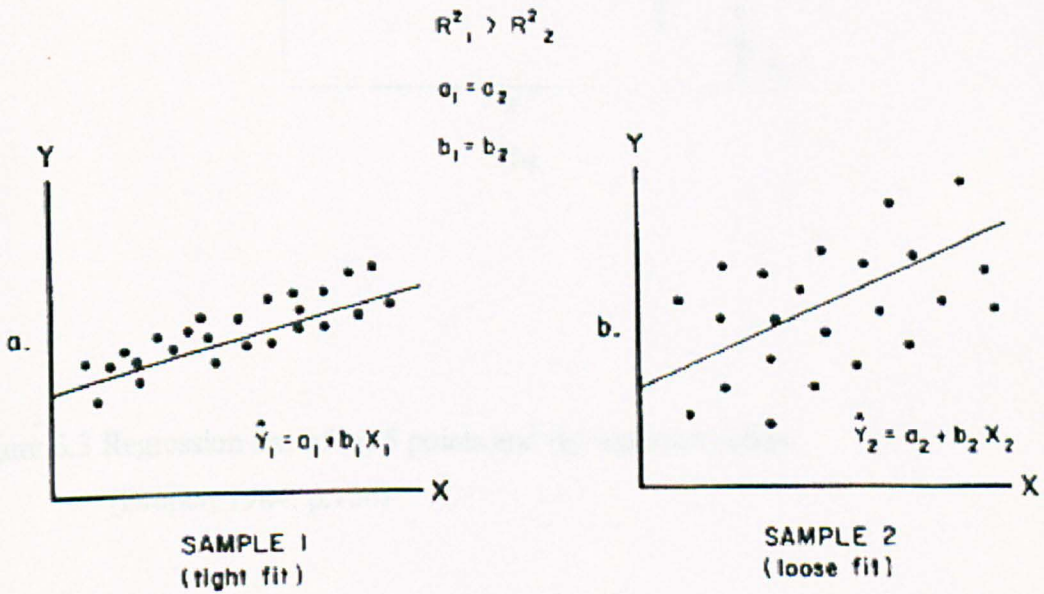
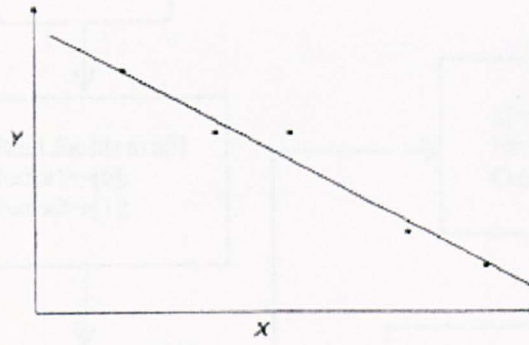
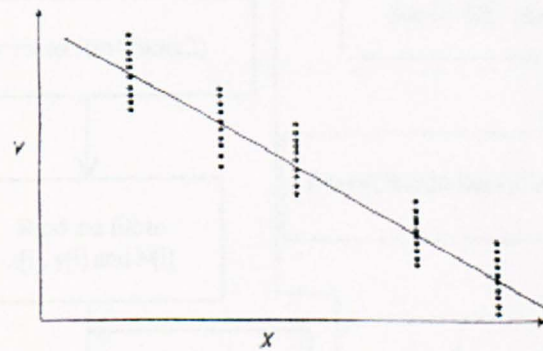


Figure 6.2 Tight fit versus loose fit of a regression line.
(Lewis-Beck, 1993, p.17, Fig 7)



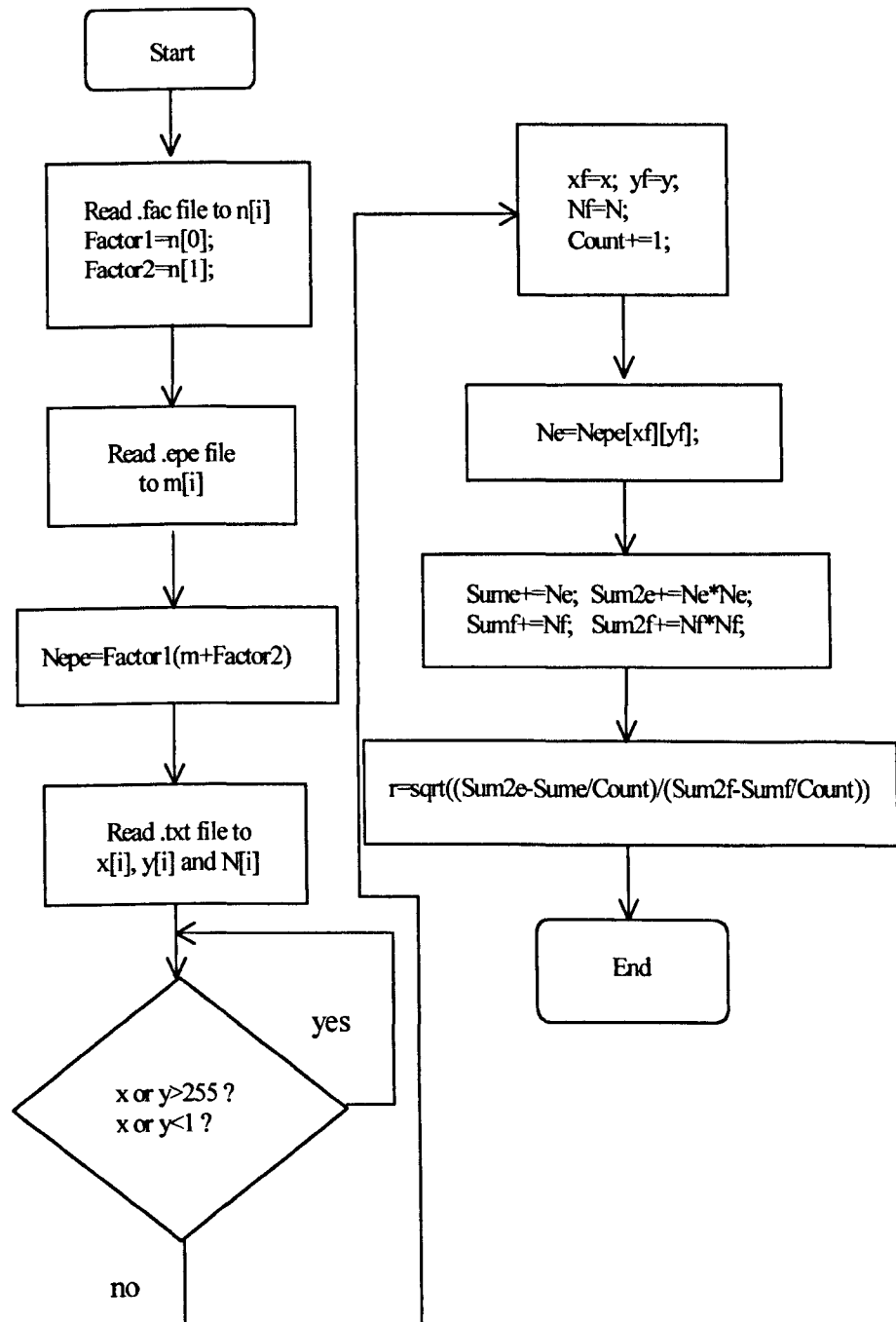
(a)



(b)

Figure 6.3 Regression line of (a) 5 points and (b) repeated points.
(Draper, 1984, p.100)

Figure 6.4 First class of program CEK 205

Figure 6.4 Flow chart of program *COCIMS*.

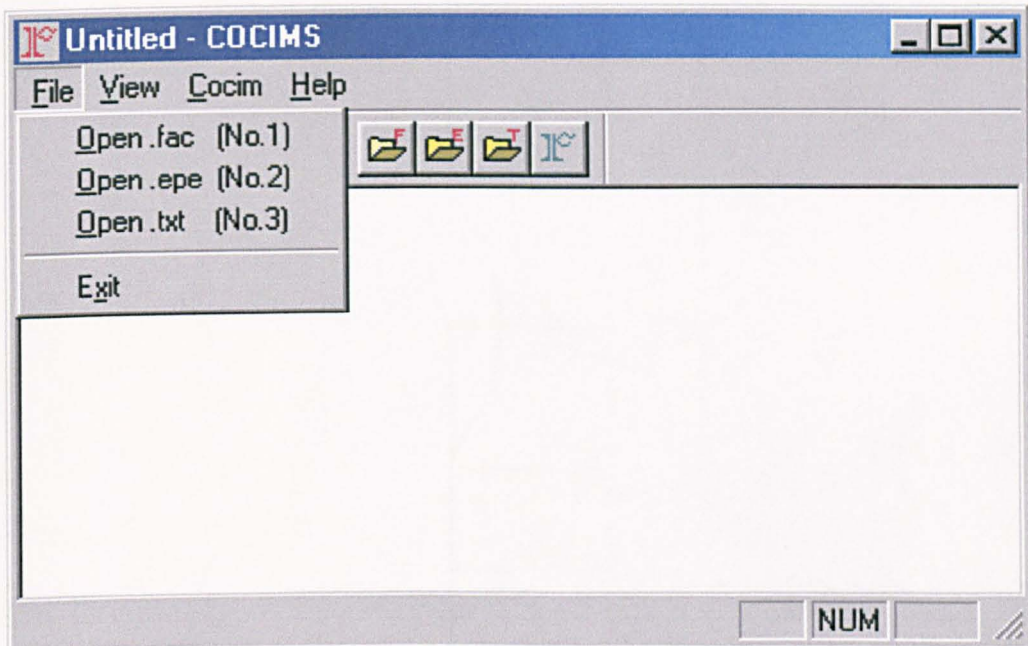


Figure 6.4 Dimensions of the curved bar.

Figure 6.5 Profile of the program *COCIMS*.

Figure 6.7 Dimensions of the circular ring.

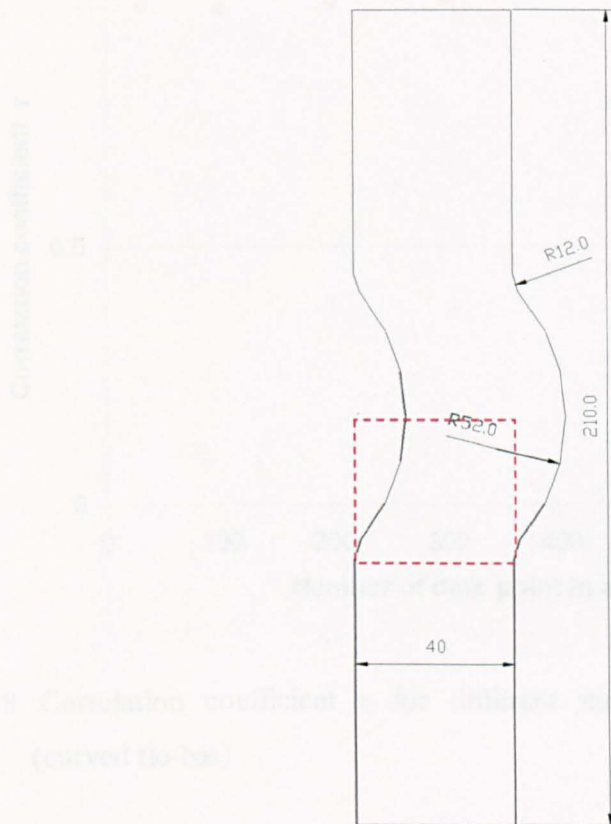


Figure 6.6 Dimensions of the curved tie-bar.

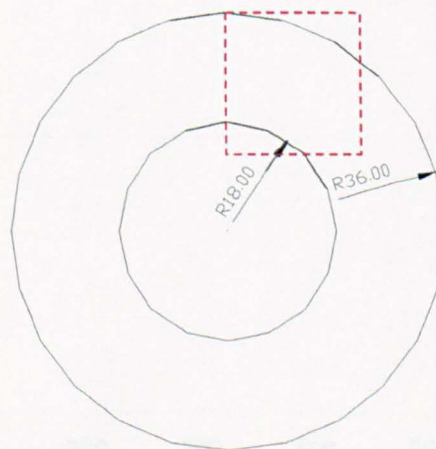


Figure 6.7 Dimensions of the circular ring.

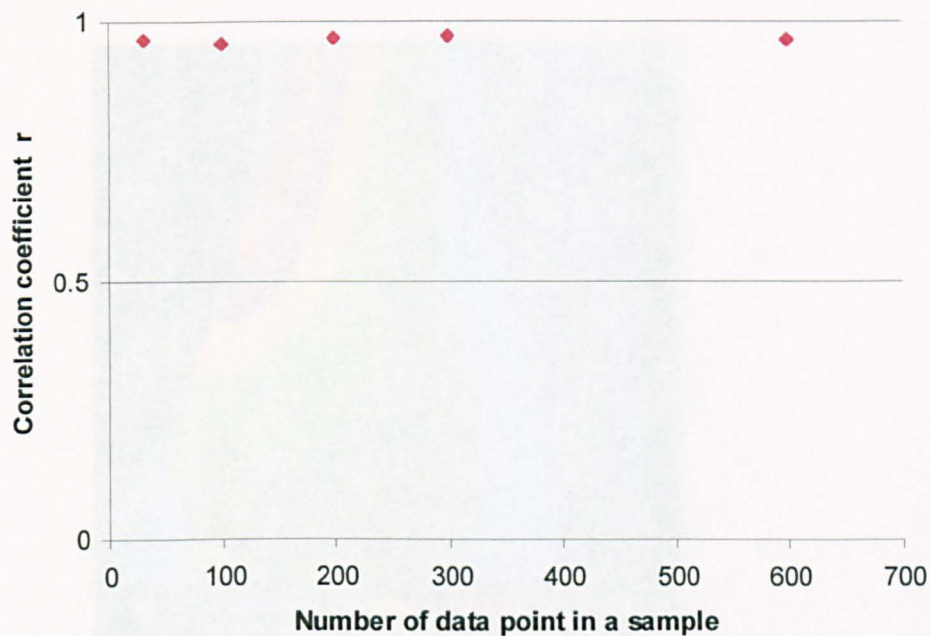


Figure 6.8 Correlation coefficient r for different number of points in samples. (curved tie-bar)

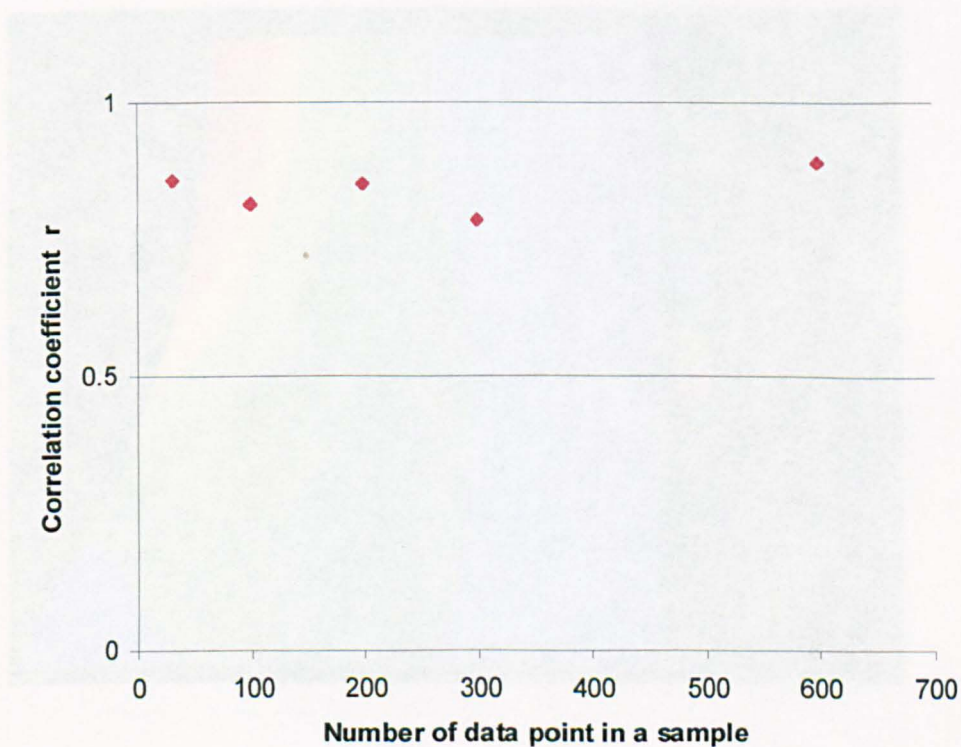


Figure 6.9 Correlation coefficient r for different number of points in samples. (circular ring).

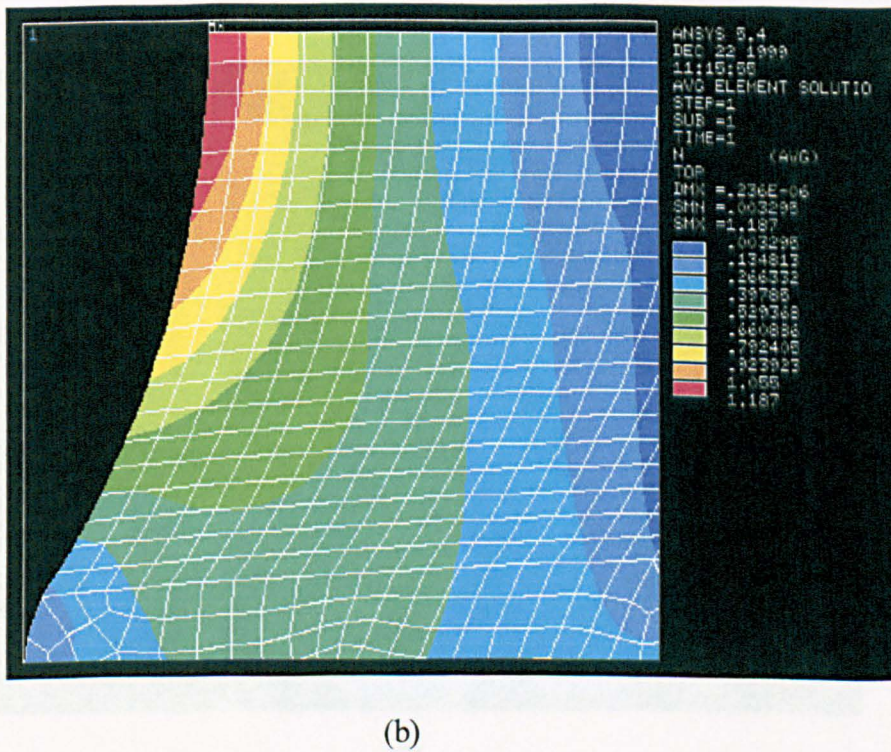
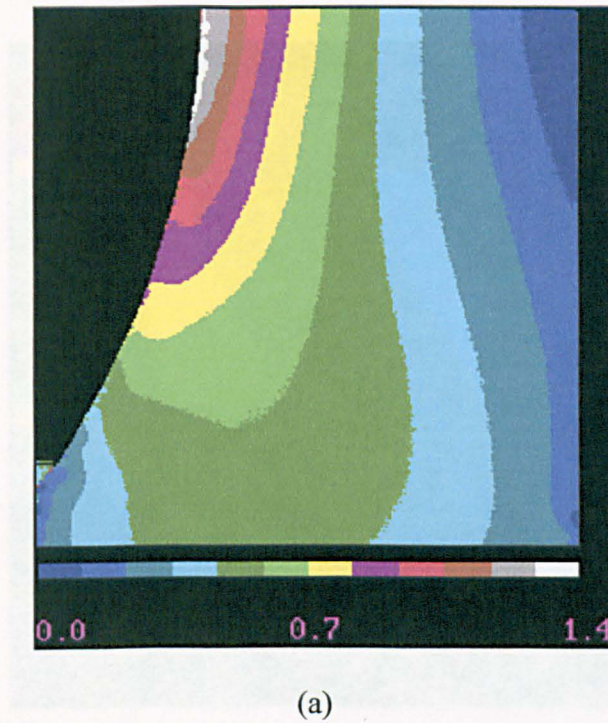
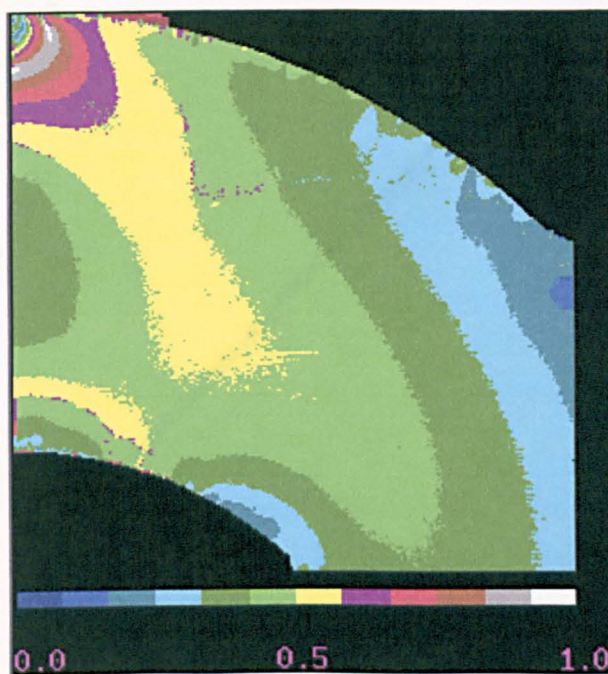
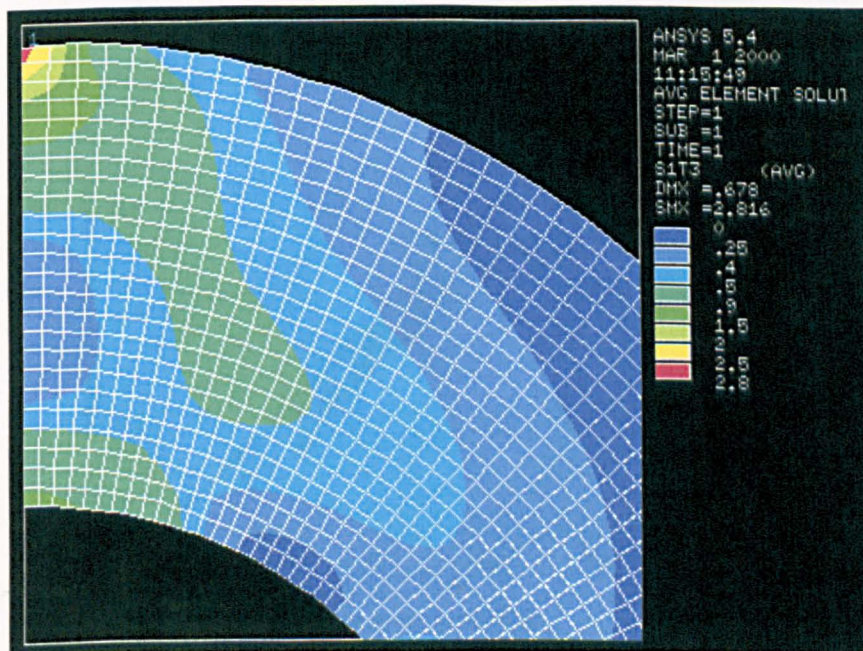


Figure 6.10 The isochromatic maps of the tie-bar (a) from photoelasticity (b) from FEM.



(a)



(b)

Figure 6.11 The isochromatic maps of the circular ring (a) from photoelasticity (b) from FEM.

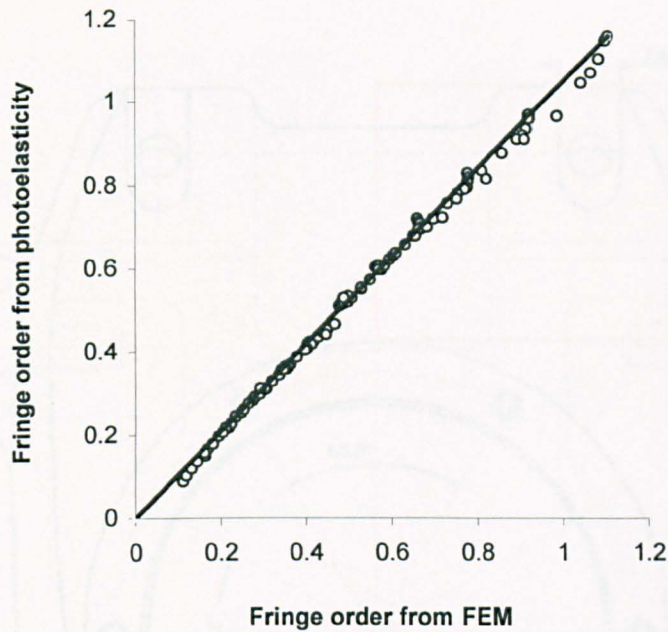


Figure 6.12 Relationship between FEM and the photoelastic method for selected 100 points. (Curved bar $r = 0.996$, $d_s = 0.019$)

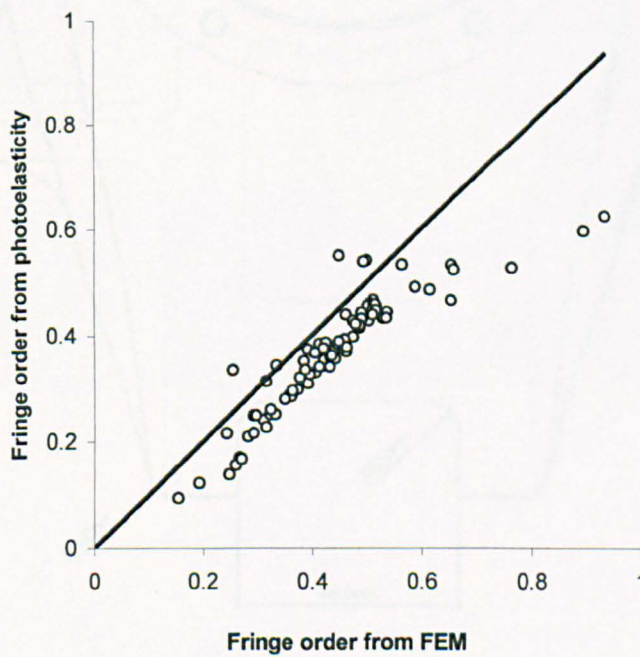


Figure 6.13 Relationship between FEM and the photoelastic method for selected 100 points. (circular ring $r = 0.837$, $d_s = 0.102$)

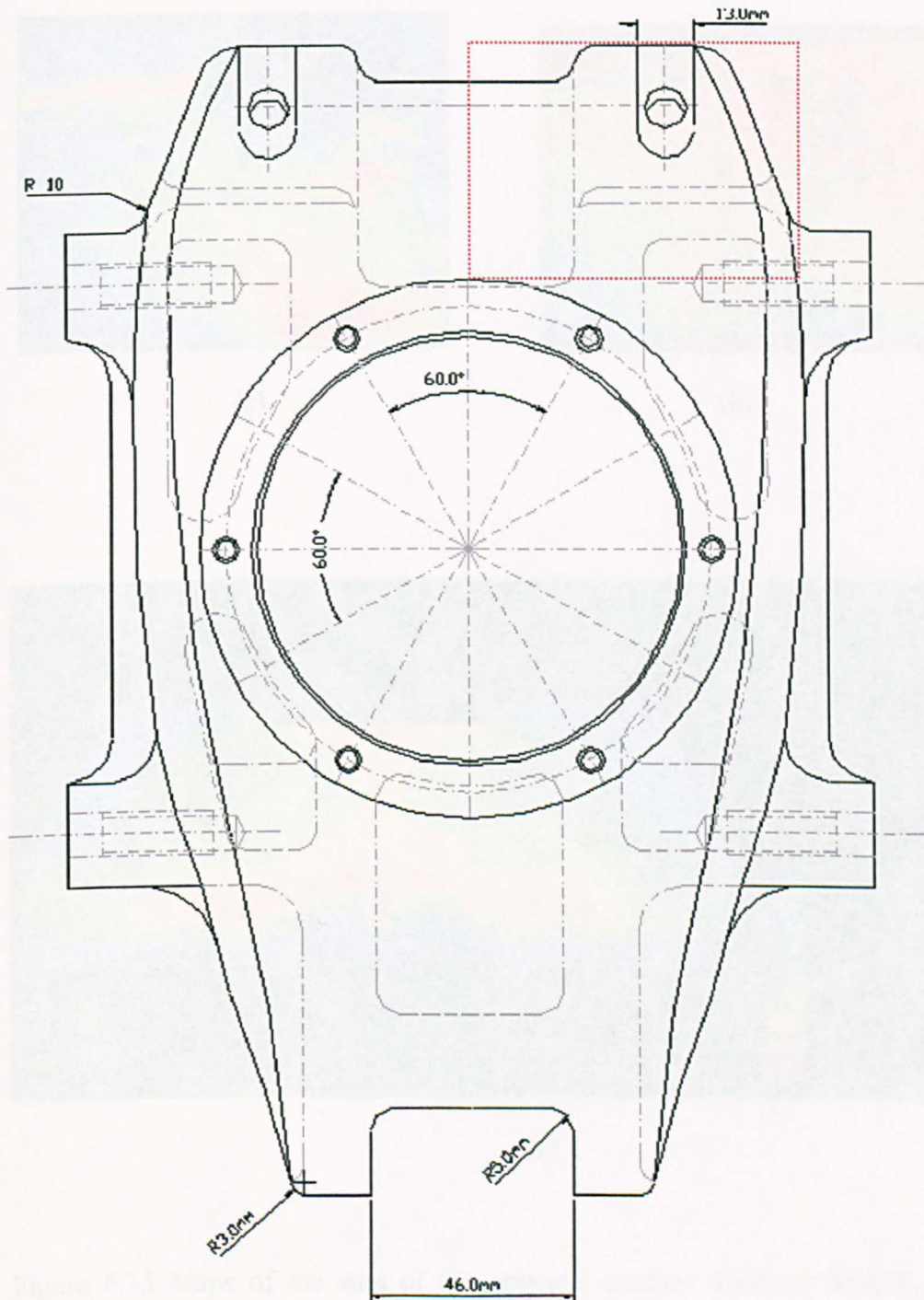
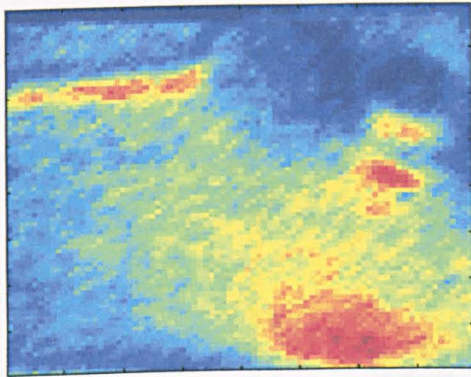
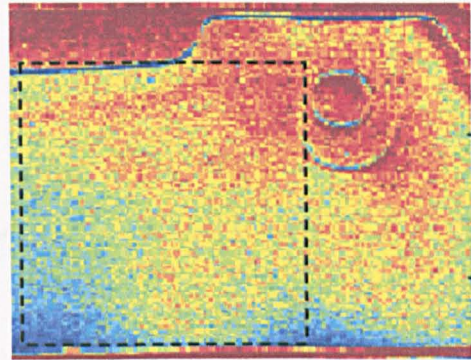


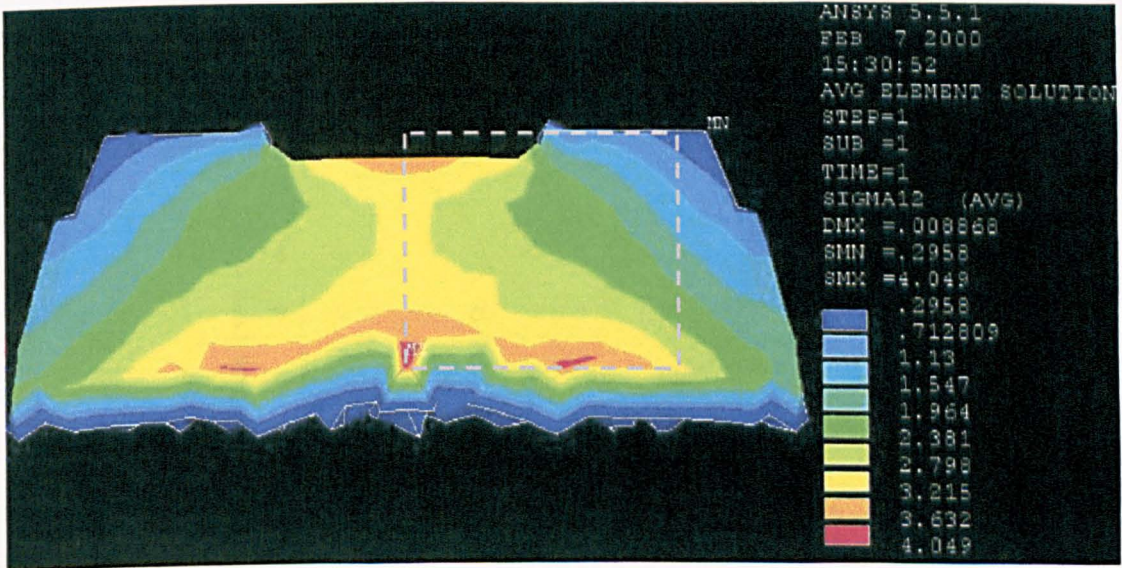
Figure 6.14 Dimensions of the car hub carrier.



(a)



(b)



(c)

Figure 6.15 Maps of the sum of the principal stresses from (a) SPATE, (b) Delta Therm and (c) FEM.

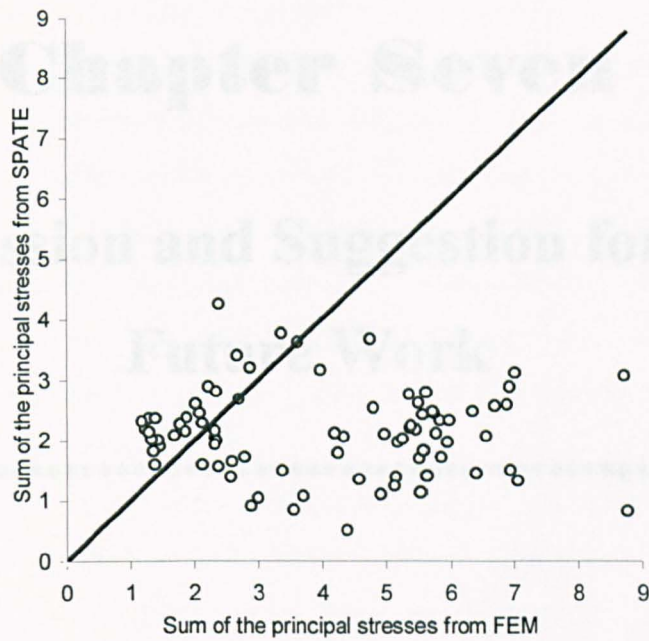


Figure 6.16 Relationship between FEM and the SPATE for selected 82 points.

(hub carrier $r = 0.3615$, $d_s = 0.332$)

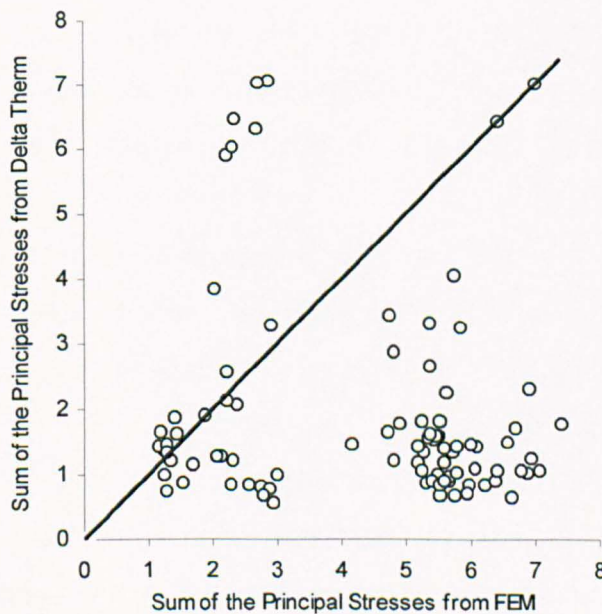


Figure 6.17 Relationship between FEM and the Delta Therm for selected 87 points.

(hub carrier $r = 0.8464$, $d_s = 0.4908$)

Chapter Seven

Discussion and Suggestion for the Future Work

7.1 Discussion

7.2 Suggestion for the Future Work

7.1 Discussion

The literature review in chapter 2 highlighted many aspects of photoelasticity. It was found for full-field automated photoelasticity that noise in intensity image has an influence on the photoelastic parameters, and that noise in images obtained from automated reflection photoelasticity is severe. The sources of error in the use of an automated transmission polariscope have been recognised by Ji (1998), and the finding is applicable to automated reflection photoelasticity. However, since different components such as photoelastic coating, are used in the reflection photoelasticity, it requires further investigation in order to find the sources of noise in automated reflection photoelasticity.

In the initial assessment of the automated reflection polariscope PSIOS in chapter 3, the stress intensity factors from three different procedures using reflection photoelasticity are compared with those from strain gauges and from Newman's (1971) numerical solutions for a tensile plate with double cracks from the edge of a central hole. The three photoelastic procedures were point-by-point readings from a conventional reflection polariscope; extracting data from a colour photograph obtained using a conventional polariscope and digital data from the automated polariscope PSIOS. It was found that the automated reflection polariscope, PSIOS is sensitive, so the fringe order can be detected even the load is small. The accuracy of the results is comparable to other methods. The error is mainly caused by the noise in the intensity images because of the noise caused problem in the unwrapping process.

The investigation of major sources of noise in intensity data obtained from the PSIOS and evaluation of some smoothing methods were described in chapter 4. Four experiments were performed in order to find sources of noise. From the experiments using both transmission and reflection specimens and conventional transmission polariscope with automatic data acquisition device and the PSIOS system, the major sources of noise were found to be the photoelastic coating and electronic instrumentation. These sources of noise cannot be removed during the operation, so a smoothing method should be applied on the intensity data to reduce the effect of noise. The methods for full-field image processing reviewed in chapter 2 were assessed using the intensity data obtained from a computer generated image

and an image from the PSIOS system. None of them satisfy the requirement of effective and flexible to different applications. The Butterworth filter that is commonly used in signal processing and satisfies the requirement was introduced to smooth the intensity images. Smoothness of intensity image could be adjusted by selecting the cut-off ratio in range 0 to 1. It was found from experiment in the chapter 5 that for intensity data from the PSIOS system, the cut-off ratio in range 0.15 to 0.25 gives reasonable results. The Butterworth filter has been incorporated in software and will be used routinely in SNECMA, Paris and BAe UK.

The purpose of developing the PSIOS system is to validate the results from numerical analysis. However, the stress map from the experiment is a digital image and this cannot be simply compared with the stress map from numerical analysis because the interpolation may not be properly used for the non-linear elastic fracture mechanics. Traditional method for comparison of such stress maps is to select lines across the stress map and plot the result from different methods on the same axes. This method can be used for a quantitative comparison, but using a few lines on the stress map cannot represent the information given in the entire map. Another method is to compare the hot spots of the two maps, and here it is obvious that a quantitative comparison cannot be made. In the chapter 6 the correlation coefficient r derived from the coefficient of determination R^2 is used to compare the stress maps. The evaluation of the correlation method and residual analysis were performed using stress maps from transmission photoelasticity and thermoelasticity and finite element method as examples. The results from the experiments using the curved tie-bar, circular ring and the real engineering component race-car hub carrier showed that the correlation coefficient r does not always give the proper indication of the fitness of stress maps. It is found that the scaled standard deviation properly represents the fitness between the two stress maps. If the scaled standard deviation is smaller than 0.1, the full-field experimental data and the numerical data can be considered to be in good agreement.

7.2 Suggestion for the Future Work

The method for comparing two stress maps from full-field experiments and numerical analysis can be used to measure the fitness of the two stress maps when the maps satisfy the close-to-linear condition. However, this is a limitation to its use since the method can only be used for regions of stress maps away from the stress raiser. It would be very useful if a method of comparison applicable to general non-linear distributions could be developed for stress correlation.

Chapter Eight

Conclusions

The main conclusions drawn from the present study are:

- (1) The low pass, zero-phase Butterworth filter is an effective, flexible smoothing method for improving intensity images obtained from the automated reflection polariscope PSIOS. It generates an enormous improvement in the quality of the map of photoelastic fringe order and isoclinic, render the instrument useful for demanding analyses, such as those involving vibration studies with reflection coatings.
- (2) The standard deviation, a parameter in statistics, can be used to indicate fitness of the stress maps from the full-field experimental method and the numerical analysis. If the scaled standard deviation is smaller than 0.1, the full-field experimental data and the numerical data can be considered in good agreement. This approach allows one parameter to completely describe the quality of fit between two stress maps representing the same stress field.
- (3) The automated reflection polariscope, PSIOS has been found to be capable of performing stress analysis in both static and dynamic applications under service conditions. It is also capable of being used for the determination of stress intensity factors.

References

Ahmed, N. and Natarajan, T (1983)

Discrete-time signals and systems. Reston Publishing Company, Inc. A Prentice-Hall Company, USA.

Ajovalasit, A., Barone, S. and Petrucci, G (1995)

Towards RGB photoelasticity: full-field automated photoelasticity in white light. *Experimental Mechanics*. Vol. 35, No.3, pp.193-200.

Ajovalasit, A., Barone, S. and Petrucci, G (1998)

A review of automated methods for the collection and analysis of photoelastic data. *Journal of strain analysis*. Vol. 33, No. 2, pp.75-91.

Allison, I. M. & Nurse, P. (1971)

Optimal data acquisition for an automatic polariscope. *7th All-Union Conference on Photoelasticity, Tallinn, Nov. Proc. pt. 1, pp.93-105.*

Allison, I. M. & Nurse, P. (1972)

Automatic acquisition of photoelastic data. *Proc. JBCSA Conference on the Recording and Interpretation of Engineering Measurements, Inst. Mar. Engrs., London, pp. 203-207.*

Ames, W. F. (1977)

Numerical methods for partial differential equations. Second edition. Academic Press, Thomas Nelson & Sons, London.

Barone, S. and Patterson, E. A. (1998)

An alternative finite difference method for post-processing thermoelastic data using compatibility. *Journal of strain analysis*, Vol. 33, No. 6, pp.437 – 447.

Brown, A. F. and Hickson, V. M. (1950)

Improvements in photoelasticity technique obtained by using a photometric method. *British journal of applied physics*. Vol. 1, pp. 29-44.

Caulcott, E (1973)

Significance tests. Routledge and Kegan Paul, London.

Carazo-Alvarez, J. Haake, S. J. and Patterson. E. A. (1994)

Completely automated photoelastic fringe analysis. *Optics and Lasers in engineering*, Vol. 21, pp. 133-149.

Chen, T. Y. (1997)

Digital determination of photoelastic birefringence using two wavelengths. *Experimental mechanics*, Vol. 37, No. 3, pp.232-236.

Cloud, G. (1995)

Optical Methods of Engineering Analysis. Cambridge University Press.

Dally, J. W. & Sanford, R. J. (1987)

Strain-gage methods for measuring the opening mode stress intensity factor K_I , *Experimental Mechanics*, Vol.27, No.4, pp. 381-389.

Dally, J. W. & Riley, W. F. (1991)

Experimental stress analysis. (3rd edition), p. 323 & p. 131 McGraw-Hill, New York.

Draper, N. R. (1984)

The Box - Wetz Criterion Versus R^2 . *Journal of Royal Statistics Society. A (1984)*, 147, part 1, pp. 100-103.

Driver, D., Hall, D. W. and Meetham, G. W. (1981)

The gas turbine engine. p.23-24. in *The Development of gas turbine materials*. Edited by Meetham. Applied Science Publishers Ltd. London.

Duffy, J. (1961)

Effects of the thickness of birefringent coatings. *Experimental mechanics*, Vol. 1, No.3 pp. 74-82.

Ekman, M. J. and Nurse, A. D (1998)

Load-stepping automated photoelasticity. *Experimental Mechanics*, Allison (ed.) Balkema, Rotterdam, pp.533–538..

Elliott, D. F. (1987)

Transforms and transform properties. In *Handbook of digital signal processing – engineering applications*. Edited by Elliott, D. F., Academic Press Inc., London.

Frees, E. W. (1996)

Data analysis using regression models. Prentice Hall, Englewood Cliffs, New Jersey 07632.

Frieden, B. R. (1979)

Image enhancement and restoration, (Chapter 5). *Picture processing and digital filtering*, Edited by Huang, T. S. (1975,1979) Springer-Verlag, New York.

Gdoutos, E. E. (1985)

Photoelastic study of crack problems (chapter 6). In *Photoelasticity in engineering practice*, Edited By Paipetis, S. A. and Holister, G. S., Elsevier applied science publishers, London.

Golten, J (1997)

Understanding signals and systems. The McGraw Hill Companies, London.

Haake, S. J. and Patterson, E. A. (1992)

Photoelastic analysis of frozen stressed specimens using spectral contents analysis. *Experimental Mechanics*. Vol. 32, pp.266-272.

Haake, S. J., Wang, Z. F. and Patterson, E. A. (1993)

Evaluation of full field automated photoelastic analysis based on phase stepping.

Experimental techniques, Vol. 17, No. 6, pp.19-25.

Hamming, R. W. (1983)

Digital filters. Second edition, Prentice-Hall, Inc. Englewood Cliffs, New Jersey.

Hecker, F. W. and Morche, B. (1986)

Computer measurement of relative retardations in plane photoelasticity. Experimental stress analysis (Ed. H. Weiringa). pp.532-542. Martinus Nijhoff publishers. Dordrecht, The Netherlands.

Heywood, R. B. (1952)

Designing by Photoelasticity. Chapman and Hall Ltd. London

Huber, R., Simmonds, K., Schechter, R., Mignogna, R. and Delsanto, P. (1996)

Comparison of dynamic photoelastic visualisation of ultrasound with parallel computations. *Material science forum, Vol. 210-213, pp.373-378.*

Hussain, Z. (1991)

Digital image processing – practical applications of parallel processing techniques. Ellis Horwood.

James, G., Burley, D., Dyke, P., Searl, J., Steele, N., and Wright, J. (1993)

Advanced Modern Engineering Mathematics. Addison-Wesley Publishing Company. England.

Ji, W. (1997)

Error analysis and system improvements in phase-stepping methods for photoelasticity. PhD thesis, the University of Sheffield.

Ji, W. and Patterson, E. A. (1998)

Simulation of errors in automated photoelasticity. *Experimental mechanics, Vol. 38, No. 2, pp. 132-139.*

Kleinbaum, D, Kupper, L and Muller, K (1988)

Applied regression analysis and other multivariable methods. Second edition, PWS-KENT publishing company, Boston.

Krumbein, W. C (1959)

Trend surface analysis of contour-type maps with irregular control-point spacing. *Journal of Geophysical research, Vol. 64, No.7, pp.823-834.*

Lewis-Beck, M. S. (1993)

Applied regression - A introduction. In the 'Regression Analysis', Edited by Lewis-Beck M. S. SAGE Publications, Toppan Publishing, UK.

Lu, W. (1992)

Two-dimensional filters. Marcel Dekker, Inc. USA.

Matlab Manual (1996)

Signal processing toolbox - user's guide. Version 4. The Math works Inc.

Mesnager, M. (1930)

On the optical determination of the interior stresses of three-dimensional solids. *COMPTES RENDUS DE L'ACADEMIE DES SCIENCES, Vol. 190, No.22, pp.91-92.*

Mindlin, R. D. (1937)

Analysis of doubly refracting materials with circularly and elliptically polarised light. *Journal of the optical society of America, Vol. 28, No. 8, pp 288-291.*

Moore, D. S. and McCabe, G. P. (1999)

Introduction to the practice of statistics. Third edition, W. H. Freeman and Company, New York.

Morimoto, Y., Morimoto, Y. Jr. and Hayashi, T. (1993)

Separation of isochromatics and isoclinics using Fourier transform and its accuracy. *SEM spring conference, pp.1149-1158.*

Morimoto, Y. and Imamoto, Y. (1994)

Error causes and error reduction in fringe pattern analysis by phase shifting method using Fourier transform. Recent advances in experimental mechanics, Silva Gomes *et al* (eds), Balkema, Rotterdam.

Muller, R. K. and Saackel, L. R. (1979)

Complete automatic analysis of photoelastic fringes. *Experimental Mechanics, Vol.19, pp. 245-251.*

Murakami, Y. (1990)

Stress intensity factor handbook 1, Pergamon Press, Oxford.

Newman J. C (1971)

An improved method of collocation for the stress analysis of cracked plates with various shaped boundaries. NASA report, TND-6376.

Ng, T. W. (1997)

Photoelastic stress analysis using an object step loading method. *Experimental mechanics, Vol. 37, No. 2, pp.137-141.*

Nurse, A. D. & Patterson. E. A. (1992)

Photoelastic coatings applied to cracked plates, *Proc. Conf. Technology Transfer between High Tech Engineering and Biomechanics, Ed. E.G. Little, Limerick, 4-5 Sept., pp. 477-490.*

Nurse, A. D. & Patterson. E. A. (1993 a)

Photoelastic determination of fatigue crack stress intensity factor, *Proceedings of SPIE, Annual Symposium on Opt. Engineering, San Diego, 1993.*

Nurse, A. D. & Patterson. E. A. (1993 b)

Determination of predominantly mode II stress intensity factors from isochromatic data. *Fatigue fract. engng. mater. struct., Vol. 16, pp. 1339-1354.*

Nurse, A. D. (1997)

Full-field automated photoelasticity by use of a three-wavelength approach to phase stepping. *Appl. Optics*, vol.36, No.23, pp.5781-5786.

Olofsson, K and Lindgren, L. E. (1993)

Holographic interferometry measurements of transient bending waves in tubes and rings. *Experimental mechanics*. Vol. 33, pp.308-313.

Pashtoon, N. A (1987)

IIR digital filters. In Handbook of digital signal processing – engineering applications. Edited by Elliott, D. F., Academic Press Inc., London.

Patterson, E. A. (1988)

Automated photoelastic analysis. *Strain*, Vol.24, 1988, pp. 15-20.

Patterson, E. A. & Wang, Z. F. (1991)

Towards full field automated photoelastic analysis of complex components. *Strain*, Vol. 27, pp. 49-53.

Patterson, E. A. and Wang, Z. F. (1998)

Simultaneous observation of phase-stepped image for automated photoelasticity. *The journal of strain analysis for engineering design*. Vol. 33, No. 1, pp. 1-15.

Patterson, E. A. and Wang, Z. F. (1999)

Integration of spectral and phase-stepping methods in photoelasticity. *Journal of strain analysis*. Vol. 34, No. 1, pp.59-63.

Pacey, M. N., Wang, X. Z., Haake, S. J. and Patterson, E. A. (1999)

Application of evolutionary and maximum entropy algorithms to photoelastic spectral analysis. *Experimental mechanics*, Vol. 39, No.4, pp.265-273.

Quan, C., Bryston-Cross, P.J. and Judge, T. R. (1993)

Photoelasticity stress analysis using carrier fringe and FFT techniques. *Optics and Lasers in Engineering*, Vol.18, pp.79-108.

Ratkowsky, D. A. (1990)

Handbook of non-linear regression models. New York: M. Dekker, USA.

Redner, S. S. (1963)

New oblique-incidence method for direct photoelastic measurement of principal strains. *Experimental mechanics*, Vol. 3, No. 3, pp. 67-72.

Redner, S. S. (1962)

Stress analysis of Rocket-motor case by birefringent-coating method. *Experimental mechanics*, Vol. 2, No. 7, pp.215-221.

Redner, A. S. (1974).

A new automatic polariscope system. *Experimental mechanics*, Vol. 14, pp. 486-491.

Redner, A. S. (1984)

Photoelastic measurements by means of computer assisted spectral contents analysis. *In proceedings fifth international conference on experimental mechanics. Montreal, pp.421-427.*

Ramesh, K and Ganapathy, V (1996)

Phase shifting methodologies in photoelastic analysis c the application of Jones calculus. *Journal of strain analysis, Vol. 31, No. 6, pp.423-432.*

Ramesh, K. and Deshmukh, S. S. (1997)

Automation of white light photoelasticity by phase-shifting technique using colour image processing hardware. *Optics and lasers in engineering, Vol. 28, pp.47-60.*

Saada, A. S. (1993)

Elasticity theory and application. Second edition, Krieger publishing company, Malabar, Florida.

Sanford, R. J. & Iyengar, V. (1985)

The measurement of the complete photoelastic fringe order using a spectral scanner. *SEM Spring Conf. on Eng. Mech. pp.160-168.*

Sarma, A. V. S. S. R., Pillai, S. A., Subramania, G. and Varadan, T. K (1992)

Computerised image processing for whole-field determination of isoclinics and isochromatics. *Experimental Mechanics. Vol.32, No. 1, pp.24-29.*

Scalea, F., Hong, S. and Cloud, G (1997)

Whole-field strain measurement in a pin-loaded plate by electronic speckle pattern interferometry and the finite element method. *Experimental mechanics, Vol. 38, No. 1, pp.55-60.*

Seguchi, Y., Tomita, Y. and Watanabe, M. (1979)

Computer-aided fringe-pattern analysis --a case of photoelastic fringe. *Experimental Mechanics. Vol.19, No. 10, pp.362-270.*

Smith, C. W and Kobayashi, A. S. (1987)

Fracture Mechanics, *Chapter 20 in Hand book on experimental mechanics (edited by Kobayashi, A. S.), p. 893, Prentice-Hall, Englewood Cliffs, New Jersey.*

SPATE Manual (1996)

Ometron 4000 series operator's manual, Issue 4, section 2.

Stanley, W. D., Dougherty, G. R. and Dougherty, R. (1984)

Digital signal processing. 2nd edition, Prentice-Hall, USA.

Tsai, M. Y. and Morton, J. (1995)

Experimental and Numerical studies of a laminated composite single-lap adhesive joint. *Journal of composite materials, Vol. 29, No. 9. pp. 1154-1275.*

Tsai, K., Chiu, C. and Hsu, S. (1997)

Computer-aided photoelastic analysis of orthogonal 3D textile composites: part 1: whole-field determination of isochromatics and isoclinics. *Experimental mechanics*, Vol. 37, No.4, pp.427-432.

Umezaki, B., Tamaki, T. & Takahashi, S. (1984)

Automatic stress analysis from photoelastic fringe processing using a personal computer. *Proc. Soc. Photo. Vol.504*, pp. 127-134.

Unwin, D. L. (1981)

Introductory spatial analysis. Methuen & Co. London.

Vaillancourt, H., McCammond, D., and Pilliar, R. M. (1995)

Validation of a nonlinear two-dimensional interface element for finite-element analysis. *Experimental mechanics*, Vol. No. 3, pp.49-54.

Voloshin, A. S. and Burger, C. P. (1983)

Half-fringe photoelasticity: a new approach to whole field analysis. *Experimental Mechanics*, Vol. 23, pp.304-314.

Voloshin, A. S. and Redner, A. S. (1989)

Automated measurement of birefringence: Development and experimental evaluation of the techniques. *Experimental Mechanics*, Vol. 29, No.3, pp. 252-257.

Wang, Z. F. & Patterson, E. A. (1995)

Use of phase stepping with demodulation and fuzzy sets for birefringence measurement. *Optics and Lasers in Engineering*, Vol. 22, pp. 91-104.

Zandman, F., and Wood, M. R. (1956)

Photostress – a new technique for photoelastic stress analysis for observing and measuring surface strains on actual structures and parts. *Product engineering*, Vol. 27, No.9, pp.167-178.

Zandman, F. (1962)

Concepts of the photoelastic stress gage. *Experimental mechanics*, Vol. 2, No. 8, pp.225-233.

Zandman, F., Redner, S. S. and Post, D. (1965)

Photoelastic-coating analysis in thermal fields. *Experimental mechanics*, Vol.5, No.9, pp.215-221.

Zandman, F., Watter, M and Redner, S. S. (1962)

Stress analysis of Rocket-motor case by birefringent-coating method. *Experimental mechanics*, Vol. 2, No. 7, pp.215-221.

Zandman, F., Redner, S. S. and Riegner, E. I. (1962)

Reinforcing effect of birefringent coating. *Experimental mechanics*, Vol. 2, No. 2, pp.55-64.

Zandman, F., Redner, S. S. and Dally, J. W. (1977)

Photoelastic coatings. The Iowa State University Press& Society for Experimental Stress Analysis.

Appendix A

Calculation of the Coefficients of a Low Pass Butterworth Filter

A.1 Prewarp the Cut-off Frequency

A.2 Frequency Scale the Chosen $H(s)$

A.3 Use of Bilinear Transformation to Convert the Analog Filter into
a Digital Filter

A.1 Prewarp the Cut-off Frequency

Suppose ratio of the cut –off frequency f_c and Nyquist frequency f_N is 0.2,

$$w = \tan\left(\frac{\pi}{2} \frac{f_c}{f_N}\right) = \tan\left(\frac{\pi}{10}\right) = 0.325 \quad (\text{A.1})$$

A.2 Frequency Scale the Chosen $H(s)$

For third order Butterworth filter, the transfer function is

$$H(s) = \frac{1}{s^3 + 2s^2 + 2s + 1} \quad (\text{A.2})$$

The scaled transfer function corresponding to the $H(s)$ is

$$\tilde{H}(s) = H(s)\Big|_{s=\frac{s}{w}} = H\left(\frac{s}{w}\right) \quad (\text{A.3})$$

Where w is the prewarped frequency and equals to 0.325.

$$\tilde{H}(s) = \frac{0.325}{9.467455s^3 + 6.153846s^2 + 2s + 0.325} \quad (\text{A.4})$$

A.3 Use of Bilinear Transformation to Convert the Analog Filter into a Digital Filter

Replace s in the $\tilde{H}(s)$ by $\frac{z-1}{z+1}$ to obtain $H(z)$.

$$H(z) = \frac{0.018109 + 0.054329z^{-1} + 0.054329z^{-2} + 0.018109z^{-3}}{1 - 1.759767z^{-1} + 1.1826226z^{-2} - 0.277979z^{-3}} \quad (\text{A.5})$$

The coefficients of low pass third order Butterworth filter with cut-off ratio 0.2 are

$$b_0 = 0.018109 \quad b_1 = 0.054329 \quad b_2 = 0.054329 \quad b_3 = 0.018109$$

and

$$a_0 = 1.000000 \quad a_1 = -1.759767 \quad a_2 = 1.1826226 \quad a_3 = -0.277979$$

Appendix B

Program SIUP: software description

B.1 Introduction

B.2 Running the program

B.3 Image Processing

B.4 Dialogue Boxes

B.5 Source code in the program SIUP

Figures

B.1 Introduction

The program *SIUP* is for use of smoothing the images with noise obtained using the automated reflection polariscope. It was written using *Microsoft Visual C++*, version 5 and works under *Microsoft Windows 95* environment. The program has not only some basic functions in window, such as *File*, *Edit*, *View*, *Window* and *Help*, but also three functions for image processing in the main menu bar. These functions particularly for smoothing images are called *Processing*, *Filter* and *Filter_1*. Description of these functions is in section B.3.

B.2 Running the Program



is icon of the program *SIUP*.

To execute the program *SIUP* just simply double click on the icon of the program from windows. The first step is to open a RGB image to be processed in *.bmp* file. The functions in the menu for image processing can be selected for particular problems. Each of the functions and their usage is described in the next section.

B.3 Image Processing

The three functions in the program *SIUP* for use of smoothing the images are *Processing*, *Filter* and *Filter_1*.

B.3.1 Processing

Under the menu of *Processing*, there are three subroutines. These functions can be used to separate the RGB image into red, green and blue plane images respectively. The setting of the function is two fold. First, in application of the automated reflection polariscope, it is often need a certain plane of the RGB image to get particular information and secondly it can be used before the use of functions *Filter* and *Filter_1* for a trial of smoothing. It is easy to judge the smoothing effect on single plane than on the combined RGB image. Hence, a satisfied smoothing effect can be obtained.

Source code for the function *Processing* is listed in B.5.1.

B.3.2 Filter

The *Filter* stands for a smoothing method using the Butterworth filter. It is divided into three subroutines for using the filter in three planes (R, G and B) respectively. The subroutines for each plane is divided into two functions for smoothing on the horizontal and vertical direction. It can be used for specific problem that need the filter only in horizontal or vertical direction. If smoothing is needed in both direction on a plane, the subroutines *Horizontal* and *Vertical* should be clicked respectively.

In use of the Butterworth filter, a cut-off ratio should be given according requirement of the smoothing effect. A default cut-off ratio has been set as 0.2 in the program but users can change it to one that desired. The default value is obtained by experiment using images obtained from the automated reflection polariscope. A trial can be done using different cut-off ratios on a single plane image from the menu *Processing*.

The filtered image can be saved as a *.bmp* file for further processing. Source code for the function *Filter* is listed in B.5.2.

B.3.3 Filter_1

Under the menu *Filter_1* is Liebmann smoothing method. It is divided into three planes, namely, R, G and B. Effect of the smoothing method can be seen in a trial using a single plane image from the menu *Processing*.

Source code for the function *Filter_1* is listed in B.5.3.

B.4 Dialogue Boxes

There are two dialogue boxes in the program, a warning dialogue box and a input dialogue box.

B.4.1 Warning dialogue box

The program is specially written for 24-bit (RGB) images. When users open a colour image that is not a 24-bit image, the program can detect the mistake and display a warning message as shown in Figure B.4.1.

B.4.2 Input dialogue box

Cut-off ratio has to be given when using the Butterworth filter. Dialogue box shown in Figure B.4.2 is input dialogue box for cut-off ratio and default value is 0.2.

B.5 Source Code in the Program SIUP

B.5.1 Source Code for *Processing*

```

void CDibDoc::OnProcessBlueplane()
{
    int PlaneNo = 503;
    Processplane(PlaneNo);
}

void CDibDoc::OnProcessGreenplane()
{
    int PlaneNo = 502;
    Processplane(PlaneNo);
}

void CDibDoc::OnProcessRedplane()
{
    int PlaneNo = 501;
    Processplane(PlaneNo);
}

void CDibDoc::Processplane(int PlaneNo)
{
    WORD wNumColors;
    LPSTR lptoDIB;
    LPSTR lpDIBBits;
    if(m_hDIB)
    {
        lptoDIB = (LPSTR) ::GlobalLock((HGLOBAL) m_hDIB);
        wNumColors = ::DIBNumColors(lptoDIB);

        if (wNumColors != 0)
        {
            MessageBeep(0xFFFFFFFF);
            AfxMessageBox("This is not a 24 - bit image");
            ::GlobalUnlock((HGLOBAL) m_hDIB);
        }
        else
        {
            BeginWaitCursor();
            UINT bmpWidth = (UINT)::DIBWidth(lptoDIB);
            UINT bmpHeight = (UINT) ::DIBHeight(lptoDIB);
            UINT bytesperrow=bmpWidth*3;
            while (bytesperrow%4)
                bytesperrow++;

            UINT uBlockSize=bmpHeight*bytesperrow;

```

```

BYTE* ptrbmpBits = new BYTE[uBlockSize];
lpDIBBits = ::FindDIBBits(lpDIB);
BYTE* ptrbmpOriginal = (BYTE*) lpDIBBits;
memcpy(ptrbmpBits, ptrbmpOriginal, uBlockSize);

for(UINT rows=0; rows<bmpHeight; rows++)
{
    UINT offset = rows * bytesperrow;
    for(UINT colm=0; colm<bmpWidth*3-2; colm+=3)
    {
        int r, g, b, k, p;
        b = offset + colm;
        g = b + 1;
        r = b + 2;

        switch(PlaneNo)
        {
            case 501:
                k = g;
                p = b;
                break;
            case 502:
                k = r;
                p = b;
                break;
            case 503:
                k = r;
                p = g;
                break;
            default:
                ;
        }

        ptrbmpBits[k]=0;
        ptrbmpBits[p]=0;
    }
}

memcpy(ptrbmpOriginal, ptrbmpBits, uBlockSize);
delete[] ptrbmpBits;
EndWaitCursor();
::GlobalUnlock((HGLOBAL) m_hDIB);
SetModifiedFlag(TRUE);
UpdateAllViews(0);
}
}
}

```

B.5.2 Source Code for *Filter*

```

void CDibDoc::OnFilterbBluehoriz()
{

```

```

        JIHAO = 31;
        WANNENGFUN(JIHAO);
        SetModifiedFlag(TRUE);
        UpdateAllViews(0);
    }
-----
void CDibDoc::OnFilterbBluevert()
{
    JIHAO = 32;
    WANNENGFUN(JIHAO);
    SetModifiedFlag(TRUE);
    UpdateAllViews(0);
}
-----
void CDibDoc::OnFilterbGreenhoriz()
{
    JIHAO = 11;
    WANNENGFUN(JIHAO);
    SetModifiedFlag(TRUE);
    UpdateAllViews(0);
}
-----
void CDibDoc::OnFilterbGreenvert()
{
    JIHAO = 12;
    WANNENGFUN(JIHAO);
    SetModifiedFlag(TRUE);
    UpdateAllViews(0);
}
-----
void CDibDoc::OnFilterbRedhoriz()
{
    JIHAO = 21;
    WANNENGFUN(JIHAO);
    SetModifiedFlag(TRUE);
    UpdateAllViews(0);
}
-----
void CDibDoc::OnFilterbRedvert()
{
    JIHAO = 22;
    WANNENGFUN(JIHAO);
    SetModifiedFlag(TRUE);
    UpdateAllViews(0);
}
-----
void CDibDoc::Coefficient(double m_Butter)
{
    double PAI=3.1415926535;

    double Butt_c1, Butt_c2,Butt_c3, Butt_c;

    double ButtTemp=PAI*m_Butter/2;

    Butt_c1=tan(ButtTemp);
}

```

```

    Butt_c2=Butt_c1*Butt_c1;

    Butt_c3=Butt_c1*Butt_c2;
    Butt_c=Butt_c3+Butt_c2*2+Butt_c1*2+1;

    Butt_0b=Butt_c3/Butt_c;
    Butt_3b=Butt_0b;

    Butt_1b=Butt_c3*3/Butt_c;
    Butt_2b=Butt_1b;

    Butt_1a=(Butt_c3*3+Butt_c2*2-Butt_c1*2-3)/Butt_c;
    Butt_2a=(Butt_c3*3-Butt_c2*2-Butt_c1*2+3)/Butt_c;
    Butt_3a=(Butt_c3-Butt_c2*2+Butt_c1*2-1)/Butt_c;

}
-----
void CDibDoc:: WANNENGFUN(int JIHAO)
{
    WORD wNumColors;
    LPSTR lptoDIB;

    if(m_hDIB)
    {
        lptoDIB = (LPSTR) ::GlobalLock((HGLOBAL) m_hDIB);
        wNumColors = ::DIBNumColors(lptoDIB);

        if (wNumColors != 0)
        {
            MessageBeep(0xFFFFFFFF);
            AfxMessageBox("This is not a 24 - bit image");
            ::GlobalUnlock((HGLOBAL) m_hDIB);
        }
        else
        {
            CCutRatioDlg CR_dlg;
            int cr_results=CR_dlg.DoModal();

            double m_Butter;
            if(cr_results==IDOK)
                m_Butter = CR_dlg.m_CutRatio;

            BeginWaitCursor();

            switch(JIHAO) {
                case 11:
                    CalBGreenHoriz(m_Butter);
                    break;
                case 12:
                    CalBGreenVert(m_Butter);
                    break;
                case 21:
                    CalBRedHoriz(m_Butter);
                    break;
            }
        }
    }
}

```



```

        uNewValue = 0;
        if(uNewValue > 255)
            uNewValue = 255;

        ptrTemptwo[g+9]=(BYTE)uNewValue;
    }

}

memcpy(ptrTempone, ptrTemptwo, uBlockSize);

for(rows = 0; rows<bmpHeight; rows++)
{
    UINT offset = rows * bytesperrow;
    for(UINT colm = bmpWidth*3; colm>11; colm-=3)
    {
        int r, g, b;
        b = offset + colm;
        r = b - 1;
        g = b - 2;

        double uNewValue = ptrTempone[g]*Butt_3b +
            ptrTempone[g-3]*Butt_2b+ ptrTempone[g-6]*Butt_1b
            + ptrTempone[g-9]*Butt_0b -ptrTemptwo[g]*Butt_3a
            - ptrTemptwo[g-3]*Butt_2a
            - ptrTemptwo[g-6]*Butt_1a;

        if(uNewValue < 0)
            uNewValue = 0;
        if(uNewValue > 255)
            uNewValue = 255;

        ptrTemptwo[g-9] = (BYTE)uNewValue;
    }
}
memcpy(ptrbmpOriginal, ptrTemptwo, uBlockSize);

delete[] ptrTempone;
delete[] ptrTemptwo;
::GlobalUnlock((HGGLOBAL) m_hDIB);
}

-----
void CDibDoc::CalBGreen Vert(double m_Butter)
{
    Coefficient(m_Butter);
    LPSTR lptoDIB;
    LPSTR lpDIBBits;

    lptoDIB = (LPSTR) ::GlobalLock((HGGLOBAL) m_hDIB);

    UINT bmpWidth = (UINT)::DIBWidth(lptoDIB);
    UINT bmpHeight = (UINT) ::DIBHeight(lptoDIB);
    UINT bytesperrow=bmpWidth*3;
    while (bytesperrow%4)
        bytesperrow++;
}

```

```

UINT uBlockSize=bmpHeight*bytesperrow;
lpDIBBits =::FindDIBBits(lptoDIB);
BYTE* ptrbmpOriginal = (BYTE*) lpDIBBits;
BYTE* ptrTempone = new BYTE[uBlockSize];
BYTE* ptrTemptwo = new BYTE[uBlockSize];

memcpy(ptrTempone, ptrbmpOriginal, uBlockSize);
memcpy(ptrTemptwo, ptrbmpOriginal, uBlockSize);

for(UINT rows=0; rows<bmpHeight-3; rows++)
{
    UINT offset = bytesperrow;
    for(UINT colm=0;colm<bmpWidth*3-2; colm+=3)
    {
        int r, g, b;
        b = colm;
        g = b + 1 ;
        r = b + 2;

        double uNewValue = ptrTempone[g+offset*rows]*Butt_3b
            +ptrTempone[g+offset*(rows+1)]*Butt_2b
            +ptrTempone[g+offset*(rows+2)]*Butt_1b
            +ptrTempone[g+offset*(rows+3)]*Butt_0b
            -ptrTemptwo[g+offset*rows]*Butt_3a
            -ptrTemptwo[g+offset*(rows+1)]*Butt_2a
            -ptrTemptwo[g+offset*(rows+2)]*Butt_1a;

        if(uNewValue < 0)
            uNewValue = 0;
        if(uNewValue > 255)
            uNewValue = 255;

        ptrTemptwo[g+offset*(rows+3)]=(BYTE)uNewValue;
    }
    memcpy(ptrTempone, ptrTemptwo, uBlockSize);

    for(rows=bmpHeight-1; rows>2; rows--)
    {
        UINT offset = bytesperrow;
        for(UINT colm=0; colm<bmpWidth*3-2; colm+=3)
        {
            int r, g, b;
            b = colm;
            g = b + 1 ;
            r = b + 2;

            double uNewValue = ptrTempone[g+offset*rows]*Butt_3b
                +ptrTempone[g+offset*(rows-1)]*Butt_2b
                +ptrTempone[g+offset*(rows-2)]*Butt_1b
                +ptrTempone[g+offset*(rows-3)]*Butt_0b
                -ptrTemptwo[g+offset*rows]*Butt_3a
                -ptrTemptwo[g+offset*(rows-1)]*Butt_2a
                -ptrTemptwo[g+offset*(rows-2)]*Butt_1a;

            if(uNewValue < 0)

```

```

        uNewValue = 0;
        if(uNewValue > 255)
            uNewValue = 255;

        ptrTempTwo[g+offset*(rows-3)]=(BYTE)uNewValue;
    }
}
memcpy(ptrbmpOriginal, ptrTempTwo, uBlockSize);

delete[] ptrTempOne;
delete[] ptrTempTwo;
::GlobalUnlock((HGGLOBAL) m_hDIB);
}

```

B.5.3 Source Code for *Filter_1*

```

void CDibDoc::OnFilter1Blueplane()
{
    int Liebplane = 303;
    LiebmannFun(Liebplane);
}

```

```

void CDibDoc::OnFilter1Greenplane()
{
    int Liebplane = 302;
    LiebmannFun(Liebplane);
}

```

```

void CDibDoc::OnFilter1Redplane()
{
    int Liebplane = 301;
    LiebmannFun(Liebplane);
}

```

```

void CDibDoc::LiebmannFun(int Liebplane)
{
    LPSTR lptoDIB;
    LPSTR lpDIBBits;
    WORD wNumColors;

    if(m_hDIB)
    {
        lptoDIB = (LPSTR) ::GlobalLock((HGGLOBAL) m_hDIB);
        wNumColors = ::DIBNumColors(lptoDIB);

        if (wNumColors != 0)
        {
            MessageBeep(0xFFFFFFFF);
            AfxMessageBox("This is not a 24 - bit image");
            ::GlobalUnlock((HGGLOBAL) m_hDIB);
        }
        else
        {

```

```

BeginWaitCursor();
UINT bmpWidth = (UINT)::DIBWidth(lpDIB);
UINT bmpHeight = (UINT)::DIBHeight(lpDIB);
UINT bytesperrow = bmpWidth*3;
while (bytesperrow%4)
    bytesperrow++;

UINT uBlockSize = bmpHeight*bytesperrow;
lpDIBBits =::FindDIBBits(lpDIB);
BYTE* ptrbmpOriginal = (BYTE*) lpDIBBits;

BYTE* ptrTempone = new BYTE[uBlockSize];

memcpy(ptrTempone, ptrbmpOriginal, uBlockSize);

for(UINT rows=0; rows<bmpHeight-2; rows++)
    {
        UINT offset = (rows+1) * bytesperrow;
        for(UINT colm=0;colm<bmpWidth*3-6; colm+=3)
            {
                int r, g, b, k;
                b = offset + colm;
                g = b + 1;
                r = b + 2;

                switch(Liebplane){
                case 301:
                    k = r;
                    break;
                case 302:
                    k = g;
                    break;
                case 303:
                    k = b;
                    break;
                default:
                    }

                }
        UINT uNewValuered=(ptrTempone[k]+ptrTempone[k+6]
            +ptrTempone[k-
                bytesperrow+3]+ptrTempone[k+bytesperrow+3])/4;

                ptrTempone[k+3]=(BYTE)uNewValuered;
            }
        }
    MessageBeep(0xFFFFFFFF);
    memcpy(ptrbmpOriginal, ptrTempone, uBlockSize);
    delete[] ptrTempone;
    EndWaitCursor();
    ::GlobalUnlock((HGLOBAL) m_hDIB);
    SetModifiedFlag(TRUE);
    UpdateAllViews(0);
    }
}
}

```

Figures

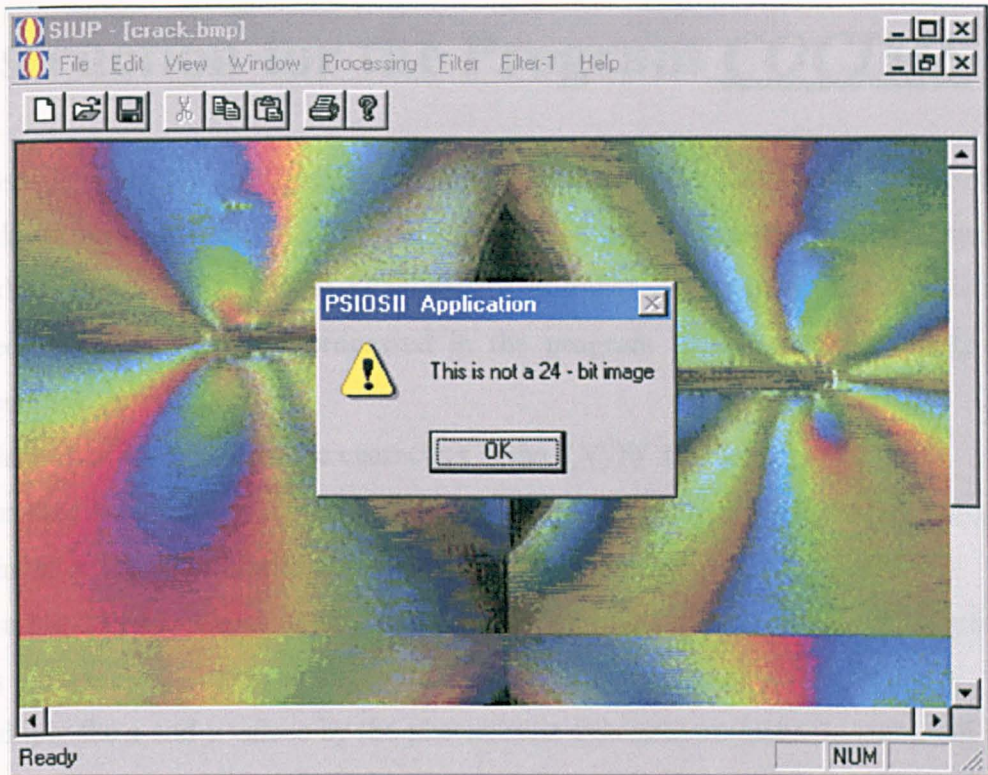


Figure B.4.1 Warning message for image that is not a RGB image.

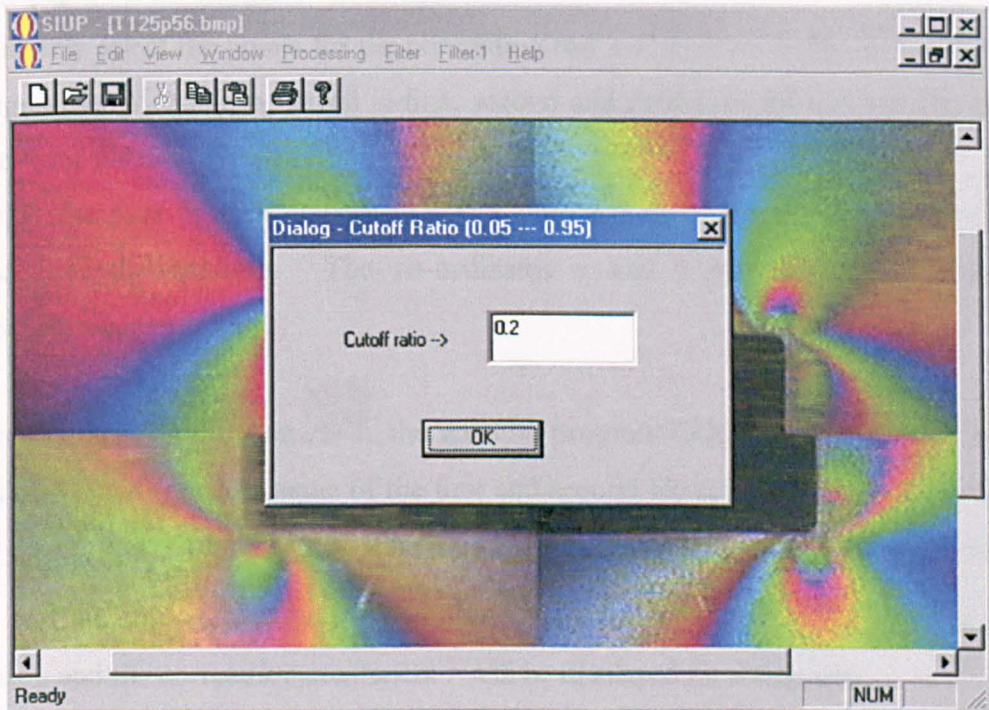


Figure B.4.2 Dialogue box for input cut-off ratio in *Filter*.

Appendix C

Instruction for the Program COCIMS

To use the program COCIMS, you need to provide three files – two files from photoelastic analysis using VIZION or PECAN and a file from the Finite Element Method (FEM). The file from FEM can be in either .txt or .prn format. Data obtained from FEM can be processed in the program EXCEL using procedure described below.

- (1) Delete all of the non-numeric characters in the ANSYS .txt file.
- (2) Translate the origin of the co-ordinates of the finite element data to the top-left point as in the photoelastic map.
- (3) You may need to create negative y co-ordinates to make sure that the FEM map has the same orientation as the photoelastic map.
- (4) Multiply the x and y values by the photoelastic enlargement factor to get x and y in pixels that match the photoelastic map. The photoelastic enlargement factor is number of pixels per mm in the photoelastic map. It can be obtained using a scale paper on the images.
- (5) Randomly select the points for the correlation test and their co-ordinates x , y and fringe order N should be saved in first, second and third columns sequentially of a new .txt file.
- (6) Check the data in each column to make sure that there are no characters, or spaces in the columns. The co-ordinates x and y should be inside the photoelastic map.

When you click on the icon  , the window program COCIMS will open. The user will be asked to select name of the first and second file and a .txt or .prn file in the file dialog box. Afterwards you should click on the *Coefficient* inside the menu Cocim or click the icon  on the tool bar. Number of points selected for the calculation and the correlation coefficient r will be displayed on the screen.

The program is designed to process a maximum of 1000 data points.

D.1 Source Code for the Filename: co_fem.h

```

#include <fstream>
using namespace std;

int round(float num);

class N_fem {
    int count, countnum;
    float *p1,*N_n;
    char str[10], *p;
    char ch1;
    char strf[80];
    int *N_x, *N_y;
    char *sf;
    float *n_p;

public:
    N_fem();
    ~N_fem() {
        delete [] n_p;
        delete [] N_x;
        delete [] N_y;
        delete [] N_n;
        delete [] sf;
    }
    float *get_fem(ifstream &fin);
    void calcu(float *pk);
    int *Get_x(void) {return N_x;}
    int *Get_y(void) {return N_y;}
    float *Get_n(void) {return N_n;}
    int Get_count(void) {return count;}
    int Get_countnum(void) {return countnum;}
    char *Get_namestr(void) {return sf;}
    float *Get_np(void) {return n_p;}
};

float coefficient(float *te, float *tf, int count);

```

D.2 Source Code for the Filename: co_epe.h

```

#include <iostream>
#include <cstring>

using namespace std;

class V_fac {
    char str1[80], str2[80];
    char *s1, *s2;
    float factor_1, factor_2;

public:
    V_fac();
    ~V_fac() {
        delete [] s1;
        delete [] s2;
    }
}

```

Appendix D

Source Code of the Program Cocims

D.1 Source Code for the Filename: co_fem.h

D.2 Source Code for the Filename: co_epe.h

D.3 Source Code for the Filename: COCIMS.cpp

D.4 Source Code for the Filename: co_fem.cpp

```

char *Get_names1(void) {return s1; }
char *Get_names2(void) {return s2; }
float get_fac1(float *pef1) {
    factor_1 = pef1[0];
    return factor_1;
}
float get_fac2(float *pef2) {
    factor_2 = pef2[1];
    return factor_2;
}
};

/* Constructor input filenames from program PECAN */

V_fac::V_fac() {
    cout<<"\nEnter the FAC file name: ";
    cin>>str1;
    strcpy(str2,str1);
    strcat(str1, ".fac");
    strcat(str2, "1.epe");

    int l;
    l=strlen(str1);
    l+=1;
    s1=new char [l];
    l+=1;
    s2=new char [l];

    strcpy(s1,str1);
    strcpy(s2,str2);
}

/* Function for calculate fringe order from the .fac and .epe file */

float &get_Nepe(short *m, float fact1, float fact2, float *p_epe)
{
    int i;

    for(i=0; i<65536; i++)
        p_epe[i] = fact1 * (fact2 + m[i]);

    return p_epe[i];
}

/* Function for printing error message */

void printerror(char *p)
{
    char *str;
    if(*p)
        str = p;

    cout<<str;

    cout<<"\nPress any charactor to terminate.\n";
    char ch;
    cin>>ch;
}

```

```

/* Function for instruction */

void instruction(void)
{
cout<<"The program is written by S. J. Zhang and E. A. Patterson \n";

cout<<"for calculating correlation coefficient of image maps. \n";
cout<<"You need provide a .fac, a .epe file and a data file in .txt or .prn from FEM. \n";
cout<<"Following the instruction\n";
}

```

D.3 Source Code for the Filename: COCIMS.cpp

```

/* Read data from the fac file */
#include <iostream>
#include <fstream>
#include <iomanip>
#include "coc_epe.h"
#include "co_fem.h"
using namespace std;

int main()
{
    instruction();

    char chr;
    do {
/* Input a .fac file to get two factors for the .epe file */
V_fac ob;
char pname1; /* Pointer to fac filename */
pname1 = ob.Get_names1();

ifstream in_fac(pname1, ios::in|ios::binary);

if(!in_fac){
    perror("\nCannot open the (.fac) file\n");
    exit(1);
}

float n[6]; /* Hold data in .fac */
in_fac.read((char *) &n, sizeof(n));

float factor1, factor2; /* First two data in .fac file */
factor1 = ob.get_fac1(n);
factor2 = ob.get_fac2(n);
in_fac.close();

/* Input a .epe file to get raw data */
char pname2; /* Pointer to .epe filename */
pname2 = ob.Get_names2();

ifstream in_epe(pname2, ios::in|ios::binary);

if(!in_epe){
    perror("\nCannot open the (.epe) file\n");
    exit(1);
}
}

```

```

    }
    short m[256*256]; /* hold data from epe file */
    in_epe.read((char *) &m, sizeof(m));

/* Calculating fringe order N in the epe file */
    float *p_epe;
    p_epe = new float [65536];
    get_Nepe(m, factor1, factor2, p_epe);
    in_epe.close();

/* Open file for reading data from FEM */
    N_fem obf; /* create a object */

    char nstr; /* pointer to filename */
    nstr = obf.Get_namestr();

    ifstream in_fem(nstr, ios::in|ios::binary);

    if(!in_fem){
        perror("\nCannot open the file from FEM\n");
        exit(1);
    }
    obf.get_fem(in_fem);
    in_fem.close();

    float pnp; /* Receive the array of x,y, and N */
    pnp = obf.Get_np();
    obf.calcu(pnp);

    int count1, count2; /* count2 is No. element after B checking */
    count1 = obf.Get_count();
    count2 = obf.Get_countnum();

    int px, py; /* Receive array of x, y */
    px = obf.Get_x();
    py = obf.Get_y();

    float *pn; /* Receive fringe order N */
    pn = obf.Get_n();
    cout<<"\n";

/* Find N from the .epe file according to coordinates x, y */

    float *pe;
    pe = new float [count2];

    int i;
    for(i=0; i<count2; i++){
        int k;
        k = 256 * py[i] + px[i];
        pe[i] = p_epe[k];
    }
    float c; /* Receive the r */
    c = coefficient(pe, pn, count2);

    delete [] pe;
    delete [] p_epe;

```

```

cout<<" "<<count2<<" points were selected for the calculation. \n\n";
cout<<"Correlation Coefficient of two maps is "
<<setprecision(4)<<c<<"\n\n";
cout<<"Press (Y) to continue OR ";
cout<<"Press other charactor to terminate: ";

    cin>>chr;
    if(chr=='Y')
    chr='y';
    }while(chr=='y');
    return 0;
}

```

D.4 Source Code for the Filename: co_fem.cpp

```

#include <cstring>
#include <cctype>
#include <cmath>
#include <iostream>
#include "co_fem.h"
using namespace std;

/* Construct filename for data from the FEM */

N_fem::N_fem(){
    cout<<"Enter file name with extention (FEM): ";
    cin>>strf;
    int l;
    l=strlen(strf);
    l+=1;
    sf=new char [l];
    strcpy(sf,strf);

    n_p=new float[3001];
    p1=n_p;
}

/* Read .txt or .prn file and convert them to float numbers*/

float *N_fem::get_fem(ifstream &fin){
    count=0;
    do {
        p=str;
        ch1 = fin.peek(); /* What type of char is next */

        if(isdigit(ch1)) {
            count++; /* Number of data in the file */

            while(!(isspace(*p=fin.get())) && !fin.eof())
                p++;

            fin.putback(*p); /* Return char to the stream */
            p = '\0'; /* Null-terminate the string */
            *p1 = atof(str);

            if(!fin.eof())

```

```

                p1++;
            }
            else
            fin.get();    /* ignore */
            } while(!fin.eof());

        count/=3;
        return p1;
    }

/* Function for round of X, Y from float to int */

int round(float num){
    double frac;
    double val;
/* Decompose num into whole and fractional parts */
    frac = modf((double)num, &val);
    if(frac < 0.5) num = val;
    else num = val + 1.0;
    return (int)num;
}

/* Function for calculate correlation coefficient of maps */
float coefficient(float *te, float *tf, int count){
    float sume, sumse;    /* sum for .epe file, s means squared sum */
    float sumf, sumsf;    /* sum for .fem file */
    sume = 0;
    sumse = 0;
    sumf = 0;
    sumsf = 0;
    int i;
    for(i=0; i<count; i++){
        sume += te[i];
        sumf += tf[i];
        sumse += (te[i] * te[i]);
        sumsf += (tf[i] * tf[i]);
    }
    sume *= sume;
    sumf *= sumf;

    float f;
    float e;
    f = sumsf - sumf*sumf/count;
    e = sumse - sume*sume/count;

    float R; /* R is the squared coefficient */

    if(f/e<1)
        R = f/e;
    else
        R = e/f;
    float Ra; /* Ra is adjusted coefficient */
    int counta1, counta3;
    counta1 = count-1;
    counta3 = count-3;

    Ra = (R*counta1 - 2)/counta3;

```

```
    Ra = sqrt (Ra);

    return Ra;
}

/* Boundary check of the image and delete data outside the B */

void N_fem::calcu(float *pk){
    countnum = 0;
    int i;
    for(i=0; i<count; i++){
        iff((pk[3*i]>255) || (pk[3*i]<1) || (pk[3*i+1]>255) || (pk[3*i+1]<1))
            ;
        else
            countnum++;
    }
    N_x = new int [countnum];
    N_y = new int [countnum];
    N_n = new float [countnum];
    int k =0;
    for(i=0; i<count; i++){
        iff((pk[3*i]>255) || (pk[3*i]<1) || (pk[3*i+1]>255) || (pk[3*i+1]<1))
            ;
        else {
            N_x[k] = round(pk[3*i]);
            N_y[k] = round(pk[3*i+1]);
            N_n[k] = pk[3*i+2];
            ++k;
        }
    }
}
```